University of Alberta

$[\pm 60°_3]_T$ Glass Fibre Reinforced Epoxy Tubes and the Influence of an Interleaf on Transverse Cracking and Fluid Containment

by

Garret Meijer

A thesis submitted to the Faculty of Graduate Studies and Research
in partial fulfillment of the requirements for the degree of

Doctor of Philosophy

Department of Mechanical Engineering

Edmonton, Alberta
Fall 2006

Your file Votre référence
ISBN: 978-0-494-23082-4
Our file Notre référence
ISBN: 978-0-494-23082-4

ABSTRACT

It is commonly observed in unidirectional glass fibre reinforced epoxy plies that a small applied transverse stress leads to micro-cracking in the matrix that may lead to delamination of plies in a laminate or leakage in pipe and pressure vessel applications. In this investigation it is proposed that the addition of an appropriate interleaf will delay transverse cracking and prevent fluid loss from filament wound tubes.

The problem was approached from two directions: 1) propagation of a transverse crack through a thick laminate, and 2) adding an interleaf to a filament wound, glass fibre reinforced epoxy tube.

Testing of notched, thick cross-ply, coupon specimens with a polyethylene interleaf demonstrated that rapidly growing cracks were stopped by the interleaf and only continued to grow after delay of numerous stress cycles. It was concluded that the crack delay was the result of poor bonding of the interleaf to the composite structure, requiring the initiation of a new crack within the remaining intact composite layers.

A nonlinear transversely isotropic, viscoelastic material model was developed to represent the time dependent response of the fibre reinforced polymer. The creep moduli employed in the model are a function of the von Mises effective stress within the matrix as estimated from simplified unit cell analysis and are dependent on the fibre orientation..

A parametric, viscoelastic finite element study of the transverse crack specimen demonstrated that the strain energy release rate increases as the crack tip approaches the soft interleaf but then rapidly drops to a minimum value as the crack tip traverses the interleaf. The minimum strain energy release rate is reduced by decreasing the interleaf

stiffness, moving the interleaf towards the crack initiation surface, increasing the interleaf thickness and accounting for stress relaxation and creep strain around the crack tip due to the viscoelastic material response.

Testing of filament wound tubes showed that the interleaf does increase strength over a narrow range of hoop/axial stress ratios. However, poor bonding of the interleaf led to segregation of the internal structural layers resulting in lower failure stresses at larger strains when the hoops stress was large. A maximum strain failure criterion was found to enclose the experimental failure envelope but did not adequately account for local leakage and axial compression type failures.

ACKNOWLEDGEMENTS

The author wishes to thank all those that contributed to this research and graduate studies experience.

A special thank you to supervisors Dr. Fernand Ellyin and Dr. Zihui Xia for their leadership and guidance.

Thank you also to the machinists and technicians of the Department of Mechanical Engineering. The author would like to recognise, in particular, Bernie Faulkner for maintaining and modifying the test equipment and Rick Bubenko for machining the tube specimen grips and tabs.

The author also wishes to express appreciation to Rick Patsula and Mark Ackerman who assisted this research by providing computer hardware support, as well as moral support.

Finally, a thank you to the members of the Advanced Composite Materials Engineering research group whose comments and criticisms have contributed to this research. Thank you also for all the extracurricular activities that made this an enjoyable and interesting experience.

This thesis is dedicated to Michele and Michael.

Everyday I learn more about being a husband and father
and it is this education that is most rewarding.

TABLE OF CONTENTS

TABLE OF CONTENTS

LIST OF TABLES

LIST OF FIGURES

LIST OF FIGURES

CHAPTER 1 INTRODUCTION

A composite material may be described as one produced by the combination of two or more separate materials in order to take advantage of specific properties of the individual constituents or characteristics of the resulting composite material. While the basic concept of a composite material has been taken advantage of for thousands of years and basic analysis techniques have been understood for at least a century, it is only recently that these advanced materials have been used to replace conventional materials in demanding applications and the composite design methodology developed.

A contribution to the slow evolution of composite materials is the broad range of constituent materials available. Not only may the matrix and reinforcement be of ceramic, metal, thermoset or thermoplastic but the reinforcement may also be of various geometries such as fibre, whisker or particle. This leads to anisotropy of the mechanical properties including stiffness, strength as well as the failure mechanisms. Therefore, compared to conventional isotropic materials, composite materials often require a more elaborate and technically difficult design process.

1.1 USE OF COMPOSITE MATERIALS

Even though they may be more difficult to apply, composite materials have found use in a broad range of applications due to specific properties and the ability to have the engineer design the material for optimum strength and stiffness in preferred orientations. Composite materials are used extensively in the aerospace industry to reduce structural weight in order to increase fuel efficiency and payload. While initially applied to non-structural applications or on specialized equipment, composites structures are now being implemented for load bearing members on commercial aircraft. (Marsh, 2005)

Corrosion resistant composite materials have found extensive use in chemical environments and for transporting highly corrosive fluids. Applications in natural resource extraction, whether for fire water distribution on off shore platforms or in stringers and down-hole tubulars, take advantage of the corrosion resistance, light weight and high specific strength (Lundberg et al., 2001; Ellyin et al., 2000; Frost and Cervenka,

1994). The light weight decreases transportation, handling and installation costs by reducing the capacities of equipment and, in turn, the fuel consumed. It is also noted that composite pipe may be produced with an exceptional interior wall smoothness resulting in less pressure loss and reduced fouling of the pipe (Lundberg et al., 2001).

Of course there are also many concerns with the use of composites in pipelines. The industry has very little experience with these advanced materials thus design methods must be developed and the solutions proven. Conventional means of installation and joining cannot be used so there is the requirement of replacing expensive infrastructure and further development of processes. It is also well known that typical composite laminates are susceptible to damage. While yielding in metals will allow for stress redistribution around defects and damage, glass fibre reinforced epoxy tends to display brittle elastic behaviour and defects and damage tend to increase rapidly with increases in load and service life. This raises particular concern with installation conditions and procedure.

While tolerant to many hydrocarbons, epoxy does absorb water resulting in swelling and possible damage (Ellyin, 2004; Ellyin and Maser, 2004; Ellyin and Rohrbacher, 2003; Ellyin and Rohrbacher, 2000; Perreux and Suri, 1997; Chateauminois et al., 1993). It has also been observed that glass fibre is prone to stress corrosion cracking (Ehrenstein and Spaude, 1984; Jones et al., 1983). These issues must be studied and consequences of such conditions evaluated. These challenges may be overcome by modifications to the constituents, the fabrication process or as part of the design solution. For example, ECR-glass is now produced with a greater corrosion resistance and epoxy formulations have also been modified for greater toughness and moisture resistance.

Composite materials are slowly being used for more and more structurally demanding components in more severe service environments, however there is still reluctance in industry to use composite materials in critical load bearing roles such as high pressure pipelines. This is due to a number of reasons including lack of reliable failure data and design procedures, significantly different handling and installation methods than for metal components, costs of required new and updated equipment as well as the costs and

availability of the raw materials (Ellyin et al., 2000). It is anticipated that increasing the knowledge of and experience with composite materials, and fibre reinforced polymers in specific, will lead to greater use of these materials.

1.2 MATERIAL SYSTEMS

There is a broad range of materials available for both the matrix and reinforcement phases of the composite material. The selection of materials is based upon the desired mechanical, thermal, chemical and electrical properties, production and finishing facilities available and design experience.

1.2.1 Matrix Materials

In structural composites, the matrix is required to maintain the reinforcement position and orientation and transfer load between the reinforcement. Matrix materials include metals, ceramics and thermoplastic and thermoset polymers.

Metal matrix composites are commonly used in applications where greater stiffness and wear resistance are required. For example, alumina and silicon carbide particulate reinforced aluminum are used in suspension components, engine cylinder linings and brake disks. Another example, carbon matrix reinforced with carbon fibre (referred to as carbon/carbon composite) has become the choice material for high temperature applications such as brake components in high performance vehicles and aircraft. Phenolic polymers are also used as a matrix in high temperature composites. Thermoplastic polymers are gaining acceptance because of the greater toughness than thermosets, resistance to moisture and the ability to reform the part with the application of heat. This last point is of considerable importance not only when discussing ease of repair but also when the composite must be recycled. However, the most popular matrix materials are the thermoset polymers.

While polyester is used for many low stress applications such as recreational watercraft, automotive body panels, sports equipment, tanks and low pressure pipes, the more expensive epoxies are used in structural applications such as aircraft and aerospace applications and light weight performance vehicle structural components. Numerous

formulations of epoxies are available, optimized for specific manufacturing processes and specific material properties. Epoxies of various pot life and viscosity have been developed to suit production methods. For example, resins for filament winding have a low viscosity to allow fibre wetting in the resin bath and a long pot life so that gelation and cure will commence only after the entire component is completed. Epoxies may also be modified to increase toughness, change chemical compatibility or increase temperature operating range. Therefore an extensive range of matrix materials is available to the design engineer.

1.2.2 Reinforcement Materials

The selection of reinforcement materials is also large and covers a wide range of metals, ceramics and polymers. Geometry of the reinforcement is also of great importance as it will contribute to the material properties and anisotropy, machinability and cost of constituents. Boron fibres have been used in metal matrix composites as have alumina and silicon carbide whiskers and particles. Particulate reinforcement is often further divided into sub categories based on geometry such as spheres or platelets. While aligned fibre reinforcement results in highly directional material properties, particulate is generally considered to result in an isotropic response. Whisker reinforcement may be aligned, depending on fabrication methods, resulting in slightly anisotropic behaviour. Ceramic matrix composites are often reinforced with softer elastomeric particulate to increase the toughness and ductility. Recently thermoplastic fibres such as nylon, polyethylene, and polypropylene have been developed. As with the more conventional fibre reinforcement, it has been found that thermoplastics exhibit greatly increased strength when drawn into a fibre of well aligned and defect free polymer chains. These fibres are favoured for ductility and corrosion resistance.

Currently, the most common reinforcements for reinforced polymers are glass, carbon and aramid fibre. While glass fibre is of high strength it has relatively low stiffness and high density compared to carbon and aramid fibres, it has generally been less expensive and thus commonly used. The impressive toughness of aramid fibre comes at a great expense and with low compressive strength and low shear strength. Therefore aramid

fibre is mostly limited to specialised applications, often as an additional reinforcement only in specified locations of a structure. While carbon fibre has been considered a high price, high performance reinforcement, production has been increased and it is now readily available at costs only marginally higher than that of high strength glass fibre.

Fibre reinforcement is available in many forms depending on application and manufacturing process. In its basic form, fibre is provided as an untwisted yarn at a specified weight per unit length. The yarns, provided on creels, are directly applied to processes such as filament winding and chopped fibre spray-up. Random oriented fibre mats are produced by coating continuous or chopped fibre with a binder and then spraying or placing it on a sheet mould. Glass, carbon and aramid fibre may also be woven into fabric. In its most common form the fabric is woven with an equal amount of reinforcement oriented perpendicularly however angles may be manipulated and the amount of reinforcement in any direction varied to suit the application. Fabrics are available in various weights (g/m^2) and denier.

Having discussed the various types of matrix and reinforcement materials available and the various geometries of reinforcement, the remainder of the text shall concentrate on E glass fibre reinforced epoxy composite. E glass fibre is formulated for corrosion resistance rather than high strength and is much more economical to use. However, references to various matrix and reinforcement types will be used to demonstrate differences or as examples of studies not conducted on glass fibre reinforced epoxy.

1.3 COMPOSITE MATERIAL PROPERTIES

Glass fibre reinforced epoxy is often used because of enhanced beneficial material properties. However, it is inevitable that this engineered composite may also have some detrimental properties due to either the glass or epoxy constituents or having combined the two.

Fibre reinforcement results in highly directional material properties thus a component may be engineered to have great strength and stiffness in the anticipated load direction with little strength or stiffness in the others. The large differences in the material

properties of the constituents may also lead to situations which are opposite to the intuition of an engineer trained in the mechanics of isotropic materials. For example, using orthotropic composite laminae it is realistic to produce laminates with a negative Poisson's ratio.

Not only is the load displacement response very anisotropic but the strength is as well. While the glass fibre has high strength, the epoxy matrix has relatively low strength and high ductility. However, the matrix filling the space between the fibres is subject to large stress and strain concentrations leading to a low transverse strength of the composite. It is often considered that the strength lies only along the axis of the reinforcement and that no loads should be applied in the transverse direction. This is the assumption of the simple netting analysis approach that is often used as a first approximation in design problems.

As with the stiffness and strength, the thermal-mechanical response of the composite is also dependent on the characteristics of the constituents and the geometric arrangement. The coefficient of thermal expansion of the epoxy matrix is approximately $56x10^{-6}/°C$ (Resolution Performance Products, 2001) as compared to $5.4x10^{-6}/°C$ for the glass fibre (Owens Corning, 1999). Thus cooling from cure to operating temperature may result in large thermal strain and stress within the composite. At best, this results in warping of components that must be considered in the design of moulds and the selection of the fabrication process. At worst, processing induced thermal stresses and strains may result in micro and even macroscopic damage (Rodriguez, 1989). Laminate wrinkling is often the result of these thermal strains in flat long fibre laminates. Of course, as with the stiffness, these thermal characteristics may be an advantage as well. Laminate materials and geometry may be defined such that in specified orientations, the composite has no deformation under thermal loading.

It is well documented that most polymers demonstrate time dependent mechanical behaviour. Under constant external load they creep and under constant external displacement they relax. This viscous behaviour is also observed in fibre reinforced composites in which the matrix is polymeric (Kujawski and Ellyin, 1995). However,

depending on the reinforcement material, the viscous effect will be anisotropic like the stiffness.

While a fibre reinforced composite material may be highly optimized for an application and applied to a structure in a very efficient manner, the design procedure is very complex and relies on more extensive calculations and experience. The engineer may take advantage of the mechanical properties to optimize the composite only if they have considered the highly anisotropic nature of the stiffness and strength and have ensured processing is compatible, accounting for the large mismatch in the coefficients of thermal expansion of the constituents.

1.4 FABRICATION OF COMPOSITE LAMINATES

There are numerous methods of producing laminates such as hand lay-up, resin transfer moulding, etc. This discussion will consider the two methods used in this investigation: hand lay-up of pre-impregnated composite sheet and wet filament winding.

1.4.1 Hand Lay-Up of Pre-Impregnated Sheet

A difficult part of manufacturing fibre reinforced polymers is ensuring that the fibres are well coated with the matrix material and controlling the ratio of polymer matrix to reinforcing fibre. The use of pre-impregnated sheet eliminates this concern from the assembly process. Pre-impregnated sheet, often referred to as pre-preg, is manufactured in a controlled environment by a precision machine. A partially cured composite is produced by laminating a sheet of dry fibre with a sheet of B-stage cured neat epoxy and pressure is then applied to consolidate the resin into the fibre structure. Reinforcement types include glass, carbon and aramid in unidirectional, random or woven layers. The result is a high quality, raw laminate material of constant thickness, fibre volume fraction and reinforcement orientation.

The laminae may be assembled by hand lay-up over a mould. Generally, simple geometries are required because the partially cured lamina does not drape well over the mould. However, narrow pre-preg tape is now used on automated, three dimensional fibre placement equipment to lay-up complicated components. The final component is

often cured by applying heat, pressure and vacuum to consolidate the laminate and withdraw volatiles which may produce voids or surface imperfections.

1.4.2 Filament Winding

In its most basic form, filament winding is the wrapping of a tow, or multiple tows of fibre around a rotating mandrel by feeding the fibre through a payout eye attached to a carriage that travels up and down the length of the mandrel. By coordinating the mandrel rotation and the carriage speed, the winding angle is easily controlled. This method of producing composite parts was developed in the 1950's and has evolved to become a highly automated means of producing quality composite parts. Filament winding machines that produce a number of geometries, from small to very large, are commercially available or may be custom built. There are a number of parameters that may be varied to control the characteristics of the composite component and this must now be included in the design process (Lossie and van Brussel, 1994).

In filament winding, a number of tows are used to produce a larger bandwidth and decrease the winding time. If the bandwidth is wide enough an entire ply of unidirectional reinforcement is applied in a single pass, but it is common to require a number of passes to produce full coverage of the mandrel. The number of passes required is dependent on the bandwidth of fibre placed on each pass, the mandrel diameter and the reinforcement angle. Full coverage by a unidirectional ply may still be applied by using a geodesic winding pattern (requiring a closed end mandrel), reversing the mandrel on the return trip or cutting the fibres. The latter two options clearly require specialised retention of the reinforcement to prevent slippage. In the production of open ended tubes, it is more common to continue winding on the return stroke at the opposite angle producing an interwoven $\pm\theta$ layer shown in Figure 1.1.

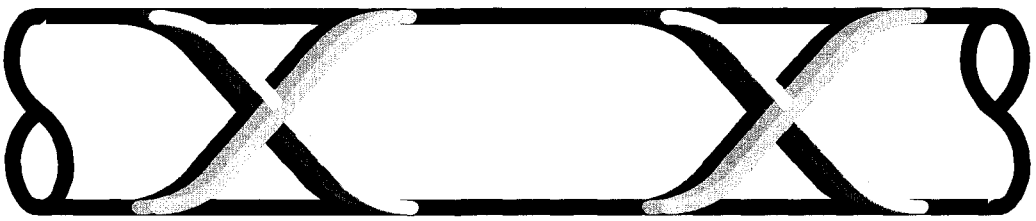

Figure 1.1: Schematic of helical winding process as coverage increases with number of passes. The band is shown in a lighter shade for each consecutive pass.

However, the cross-overs in the weave pattern lead to undulations of the fibre and resin rich reticular regions as demonstrated in Figure 1.2. Studies have found that the weaving has little effect on the stiffness of the component but that the strength will vary with the number of cross-overs (Lossie et al., 1989; Rousseau et al., 1999). Another important variable in this filament winding process is the dwell angle. The dwell angle is used to increase contact area at the ends of the mandrel to reduce slippage as the orientation of winding is reversed for the return stroke. It is calculated and controlled to ensure that the current fibre band being wound lies next to the previous one with minimal overlap and no gap between the two. For a simple constant radius, cylindrical mandrel the calculation of the required parameters is relatively simple (Rousseau et al., 1999).

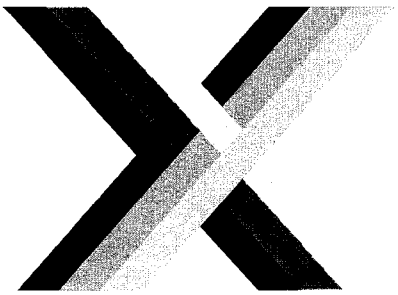

Figure 1.2: Helical winding interweaving that leads to fibre undulation.

The mandrel is an integral component that supports the reinforcement and wet matrix during winding and cure yet must be easily removable without damaging the composite structure. Mandrels are commercially available for a number of geometries and scales. For open ended structures, such as pipe, the mandrel may be a simple solid shape that is forcefully extracted following cure. Mandrels may also be made collapsible to reduce extraction loads or from soluble materials so that it may be flushed through a small end

opening. Care must be taken when selecting mandrel materials, as the mandrel will be subject to cure temperatures and will undergo thermal deformation having an effect on the geometry and residual stresses/strains in the resulting composite part.

The addition of epoxy resin to the composite system may occur during winding by pulling the fibres through a resin bath, prior to winding by employing a pre-impregnated tape or after winding by resin infusion. The first two are referred to as wet winding and tape winding respectively. Resin infusion into a filament wound pre-form is not a common procedure, but may become more acceptable as resin infusion techniques are improved. Wet winding requires the use of a resin bath which provides some means of separating the fibres, within the tow, and saturating them with resin. This is usually done by pulling the tensioned tows over a drum that is either submerged or coated with resin. The amount of resin carried on the fibre from the resin bath is controlled by the resin viscosity, fibre speed and fibre tension. Obstacles such as guiding pins, along the remainder of the fibre path will also affect the amount of resin that reaches the mandrel.

Additional equipment required for filament winding includes a creel stand to hold the bundles of fibre. Tensioning of the fibres in commercial applications is often done using the friction of pulling the tows through a number of ceramic eyelets but may be done using a specialised tensioning stand. Tensioning of the fibre promotes consolidation of the composite layers on the mandrel and therefore has influence on fibre volume fraction in the resulting component. Fibre tensioning is also applied to counteract the thermal stresses and strains developed during cooling from cure temperatures. It has been observed that increasing volume fraction and/or fibre tension produces greater strength in tubular specimens (Cohen, 1997; Cohen et al., 2001; Mertiny and Ellyin, 2002)

Should the epoxy resin require heat to cure or to increase the rate of cure, an oven or radiant heater is also required.

It should be noted that this process has been highly automated and the generation of filament winding patterns and actual control of the equipment is often done on a computer. This process has also been adapted to produce continuous pipe with diameters

around 100 mm in segments 100's of metres long. This product, however, is designed to be flexible so that it can be coiled on spools for transportation to the worksite (Lundberg et al., 2001).

Filament winding is not restricted to the use of epoxy or thermoset resins. There is great interest in filament winding tubes using fibre reinforced thermoplastic. This may be achieved by a change in resin impregnation of the fibre and the addition of fibre path heating, however, careful consideration of processing properties such as resin viscosity and mandrel temperature are necessary to produce quality components (Henninger and Friedrich, 2002a; Henninger et al., 2002b; Gibson et al., 2000). Winding and placement of fibre reinforced thermoplastic tape are alternative manufacturing methods (Kruijer et al., 2005).

Details of the filament winding process and facility used to produce the tubular specimens in this investigation may be found in Appendix A and in Wolodko et al. (2001). The author contributed to the development of this facility through participation in the selection of the key equipment as well as designing the structural components of the glass fibre tensioning system and the tension control system programming.

1.5 COMPOSITE PIPE FAILURE

It is of great importance to the designer to understand under what conditions the composite component will fail. While this will also include the influence of environment and aging the following discussion will consider only failure due to mechanical load conditions. As with the stiffness, the failure stresses and strains and failure mode are very dependent on the orientation and type of loading.

1.5.1 Functional Failure: Weepage and Local Leakage

When using composite materials for a pipeline application one must not only consider the structural failure of the pipe but also when it can no longer fulfill the requirements of the application. For example, it is observed that under some load conditions, glass fibre reinforced epoxy may leak while maintaining the structural loads. Therefore two failure points are defined as: 1) structural failure when structural collapse occurs and can no

longer carry load and 2) functional failure when the pipe can not contain a pressurised fluid. Clearly when a pipe is leaking, it is no longer fulfilling its requirement to contain a pressurised fluid.

Functional failure is often found to be in the form of weepage, which is described as the slow leakage of fluid through the wall of the pipe and observed as the uniform formation of fluid droplets on the pipe exterior. As time progresses the droplets accumulate and fluid begins to drip. Weepage occurs due to the coalescence of transverse cracks forming well distributed fluid paths through the pipe wall.

In this investigation it was also observed that functional failure may also be in the form of local leakage. This phenomenon was found to occur at a higher internal pressure than weepage and takes the form of very well defined jets of fluid spraying from the tube. Leakage of this manner was much more rapid. (Soden et al., 1989)

1.5.2 Transverse Cracking

The transverse cracking that leads to weepage and local leakage is a well observed and studied failure mode in fibre reinforced laminates. Although the polymer matrix may have high ductility, the large stress and strain concentrations in the matrix between the tightly packed fibres in a composite with a high volume fraction of reinforcement, result in damage at low transverse stresses and strains. As a result, it is common in some applications to produce a laminate using a number of fibre orientations to reduce the risk of transverse failure. However, the high strength but relatively low stiffness of glass fibres allows for moderate longitudinal strains and therefore transverse strains in neighbouring plies of different orientation may be sufficient for matrix cracking and fibre debonding (Bailey and Parvizi, 1981). For example, in a glass/epoxy $[0°_2, 90°_3]_s$ cross-ply, it was observed that transverse cracking initiated at approximately 0.5% strain (Hoover et al., 1997). The number of cracks then increased as the load was increased, corresponding to a significant drop in specimen stiffness.

Transverse cracking is characterised by numerous, approximately equally spaced, matrix cracks parallel to the reinforcement. It is observed that as the stress or strain is increased

the crack density increases and a characteristic damage state may be reached (Highsmith and Reifsnider, 1982). Numerous techniques of analysing the stiffness drop associated with transverse cracking assume that load is transferred to the 90° ply from the constraining plies via shear. As the external load is increased sufficient stress is developed in the segment of 90° ply, already bounded by transverse cracks, to develop a new crack in the middle of the segment.

A thorough review of experimental observations and stiffness loss modelling techniques is provided by Berthelot (2003) and further comparison of stiffness prediction techniques is provided by McCartney et al. (2000). Micromechanical models have also been employed in numerical techniques to study the effects of reinforcement distribution and material properties (Knight et al., 2003; Vejen and Pyrz, 2002)

Transverse cracking is not always considered of serious consequence in structural applications, however, delaminations may initiate at transverse cracks. In the pipeline application, transverse cracking is detrimental as it leads to weepage and local leakage of the pressurised fluid.

1.5.3 Delamination

Delamination, the separation of neighbouring plies, may be caused by interlaminar shear stresses due to large differences in ply stiffness, reinforcement realignment or normal tensile stress associated with edge effects and defects such as transverse cracks (Wang, 1989; Wang, 1998; Sheinman and Soffer, 1989; Wang, 1988; Berthelot, 2003; Salpekar et al., 1996). The delamination results in reduced structural capacity and buckling resistance (Tafreshi, 2004, Sheinman and Soffer, 1989).

In filament wound composite tubes, transverse fibre pullout, or transverse delamination, is observed as the separation of reinforcement bands from the internal surface of the tube or curved laminate (Foral and Gilbreath, 1989; Foral, 1988). This failure mechanism may be demonstrated by stretching a helically wound wire. As the axial deformation is increased, the radius of the helix is decreased. It is noted that the smaller the angle of the helix (with respect to the axis of rotation), the greater the reduction of the radius for a

given axial tensile deformation. Therefore, radial stresses are developed within the inner layers of the pipe that may become large enough to fracture the matrix and lead to transverse delamination. This is most notable in filament wound structures of multiple winding angles. It becomes clear that, for axial tensile loading of a tube, it is beneficial to support layers of smaller reinforcement angles with layers of high reinforcement angles on the tube interior. Foral has demonstrated in $[90°, \pm 20°, 90°, \pm 20°, 90°]_T$ and $[\pm 20°, 90°, \pm 20°, 90°]_T$ carbon fibre/epoxy filament wound tubes that those without the 90° internal support layer have only 60% of the axial strength of those with the support layer, at room and elevated temperatures. While this mode of failure is very local in nature, resulting in the peeling of narrow bands of reinforcement from the interior surface, the impact on a tensile loaded tube containing internal pressure has not been described in the literature.

1.5.4 Failure Envelopes

Transverse cracking is one mode of failure in composite plies. Fibre fracture, microbuckling, delamination, shear fracture as well as out-of-plane failures are other modes which may occur depending on load orientation. Because of this anisotropy of failure modes in composite plies and laminates, the failure mechanisms in laminates are many and difficult to predict. To describe the strength of a laminate, the results of many experimental analyses at various load conditions and orientations are compiled into failure envelopes. In the study of tubes, failure envelopes are generated by conducting tests at various ratios of hoop (circumferential) stress to axial stress. If the tube wall thickness is small compared to the diameter, a biaxial state of stress is approximated and radial stress is neglected. The failure envelopes are then expressed as stress in the σ_{Hoop}-σ_{Axial} plane or strains in the ε_{Hoop}-ε_{Axial} plane.

The mechanical characteristics of composite tubes, of various material systems and lay-ups, is slowly being developed. A number of commercially produced and laboratory fabricated pipes have been tested under monotonic biaxial loads by Ellyin et al. (Martens and Ellyin, 2000; Ellyin et al., 1997; Carroll et al., 1995). Biaxial fatigue loads have also been conducted (Ellyin and Martens, 2001). Extensive testing has also been conducted by

Soden et al. (Kaddour et al., 2003; Soden et al., 2002; Kaddour et al., 1998; Soden et al., 1993; Soden et al., 1989; Soden et al., 1978). Perreux and co-researchers have done numerous studies on glass fibre reinforced epoxy tubes (Perreux et al., 1994; Perreux and Joseph, 1997) and Swanson has done multiaxial tests on carbon fibre reinforced epoxy (Swanson, 1998)

1.5.5 Failure Criteria

While yield and failure concepts are well established for metals and ceramics, there is currently a great amount of effort being expended on developing a failure criterion for fibre reinforced polymers. The situation is clearly quite complicated due to the many failure modes observed in composite laminates. In 1998 the "World-Wide Failure Exercise" was initiated to test and compare the accuracy of a number of proposed failure criteria developed in research institutes and industry around the world. The results of this exercise have been published in a special publication (Failure Criteria in Fibre Reinforced Polymer Composites: The World-Wide Failure Exercise, M.J. Hinton, A.S. Kaddour and P.D. Soden (eds.) Elsevier, New York, 2004). The diverse range of criteria included well established methods developed for isotropic materials, empirical techniques, approaches based on failure mechanisms, applied design codes and applied stress or strain limits. Each was judged based on the ability to predict the stress-strain response to failure as well as the failure envelope. This was done for a number of material systems with a number of cross-ply, angle-ply and quasi-isotropic laminates in the form of plates and tubes. The experimental data set required for comparison demonstrated that there is also a lack of reliable and repeatable test data.

It is important to note that, in general, these criteria are for the failure of a lamina and not a complex laminate. Therefore, when analysing a laminate it is the "first failure" (the first point at which any ply fails) that is found although the load may be redistributed to the rest of the laminate and the structure continues to carry load. This method may be used with the ply-discount method under incremental loading to determine a stress strain curve. Delamination of the lamina within a laminate is generally not considered by the

emerging failure criteria. This mode of failure was not addressed in the "World-Wide Failure Exercise" (Soden et al., 2004).

There are many different categories that may be used to distinguish the existing failure criteria. However, perhaps the most notable is whether the failure mechanisms of the constituents are interactive or non-interactive. Non-interactive failure mechanisms would suggest that each failure mechanism is unique and independent of the others within the composite. In the following sections some of the more common failure criteria are briefly discussed.

1.5.5.1 Interactive Failure Criteria

The Tsai-Wu failure criteria (Tsai, 1992) is arguably the most used failure criteria for fibre reinforced polymers. It is based on the assumption that the failure envelope for a *unidirectional ply* is represented by a quadratic relation such as an ellipse in the stress or strain space represented by the following equation.

$$\begin{aligned} &F_{11}\sigma_{11}^2 + 2F_{IT}\sigma_{11}\sigma_{22} + F_{22}\sigma_{22}^2 + F_{12}\tau_{12}^2 + F_1\sigma_{11} + F_2\sigma_{22} = 1 \\ &-1 \le F_{IT}/\sqrt{F_{11}F_{22}} \le 1 \quad \text{for a closed envelope} \end{aligned} \tag{1.1}$$

For plane stress in a thin lamina, six data points are required to define the envelope and these are usually the results of axial and transverse tensile and compressive loading, pure shear and one test under biaxial loading. The latter is required to determine the so-called interaction parameter, F_{IT}. This last test is much more difficult to perform therefore the value of the interaction parameter is often assumed, within limits of geometric bounds. The Tsai-Hill, Tsai-Wu and Hoffman failure are differentiated by their assumption of the interaction parameter (Tsai, 1992). This criterion is relatively simple to use but provides no indication of the constituent or mode of failure. Therefore this method is widely represented in design texts and applied in commercial finite element analysis packages but is generally of limited value as a research tool.

Applied to a laminate, this criterion may be used to find the first ply to fail (often called first ply failure). Furthermore, this failure criterion may be coupled with the ply discount progressive failure model to produce a final failure envelope and a stress-strain response.

Simple procedures often eliminate the ply that has failed and do the linear elastic laminate calculation again. The loads are then redistributed and the next lamina to fail is identified. This technique is improved by considering the failure modes of the lamina and eliminating, or reducing by a set factor, the appropriate stiffness component. The failures are generally divided in to transverse tensile and compressive failure, longitudinal tensile and compressive (microbuckling of fibres) failures and shear failure. This method of determining the final failure envelope and material response, while practical in use, has been criticised for being unrelated to and unable to differentiate the various failure modes as well as for the rather unscientific reduction of stiffness. However, the results of the "World-Wide Failure Exercise" demonstrate that this criterion and procedure of progressive failure is among the more reliable methods tested (Kaddour et al.,2004).

1.5.5.2 Non-Interactive Failure Criteria

The non-interactive failure criteria are more numerous and diverse in development. These range from the maximum stress/strain criteria to more elaborate models of micromechanics. However, they are similar in evaluating the failures of the constituents separately rather than a homogenised material. Three non-interactive criteria will be briefly discussed here: 1) Maximum Stress/Strain Criteria; 2) Maximum Shear Stress/Strain Criteria; and 3) a Phenomenological Model proposed by Puck and Schurman (1998).

The maximum stress/strain failure criteria are based on four failure modes in a planar orthotropic lamina: tensile and compression in each the longitudinal and transverse directions. This results in a rectangular failure envelope for a ply, independent of any neighbouring plies of different orientation, which is typically unsymmetric about the coordinate axes. An additional in-plane maximum shear stress/strain may also be applied as a fifth condition. Often, in the application of these criteria to fibre dominated carbon fibre laminates in the aerospace industry, the tensile matrix failure is adjusted so that no matrix cracking occurs prior to fibre failure (Hart-Smith, 1998a). This may be an acceptable practice for the quasi-isotropic carbon fibre laminates used in the aerospace

applications but is of questionable value for glass fibre reinforcement with both higher strength and greater strain to failure.

The maximum shear stress/strain criterion is identical to the Tresca criterion for isotropic materials but generalised to orthotropic planar lamina. It is based on the assumption that laminate failure is due to fibre failure which is governed by a maximum shear stress/strain criterion (Hart-Smith,1998b, 1994, 1990). Originally represented in the stress plane, it is found to be more accurately represented in the strain plane as are the other criteria described here. This method also presumes that matrix failure will be avoided through design by using thin laminae at a number of orientations. However, this approach fails to recognise that optimisation by orienting the reinforcement in only those directions that great strength and stiffness are required is a significant benefit of using fibre reinforced polymers over traditional isotropic materials. Of course, when taking advantage of the anisotropy, the designer must still consider failure in the "weak" directions.

Puck et al. submitted to the "World-Wide Failure Exercise" a failure model that is based upon physical damage and failure mechanisms in the constituents (Puck and Schürmann, 1998; Puck, and Schneider, 1969). Their research is concerned with glass fibre reinforced polymers and therefore must consider matrix failure unlike the maximum shear stress/strain theory described above. Glass fibre is less stiff than carbon fibre therefore its strength leads to large fibre strains and therefore high strains in the matrix as well. This criterion provides five failure "conditions": tensile fibre failure, compressive fibre failure, mode A inter-fibre fracture (caused by tensile transverse normal and/or longitudinal shear stress) and modes B and C inter fibre fracture (resulting from compressive transverse normal and/or longitudinal shear stress). This is used with a continuous and progressive degradation method to calculate the elastic mechanical properties of the lamina. This is expressed in the secant modulus as opposed to using a tangent modulus in an incremental procedure for which errors are additive. This failure criteria and progressive analysis was one of the most successful methods compared in the "World-Wide Failure Exercise".

1.6 INTERLEAF TECHNOLOGY IN FIBRE REINFORCED POLYMERS

An interleaf, as used in composite structures, is an independent layer of different material placed between the layers of a laminate. The interleaf material is generally not a composite and is isotropic in behaviour. Based on a survey of the literature, it is likely that the interleaf concept was raised as a means of increasing the impact resistance of aerospace laminates. While the diversity of applications has increased, there are few papers that study interleaves and fewer yet that consider the effect of an interleaf on transverse cracking.

1.6.1 Interleaves

Materials are often selected for interleaves based on high ductility and toughness, properties that are generally low in fibre reinforced epoxies. Using the definition given in the section above an interleaf may be as simple a resin rich interlaminar layer produced during the stacking of sheets of pre-impregnated composite (Ilcewicz et al., 1991). It is clear that the neat resin has greater ductility than the composite under transverse or through-thickness tensile loading. Ogihara et al. (1999,2002) studied how the addition of butylene rubber particles to the surfaces of the pre-impregnated fibre sheets influenced damage. Further examples of interleaves toughened by particulate are given by Stevanovic et al. (1999) and Chen and Jang (1991). These have demonstrated that this manner of interleaving produces toughening in Mode I and II delamination cracking along the interleaf.

However, most of the studied interleaf materials are applied in sheet form, whether metal, thermoset or thermoplastic, since they are easily integrated into the manufacturing procedure for flat plates made from pre-impregnated reinforcements. Jorgensen and Horsewell (1997) describe how aluminum interleaves reduce damage due to indentation. While this application requires a plastic response with stiffness similar to that of the laminae, it is generally thought that the greater toughness and ductility of polymers is beneficial in reducing delaminations and transverse cracking. Papers providing experimental results for the effects of polymer interleaves on delamination cracking are available and these may be separated into thermoset and thermoplastic interleaves.

Thermoset interleaf materials applied are generally epoxy film adhesives, some with modified toughness and low flow properties. The adhesive film may be co-cured within the laminate providing for very good bonding and load transfer within the structure. Results indicate that, for delamination, a thermoset interleaf provides a significant increase in toughness in Mode I and II. Early in the development of the interleaf method, pre-impregnated plies with an integral interleaf on one surface were developed (Krieger 1985), but it was later observed that thin thermoplastic films may provide even greater benefit and that such interleaf films may be placed only at critical ply interfaces in order to reduce the inherent drop in laminate stiffness due to adding layers of low modulus material (Masters 1989). Recognising that delaminations generally initiate at the edges of coupon specimens, Tanimoto (1999,2002) has studied the effect of placing polyethylene based interleaves at only the edges of the specimen. The effect of a polyethylene terephthalate interleaf on delamination has been studied by Jiang et al. (2001). They found that the interleaf reduced the critical energy release rate by up to 70% in mode I but produced a 120% increase in mode II. Li et al. (1996) found that the addition of a polyethylene terephthalate interleaf yielded a strong bond with the epoxy and doubled the load capacity of $[0°_8]$ laminates under four point bending. Ozdil and Carlsson (1992) and Aksoy and Carlsson (1991) considered the effect of interleaf thickness for mode I and II delamination cracking, respectively. It was found that only a very thin thermoplastic interleaf ($1/11^{th}$ the thickness of the composite ply) was adequate to significantly increase G_{IC} and increases in thickness gave no appreciable advantage. However, it was found that under mode II, the plastic zone size increased with increasing interleaf thickness and therefore G_{IIC} increased as well. More discussion of the impact of interleaf films on delamination may be found in Chan et al. (1986), Chan (1986) and Lagace and Bhat, (1992).

While thermoplastic polymer interleaves provide greater improvements to toughness, it is acknowledged that they have low surface reactivity resulting in a weak bond to the epoxy matrix. Tanimoto (1999, 2002) used the polyethylene interleaf sandwiched between sheets of thermo-adhesive activated by post-cure temperatures. Alternatively, Jang et al.

(2001) compared the effects of polyethylene terephthalate interleaf with and without plasma treatment. It was found that plasma treatment greatly increased the strength of the bond therefore increasing both the Mode I and II critical energy release rates over that of the untreated interleaf. Nay et al. (1995) provide a more detailed discussion of the effects of plasma process parameters and effects on interleaf behaviour.

1.6.2 Interleaves and Transverse Cracking

As noted above, there is little published experimental information of the influence of an interleaf on transverse cracks and stiffness reduction. Lee-Sullivan et al. (1995) tested $[\pm 30°, I, 90°_n]_s$ and $[+30°, I, -30°, 90°_n]_s$ and found that in both cases the addition of the polyethylene terephthalate thermoplastic interleaf significantly delayed transverse cracking and reduced stiffness loss. This delayed the onset of delamination and specimen failure. Furthermore, when the interleaf is at the -30°/90° interface the delaminations occur at the +30°/-30° interface away from the transverse cracks that end in the interleaf material.

This topic is also of analytical interest and relevant literature ranges from analyses of cracks approaching a material interface to the study of a transverse crack in a lamina with bounding interleaf and constraining plies. Initial analyses considered a crack approaching an elastic material interface at a right angle (Cook and Erdogan, 1972) and this has been extended to viscoelastic materials by Han et al. (2001). They found that for a crack in a viscoelastic material the stress intensity factor and energy release rate decrease with time under constant load. It is also observed that the energy release rate decreases as the crack tip approaches a stiff material from a relatively soft material. A number of analyses of discrete plies with bounding adhesive or interleaf layers have also been conducted (Gecit and Erdogan, 1978; Goree and Venezia, 1977a; Goree and Venezia, 1977b; Kaw and Goree, 1990a; Kaw and Goree, 1990b; Gillespie and Hansen, 1997). Gillespie and Hanson used a variational shear lag method to predict transverse cracking in a 90° ply bounded by interleaves in a cross-ply laminate. Their results indicate a much lower transverse crack density although cracking initiates at the same applied strain as a laminate without interleaves. Kaw and Goree (1990a, 1990b) used the method of integral

equations to demonstrate that the stress concentrations in the interleaf and 90° plies decrease as the interleaf thickness is increased. It is also acknowledged that if the cracked layer is actually stiffer than the constraining plies, the soft interleaf will promote crack growth into the constraining plies.

The analysis of a crack intersecting a soft interleaf is very similar to that done for soft inclusion toughened brittle materials. Li et al. (1993) have shown in an elastic finite element analysis that as the crack tip approaches a soft inclusion the strain energy release rate increases but then decreases as the crack tip passes through the inclusion. Therefore the crack may be arrested in the soft inclusion. The opposite trends are observed for stiff inclusions. They then experimentally verified this numerical result.

Due to the limited experimental results for transverse cracking in laminates with interleaves, these analytical results provide indications of the mechanisms at work and requirements for a beneficial interleaf specification.

1.7 NUMERICAL ANALYSES

Numerical analysis is now very popular for investigating material and structural response for problems for which no analytical solution is available or is very difficult to solve. This technique allows for complicated finite geometries and may be solved to a high degree of accuracy depending on the computing power and time available. Currently, the finite element method is the most popular numerical method of structural analysis.

1.7.1 Finite Element Method and Software

In its most basic form, the finite element method may be described as the discretisation of a geometric model into a number of finite sized elements with boundaries defined by nodes. Each element is represented mathematically by a stiffness matrix and these element stiffnesses are assembled to form the global stiffness matrix recognizing that the nodes shared among elements must only have one value of displacement and force. Boundary conditions and body loads are applied via the nodal points. A thorough derivation and explanation of the methodology may be found in any of a number of textbooks on this subject. A number of commercial software packages have been

developed around the finite element method. The package used in this investigation was ANSYS of Swanson Analysis Inc.

1.7.2 Modelling the Viscoelastic Material

It is recognised that, unlike most metals at room temperature, the response of polymers is time dependent. That is they tend to display creep under loading, stress relaxation when subject to displacements and recovery of creep strains when unloaded. This behaviour is of importance when considering the extreme stress and strain concentrations within the matrix of the fibre reinforced polymer. Derivation of a nonlinear creep constitutive relation may be based on either of the integral or differential expressions. The integral derivation has been thoroughly characterised by Schapery (Schapery, 1969; Lou and Schapery, 1971) and has led to three-dimensional implementations (Lai and Bakker, 1996). A three-dimensional material model, based on the differential representation, has been proposed by Xia and Ellyin (1998) that yields an expression similar to that of Zienkiewicz et al. (1968).

The viscoelastic material model developed by Xia and Ellyin is based on a series of Kelvin-Voigt type elements (spring damper combinations) in series with a single elastic spring. The elastic spring provides the elastic response while the Kelvin elements provide the viscous response. Close agreement with experimental results can be achieved by using a number of Kelvin elements of varying characteristics.

The derivation is based on the assumption that the strain rate increment may be separated into elastic and time dependent parts and that the time dependent component is the sum of the creep strains of the Kelvin elements. This may be expressed as:

$$\dot{\varepsilon}_{total} = \dot{\varepsilon}_{elastic} + \sum_{i=1}^{n} \dot{\varepsilon}_{creep,i} \quad \text{where} \quad \dot{\varepsilon}_{creep,i} = \frac{\sigma}{\eta_i} - \frac{E_i}{\eta_i}\varepsilon_{creep,i} = a_i\sigma - b_i\varepsilon_{creep,i} \qquad 1.2$$

Where E_i and η_i are the elastic and viscous moduli, respectively and n is the number of Kelvin elements. For a multiaxial state of stress the creep strain rate increment becomes

$$\{\dot{\varepsilon}_{creep}\} = \sum_{i=1}^{n}\left(a_i[A]\{\sigma\} - b_i\{\varepsilon_{creep,i}\}\right) \quad \text{and} \quad \{\dot{\sigma}\} = E[A]^{-1}\{\dot{\varepsilon}_{elastic}\} \tag{1.3}$$

where [A] is a matrix related to the Poisson's ratio.

While the above is a linear formulation it has been found that a more accurate multiaxial response is achieved from a nonlinear expression dependent on the equivalent stress. The creep strain rate is then expressed as

$$\{\dot{\varepsilon}_{creep}\} = \sum_{i=1}^{n}\left(a_i[A]\sigma_{equivalent}\{\sigma\} - b_i\{\varepsilon_{creep,i}\}\right) \tag{1.4}$$

$$\sigma_{equivalent} = \frac{(R-1)I_1 + \sqrt{(R-1)^2 I_1^2 + 12\cdot R\cdot J_2}}{2\cdot R} \tag{1.5}$$

where R is the ratio of compressive over tensile yield stress, $I_1=\sigma_1+\sigma_2+\sigma_3$ the first invariant of stress and $J_2=s_{ij}s_{ij}/2$ the second invariant of the deviatoric stress.

This model has been compared to Schapery's integral formulation and thoroughly tested for the epoxy system used to filament wind the tubes in this investigation (Hu et al., 2003; Xia et al., 2003). Testing was completed under monotonic loading and unloading, and in proportional and non-proportional biaxial tests. The routine shows improved prediction of the unloading behaviour due to the use of a maximum stress surface. The creep modulus is a function of the radius of this surface and therefore remains constant if the stress lies inside this surface (as in unloading) or updates as the stress surface grows. Thus the load history is required and stored in the material model. Details may be found in Xia et al. (2003).

A powerful feature of modern finite element method packages is the ability to incorporate user written routines such as material models. New implementations of user routines allow the programmer to save an adequate number of variables between solution increments. This formulation of the three-dimensional isotropic viscoelastic material response has been implemented in the ADINA and ANSYS user material subroutines with a minimal number of lines of code. Examples of this use are by Ellyin et al. (2002)

and Zhang et al. (2005). In Chapter 6 this model is adapted to transversely isotropic materials such as a unidirectional fibre reinforced composite ply.

1.8 FRACTURE ANALYSES

Fracture analysis, as an engineering discipline, was developed through the 20th century following a logical progression from solving problems in elastic bodies to developing methods for elastic-plastic fracture mechanics. It may be said that the topic was initiated by Griffith in the 1920's who considered a relationship between failure stress and crack size from studies of glass. Further advancement occurred following the Second World War due to a number of large scale fracture failures of military equipment. At this time Irwin and Orowan separately extended Griffith's theory to metals by considering the plastic energy and the crack surface energy in the strain energy release rate and the stress intensity factor. It was recognised, and experimentally verified, that the deformation at a crack tip in metal would not remain linear elastic but produced a zone of plastic deformation. And crack tip plasticity models were developed. This yielded a plasticity modified stress intensity factor, the crack opening displacement technique and development of the J-integral by Rice.

The fracture parameters, G, K and J are used as an indication of crack driving force and are compared with material parameters to determine if the driving force is large enough to propagate the crack. Standardised methods have been developed to determine the fracture parameters of various classes of materials for physical testing. The test data is used to represent the crack toughness as G_{Crit} for the material. G_{Crit} for a crack in a tyical epoxy is 150 to 900 MPa/m^2 and for the transverse direction in a glass fibre reinforced epoxy composite is 500 to 1200 MPa/m^2. For comparison, the critical strain energy release rate, GCrit, is 280 to 400 MPa/m^2.

A thorough description of the history of fracture mechanics and the development of the fracture parameters is provided by Kanninen and Popelar (1985).

Three different modes of fracture may be identified; Mode I , Opening mode; Mode II, Sliding mode; and Mode III, Tearing mode. Only Mode I, Opening mode, will be considered in this investigation.

1.8.1 Strain Energy Release Rate

Initial linear elastic fracture analyses were based on the calculation of the crack driving force, strain energy release rate, represented by G. Griffith proposed that during crack growth, the total energy of the body does not change. The total energy, E, is defined as the sum of the potential energy due to deformation, Π, and the crack surface energy, S. Therefore, for a crack increment

$$dE = d\Pi + dS = 0$$
where
$$dS = 2\gamma da \quad \text{and} \quad G = 2\gamma. \tag{1.6}$$

In eqn. 1.8, γ is the surface energy density per unit area. It follows that

$$G = -\frac{d\Pi}{da}. \tag{1.7}$$

The potential energy, Π, may be defined as the strain energy in the body, U, minus the work done by the external load. This is written in terms of load P and displacement of the load, Δ, as

$$\Pi = U - P\Delta = -U^*. \tag{1.8}$$

where U* is the complementary strain energy.

For a linear elastic material U = U* therefore

$$\Pi = -U^* = -\frac{P\Delta}{2} \tag{1.9}$$

Two separate load cases may now be specified; constant load and constant displacement resulting in the following potential energy increments.

$$d\Pi = -\frac{P}{2}d\Delta \quad \text{constant stress}$$
$$d\Pi = -\frac{\Delta}{2}dP \quad \text{constant displacement} \qquad 1.10$$

Substituting eqn. 1.12 into eqn. 1.9 yields

$$G = \frac{P}{2}\frac{\partial \Delta}{\partial a} \qquad 1.11$$

for constant stress and

$$G = \frac{\Delta}{2}\frac{\partial P}{\partial a} \qquad 1.12$$

for constant displacement.

It is observed that the energy release rate is independent of whether the load, P, is changing or the displacement, Δ, is changing.

1.8.2 Stress Intensity Factor

Stress intensity factors, introduced by Irwin, provide scalar values for fracture modes I, II and III, to describe the stress distribution along the crack surface in linear elastic fracture mechanics. In opening mode I the normal stress in front of the crack tip may be specified by

$$\sigma_y(x,0) = K_I(2\pi x)^{-1/2}. \qquad 1.13$$

The variable, x, is the distance in front of the crack tip, parallel to the crack.

The stress intensity factor is geometry dependent with the value

$$K_I = \sigma\sqrt{\pi a} \qquad 1.14$$

where σ is the global stress normal to a centre crack and a is the crack depth.

The stress intensity factor, K_I, has closed-form solutions for only a limited number of geometries but may be determined through experimental or numerical analyses.

1.8.3 The J-Integral

The J-integral was employed by Rice for fracture mechanics of nonlinear elastic materials and has since been extended to use in elastic-plastic fracture. The J –integral is the path independent integral of the strain energy density and the tractions along a path surrounding the crack tip.

$$J = \int_{\Gamma} W \cdot dx_2 - \sigma_{ij} n_j \frac{\partial u_i}{\partial x_1} ds \qquad 1.15$$

At the extreme the path may be the boundaries of the cracked body and often geometry can be used to an advantage to reduce the complexity of the integral.

Dougdale and Barenblatt introduced yielded thin zones extending from the crack tip. Since the gradient of the plastic strain, perpendicular to the crack plane is very steep it is reasonable to assume that the entire body is elastic except along the crack. Taking advantage of the path independence of the J-integral, it can be shown that

$$\frac{K^2}{E'} = G = J \qquad 1.16$$

A much more thorough discussion of the J-integral is found in Kanninen and Popelar (1985).

While many other fracture parameters have been formulated, the C* integral is of importance in this analysis. This integral is formulated for time dependent fracture analysis and is therefore based on strain rate.

$$C^* = \int_{\Gamma} W(\dot{\varepsilon}_{ij}) dx_2 - \sigma_{ij} n_j \frac{\partial \dot{u}_i}{\partial x_1} ds$$
$$\text{where} \quad W(\dot{\varepsilon}_{ij}) = \int_0^{\dot{\varepsilon}_{ij}} \sigma_{kl} d\dot{\varepsilon}_{kl} \qquad 1.17$$

The similarity between the J and C* path independent integrals is obvious. More details may be found in Ellyin (1997) and Kanninen and Popelar (1985).

1.8.4 Fracture Analysis in Finite Element Analysis

Finite element analysis has found use in fracture and fatigue problems with complicated geometry for which there are no analytical solutions. It is very suitable for modelling the geometry around a sharp crack, however special consideration must be given to the large stress and strain gradients around the crack tip. The stress singularity may generally be handled by using properly shaped higher order elements in the finite element mesh. Unfortunately this modelling of the geometry is often impractical when trying to investigate a propagating crack for which the mesh must be modified for each crack growth step. This is of particular difficulty when the material response is dependent on the load history (as is the case for the viscoelastic material used here) since it is difficult to transfer the results of a solved model to a new one with a different mesh of elements and nodes. Therefore in this, and many other investigations, simple linear elements of much reduced size are used along the crack tip path. This approach generally requires building a model incorporating significant gradients in element size, but such a mesh need only be constructed once.

The act of propagating the crack is then done by releasing nodes along the crack tip path. Care must be taken to release a node slowly, by changing the stiffness of the constraint or applying nodal forces, such that the change of stiffness of the model is gradual and convergence achieved. Releasing a node within too few solution steps leads to large changes in stiffness and instability.

1.8.5 Application of Fracture Mechanics to Composite Materials and the Interleaved Laminate

The fracture mechanics and the parameters G, K and J discussed in the previous sections are formulated for self similar cracks in homogeneous isotropic media. The composite is neither isotropic nor homogeneous and crack growth through a composite may not necessarily be such that its shape remains the same. Furthermore, damage in a glass fibre reinforced epoxy occurs by a number of mechanisms related to the individual constituents and the combination of the constituents.

If one considers an orthogonal unidirectional fibre reinforced ply, by the rule of mixtures it may be assumed to be homogeneous. In addition, if the mode of damage remains similar and the crack grows parallel to one of the material planes the previously defined parameters may be used with minor modification for the anisotropic response. However, a laminate composed of a number of plies at various angle introduces greater complexity that is not easily handled. This has led to mechanism based fracture models such as those described for transverse cracking in Section 1.5.2.

In this investigation of a crack propagating through a thick cross-ply with an interleaf the laminate structure leads to difficulty in using the classically defined fracture parameters. The variation of material properties along the crack plane voids the assumption of superposition of the stress states required by the J-integral. Therefore the J-integral calculated from finite element results was found to have poor sensitivity to the change in crack driving force as the crack tip progressed through the various material interfaces.

1.8.6 Calculation of Strain Energy Release Rate from Finite Element Results

The fracture parameters G, K and J can be determined from the results of a finite element analysis. While G and J may be calculated directly, the stress intensity factor, K, is usually determined based on the results of G or J.

The value of the J-integral can be found by performing the integration of the closed path surrounding the crack tip. This requires the use of the element stress and strain ad the nodal displacements. Such calculations require singular elements or sufficiently small elements to adequately represent the stress and strain gradients to produce adequate accuracy. Most commercial finite element packages have such elements and provide functions to assist in calculating various fracture parameters. However, it should be noted that producing successive finite element discretisations modelling crack propagation and employing singular elements is time consuming and unrealistic. This is particularly true if the stress, strain or displacement distributions must be remembered for the following analysis steps.

The strain energy release rate can be determined by no fewer than three methods: 1) change in potential energy from the global stress and displacement; 2) using the virtual crack closure technique based on the nodal force and displacement values near the crack tip; and 3) change in crack body compliance or stiffness. Other techniques may be found in the literature.

The strain energy release rate may be determined by the change in stiffness of the cracked body as calculated using eqn. 1.13 or eqn. 1.14, depending on the method of loading. The nodal forces and displacements are generally available to the users and therefore the strain energy may be calculated. Since energy is scalar, the products of load and displacement along the boundary of the cracked body may be summed to generate the strain energy release rate. In the analyses completed in Chapter 7 all the nodes along the boundary are displaced an equal amount under a prescribed total stress. Therefore eqn. 1.13 may be applied directly. While this method is accurate, it requires multiple solutions employing different models simulating a growth in the crack length, a.

The virtual crack closure can determine the strain energy release rate in one solution set using only the nodal forces and displacements on the crack plane near the crack tip. This method was initially introduced by Rybicki and Kanninen (1977) and was presented in a more functional format by Shivakumar et al. (1988). This method, as indicated by the name, calculates the stress intensity factor from the work required to close the crack to the nodal point one element length behind the crack tip. The work is approximated by the displacement of the node behind the crack tip times the force at the crack tip node. This may be represented in a two dimensional analysis by

$$G_I = \frac{1}{2\Delta} F_i v_{i-1} \qquad 1.18$$

where Δ is the length of the finite element and equal to the crack increment, F_i is the normal force at the crack tip node and v_{i-1} is the normal displacement at the first node behind the crack tip. G in eqn 1.18 is expressed as strain energy density per unit of model thickness. The virtual crack closure technique has been found to be quite accurate without

the need for special crack tip elements. While it is simpler if the crack tip elements are of a regular length, this is not strictly required.

The strain energy release rate may also be calculated by determining the change in stiffness of a crack body as the result of crack growth by a specified interval. Like the potential energy method this may require multiple solutions however it may also be determined directly from the model stiffness matrix. More commonly the compliance is calculated from the applied loads and subsequent deformations leading to a procedure very similar to the first described.

1.9 THESIS OUTLINE

This investigation is focussed on the implementation of an interleaf applied in the structure of a tube to increase the load capacity at which first, or functional, failure occurs.

Chapter 2 describes the tubular test procedure including the grip design produced for this investigation. A numerical analysis of the specimen is discussed in terms of the influence of the bonded specimen end tabs on the experimental results.

The glass fibre reinforced epoxy tubes, produced by filament winding, are fully characterised in Chapter 3. Procedures for determining the fibre and void volume content are discussed and the results provided. Methods of estimating lamina properties are then discussed and implemented. These include the Halpin-Tsai equations, and various modifications, and finite element analysis of representative volume elements. The results of these methods are compared and used in the classical laminate theory to calculate the mechanical properties of the tubes. These calculated values are compared to test data as well as values calculated from a representative volume element model of the laminate.

The results of the tests on tubular specimens are provided in Chapter 4. Test observations and descriptions of the failed specimens are provided with an emphasis on failure in the specimen coordinates as well as aligned to the material coordinate system. Stress-strain response is also given. A failure criterion for the tube specimens, without interleaf, is discussed.

The implementation of a polyethylene tape interleaf in tubular and coupon specimens is the topic of Chapter 5. Specimens were produced and tested and the results are provided and discussed. Unique phenomena such as discontinuous crack path and reduction of load carrying structure are displayed and examined.

Chapter 6 demonstrates the modification of a three-dimensional isotropic viscoelastic constitutive relation for transversely isotropic materials. The assumptions are noted and the calibration, using the representative volume element method, is described.

The transversely isotropic viscoelastic material model is then applied to simulate crack progression in the coupon specimen in Chapter 7. A parametric analysis of interleaf geometry and material properties is provided with comments on optimum interleaf design.

Finally, conclusions and recommendations are made in Chapter 8.

CHAPTER 2 $[\pm 60°_3]_T$ FILAMENT WOUND GLASS FIBRE REINFORCED EPOXY TUBES: PRODUCTION AND TESTING METHODS

Multiaxial testing may be approximated by applying axial loads and internal/external pressure differential to a thin wall tubular specimen. This will generally produce a more representative stress/strain distribution than a cruciform specimen of complex geometry. Composite tubes were produced by filament winding E-glass reinforcement with epoxy resin on an automated filament winding machine with strict tension control. The composite tubes were tested by a combination of axial load and internal pressure. Tests were conducted at constant proportional load rates using an existing material testing system with an additional pressure intensifier.

2.1 TUBULAR SPECIMEN PRODUCTION

Tubular specimens were produced in the Advanced Composite Materials Engineering composites production facility described in Wolodko et al. (2001) and in Appendix A. It is the intention to only provide the specific details of the process here. The mechanical properties of the constituents and resulting composite tube will be provided in Chapter 3.

Filament winding was done on the McClean-Anderson commercial filament winding machine, shown in Figure 2.1 with all programming done using the associated software. Eight tows of Owens Corning 158B Type 30, E-glass fibre, 735 TEX (735 g/1000 m) were pulled to form a band width 20.3 mm wide. The specified winding angle was 60° and a lag wind was selected. A lag wind occurs when helical bands are placed one behind the other and is generally more favourable as it tends to pull the bands together rather than spread them apart as in a lead wind. Three ±60° layers, resulting in 600% coverage, were produced by running the identical winding program three times. Each required five circuits (carriage travel to the end of the mandrel and back) to produce a 200% coverage.

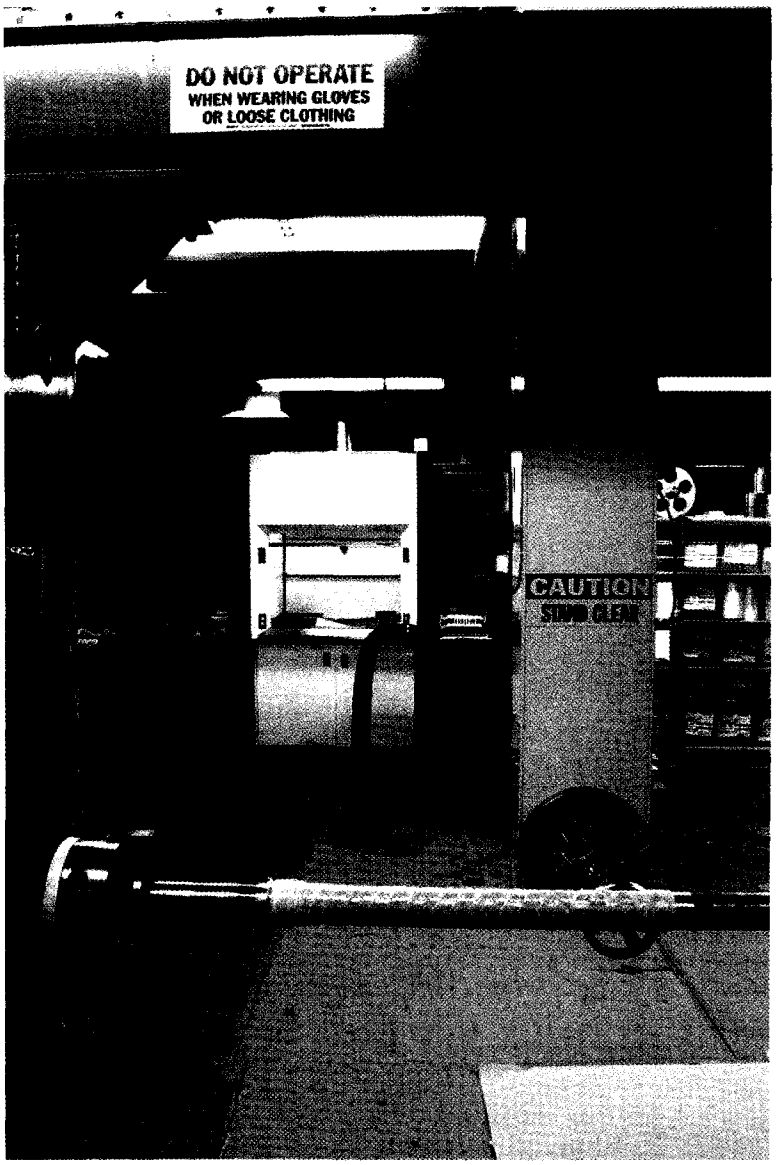

Figure 2.1: Filament winding in the Advanced Composite Materials Engineering research group laboratory.

The EPON 826/EPICURE 9551 resin system was combined at the manufacturer recommended ratio of 100 parts resin to 36 parts curing agent by mass and was mechanically mixed for five minutes. The mixed resin was then placed in the resin bath and warmed to 30 °C prior to winding.

The wet fibres were wound onto a steel mandrel with chrome surface made from stock used in the production of hydraulic cylinder rods. The ends were fitted with flanges as

described in Wolodko et al. (2001) and these were clamped in the chucks. The mandrels were coated with Freekote 770-NC release agent (now a product of Loc-tite) and allowed to dry prior to winding.

The reinforcement was tensioned using the described tensioning rig and control system (Wolodko et al., 2001). The tension applied was 26.7 N per tow for the first ±60° layer and 44.5 N per tow for the latter two ±60° layers. This tension is found to consolidate the part, increasing fibre volume fraction and reducing void volume fraction. Preloading the reinforcement also compensates for thermal residual stresses produced during high temperature curing (Dvorak and Suvorov, 2000).

Cure was completed in a large convection oven following the temperature profile shown in Figure 2.2. The temperature of the curing composite was not monitored and will be influenced by the time to heat the heavy mandrel. The slow temperature response of the mandrel will lead to a temperature gradient in the composite which may affect the rate and degree of cure. This may result in residual thermal stresses through the thickness of the final part. The post cure temperature, 120° C, does ensure that cure temperatures are achieved throughout the part. The heavy mandrel leads to a slower cooling rate for the composite than specified for the oven. The part was rotated during cure to prevent sag and dripping of the resin.

Extraction was done by pulling the mandrel through a brass eye effectively pushing the composite tube off the mandrel.

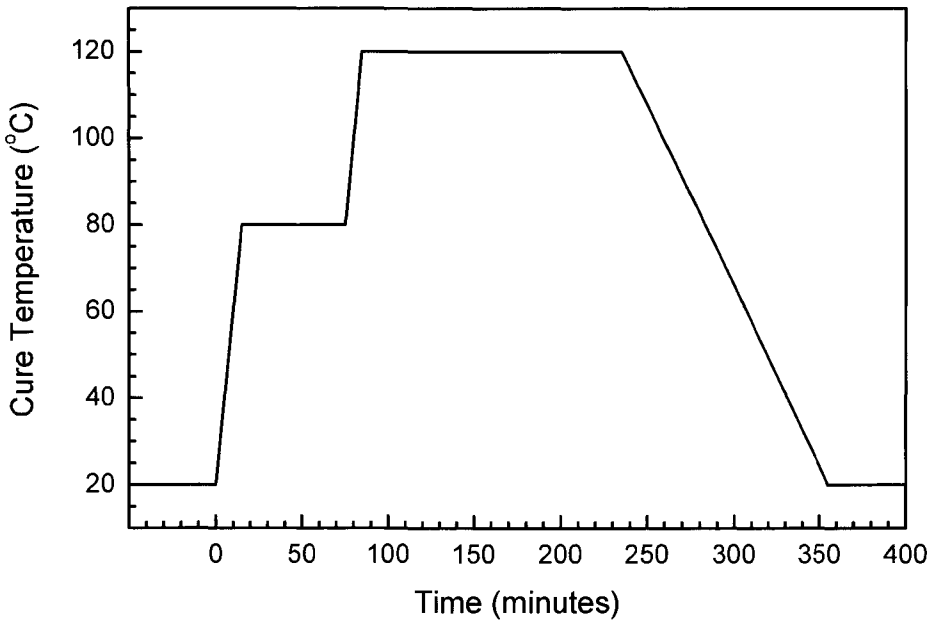

Figure 2.2: Cure schedule for E-glass reinforced epoxy filament wound tubes.

2.2 TESTING TUBULAR COMPOSITE SPECIMENS

Multiaxial or combined load testing of materials using tubular specimens under axial loads and internal pressure has become common for verifying material response and pipeline performance. Such loading provides an approximately biaxial state of stress with the dominant stress components in the hoop and axial directions.

2.2.1 The Biaxial Stress State

The combination of axial load and internal pressure used in this study approximates a biaxial stress state within a thin wall tube as shown in Figure 2.3.

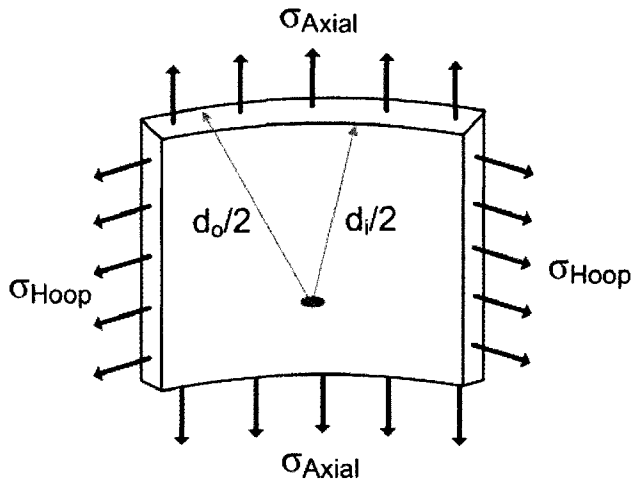

Figure 2.3: Schematic of stress state in tube wall.

The stresses in the principal directions may be calculated by equation 2.1 where F_A is the applied axial load, P is the applied Pressure and d is diameter and the subscripts i and o indicate interior and exterior diameters respectively.

$$\sigma_A = \frac{\frac{4}{\pi}F_A + (P_i - P_o)\cdot d_i^2}{(d_o^2 - d_i^2)}$$

$$\sigma_H = \frac{(P_i - P_o)\cdot(d_o + d_i)}{2\cdot(d_o - d_i)} \qquad 2.1$$

$$\sigma_R \approx \frac{-(P_i - P_o)}{2}$$

In this study the pressure outside the specimen is atmospheric and the measured pressure was the gauge value. Thus P_o is removed from equation 2.2. Furthermore, the approximation that both internal and external pressure act on the average diameter, $(d_o+d_i)/2$, is replaced by the more physically representative case, internal pressure acting on the inside diameter, d_i.

$$\sigma_A = \frac{\frac{4}{\pi} F_A + P_i \cdot d_i^2}{\left(d_o^2 - d_i^2\right)}$$

$$\sigma_H = \frac{P_i \cdot d_i}{\left(d_o - d_i\right)} \qquad 2.2$$

$$\sigma_R \approx \frac{-P_i}{2}$$

The resulting change in hoop stress due to this representation is a decrease of 2.3%.

In this study the maximum hoop stress, σ_H, and axial stress, σ_A, were approximately 1100 MPa and 150 MPa respectively while the maximum magnitude of radial stress, σ_R, was approximately 23 MPa.

2.2.2 Specimen Preparation

Once extracted from the mandrel the ends of the composite tube, including the built-up turn-around region, were removed to leave a 406.4 mm long tube. The cut ends were then potted in aluminum end tabs using an alignment jig to ensure that the tube is centred within the tabs and misalignment is minimized. Misalignment of the end tabs will lead to bending of the specimen when it is loaded into the material testing system. The aluminum tabs provide a means of clamping the specimen in the testing machine grips without damaging the composite structure. This method also avoids attempting a high-pressure seal on the unreliable surface of the composite tube.

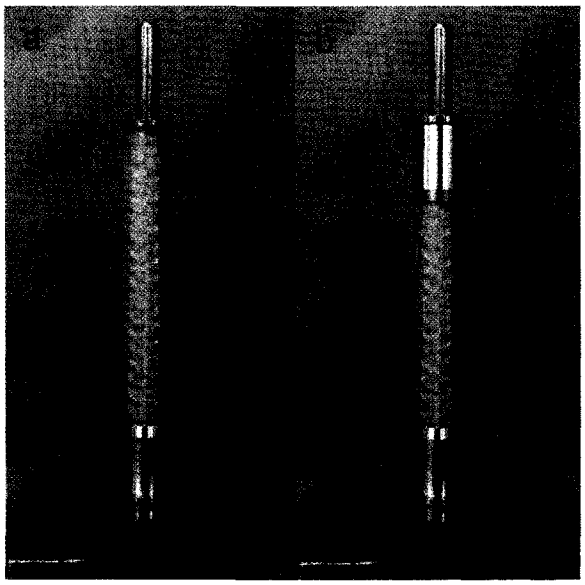

Figure 2.4: End tab bonding jig on the hot plate. a) First end tab is aligned and bonded, b) Second end tab is aligned and bonded.

The aluminum tabs are applied using 3M Scotchweld DP-460 epoxy adhesive, a hot plate and an alignment jig. The alignment jig consists of a vertical steel rod on to which slide sleeves that match the inner diameters of the aluminum tabs and the fabricated composite tubes. The tab to be applied is always centred on the rod at the bottom of the jig as shown in Figure 2.4.

This method and system have been found to be fairly quick, allowing for three tabs to be applied each hour and has produced reliable alignment of the end tabs on all of the tested specimens.

The resulting specimen length, between the aluminum tabs, was 254 mm and the measured wall thickness was approximately 1.5 mm. These are compared to an internal diameter of 50.8 mm resulting in a diameter to thickness ratio of $d/t = 33.9$ and a length to diameter ratio of $l/d = 5$. These ratios satisfy the commonly accepted practice in testing thin-walled tubes that $d/t \geq 10$ to ensure a uniform radial stress distribution and $l/d \geq 5$ for the elimination of end effects within the gauge length.

Two biaxial strain gauge rosettes, type MicroMeasuremnts CEA-13-125WT-350, were applied on opposite sides at the centre of the gauge length with the gauges oriented in the

principal directions; axial and circumferential. These gauges have a length and width of approximately 3.5 mm. The strain gauges are subject to irregularities in the outside surface of the wound tube such as transitions in reinforcement direction and overlap regions. However, strain gauges were preferred over extensometers due to the often catastrophic failures that would damage extensometer elements. It has also been observed from tests on neat resin samples that the knife edges of the extensometer, in contact with the sample, often create damage which leads to the early failure of the epoxy samples.

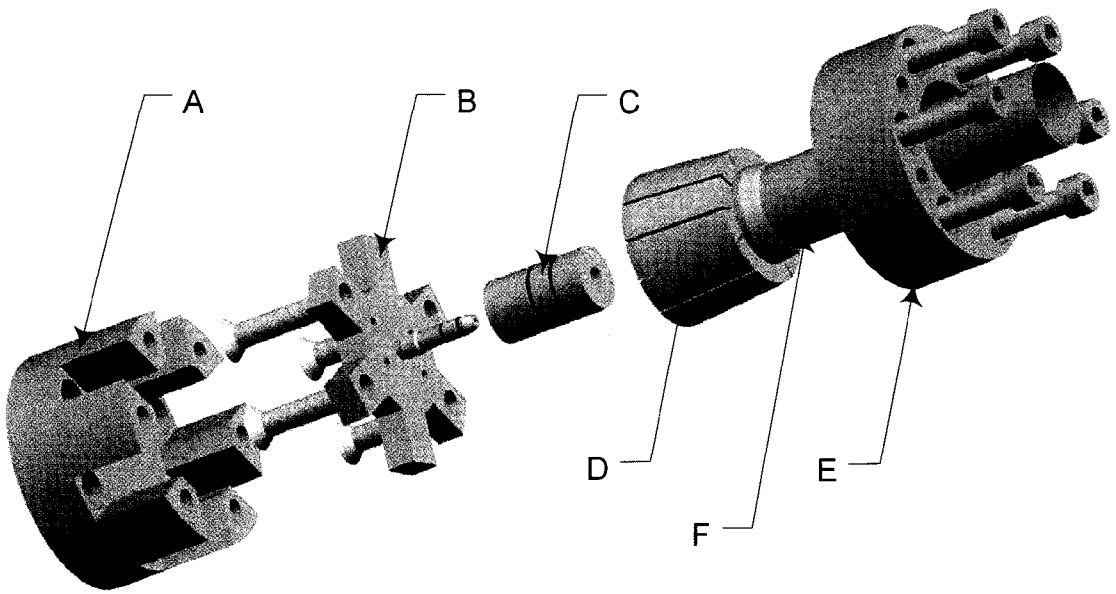

Figure 2.5: Schematic of grip assembly designed by the author for testing 50.8 mm internal diameter composite tubes. Parts are labelled as A) the crown which is bolted to the material testing system; B) spoked hub; C) end plug with o-rings; D) collet; E) the collar; and F) the specimen. (drawn by Andrew Ng)

Following the application of the strain gauges, the specimen, with end tabs, is mounted in the grips one end at a time. One grip is shown in Figure 2.5. The collet (D) was placed around the tab and the lubricated plug (C), with spoked endplate (B), gently pushed into the end of the specimen (F). The collet (D) was lubricated on the outside surfaces and the collar (E) was placed over the collet and bolted snug to the spoked endplate (B) so that the grip would not fall off under normal handling. The specimen/grip assembly was then placed on the preloading jig, in an Instron screw driven load frame, with collar supported

on the top of the jig and the sample protruding down. The Instron test system cross-head was then brought down into contact with the end plate pushing it down and squeezing the collar and endplate together. When a load of 89.0 kN was achieved the endplate was bolted to the collar using four machine screws. This procedure was then repeated for the other end of the specimen.

The strain gauge wires were then soldered in place, the gauges tested for continuity, zeroed and left for a period of time to check for stability. Any strain gauge problems were resolved prior to installing the specimen in the test set-up. Before installing the specimen, all strain gauge readings were zeroed with the specimen cradled on its side. Adequate support is provided by the grips to eliminate bending and this was presumed to be the zero stress state. The test system axial load and pressure readings were also zeroed.

2.2.3 Multiaxial Load Testing

All testing of the composite tubular specimens was done using a MTS uniaxial resonant material testing system. The system load cell has a capacity of 373,650 N with an accuracy of ±0.15%. a pressure intensifier to apply 103.4 MPa with a displacement of 650 ml was added to the system. The load frame and attached pressure intensifier are shown in Figure 2.6.

To mount the specimen in the testing system, the specimen (with grips) is placed on the lower cross head and the upper crosshead brought down so that the points of the crown (Part A in Figure 2.5) fit the spokes on the upper grip. The top grip is then bolted, finger tight, to the crosshead. The ram is then fully retracted and the bolts fully tightened. This procedure is done to prevent applying torque to the specimen since the top crosshead is attached directly to the hydraulic ram and is free to rotate when not fully retracted. The bottom grip is then engaged in the lower crown, which is fixed solid to the load cell and machine base, and the two bolted together.

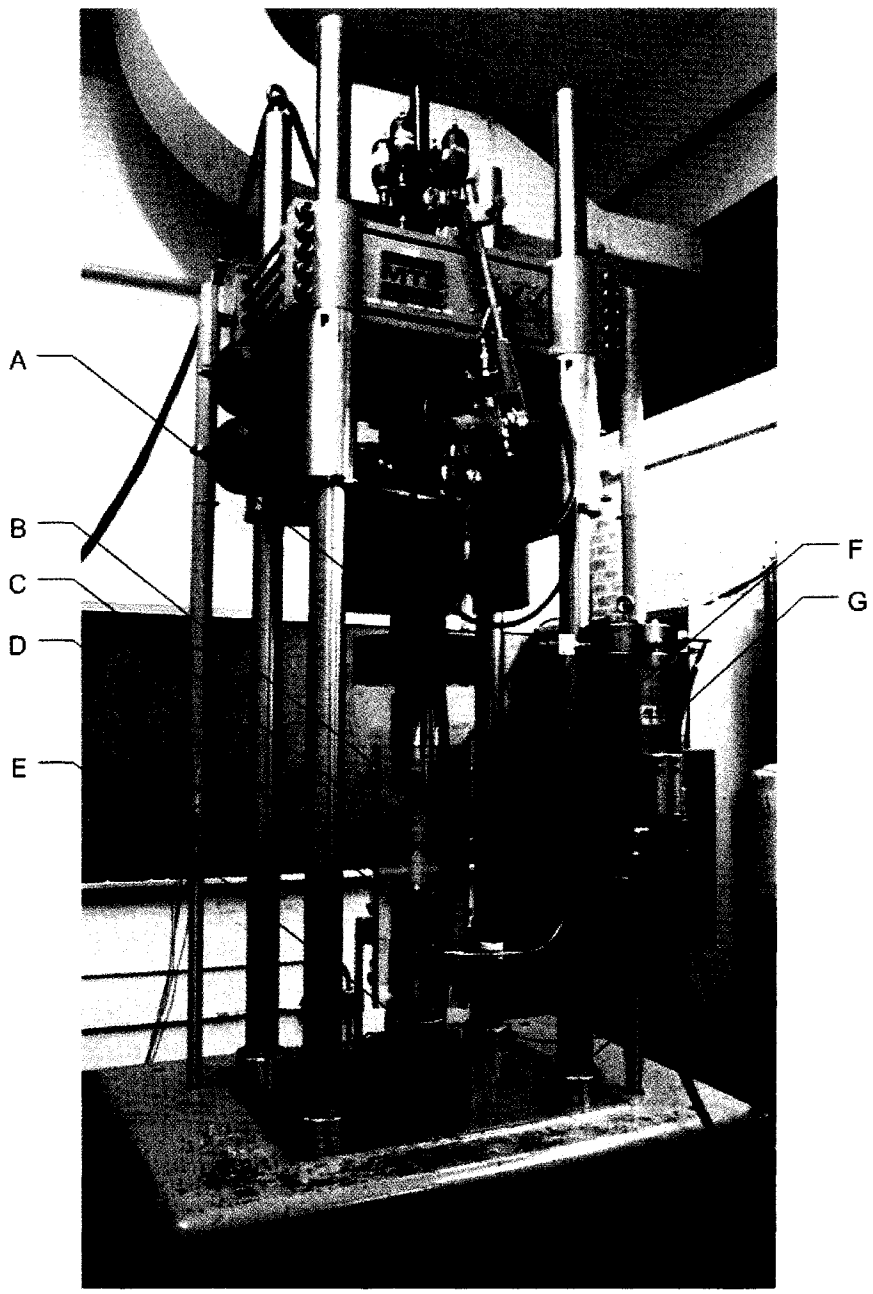

Figure 2.6: Modified MTS material testing system. Labelled components are: A) hydraulic ram, B) upper grip, C) tubular specimen, D) lower grip, E) load cell, F) protective shield and G) internal pressure intensifier.

The pressure line is attached to the port on the lower grip, and the specimen filled with oil by carefully opening the intensifier fill valve and the specimen supply valve. The specimen is only considered filled when oil runs without air bubbles from the port on the

upper grip. The port is capped ensuring that no air can return into the system. It is expected that some will remain in the small volumes between the tight clearances of the plug and the end tab but minimising the amount of air reduces the stored energy upon pressurisation decreasing the explosive nature of the failure.

The test apparatus is monitored and controlled by a MTS control panel, an external function generator and a personal computer. The dedicated control panel regulates the hydraulic servo valves to provide control of the load, stroke or external strain signal. All tests were conducted in load control with the exception of the fixed end tests which required stroke control to maintain zero displacement of the ram. The main panel also controls the pressure output from the hydraulic intensifier that provides the internal pressurisation. Of primary importance in the control systems are the "set point" and "span" dials which define the initial load point and the magnification of the command signal respectively. The function generator provides the command signal for both axial loading and internal pressurisation with the option to invert (make negative) the axial load signal. The personal computer incorporates a Keithley MetraByte DAS-16 data acquisition card with 12 bit resolution. A user created program sends a signal to the function generator to start the test and captures pressure, load, stroke, intensifier displacement and strain data. Four channels of strain are captured at a specified interval (a minimum of one second). Data is saved as raw voltages and is later manipulated in a spread sheet software package.

Tests were conducted at a internal pressure rate of 0.575 MPa/minute with the axial loading rate depending on the applied hoop stress to axial stress ratio. For axial loading tests the axial force was applied at a rate of 1.12 kN/minute.

Two data calculations are of special note: a moving median process to remove noise and the calculation of specimen oil loss volume. The data recorded from the material testing system was found to have a large amount of noise in the axial load signal. This noise is carried to the stress values through the calculations. The reason for the large visible noise is likely due to the fact that the axial loads achieved in the testing of these thin wall composite tubes is only a small fraction of the capacity of the test rig. To remove large

spikes from the displayed data, a moving median over seven local points, including three leading and three trailing values, was used. This method was found to be more successful than using a moving average. The specimen oil loss volume was calculated from the displacement of the internal pressure intensifier piston. The motion of the piston is measured via a linear rotary potentiometer measuring the rotation of a roller in contact with a rod, directly attached to the piston and protruding from the intensifier body. The known displacement of the intensifier is 650 ml. The measured displacement cannot be directly interpreted as fluid loss without accounting for expansion of the hydraulic tubing as well as the specimen. Linear expansion is accounted for by determining the linear equation for the initial intensifier volume loss, before strains become nonlinear and subtracting this from total volume loss. In many cases there is a short nonlinear rise at the beginning of the test. This is due to the intensifier piston sticking at the bottomed-out position and the compression of a very small amount of air still trapped within the specimen and intensifier. This nonlinearity is brief and is omitted when calculating the linear curve. Still the results must be carefully interpreted since an increase in the modified volume loss rate does not necessitate leakage. This may also occur when specimen deformation is nonlinear.

2.3 STRESS/STRAIN DISTRIBUTION WITHIN THE SPECIMEN

The stress distribution within the specimen during testing is of primary concern, and often the manner in which the specimen is attached to the loading system can influence the results. Special consideration must be given to composites which, depending on the lay-up, may be particularly susceptible to stress concentrations at the grips. For tubular composite specimens, that are not easily machined without introducing damage, the ends are often built up with increasing thickness by winding 90° layers. This is intended to increase the cross-sectional area held in the grips but with a gradual change in stiffness. In this investigation, the specimens were potted in aluminum tabs as described above.

A three-dimensional finite element analysis of the aluminum end tabs, adhesive and composite tube was performed. The geometry is shown in Figure 2.7. The aluminum and adhesive were modelled as linear elastic materials, with properties provided in Table 2.1,

while the laminate was simulated using the ANSYS layered elements which allow for multiple layers of orthotropic properties in each element. The properties for the layered elements are those determined by the Halpin-Tsai equations in Chapter 3.

Table 2.1: Aluminum and adhesive isotropic material properties.

Property	6061-T6 Aluminum	3M Scotchweld DP 460
E, Modulus, (MPa)	69,500	4800
G, Rigidity, (MPa)	26,100	1700
ν, Poisson's Ratio,	0.33	0.40

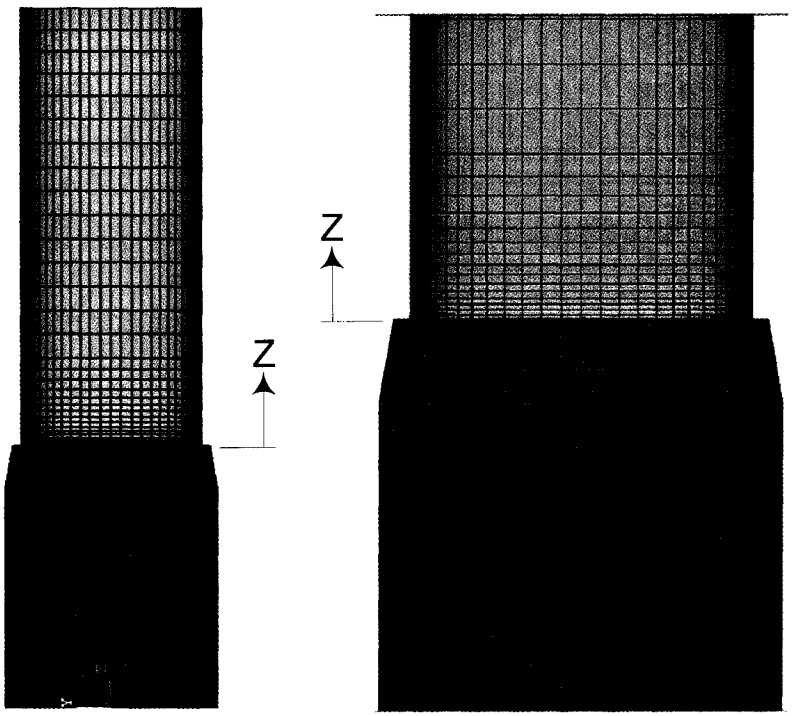

Figure 2.7: Cross-section view of finite element geometry for study of grip effect.

Figure 2.8 shows the axial and hoop stresses along longitudinal paths on the inside and outside surfaces of the composite specimen under axial tensile loading (stress ratio 0:1). The stresses have been normalised by the axial stress achieved in the centre of the gauge

length. Figure 2.9 shows the same results but for the 1:0 stress ratio. In this figure the stresses have been normalised by the hoop stress at the centre of the gauge length.

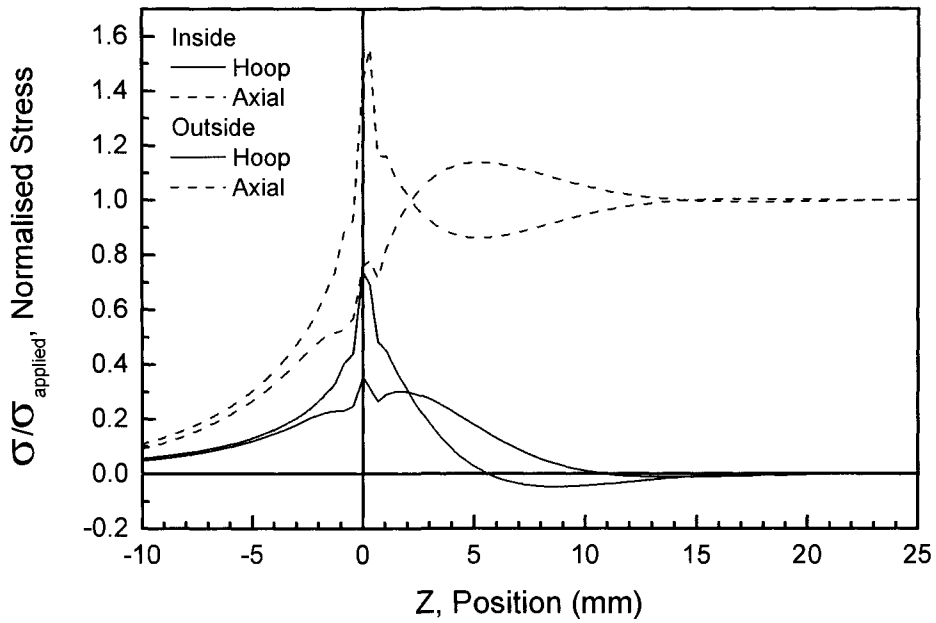

Figure 2.8: Stress distributions along longitudinal paths on the inside and outside surfaces of the composite specimen under a 0:1 stress ratio.

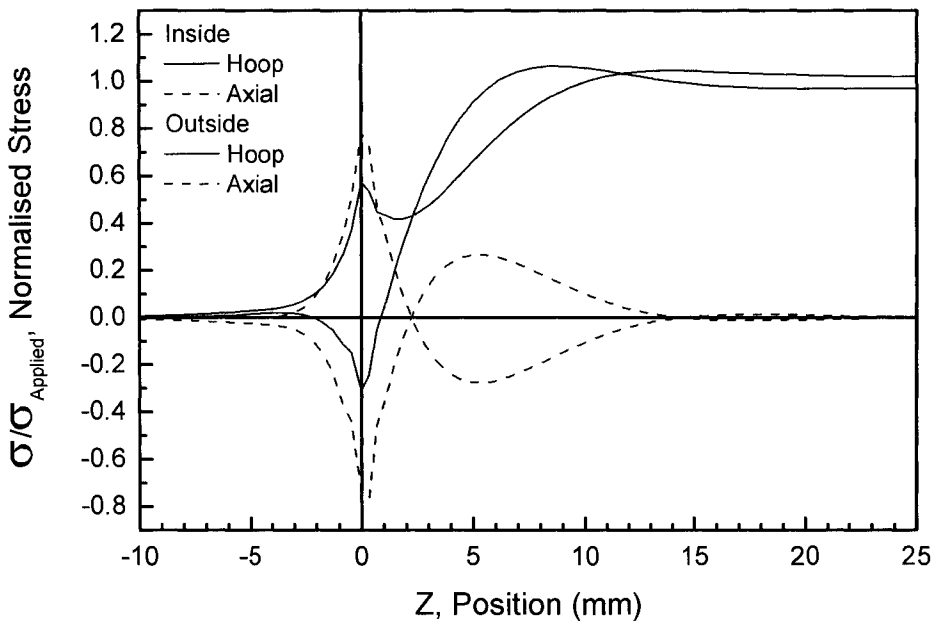

Figure 2.9: Stress distributions along longitudinal paths on the inside and outside surfaces of the composite specimen under a 1:0 stress ratio.

In both cases there is a stress concentration at the end of the aluminum tab. It is shown that applying axial load results in a hoop stress at the ends of the gauge length near the aluminum tabs as applying internal pressure produces axial stresses near the end tabs. Comparison of the axial stress distributions under the 1:0 stress ratio, on the inside and outside surfaces of the composite tube, indicate that there is bending as the rigid grips constrain the diametral expansion. While such constraint is difficult to avoid, it is understood that in the $[\pm 60°_3]_T$ filament wound tubes, high internal pressures may be achieved resulting in large axial strains due to this bending.

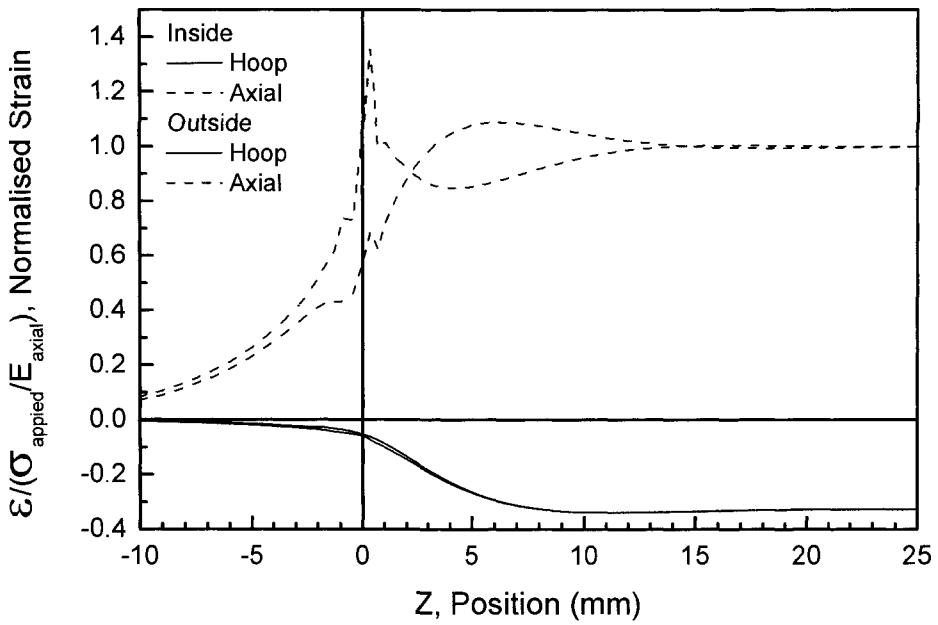

Figure 2.10: Normalised strain response along longitudinal paths on the inside and outside surfaces of the composite tube under axial tensile loading.

Figure 2.10 and Figure 2.11 show the strain results for the 0:1 and 1:0 stress ratios, respectively. The strains are normalised with respect to theoretical strains calculated using the applied stress and the theoretical modulus. The same trends are shown as in the stress plots and again the bending under internal pressure is very evident. The large tensile axial strain on the exterior surface of the tube will result in matrix cracking however leakage will not occur if the interior layers are not damaged.

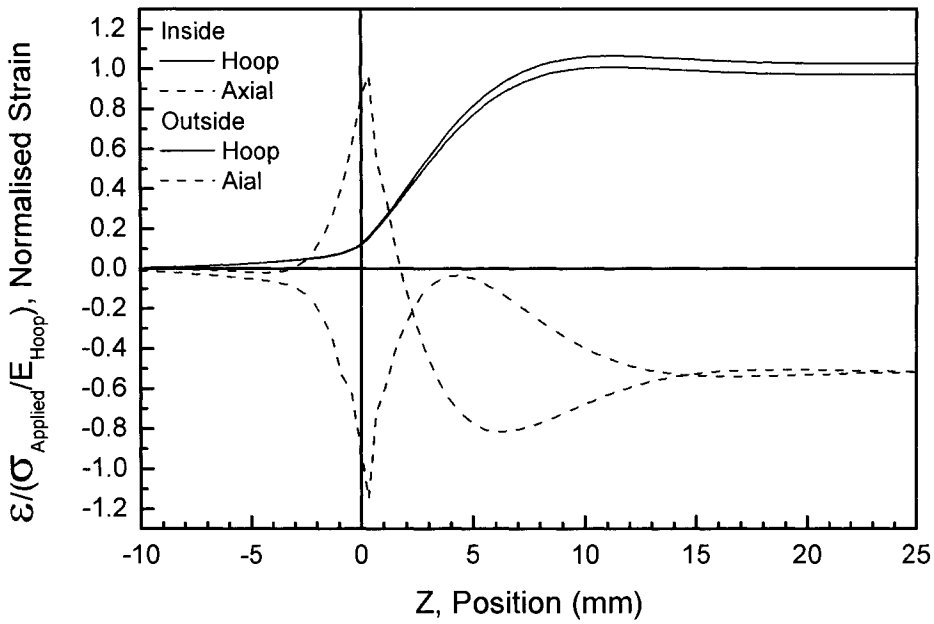

Figure 2.11: Normalised strain response along longitudinal paths on the inside and outside surfaces of the composite tube under internal pressure loading.

The use of a symmetric angle-ply lay-up results in layers with symmetric orthotropic material response in the specimen coordinate system. Therefore, the elastic results for axial tension and internal pressure loads, stress ratios 0:1 and 1:0 respectively may be combined using superposition to provide results for different load states.

2.4 SUMMARY OF TUBULAR TEST PROCEDURE

Multiaxial testing of tubular composite specimens was conducted on a modified material testing system. Specimens were produced by filament winding of glass fibre and epoxy in a controlled environment. Tension was applied to the glass fibre tows to aid in consolidation and compensate for residual thermal stress. The multiaxial stress state was achieved by applying internal pressure and axial force simultaneously. Special grips were constructed for the 50.8 mm inside diameter tubes. These grips provided gripping without slippage or leakage but are easy to assemble. However, while this type of grip system has been used successfully in the past, it is shown that they do result in stress concentrations in the specimen and this must be considered in the failure analysis.

CHAPTER 3 $[\pm 60°_3]_T$ FILAMENT WOUND GLASS FIBRE REINFORCED EPOXY TUBES: CHARACTERISATION AND THEORETICAL MECHANICAL PROPERTIES

The mechanical properties of a composite material lamina are not only dependent on the properties of the constituents but also on the ratio of constituents, the fabrication method and fabrication conditions. Therefore, it is important that the ply be carefully analysed for volume fraction of reinforcement and that this be applied to a reliable procedure for determining the ply properties. The volume fraction of voids in the structure is also determined as a means of measuring the manufacturing quality. The empirical formulas for ply properties are discussed, applied to the composite system and compared to the results of representative volume element studies. The ply properties are then used in the calculation of the classical lamination theory to determine the laminate in-plane properties. The through thickness properties are also determined and values are compared to the experimental results from the $[\pm 60°_3]_T$ filament wound tubes.

3.1 SPECIMEN DENSITY AND VOLUME FRACTION MEASUREMENTS

Specimens were taken from two tubes from separate filament winding sessions and samples of neat resin (no reinforcement) were cast separately but cured under the same temperature schedule. Two types of composite samples were measured: 1) cut from the pipe as is; and 2) machined to an outside diameter of 52.83 mm to remove the resin rich outside layer. Six samples, each approximately 25.4 mm long, were taken from each tube, two from each end and two from the middle with one from each location machined to the reduced diameter.

The specific gravities and densities of samples of the resin matrix and the composite tube were measured using the displacement/submersion technique in distilled water as per the ASTM D792 specification. The composite density may be used to estimate the volume fractions of the constituents, assuming no voids exist in the composite, but more importantly, accurate measurements of sample volume and matrix density are required to closely calculate the void content. The density and volumes were calculated using:

$$\rho_{sample} = \frac{m_{air}}{m_{air} - m_{water}} \cdot \rho_{water} \qquad 3.1$$

$$vol_{sample} = \frac{m_{air}}{\rho_{sample}} \qquad 3.2$$

In which m_{air} is the mass of the sample measured in air, m_{water} is the mass of the sample measured submerged in distilled water and ρ_{water} is the density of distilled water corrected for temperature.

Burn-out tests were done following ASTM D3171 and ASTM D2584 specifications to determine the volume fraction of glass fibre reinforcement and voids in the composite system. Samples were conditioned by storing in a desiccator jar at room temperature. The burn out was done in a furnace (preheated to 427°C) at a temperature of 566°C for two hours. The resulting glass fibre bundles were cooled in the desiccator jar at room temperature and then weighed. The volume fraction, V_f, of the samples was determined using equation 3.3.

$$V_f = \frac{\frac{m_r}{\rho_r}}{vol_{sample}} \qquad 3.3$$

Where vol_{sample} is the sample volume measured by the displacement technique, m_r is sample mass after burn-out and ρ_r is density of the glass fibres. Samples of virgin fibre and neat resin were also burned to check for changes in mass and complete combustion.

The volume fraction of voids can then be determined from the mass of matrix burned away, m_m, and the measured density of the matrix, ρ_m.

$$V_V = \frac{vol_{sample} - \left(\frac{m_r}{\rho_r} + \frac{m_m}{\rho_m}\right)}{vol_{sample}} \quad \text{where } m_m = m_{sample} - m_r \qquad 3.4$$

Preliminary measurements were done to determine the density of the neat resin cast in thin plates and subject to the same cure schedule as the composite. From observations of the casting production, it is noted that if the resin layer is thin and the free surface large

the volatiles produced by the chemical reaction will escape prior to gelling of the resin. Sample surfaces in contact with mould, to which bubbles may cling, were removed and the final specimen polished. No voids were observed within the samples. The average density from all neat matrix density measurements was 1.1441 g/ml and this value was used for the calculation of reinforcement and void volume fractions.

A reinforcement density of 2.58 g/ml was used as provided by the manufacturer. It is presumed that this density includes the influence of the sizing applied to the glass fibres or that this component may be neglected.

To ensure valid burn out test data, the base constituents, neat resin and glass fibre, were independently put through the burn out procedure. This is done to verify the existence of any residual matrix after burnout and detect if the fibres lose or gain any mass during the process. Results show that the average remaining residual mass was -0.099% of the original matrix sample. Clearly a negative value is unrealistic but these small percentages are within the accuracy capable in such a measurement. The subsequent calculations were done based on zero percent matrix residual. Likewise, the burn of the neat fibre samples indicated that they lost an average of 0.634% of their mass during the burn out procedure. This amount cannot be ignored, therefore a corrected fibre mass was used to calculate reinforcement and void volume fractions.

As noted, six samples were cut from each tube and three were machined to remove the resin rich outside layer. There was no trend among the position of sample suggesting the tube is of uniform construction and volume fraction, however removing the resin rich outside layer increased the overall fibre volume fraction from 67.88% to 72.69%. The inconsistency of the resin rich outside layer is demonstrated by the standard deviation that decreased from 0.43% to 0.10% when the resin rich outside layer was removed. It is believed the volume fraction of reinforcement value of 72.69% is more representative of the structural composite layers. Void volume fractions increased from an average of 1.68% with a standard deviation of 0.12% to 2.06% with a standard deviation of 0.33% when the resin rich outside layer was removed. This increase is attributed to the rough exterior surface produced by machining that trapped air during the submersion

measurements. This problem also results in greater variability as shown by the much larger standard deviation. The air trapped on the rough surface results in the calculation of a lower composite density and this leads to the calculation of the greater void volume fraction. Therefore it is expected that the lower value, 1.68%, is more representative of the void volume fractions in the composite tubes. This amount of voids suggests extremely good consolidation under tow tensioning and is small even for filament wound parts that tend to have low values among composite components.

3.2 USE OF A CALCULATED WALL THICKNESS

The method of filament winding and cure can have a significant effect on the distribution of matrix and reinforcement in the resulting pipe as well as on the surface characteristics. The winding/cure procedure adopted in this investigation did not use any special means to eliminate a resin rich layer on the outside of the tube. In fact, in commercial use, this layer is often considered to protect the fibres from damage under normal handling. Excess resin was removed from the surface after completion of winding however it is expected that consolidation due to fibre tension would continue in the curing oven when the part is heated and the matrix viscosity decreases. The resin rich outside layer was observed to be in the range of 0.3 mm but was found to vary widely, even on a single sample, due to the surface undulations caused by the winding of a narrow fibre band in helical weaving pattern. As discussed in the previous section, whether the resin rich outside layer is considered, or not, can vary the volume fraction of the reinforcement by almost 5% and this becomes of great importance when calculating stress and the composite ply mechanical properties.

Because of the existence of and large variation in the resin rich outside layer, a standard means of calculating layer and pipe wall thickness based on the amount of fibre and the volume fraction of fibre in each ply has been employed. This method considers the volume fraction to be consistent throughout the length of the sample and the fibre tow weight to be constant. These have been verified by measurement. As a basic assumption, the interweaving of the filament wound structure is neglected. The following method is adapted from Mertiny and Ellyin (2002) which was originally based on a method in

Peters et al. (1999). In its basic form, the tube is analysed layer by layer where a layer is one ±α cover.

$$A_{CS,j} = \frac{2 \cdot \rho_{t,j} \cdot n_{tows,j} \cdot n_{circuits,j}}{V_{f,j} \cdot \rho_{r,j} \cdot \cos(\theta_j)}$$

$$d_j = \sqrt{\frac{4 \cdot A_{CS,j}}{\pi} + d_{j-1}^2} \qquad j = 1, 2, 3 \ldots k \quad \text{when } j = 1,\ d_{j-1} = d_i \quad \text{when } j = k,\ d_j = d_o \qquad (3.5)$$

$$t_j = \frac{d_j - d_{j-1}}{2}$$

First the cross sectional area of each layer, $A_{CS,j}$, is calculated based on the tow weight, $\rho_{t,j}$, the number of tows in the bandwidth, $n_{tows,j}$, the number of circuits per layer to produce full coverage, $n_{circuits,j}$, the volume fraction of reinforcement, $V_{f,j}$, the density of the reinforcement, $\rho_{r,j}$, and the reinforcement angle, θ_j. The outside diameter of the layer is then calculated based on the cross sectional area of the layer and the calculated outside diameter of the previous layer. For the first layer, d_{j-1} is equal to the measured inside diameter of the tube, d_i.

In this investigation, all of the layers were filament wound using similar parameters and the reinforcement volume fractions are assumed to be similar for all three layers. Therefore equation 3.5 may be reduced to the following.

$$A_{CS} = \frac{2 \cdot \rho_t \cdot n_{tows} \cdot n_{circuits} \cdot n_{layers}}{V_f \cdot \rho_f \cdot \cos(\theta)}$$

$$d_o = \sqrt{\frac{4 \cdot A_{CS}}{\pi} + d_i^2} \qquad (3.6)$$

$$\bar{t}_{layer} = \frac{d_o - d_i}{2 \cdot n_{layers}}$$

$$\bar{t}_{ply} = \frac{\bar{t}_{layer}}{2}$$

The average ply thickness, $\bar{t}_{ply}$, for use in Classical Laminate Theory calculations is one half of the average layer thickness, $\bar{t}_{layer}$.

From this method a tube wall thickness of 1.162 mm was found and used to calculate the stresses presented in the following chapter. The volume fraction used for this calculation was 72.69% therefore the resin rich outside layer has been omitted from the resultant wall thickness. The effect of disregarding the resin rich layer is investigated later in this chapter. The composite tube characteristics are provided in Table 3.1.

Table 3.1: Characteristics and process parameters of glass fibre reinforced epoxy filament wound tube produced and tested.

Filament Wound Laminate Properties	Value	Source
d_i, Inside Diameter, (mm)	50.37	Measured
$d_{o,measured}$, Outside Diameter, (mm)	53.29	
d_o, Calculated Outside Diameter, (mm)	52.70	Equation 3.6
$\bar{t}_{ply}$, Calculated Average Ply Thickness, (mm)	0.194	Equation 3.6
V_r, Volume Fraction Reinforcement, (%)	72.69	Equation 3.3
V_v, Volume Fraction Voids, (%)	1.68	Equation 3.4
ρ_m, Matrix Density, (g/cm^3)	1.1445	Measured
ρ_r, Glass Fibre Density, (g/cm^3)	2.58	Manufacturers Data
ρ_t, Tow Weight, (g/1000 m)	735	
α, Winding Angle, (with respect to axis of the pipe)	±60°	Process Parameters
n_{tows}, Number of Tows in Bandwidth	8	
$n_{circuits}$, Number of Circuits Per Layer	5	
n_{layers}, Number of Layers	3	

3.3 THEORETICAL LAMINA PROPERTIES

The theoretical mechanical properties of the lamina, or individual ply, must be determined prior to calculating the laminate properties for comparison with the experimental results. The ply properties, E_{11}, E_{22}, G_{12} and ν_{12} were found using the Halpin-Tsai analytical technique and its variations. Table 3.2 provides the properties of the constituent materials and the specimen parameters relevant to the calculation of the

mechanical properties of the ply. The values provided for the glass fibre are based on the manufacturer's specifications but the shear modulus was calculated assuming the fibre is isotropic. It must be noted that these calculations neglect the existence of voids but this will have little impact on the results due to the very low volume of voids measured in the samples.

Table 3.2: Ply Constituents Mechanical Properties.

Property	Value	Source
V_r, Volume Fraction Reinforcement, (%)	72.69	Equation 3.3
V_v, Volume Fraction Voids, (%)	1.68	Equation 3.4
E_r, Fibre Modulus, (MPa)	72,400	Manufacturer
ν_r, Fibre Poisson's Ratio	0.22	Manufacturer
G_r, Fibre Shear Modulus, (MPa)	29,700	Assumed Isotropic Material
E_m, Matrix Modulus, (MPa)	3400	Manufacturer and in-house tests
ν_m, Matrix Poisson's Ratio	0.42	Ref. Hu (2002)
G_m, Matrix Shear Modulus, (MPa)	970	Assumed Isotropic Material

3.3.1 Halpin-Tsai Empirical Equations

The Halpin-Tsai equations (Halpin and Kardos, 1976) for determining the elastic properties of composite materials are derived from simplifications of the results of the self-consistent micromechanics model developed by Hill and Hermans. Hill (1964) arrived at the formulations for the longitudinal modulus and Poisson's Ratio for composites with aligned fibres as:

$$E_{11} = V_r \cdot E_r + V_m \cdot E_m - 4 \cdot \left[\frac{\nu_r - \nu_m}{\frac{1}{k_r} - \frac{1}{k_m}} \right]^2 \cdot \left(\frac{1}{k_{23}} - \frac{V_r}{k_r} - \frac{V_m}{k_m} \right) \quad 3.7$$

$$\nu_{12} = V_r \cdot \nu_r + V_m \cdot \nu_m + \left[\frac{\nu_r - \nu_m}{\frac{1}{k_r} - \frac{1}{k_m}} \right] \cdot \left(\frac{1}{k_{23}} - \frac{V_r}{k_r} - \frac{V_m}{k_m} \right) \quad 3.8$$

where k is the plane-strain bulk modulus.

Halpin and Tsai reduced these to the following form by assuming a parameter ζ that is independent of Poisson's ratio and that the final terms in Hill's equations may be neglected.

$$\frac{P}{P_m} = \frac{1 + \zeta \cdot \eta \cdot V_r}{1 - \eta \cdot V_r}$$

$$\eta = \frac{\frac{P_r}{P_m} - 1}{\frac{P_r}{P_m} + \zeta} \quad 3.9$$

In this form P is the composite property to be determined, and P_m and P_r are the complementary properties for the matrix and reinforcement, respectively. When $\zeta \rightarrow \infty$ the Halpin-Tsai equation reduces to the Rule of Mixtures (ROM):

$$P = V_r \cdot P_r + V_m \cdot P_r \quad 3.10$$

When $\zeta = 0$ it becomes the Inverse Rule of Mixtures

$$\frac{1}{P} = \frac{V_r}{P_r} + \frac{V_m}{P_m} \quad 3.11$$

For the calculation of aligned fibre reinforcement composites the Rule of Mixtures ($\zeta \rightarrow \infty$) is used for the calculation of E_{11} and ν_{12}. For E_{22} calculations $\zeta = 2$, and $\zeta = 1$ for the calculation of G_{12}. Other values of ζ are used based on the reinforcement geometry.

The results of this method are accurate for E_{11} and are suitable for ν_{12} when the matrix and reinforcement have similar Poisson's ratios. However, a large error exists in the values of E_{22} and G_{12} when calculated for volume fractions greater than 70%. Hewitt and de Malherbe (1970) suggested a correction for ζ as a function of the volume fraction.

$$\varsigma = 1 + 40 \cdot V_r^{10} \tag{3.12}$$

was found to empirically match the data for G_{12} and

$$\varsigma = 2 + 40 \cdot V_r^{10} \tag{3.13}$$

for E_{22} (Halpin and Kardos, 1976). For the calculation of ν_{12}, greater accuracy can be achieved using Hill's original formulation in equation 3.8.

The transverse shear stiffness, G_{23}, and Poisson's ratio, ν_{23}, are less studied. Hill (originally derived by Hermans) provides an estimate for G_{23} that is identical to a lower bound derived by Hashin (Tucker and Liang, 1999). More accurate values are provided using a method proposed by Clyne (1990) that uses the bulk modulus of the composite to determine the transverse Poisson's ratio (given the longitudinal Poisson's ratio) based on the material compressibility. Then

$$\nu_{23} = 1 - \nu_{21} - \frac{E_{22}}{3k_{23}} \tag{3.14}$$

and the transverse shear stiffness is then calculated assuming an isotropic material on the 2-3 plane.

The calculated ply properties are provided in Table 3.3.

Table 3.3: Resulting ply properties calculated using modified Halpin-Tsai method and constituent property values in Table 3.2.

Ply Property	Value	Source/Equation
E_{11}, Longitudinal Elastic Modulus, (MPa)	53,400	Equation 3.10
E_{22}=E_{33}, Transverse Elastic Modulus, (MPa)	23,100	Equation 3.13
ν_{12}=ν_{13}, Longitudinal Poisson's Ratio	0.27	Equation 3.8
G_{12}= G_{31}, Longitudinal Shear Modulus, (MPa)	7500	Equation 3.12
G_{23}, Transverse Shear Modulus (MPa)	7900	Assumed transversely isotropic
ν_{23}, Transverse Poisson's Ratio	0.46	Equation 3.14

3.3.2 Lamina Properties from Representative Volume Elements

The material properties of a lamina may also be predicted using numerical modelling techniques. The representative volume element (RVE) method reduces the scope of the analysis to that of a basic repeatable block of the composite material. This generally requires the assumption of a periodic distribution of reinforcement geometry and material properties. Of primary concern in such an analysis is that the applied loads and boundary conditions enforce the periodicity and that the RVE geometry reflect that of the system being modelled.

3.3.2.1 RVE Geometry

The geometry of the RVE is dependent on the assumed fibre packing arrangement. The fibre packing must be regular and periodic, however there may still be variation in RVE's due to orientations and selecting different lines of symmetry. Three packing arrangements are analysed here: square packing, diagonal packing and hexagonal packing. **Error! Reference source not found.** shows that the diagonal packing is identical to the square packing, but rotated by 45°. While square packing has been used to successfully model a number of composite materials, hexagonal packing is accepted as representative of

transversely isotropic materials such as unidirectional fibre reinforced composites. The finite element models for each of the RVE's are also shown in Figure 3.1.

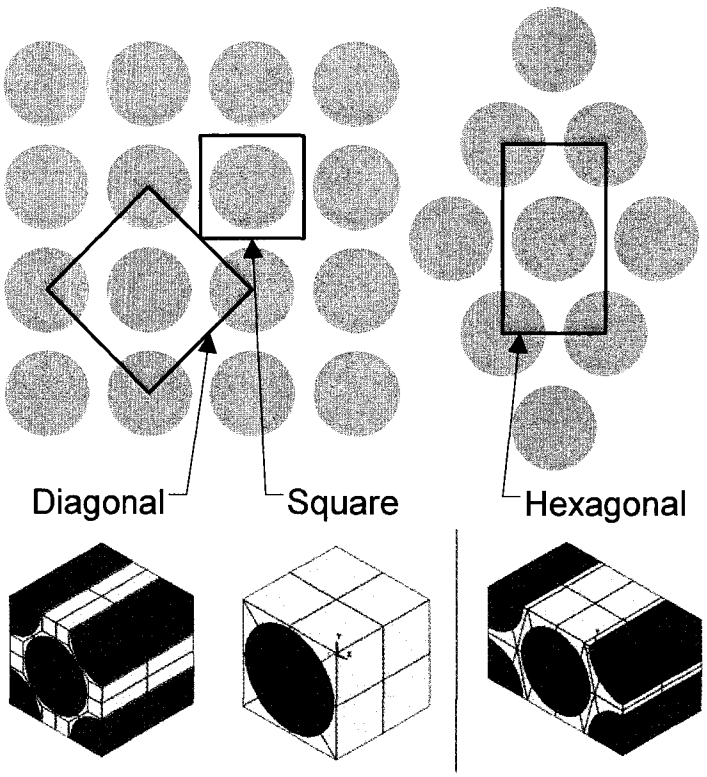

Figure 3.1: Reinforcment packing arrangements and representative volume elements.

3.3.2.2 RVE Boundary Conditions

Three dimensional finite element analysis was used to calculate the response of each RVE to a set of applied loads or displacements given appropriate constraints to reflect the periodicity of the structure. It has been common to use the simple constraint conditions of plane remains plane to enforce periodicity. While this is satisfactory for normal loads (those that result in a global stress of σ_{11}, σ_{22} or σ_{33}) for these simple, symmetric RVEs, this is not acceptable for shear loads and will result in discontinuous stress distributions. For shear loading, a more general constraint of the displacements must be specified that does not prescribe unintended tractions to maintain a specific shape. Due to the nature of the finite element method, it follows that given the correct constraints to describe

periodicity of the boundary displacements, the stress distributions along the boundaries will also be continuous and periodic.

A general boundary displacement criterion for an orthogonal coordinate system has been specified by Xia et al. (2003) to enforce periodicity of the stresses, strains and displacements through the boundaries of the RVE under all load conditions. It may be simply expressed as

$$u_i^{j+}(x,y,z) - u_i^{j-}(x,y,z) = c_i^j \qquad 3.15$$

where the subscript indicates the direction of the displacement, u, and the superscript indicates the boundary on which the displacement is applied by indicating the axis along which the normal of the surface lies and the direction, positive or negative, of the normal.

A set of boundary conditions specific for shear loading in the transverse and longitudinal directions has been used by Sun and Vaidya (1996). The benefit of their constraints is that loading is in the form of applied forces rather than displacements as above. For transverse shear, τ_{23}, these constraints are

$$\begin{aligned} &u_y^{y-} = u_y^{y+} \\ &u_z^{y-} = u_z^{y+} \\ &u_y^{z-} = u_y^{z+} \\ &u_z^{z-} = u_z^{z+} \\ &u_z^{y+} - u_z^{y-} = \delta_1 \\ &u_y^{z+} - u_y^{z-} = \delta_2 \end{aligned} \qquad \text{where force is applied} \qquad \begin{aligned} &P_y^{z+} = -P_y^{z-} \\ &P_z^{y+} = -P_z^{y-} \\ &\text{and} \\ &\ell_3 \cdot P_y^{z+} = \ell_2 \cdot P_y^{y+} \end{aligned} \qquad 3.16$$

where the same notation is used as in equation 3.15.

For longitudinal shear ,τ_{12}, the boundary constraints are

$$
\begin{aligned}
&u_x^{x-} = u_x^{x+} \\
&u_2^{x-} = u_2^{x+} \\
&u_z^{x-} = u_z^{x+} \\
&u_x^{y-} = 0 \\
&u_y^{y-} = 0 \\
&u_z^{y-} = 0 \\
&u_x^{y+} = \delta \\
&u_y^{y+} = 0
\end{aligned}
\qquad \text{where force is applied} \qquad
\begin{aligned}
&P_x^{y+} = -P_x^{y-} \\
&P_y^{x+} = -P_y^{x-} \\
&\text{and} \\
&\ell_2 \cdot P_x^{y+} = \ell_1 \cdot P_y^{x+}
\end{aligned}
\qquad 3.17
$$

In practice only one force need be specified while the remaining three are reaction forces required at finite element nodal points constrained to eliminate rigid body motion.

Equations 3.16 and 3.17 can be seen to be specific cases of equation 3.15. The results of these two constraint/load conditions have been found to give numerically identical values for the same load state, one applied through forces and the other by displacements.

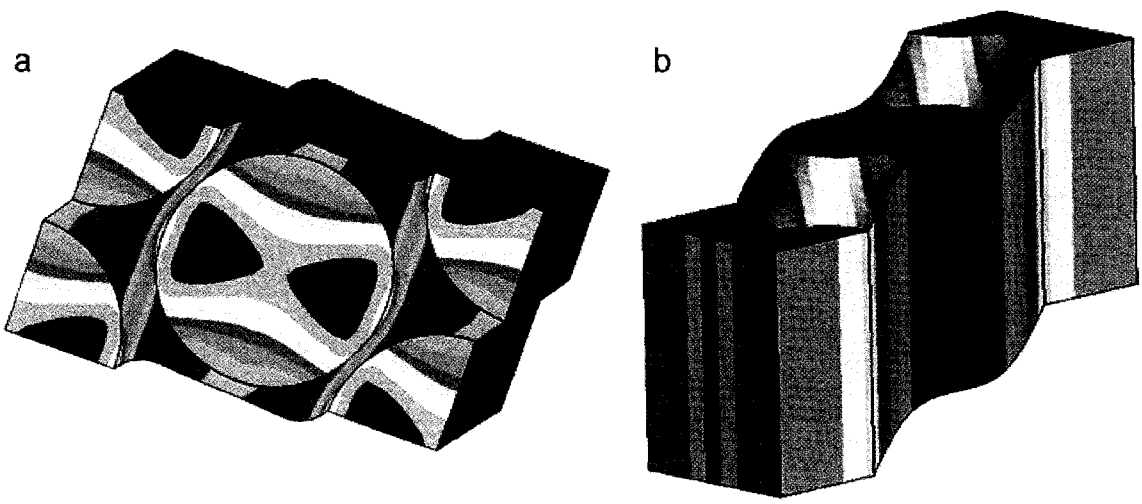

Figure 3.2: Deformed representative volume element shapes under a) transverse shear and b) longitudinal shear.

Figure 3.2 shows the irregular shape of the representative volume element deformed by transverse and longitudinal shear loads. The deformation is symmetric and periodic but clearly is not described by the plane-remains-plane criterion.

3.3.2.3 RVE Results

The results of the finite element analyses are provided in Table 3.4. Calculations were done using the material properties provided in Table 3.2 and the boundary conditions discussed in the previous section.

There is slight variation in the longitudinal properties however much greater disparity is noted in the transverse properties, E_2, E_3, G_{23} and ν_{23}. While the shear moduli for square packing and diagonal packing are similar, there is a 43% difference in the transverse moduli. Given that these two packing arrangements are similar except for orientation, one can conclude that the mechanical response of the square packing arrangement is highly anisotropic in the transverse directions. Figure 3.3 shows the results of applying a coordinate system transformation to the calculated properties, identical to the coordinate transformation procedure used in the classical laminate theory.

Table 3.4: Mechanical properties determined from elastic analysis of RVEs for cube, diagonal and hexagonal packing at 72.69% volume fraction fibre reinforcement

Mechanical Property	Square Packing	Diagonal Packing	Hexagonal Packing	Analytical Results
E_1, Longitudinal Modulus, (GPa)	53.589	53.560	53.514	53.4
E_2, Transverse Modulus (GPa)	29.437	16.714	20.832	23.1
E_3, Transverse Modulus (GPa)	29.437	16.714	20.824	23.1
G_{12}, Longitudinal Rigidity (GPa)	7.688	7.679	6.199	7.5
G_{13}, Longitudinal Rigidity (GPa)	7.688	7.679	6.196	7.5
G_{23}, Transverse Rigidity (GPa)	5.251	11.449	7.166	7.9
ν_{12}, Longitudinal Poisson's Ratio	0.263	0.263	0.269	0.27
ν_{13}, Longitudinal Poisson's Ratio	0.263	0.263	0.269	0.27
ν_{23}, Transverse Poisson's Ratio	0.287	0.595	0.452	0.46

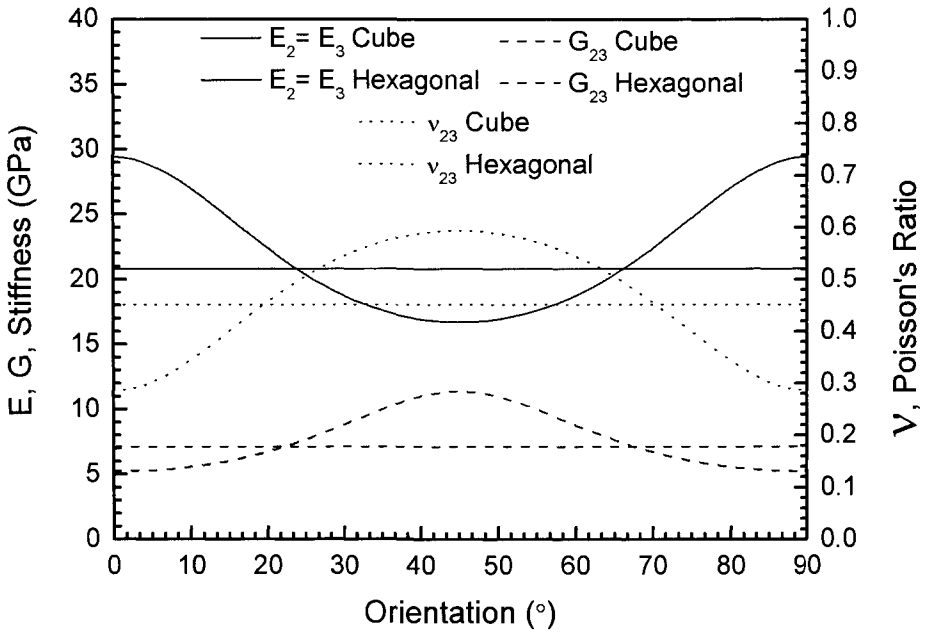

Figure 3.3: Variation of mechanical properties versus orientation for cube/diagonal and triangular packing arrangements. Vf = 72.69%.

The results for the diagonal packing arrangement are not shown since they are identical to that of the square packing but out of phase by 45°. The square packing clearly has a continuous but anisotropic transverse response where as the transverse response from hexagonal packing is very nearly isotropic. Figure 3.4, however, provides an enlargement of vertical scales and shows that the transverse results for the hexagonal packing arrangement do not yield a truly isotropic response. However, using fundamental elasticity theory it may be proven that for the hexagonal periodic array that has axis of symmetry every 60°, the response must be transversely isotropic (Edelglass, 1966). This discrepancy may be due to numerical error in the calculations or very slight dimensional errors in the model geometry.

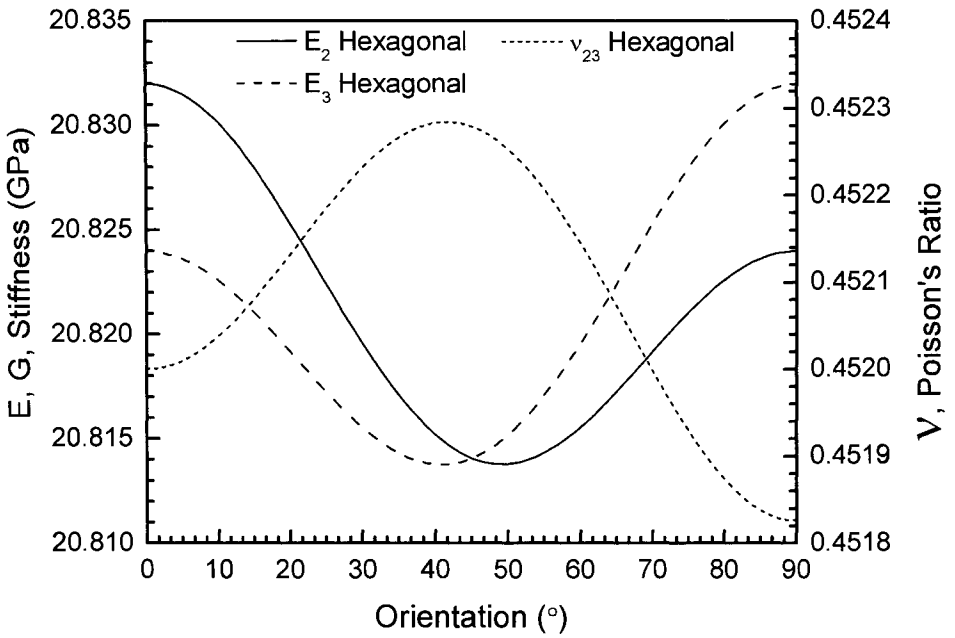

Figure 3.4: Enlargement of Stiffness and Poisson's Ratio scales to show cyclic variation of properties in the RVE for hexagonal packing. $V_f = 72.69\%$.

3.4 THEORETICAL LAMINATE PROPERTIES

Having determined the lamina properties using empirical equations and numerical methods, the next challenge is to determine the mechanical properties of the $[\pm 60°_3]_T$ laminate. Simple techniques, such as the netting analysis are often used as initial estimates in an iterative design procedure. The classical laminate theory (CLT) is a straight forward calculation of the in-plane properties using homogenised orthotropic plies. There is greater diversity in methods of calculating through-thickness properties of a laminate resulting in greater disparity of results.

3.4.1 Netting Analysis

Netting analysis is a simplified method of estimating the correct fibre reinforcement angle or the ideal load ratio by assuming that the matrix has no other purpose than to maintain the continuous fibre arrangement (i.e. The matrix does not contribute to any stiffness or strength). This is used as an initial design tool to estimate the appropriate reinforcement orientation for a given load state and provides no indication of transverse

behaviour. Given that the tubes are wound at an angle of 60° we may estimate the stress ratio at which the reinforcement fibres are ideally loaded using the netting analysis.

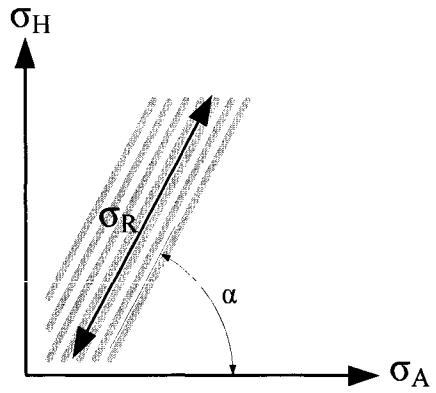

Figure 3.5 Stress components in netting analysis.

A simple derivation (Grove, 1999) is based on the equilibrium of a single ply of fibre oriented at an angle α as shown in Figure 3.5. From the translation to the primary coordinates:

$$\sigma_H = \sigma_R \cdot \sin^2 \alpha$$
$$\sigma_A = \sigma_R \cdot \cos^2 \alpha \qquad 3.18$$

For the stress ratio it follows that

$$\frac{\sigma_H}{\sigma_A} = \tan^2 \alpha \qquad 3.19$$

Therefore if α = 60° then the optimal stress ratio is exactly 3. For pressure vessel loading the stress ratio is 2 and the well known reinforcement angle is 54.7°.

3.4.2 Classical Laminate Theory

The Classical Laminate Theory (CLT) is a mathematical procedure to stack a number of orthotropic lamina, of various orientations, into a laminate. First the individual ply properties are transformed from the lamina axes to the global laminate axis using transformation on both the stress and the strain. For this the lamina are assumed homogeneous transversely isotropic sheets. Transversely isotropic suggests that the

material is isotropic around the plane with a normal parallel to the direction of reinforcement. The modified stiffness is then used in the thin plate lamination theory. This process assumes that the lamina thickness is much smaller than the other dimensions, the strains are small , stresses normal to the lamina are negligible, normals to the lamina surface remain normal after deformation, there is no strain through the thickness of the lamina, the lamina are perfectly bonded, and is an elastic analysis.

In the lamination theory thin plate analysis must be done, but unlike isotropic materials, in-plane and bending loads must be considered in combination. By enforcing the linear strain distribution through the laminate thickness, the stress distribution is found based on the modified lamina stiffnesses and their relative position within the laminate thickness. The extensional, coupling and bending stiffness matrices are found independently and then combined to produce the laminate stiffness matrix. However, in symmetric laminates the resulting coupling is balanced, the coupling matrix is eliminated and extension and bending are independent as in isotropic structures. The formulation of the classical laminate theory can be found in most introductory composite materials texts.

The properties of the $[\pm 60^{\circ}_3]_T$ laminate were then calculated using the CLT and are given in Table 3.5. The layer thicknesses were based on the calculated pipe wall thickness and the results are given in the tube cylindrical coordinate system. The tube coordinate system has the axial direction, A, along the axis of the pipe, the second direction, H, along the hoop (circumferential) direction and the third through the wall thickness, R. The results are compared to the experimental results and found to be in close agreement.

Table 3.5: $[\pm 60°_3]_T$ Glass Fibre Reinforced Epoxy Laminate Properties from Classical Laminate Theory and Experimental Results

Property	CLT Value	CLT Effective Value Resin Rich Outside Layer Added	Experimental Value
E_A, Axial Stiffness, GPa	20.6	21.3	21.2
E_H, Hoop Stiffness, GPa	33.5	34.3	36.6
ν_{AH} Poisson's Ratio	0.33	0.33	0.25
G_{AH}, Shear Modulus, GPa	14.3	14.5	

Initial laminate properties were calculated neglecting the resin rich layer on the outside surface of the tube. The extra matrix material ignored here will influence the mechanical properties because it will indeed carry load and add structure. This was verified by adding a 0.3 mm thick isotropic resin layer to the CLT analysis. When the resin rich outside layer is added the mechanical properties based the total wall thickness show the expected drop in stiffness due to the additional cross-sectional area of the soft resin. However, if effective values are determined based on the calculated wall thickness the values for elastic modulus are in close agreement with the experimental results as shown in Table 3.5.

Figure 3.6 shows the dependence of the material properties with fibre angle. It can be seen that the Poisson's ratio is sensitive to fibre angle in the vicinity of 60°, but it is not enough to explain the large difference between the calculated and measured values. It is expected that the disagreement is a result of the input values for the fibre and matrix and the use of the rule of mixtures to determine the Poisson's ratio of the ply. One must also consider that it is difficult to accurately measure the Poisson's ratio at the small strains due the sensitivity to noise and small offset values. It is also interesting to note, that within this range of reinforcement angles, 55° to 65° there is very little sensitivity of axial stiffness, E_A, to the fibre angle.

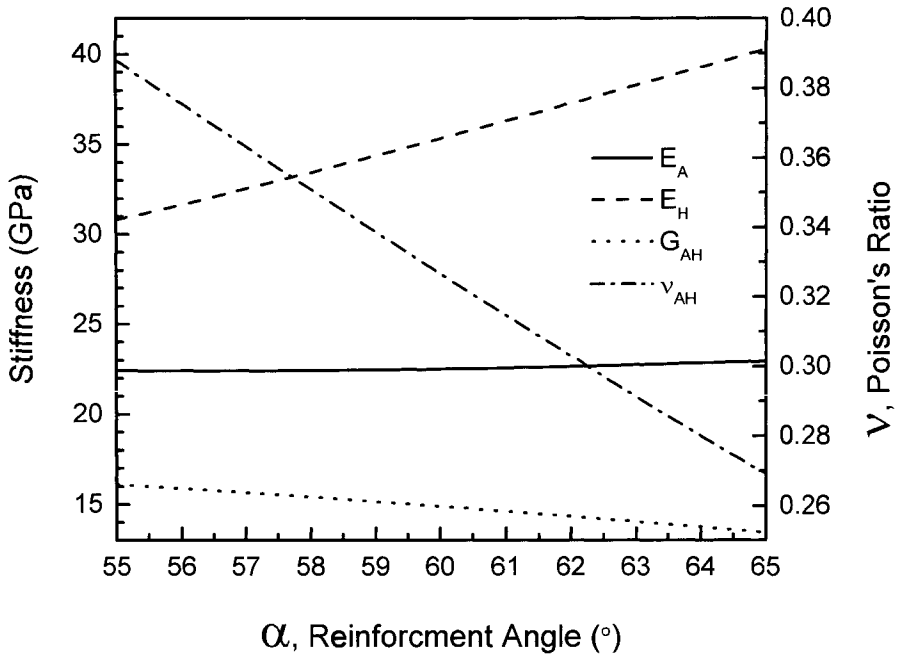

Figure 3.6: Variation of laminate mechanical properties at reinforcement angles for 55° to 65°.

3.4.3 Laminate Properties in Three Dimensions

The Classical Laminate Theory is a useful analytical method when treating laminates as plates and shells and the out of planes stresses are unimportant. The popularity of numerical methods, finite element analysis in particular, to perform complicated three-dimensional analyses now necessitates that the through-thickness material properties be known as well. Unfortunately, these properties are often much more difficult to measure therefore the availability is limited. Procedures, often an extension of the CLT have been proposed with varying degrees of complexity. Early suggestions, such as that of Enie and Rizzo (1970), have simplified the situation for balanced homogeneous laminates such that the laminate properties are the volume (or thickness) average of all the lamina properties properly transformed into the laminate coordinate system. Later approximations, are based upon constant stress and constant strain load conditions on a repeating cell (Sun and Li, 1988; Sun an Liao, 1990; Chen and Tsai, 1996; Kollar and Springer, 2003). The expressions for the stiffness tensor components may be significantly reduced for balanced laminates of a single material system. Sun and Li showed large

differences in the values of the out-of-plane Poisson's ratios. The procedure described below is from Kollar and Springer (2003).

This procedure for constructing the compliance tensor, shown in equation 3.20, is done incrementally for in-plane stresses, out-of-plane normal stresses and out-of-plane shear stresses.

$$\begin{Bmatrix} \bar{\varepsilon}_x \\ \bar{\varepsilon}_y \\ \bar{\varepsilon}_z \\ \bar{\gamma}_{yz} \\ \bar{\gamma}_{xz} \\ \bar{\gamma}_{xy} \end{Bmatrix} = [\bar{J}] \begin{Bmatrix} \bar{\sigma}_x \\ \bar{\sigma}_y \\ \bar{\sigma}_z \\ \bar{\tau}_{yz} \\ \bar{\tau}_{xz} \\ \bar{\tau}_{xy} \end{Bmatrix} \qquad 3.20$$

The first step involves specifying average in-plane stresses $\bar{\sigma}_x$, $\bar{\sigma}_y$ and $\bar{\tau}_{xy}$ while $\bar{\sigma}_z$, $\bar{\tau}_{xz}$ and $\bar{\tau}_{yz}$ remain zero. This yields

$$\begin{bmatrix} \bar{J}_{11} & \bar{J}_{12} & \bar{J}_{16} \\ \bar{J}_{21} & \bar{J}_{22} & \bar{J}_{26} \\ \bar{J}_{61} & \bar{J}_{62} & \bar{J}_{66} \end{bmatrix} = t^s [A]^{-1} \quad \text{where} \quad A_{ij} = \sum_{k=1}^{N} (\bar{Q})_k t_k^l \qquad 3.21$$

$$[\bar{J}_{31} \quad \bar{J}_{32} \quad \bar{J}_{36}] = \sum_{k=1}^{N} ([\bar{S}_{13} \quad \bar{S}_{23} \quad \bar{S}_{36}]_k t_k^l [\bar{Q}]_k)[A]^{-1} \qquad 3.22$$

Where $[\bar{Q}]$ is the transformed plane stress stiffness matrix for the lamina from the lamina stiffness tensor, $[\bar{S}]$ is the transformed three-dimension compliance tensor for a lamina, t^l is the lamina thickness, t^s is the total laminate thickness and N is the total number of lamina.

When the out-of-plane (through-thickness) normal load is applied it is found that

$$\begin{bmatrix} J_{13} \\ J_{23} \\ J_{63} \end{bmatrix} = -\begin{bmatrix} J_{11} & J_{12} & J_{16} \\ J_{21} & J_{22} & J_{26} \\ J_{61} & J_{62} & J_{66} \end{bmatrix} \frac{1}{t^s} \sum_{k=1}^{N} \left(\begin{Bmatrix} \overline{C}_{13} \\ \overline{C}_{23} \\ \overline{C}_{63} \end{Bmatrix}_k \frac{t_k^1}{(\overline{C}_{33})_k} \right) \quad 3.23$$

$$J_{33} = \frac{1}{t^s} \sum_{k=1}^{N} \left(\frac{t_k^1}{(\overline{C}_{33})_k} \right) - [J_{31} \quad J_{32} \quad J_{36}] \frac{1}{t^s} \sum_{k=1}^{N} \left(\begin{Bmatrix} \overline{C}_{13} \\ \overline{C}_{23} \\ \overline{C}_{63} \end{Bmatrix}_k \frac{t_k^1}{(\overline{C}_{33})_k} \right) \quad 3.24$$

and application of out-of-plane shear yields the following.

$$\begin{bmatrix} J_{44} & J_{45} \\ J_{54} & J_{55} \end{bmatrix} = \frac{1}{t^s} \sum_{k=1}^{N} \left(t_k^1 \begin{bmatrix} \overline{S}_{44} & \overline{S}_{45} \\ \overline{S}_{54} & \overline{S}_{55} \end{bmatrix}_k \right) \quad 3.25$$

Using the procedure described above the through-thickness mechanical properties in Table 3.6 are calculated. It is shown that the resin rich outside layer results in a significant drop in the through-thickness properties.

Table 3.6: Additional through-thickness mechanical properties for the $[\pm 60°_3]_T$ laminate calculated using ply properties provided in Table 3.3.

Property	Value	With Resin Rich Outside Layer
E_R, Radial Modulus, GPa	24.2	14.4
G_{HR}, Radial Shear Modulus, GPa	7.6	3.2
G_{AR}, Radial Shear Modulus, GPa	7.8	3.2
ν_{HR} Poisson's Ratio	0.18	0.21
ν_{AR} Poisson's Ratio	0.34	0.37

3.4.4 Laminate Properties from RVE Modelling

As in the case of the ply properties, the laminate response may be determined from a finite element analysis of a RVE representing the laminate lay-up and ply volume fractions.

3.4.4.1 Laminate RVE Geometry and Boundary Conditions

The RVE for a laminate becomes more complicated due to the representation of a number of layers of various reinforcement angles. However, representing the ±θ lay-up produced by filament winding is relatively simple using an RVE developed for the ply. Here the simple model for square packing is used to generate the laminate RVE because the other two, for diagonal and hexagonal packing, do not provide simple boundaries (ie. the RVE boundaries intersect both matrix and reinforcement).

First an RVE for a cross-ply laminate is produced by stacking the simple RVE and a copy that has been rotated through 90°. This cross-ply RVE is then rotated by 45° to produce a RVE for a ±45° lay-up. The ±60° RVE is then generated by scaling the nodal coordinates by the following parameters

$$\begin{aligned} R_H &= \ell \cdot \sqrt{2(1-\cos(180-\theta))} \\ R_A &= \ell \cdot \sqrt{2(1-\cos(\theta))} \\ R_R &= \frac{1}{\ell} \cdot \sin(\theta) \end{aligned} \qquad 3.26$$

where ℓ is the length of the side of the original cube shaped RVE. The scaling in the through laminate thickness is required to ensure that the reinforcement cross-section remains circular. The resulting RVE model is shown in Figure 3.7.

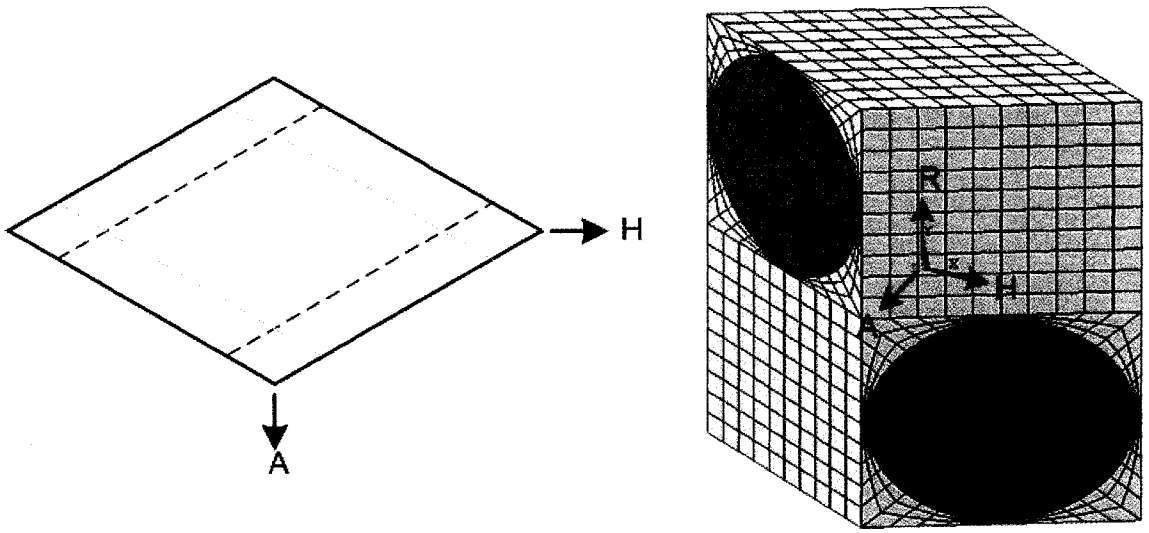

Figure 3.7: RVE used to represent the ±60° laminate in the Axial-Hoop-Radial coordinate system.

3.4.4.2 Laminate RVE Boundary Conditions

The resulting RVE is not rectangular therefore the boundary conditions described by equation 3.15 cannot be used. The more general expression by Xia et al. (2003);

$$u_i^{j+} - u_i^{j-} = \bar{\varepsilon}_{ik}\left(x_k^{j+} - x_k^{j-}\right) \qquad 3.27$$

where u is the displacement, x is the node coordinate and i, j and k are repeated indices, must be used. Due to the number of constraint equations produced a program was made which uses the cross-ply RVE to determine the boundary nodes and the ±60° RVE for the nodal coordinates. The constraint equations are saved in a file in a format that may be directly input into the finite element software. This automated method allows for the generation of displacement boundary conditions for any ±θ RVE but it must be noted that this method of generating constrain equations only works if the node meshes on each surface are identical. The generated constraint equations are a function of $\bar{\varepsilon}_{ik}$, the average strain between the surfaces upon which the opposing nodes lie.

3.4.4.3 Laminate RVE Results

Once the set of constrain equations are produced the user can enter the values for the required strains into the constraint equation file which is then input into ANSYS after the

model is generated and before solving. This was done to find the elastic and shear moduli as well as the Poisson's ratios for the laminate. The procedure for the elastic moduli required iteratively selecting the Poisson's ratios until values were found which resulted in no transverse loading. The values of the mechanical properties are provided in Table 3.7.

Table 3.7: Mechanical properties determined from the RVE representing the laminate.

Property	Calculated Value
E_A, Axial Modulus, GPa	23.6
E_H, Hoop Modulus, GPa	34.1
E_R, Radial Modulus, GPa	25.6
ν_{AH} Poisson's Ratio	0.36
ν_{HR} Poisson's Ratio	0.18
ν_{AR} Poisson's Ratio	0.26
G_{AH}, Shear Modulus, GPa	14.0
G_{HR}, Shear Modulus, GPa	6.2
G_{AR}, Shear Modulus, GPa	5.9

A comparison of these values to those in calculated by the CLT in Table 3.5 and Table 3.6 shows that the values are similar. It cannot be expected that this RVE, constructed from the simple cube packing RVE, will produce entirely accurate results since it was previously demonstrated that the simple cube packing RVE has an anisotropic elastic response. The simple cube packing RVE for the ply resulted in high transverse moduli estimates and this is reflected in the calculated values, E_R and E_A.

3.5 THERMAL EXPANSION

A large difference in the coefficients of thermal expansion of the reinforcement and matrix materials often leads to residual stresses prior to external loading. Therefore it is important that the thermo-mechanical properties are known and the effects of temperature change understood. For the composite studied here, the glass reinforcement has a

coefficient of $\alpha_r = 5.4x10^{-6}$ /°C where as the value is $\alpha_m = 56x10^{-6}$ /°C for the epoxy matrix. Formulas from Schapery (1968), based on energy principles, may be used to estimate the coefficients of thermal expansion for the ply.

$$\alpha_1 = \frac{E_r\alpha_r V_r + E_m\alpha_m(1-V_r)}{E_r V_r + E_m(1-V_r)} \qquad 3.28$$

$$\alpha_2 = \alpha_r V_r(1+\nu_r) + \alpha_m(1-V_r)(1+\nu_m) - \nu_{12}\alpha_1 \qquad 3.29$$

These values may then be used to calculate laminate coefficients of thermal expansion using lamination theory. The resulting ply and laminate coefficients are provided in Table 3.8.

Table 3.8: Coefficients of thermal expansion of constituents, ply and laminate. ($V_f = 72.69\%$)

	Coefficients of Thermal Expansion ($x10^{-6}$ /°C)	
Constituents		
Glass Fibre	5.4	
Epoxy Matrix	56	
Ply (72.69% reinforcement by volume fraction)		
α_1	6.1	
α_2	24.9	
$[\pm 60°_3]_S$ Laminate		
	Without Resin Rich Outer Layer	**With Resin Rich Outer Layer**
α_A	20.7	22.1
α_H	6.4	7.2

Thermal stresses occur due to the thermal mismatch between the fibre and the matrix and due to the constraints within the laminate. When the composite is cooled from cure temperature to working temperature the epoxy matrix shrinks considerably more than the

glass fibre. This results in compressive stresses within the reinforcement and tensile stresses in the matrix. It is often considered that the composite becomes rigid at the glass transition temperature, the temperature at which long-range segment motion is disabled. This is a temperature of approximately 110°C for the EPON 826/EPI-CURE 9551 epoxy system. Here, it will be assumed that the composite becomes an elastic solid at the glass transition temperature, 110°C, and that it cools to a working temperature of 20°C at a constant, linear coefficient of thermal expansion and a constant stiffness.

To determine the laminate stresses due to the angle-ply lay-up, the ply coefficients of expansion must be transformed to the laminate coordinate system using equation 3.30.

$$\begin{aligned} \alpha_x^{ply} &= \alpha_1 \cos^2\theta + \alpha_2 \sin^2\theta \\ \alpha_y^{ply} &= \alpha_1 \sin^2\theta + \alpha_2 \cos^2\theta \\ \alpha_{xy}^{ply} &= 2(\alpha_1 - \alpha_2)\cos\theta\sin\theta \end{aligned} \qquad 3.30$$

The thermal strains due to a 90°C temperature drop are provided in Table 3.9.

Table 3.9: Thermal strains in laminate and ply (in laminate coordinate system) for a 90°C temperature drop.

	Axial Strain, ε_A^{therm}, (%)	**Hoop Strain, ε_H^{therm}, (%)**	**Shear Strain, γ_{AH}^{therm} (%)**
Laminate	-0.186	-0.057	
Ply (θ = 60°)	-0.182	-0.097	0.147
Difference	-0.004	0.040	-0.147

Therefore, there is a large difference in the resulting thermal strain in the laminate and that in the ply. In their native coordinate systems, the temperature change does not result in shear deformation in either the laminate or the ply. However, when the ply strains are transformed into the laminate coordinate system significant shear strains result. This constraint on the ply, within the laminate, results in thermally induced stresses which may be calculated by multiplying the transformed ply stiffness by this difference in strain and then transformed into the ply coordinate system. The resulting ply stresses for a

90 °C temperature drop in a $[\pm 60°_3]_T$ laminate are $\sigma_1 = -14.5$ MPa, $\sigma_2 = 14.5$ MPa, $\tau_{12} = 8.4$ MPa.

These stresses were calculated using the linear elastic lamination theory with constant materials properties. However it is likely that there is minor variation in the coefficient of thermal expansion of the matrix and possibly large variation of the modulus for the temperature region assumed. For greater accuracy, fibre tensioning and mandrel stiffness and thermal expansion must also be evaluated. Pre-tension in the fibres will reduce the compressive residual stresses in the reinforcement. A mandrel that has different thermal expansion properties from the laminate may result in additional deformation constraint during the cooling process and therefore alter the residual distribution. The mandrel used in the production of these specimens was solid steel with a much greater stiffness than the laminate and a coefficient of thermal expansion of 11.7×10^{-6}/°C that is larger than the laminate hoop direction, 6.4×10^{-6}/°C.

Recent analyses of glass fibre reinforced epoxy RVE's by finite element analysis show that if the matrix is viscoelastic, the residual thermal stresses will relax. Chen et al. (2001) have shown that within 40 hours the residual stresses relaxed to less than 20% of the original values. However, if one is using a strain based criteria, then the residual strain may be of consequence (Zhang et al., 2004). It is generally regarded that analysis of residual stresses and strains due to processing is a necessary part of composite component design and failure prediction (Soden et al., 1998).

3.6 COMPARISON OF IDEALISED FIBRE DISTRIBUTIONS AND LAMINATE TO FILAMENT WOUND STRUCTURE

The previous analytical, empirical and numerical calculations of ply and laminate properties made assumptions about the structure of the composite on a microscale concerning fibre distribution and mesoscale concerning laminae stacking.

The Halpin-Tsai equations, and their modifications, are generally based on fibre distributions in which the reinforcement is separated by an amount of matrix material such that the nearest neighbours are a number of fibre diameters away. Many of the

methods to estimate composite properties originate from methods assuming a single fibre in an infinite matrix. Figure 3.8, a micrograph of the $[\pm 60°_3]_T$ filament wound glass fibre reinforced tube along the tube hoop or circumferential direction indicates that the fibres are not well dispersed and there is little matrix separating them.

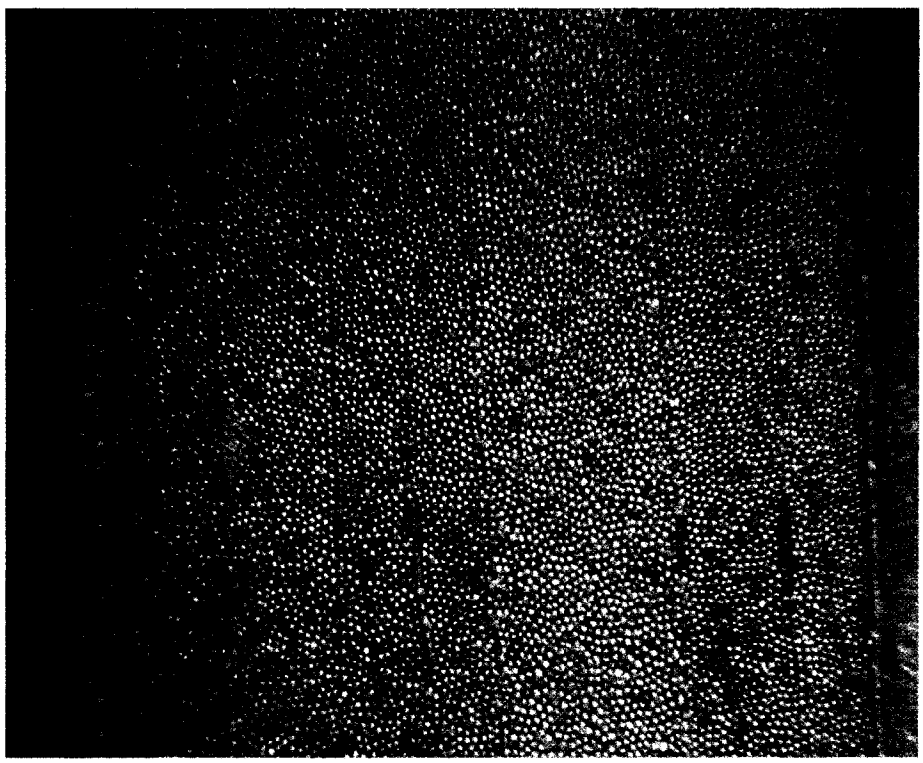

Figure 3.8: Micrograph of the $[\pm 60°_3]_T$ filament wound tube cross-section along the circumferential axis. Resin-rich outside layer is clearly visible on the left where the dark line is the outside of the filament wound tube as produced.

The resin-rich outside layer is clearly visible in this image and the inconsistency of its thickness is obvious. No such layer exists at the interior surface at the right of the image. Furthermore, resin-rich locations are observed within the composite structure.

Figure 3.8 also shows clear vertical lines demarcating the distinct layers within the laminate. This is even more visible in Figure 3.9 which is a micrograph taken along the axial direction of the tube.

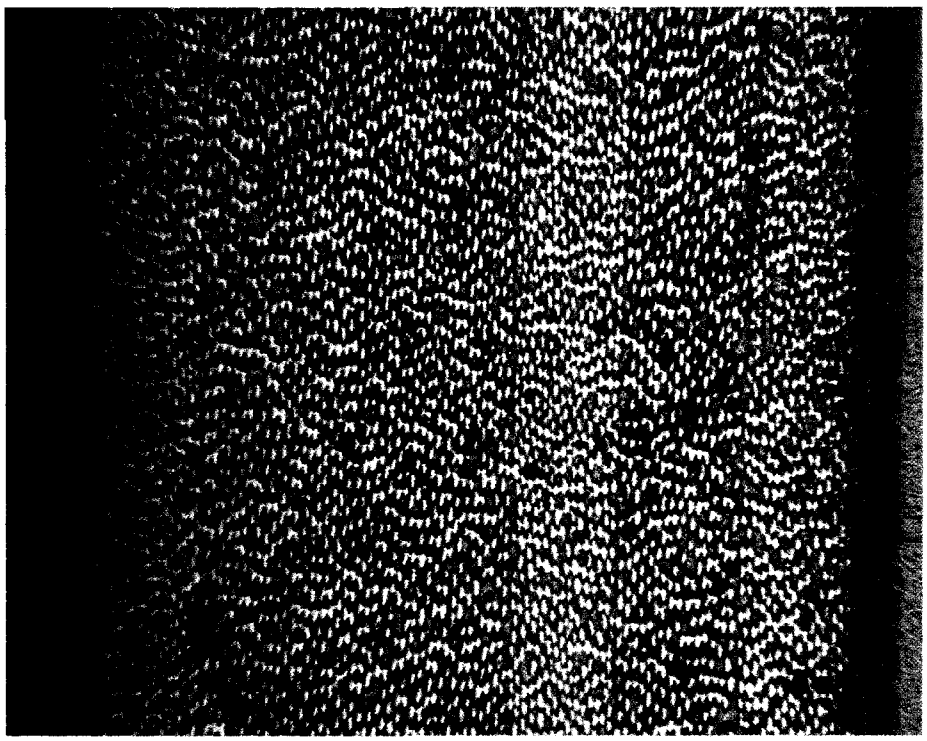

Figure 3.9: Micrograph of the $[\pm 60°_3]_T$ filament wound tube cross-section along the axial direction. Outer surface is on the left. Plane of the image is 30° off the axis of the fibres therefore fibres appear as ellipses.

The distinct banded structure of the +60° and -60° laminae are clearly visible. It is also apparent that the outer layers are not as well consolidated as the inner layers and clearly have a lower volume fraction of reinforcement.

These images demonstrate that the fibres follow neither a square of hexagonal packing structure as modeled by finite element analysis in Figure 3.1. However, if the fibre arrangement is random the average distribution over a large number of fibres may be assumed to be periodic for the prediction of global properties. Thus, there is some range of scale to which homogenisation of the composite material is valid with respect to parameters such as stiffness and Poisson's ratio. However local and distribution dependent effects such as damage initiation and crack path require knowledge of greater detail than employed in the analyses used here.

With respect to the analysis of the laminate, it is clear that each layer does not contain only one fibre layer through its depth as suggested by the representative volume element

in Figure 3.7. The results are in reasonable agreement with experimental data because of the random distribution of fibres and the scale at which the properties are desired is within a range that homogenisation is acceptable.

An example of a void at the boundary between two layers and associated with a resin rich zone is shown in Figure 3.10.

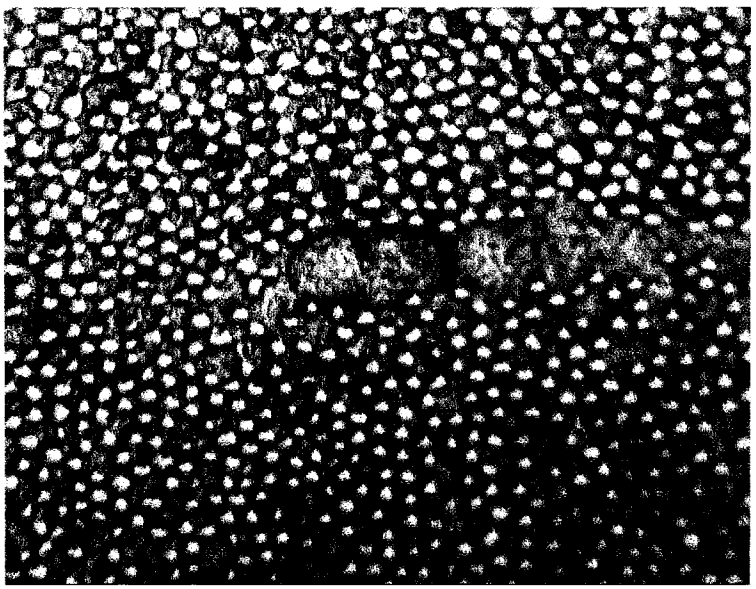

Figure 3.10: Micrograph from a $[\pm 60°_3]_T$ filament wound tube showing a void.

Voids are the result of entrapped gases either in the resin or produced by the cure reaction of the epoxy. From observations of the composite, it appears that the voids are mostly located at resin-rich zones where the bubbles can coalesce and displace resin. The gases would not be able to displace the stiff, tensioned fibres.

No effort was made to use image processing to evaluate fibre and void volume fractions in the filament wound composite structure. Such methods require numerous cross-section images, or areas, to adequately describe the volume of the composite. A carefully controlled burn-out test will yield accurate averages of fibre and void volume fraction and imaging techniques are found to yield similar results.

3.7 SUMMARY OF CHARACTERISTICS AND MECHANICAL PROPERTIES

The mechanical properties of the $[\pm 60°_3]_T$ laminate were determined from the measurements of constituent volume fractions using standard analytical techniques and numerical analysis. The volume fraction of glass fibre reinforcement was found to be 72.69% and the volume fraction of voids 1.68% using the ASTM burn-out procedure. This procedure was conducted on samples with and without the resin rich outside layer. The low volume of voids is consistent with a high quality composite component.

The volume fraction of reinforcement was used in the well known empirical Halpin-Tsai equations to determine the lamina properties. Various modifications of the original equations are found to improve the accuracy for material systems with large fractions of reinforcement. These results were found to be in close agreement with those from the finite element analysis of a hexagonal fibre packing representative volume element. The ply properties were then employed in the classical laminate theory to determine the in-plane laminate properties. These were found to be in close agreement with the experimental values and were improved by including the resin rich outside layer in the CLT analysis. Through-thickness values were then calculated for use in three-dimensional finite element modelling. The three-dimensional mechanical properties calculated compared well with those found from an RVE of the laminate.

Finally, the thermal residual stresses were evaluated. These stresses result from the large difference in the coefficients of expansion of the matrix and the reinforcement and the constraint on the ply within the laminate. Longitudinal and transverse residual thermal stresses were found to have a magnitude of 14.5 MPa.

The resulting calculated mechanical properties for the $[\pm 60°_3]_T$ E-glass fibre/epoxy filament wound tubes are compared to the available data measured from the experimental results in Table 3.10. The calculated in-plane properties are shown to have better agreement when a resin rich outside layer is included in the analyses.

Table 3.10: Calculated and measured mechanical properties of $[\pm 60°_3]_T$ E-glass fibre/epoxy filament wound tubes. Only E_A, E_H and ν_{AH} were measured.

Property	CLT & 3D Value	RVE Value	Experimental Value
E_A, Axial Modulus, GPa	20.6	23.6	21.2
E_H, Hoop Modulus, GPa	33.5	34.1	36.6
E_R, Radial Modulus, GPa	24.2	25.6	
ν_{AH} Poisson's Ratio	0.33	0.36	0.25
ν_{HR} Poisson's Ratio	0.18	0.18	
ν_{AR} Poisson's Ratio	0.34	0.26	
G_{AH}, Shear Modulus, GPa	14.3	14.0	
G_{HR}, Shear Modulus, GPa	7.6	6.2	
G_{AR}, Shear Modulus, GPa	7.8	5.9	
α_A, Coefficient of Thermal Expansion, ($x10^{-6}$ /°C)	20.7		
α_H, Coefficient of Thermal Expansion, ($x10^{-6}$ /°C)	6.4		

CHAPTER 4 [±60°3]T FILAMENT WOUND GLASS FIBRE REINFORCED EPOXY TUBES: EXPERIMENTAL FIRST FAILURE AND STRESS-STRAIN RESPONSE

The failure of composite materials results from a number of mechanisms due to failure of single constituents or the interaction of multiple constituents. Therefore, depending on the load, different failure mechanisms are encountered leading to a stress state dependent failure stress. While the prediction of the failure stresses is the topic of many papers and elaborate programs, such as the "World-Wide Failure Exercise", there is no reliable method to predict the failure stress of a composite laminate for the full load spectrum. In this chapter the results of the multiaxial tests on the $[\pm 60°_3]_T$ E-glass/epoxy filament wound tubes are provided. First macroscopic descriptions of the failures are provided followed by the stress-strain responses. Failure envelopes for stress and strain in both the specimen coordinate system and ply coordinate system are provided.

This data is then discussed with reference to the appropriateness of stress and strain transformations to the ply coordinate system and the stress distribution due to the constraint of the grip system and barrelling of the specimen.

4.1 POST FAILURE DESCRIPTIONS

After testing, the specimens were visually inspected and the observations were recorded. Details of fracture orientation, fibre breakage and matrix failure were noted however, the extent of the damage was often dependent on the actual axial displacement applied. Due to the requirement of initial axial test loads to compensate for initial system pressure, the failed specimen was continued to be loaded even though the function generator had returned to zero command signal. Thus the extent of damage in the specimen was often much more than at the recorded failure load.

Changes in appearance such as change in colour and opaqueness were observed as were more defined failure mechanisms such as striations parallel to the fibres, fibre fracture and fibre realignment. However, it is more difficult to note if the white striations are distinct as is the case with transverse cracking or opaque as associated with delamination (Jones and Hull, 1979).

In the following descriptions there is often a reference to a crack. This is more so a fracture that occurs parallel to one band of reinforcement, for example in the +60° direction, while the complementary reinforcement, in the -60° direction, is fractured. The label "complementary" is used to avoid the inappropriate use of "transverse" to describe the reinforcement that does not intersect at 90°.

0:1, Axial Tension

Specimens tested under the 0:1 stress ratio exhibited catastrophic failure by a dominant helical crack which, under large deformation, extended over the entire gauge length. The crack was observed to be located along the side of an exterior band of fibres and the complementary layers on the opposite side of the crack exhibited failure of the matrix such that the fibres were no longer supported. This is clearly demonstrated in Figure 4.1. Under the large deformations the transverse fibres had failed near the crack resulting in a brush like appearance. Fine white striations parallel to the reinforcement were visible over the surface of the tube. On the interior surface of the tube, transverse plies had severe matrix damage and the plies had delaminated in the vicinity of the crack resulting in a wrinkled appearance.

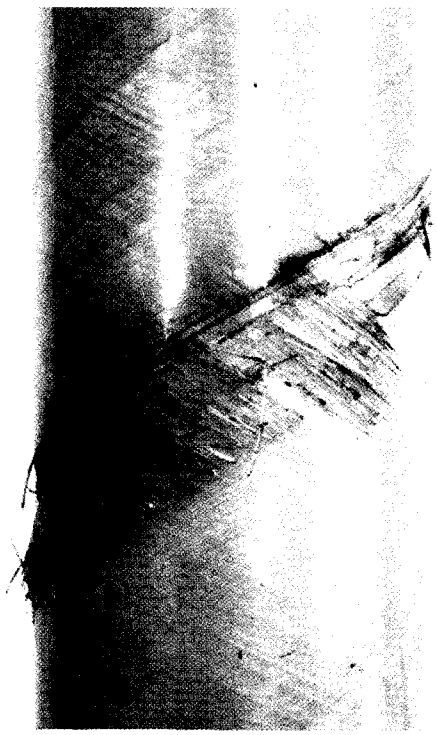

Figure 4.1: Helical crack leading to failure under the 0:1 stress ratio.

1:1, Equibiaxial Load

The specimen tested under this load ratio failed by helical crack similar to the axial load case. Failed reinforcement layers, complementary to the helical crack, displayed coarse brush-like fractures. Under large axial deformation the reinforcement in the vicinity of the failure showed significant realignment. Fine white striations were observed over the surface of the entire tube.

2:1, Pressure Vessel Loading

Specimens tested under the 2:1 stress ratio exhibited a functional failure by weepage. Since no liner was used, structural failure could not be achieved. The weepage was evident as the formation of droplets of the pressurisation fluid uniformly over the surface of the gauge length. As the internal pressure increased the specimen became covered with a film of fluid and eventually the fluid was visibly dripping from the apparatus. Post failure examination found the only evidence of damage to be fine striations over the

entire surface of the specimen. The striations were discoloured by the yellow colour of the pressurisation fluid.

≈3.5:1, Constrained Axial Extension, Pipe in the Ground

In this test case the axial position of the specimen grips was held constant throughout the test. Therefore, the axial load was controlled such that a global axial strain of zero was maintained. This resulted in a variable stress ratio as the relationships between the hoop and axial modulii and the strain ratios changed due to nonlinear effects including damage. This load case corresponds to a standard pipeline installation where the axial motion is constrained by the surrounding soil, elbows or bends in the pipe.

Under this load condition, the tube failed by weepage as in the 2:1 stress ratio. However, it was observed that the weepage was not uniform over the specimen surface, but concentrated towards grips. The tested specimen was uniformly covered with fine white striations aligned parallel to the reinforcement but otherwise appeared undamaged on the exterior and interior.

4:1, 4.5:1 and 5.5:1

The specimens tested at stress ratios of 4:1 and 4.5:1 failed by localised leakage. All fluid was lost by approximately three to five confined jets within 20 mm of the grip. Damage sites on the exterior of the tube were characterized by small zones of slight lifting of the outside layer. It was observed that once leakage started, and as the test progressed, the direction of the jets of fluid would change and sites would become inactive as new sites erupted. The tube appearance changed from transparent to an overall opaque white appearance due to coarse striations parallel to the reinforcement over the entire surface. These less defined striations are associated with delaminations (Jones and Hull, 1979). While the specimen tested at a stress ratio of 5.5:1, shown in Figure 4.2, failed in a similar manner, the leak occurred at the centre of the gauge length. It was observed that the specimen was discoloured by the pressurisation oil in a small zone around the leak suggesting delamination of at least the outer layers.

Figure 4.2: Local damage leading to failure by jet leakage under 5.5:1 stress ratio

7:1, Hoop Dominated Axial Tension

Failure under this hoop dominated load condition resulted in catastrophic separation of the specimen into two pieces. The rupture occurred near the centre of the gauge length. The failure occurred by two short helical cracks which each wrap half way around the circumference on opposite sides of the tube. Each crack runs along a reinforcement band but do not show the brush like failure of the complementary angle plies like the helical cracks described above. At the intersection of the helical cracks the tube wall has burst resulting in a very coarse brush like failure along the axis of the tube. This burst extends only approximately 30 mm. Opaque white striations parallel to the reinforcement were observed near the failure.

1:0, Pure Hoop Stress,

This functional failure was by burst in the middle of the gauge length and resulted in complete separation into halves as observed in Figure 4.3. All fibres were clearly broken in both winding orientations and the matrix was thoroughly damaged resulting in a very fine brush-like appearance of the failed reinforcement. This is associated with the complete removal of the matrix due to cracking under high fibre strains. The surface of the pipe showed many opaque white striations parallel to the reinforcement. This "whitening" of the pipe has been described as crazing due to the high shear stress, by Rousseau et al. (1999).

Figure 4.3: Rupture failure under hoop stress loading (stress ratio 1:0).

7:-1, Hoop Dominated Axial Compression

Under this hoop stress dominated case, failure, by complete separation, occurred at the centre of the gauge section. The interior and exterior surfaces remained intact away from the failure but extensive opaque white striations were visible over the surface. The specimens also displayed a significant amount of crush due to the action of the axial actuator.

2:-1

Failure under the 2:-1 stress ratio was a burst resulting in complete separation of the specimen into two pieces. Post failure examination found that the dominant fracture was near the end of the gauge length and consisted of two short helical cracks meeting at two locations, on opposite sides of the tube. The cracks were parallel to a band of reinforcement and the layers of complementary reinforcement displayed a coarse brush-like fracture. Less interior damage was visible than in the more axial compression dominated load cases of 0:-1 and 1:-1.

1:-1, Pure Shear

This stress ratio results in pure shear when the stress axes are rotated by 45°. However, the 45° transformation does not correspond to the winding angle and thus the shear stress produced is not directed parallel or perpendicular to the reinforcement. To achieve a maximum shear parallel to the reinforcement a shear component must be superimposed on this load condition to produce a Stress Ratio 1:-1:±0.577 (σ_H:σ_A:τ_{HA}). This load condition could not be produced on the apparatus used.

Failure under the 1:-1 stress ratio was by two short helical cracks as described above and shown in Figure 4.4. However one specimen did have a large helical crack due to extended axial crush by the apparatus. The corresponding reinforcement layers showed little fraying of the fibres, the matrix remained intact. White striations, parallel to the reinforcement, were observed over the surface of the tested tube.

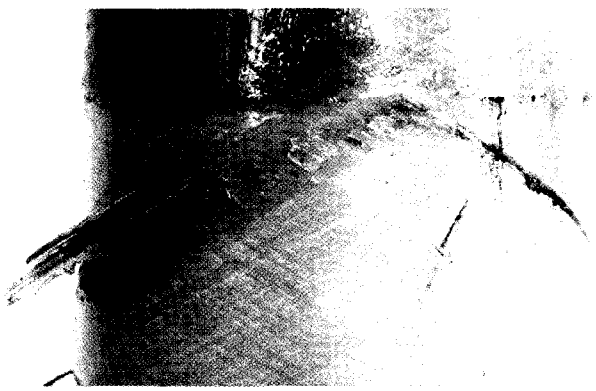

Figure 4.4: Intersecting helical cracks observed after failure under 1:-1 stress ratio.

0:-1, Axial Compression

Demonstrated in the 0:-1 stress ratio, the damage is characterized by two helical cracks parallel to the fibres that intersect in two locations on opposite sides of the tube. Figure 4.5 shows how the cracks occurred along the edge of a bandwidth and matrix failure is observed by the fraying and realignment of the complementary reinforcement in a band along one side of the cracks. This matrix damage did not occur along the full length of the crack. Under large deformation extreme local fibre realignment of the transverse fibres was observed along the helical crack.

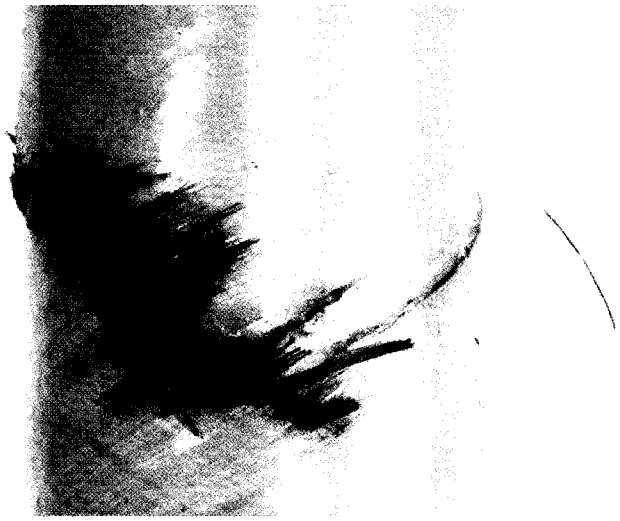

Figure 4.5: Intersecting helical cracks resulting from axial compression (stress ratio 0:-1).

4.2 OBSERVED FAILURE MODES

Due to the non-homogeneous and anisotropic nature of the composite different failure mechanisms were observed for the various internal pressure/axial load combinations. Failures occurred by matrix cracking, fibre breakage, shear parallel to the reinforcement and combinations of these three dominant mechanisms. Here they will be divided in five distinct failure modes: tensile separation, weepage, jet leakage, burst and axial crush. Failures are not confined to one of these modes. For example, all of the failures with appreciable internal pressure, stress ratios of 7:1 to 7:-1 had indications of burst but the ratios of 1:0 and 7:-1 also had indications of axial crush. Distinct boundaries cannot be drawn between the theses failure modes from the observations made in this investigation

4.2.1 Tensile Axial Separation

Tensile axial separation was found to occur under stress ratios of 0:1 and 1:1. It is characterised by a dominant helical crack parallel to a band of reinforcement and extending around the specimen as the axial deformation increases. Break down of matrix allows for realignment of the complementary reinforcement but as the deformation is increased the fibres are broken, resulting in the brush like failure surface. Axial tension produced fine white striations, consistent with matrix cracking, over the entire surface of the specimen.

4.2.2 Weepage

The functional failure under the 2:1 stress ratio is characterised by the formation of droplets uniformly distributed on the exterior surface of the composite tube. This changes to oozing of the fluid as the internal pressure is increased. This behaviour has been described in many publications and Rousseau et al. (1999) relate the weepage sites to cross-overs formed during the filament winding process. Where weepage occurred, the fine striations on the surface of the specimen were discoloured indicating that the matrix cracks were filled with the pressurisation fluid.

4.2.3 Confined Jet Leakage

This mode of failure was observed in the tests with stress ratios of 4:1, 4.5:1 and 5.5:1. It is characterised by small jets of fluid that spray from the composite tube. The intensity of the jets increases as pressure is increased and direction of jet changes as the composite structure deforms. The location of the jets is generally near the grips and roughly corresponds with the position of maximum axial stress determined by the finite element analysis in Chapter 2, Figure 2.8 to Figure 2.11. This type of failure has been described by Ellyin and Martens (2001) who tested thick walled multi-angle laminates as well as by Soden et al. (1989) from tests on ±55° angle-plies.

4.2.4 Burst

Observed under the 7:1 load case, failure is a sudden explosive burst during approximately linear behaviour. The primary failure mechanism is fibre failure. Damage is around the entire circumference but along a short distance of the gauge length. Fracture of the fibre reinforcement and destruction of the matrix leads to complete separation of the specimen into two pieces. The complete destruction of the matrix and fine bruch appearance are the result of the fibre strains under hoop loads.

4.2.5 Axial Crush

This mode was demonstrated under stress ratios with compressive axial strain, stress ratios 1:0 to 0:-1, but was most clearly shown at the 0:-1 stress ratio. The damage is characterized by two helical cracks parallel to the fibres that intersect in two locations on

opposite sides of the tubes. While local buckling of the tube cannot be discounted, global buckling was not observed and specimens with gauge lengths of 127 mm and 254 mm yielded very similar results. Under large deformation the matrix has fractured reducing the constraint on the fibres and local fibre realignment of the complementary reinforcement is observed. Soden et al. (1989) tested ±55° tubes of various thicknesses and showed that compressive strength was low for thin-walled tubes of three layers and 30% higher when the thickness was increased to seven layers. They concluded that the tube failure was a combination of local shell buckling and matrix failure. The stress-strain plots and stress failure envelopes, provided in the following sections, do not provide any indication of specimen buckling.

4.3 STRESS/STRAIN RESPONSE

The stress/strain response of the composite tubes at various stress ratios is shown in Figure 4.6 to Figure 4.11 and was found to be highly dependent on the applied stress ratio. The hoop stress vs. hoop strain paths are shown separately from the axial stress vs. axial strain plots for clarity. Also shown on the figures, as a symbol, is the point of functional failure defined as structural collapse, initiation of leakage or burst. The anisotropic behaviour of the composite system is highlighted by the distinct stress/strain responses in axial tension and axial compression. The behaviour of this composite system tends to be very non linear. In the axial direction the tension and compression stress strain curves are initially very similar, however much greater strain magnitudes are achieved under compression.

Care must be taken when considering the strain measurements as they are taken on the exterior surface of the tube and the values may be dependent on the exact location of the strain gauges on the fibre architecture (Lang and Chou, 1998). Also, the high strains associated with failure may lead to debonding of the strain gauges and erroneous readings. The strains recorded in these tests were continuous and compared well to values estimated using the cross-head movement of the material testing system.

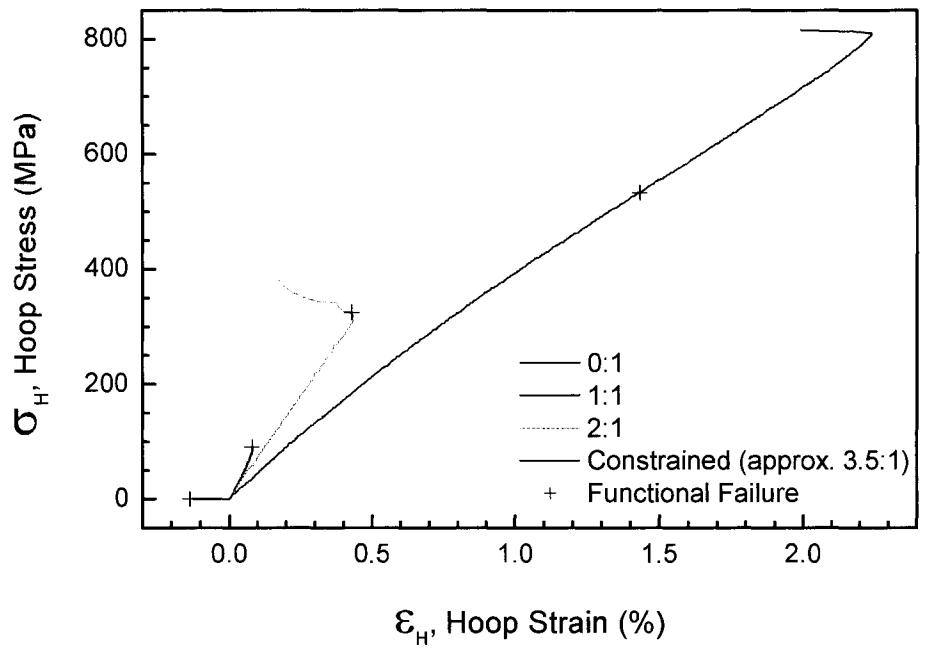

Figure 4.6: Hoop stress-strain response and functional failure of composite tube at tested hoop stress/axial stress ratios of 0:1, 1:1, 2:1 and with constrained axial deformation.

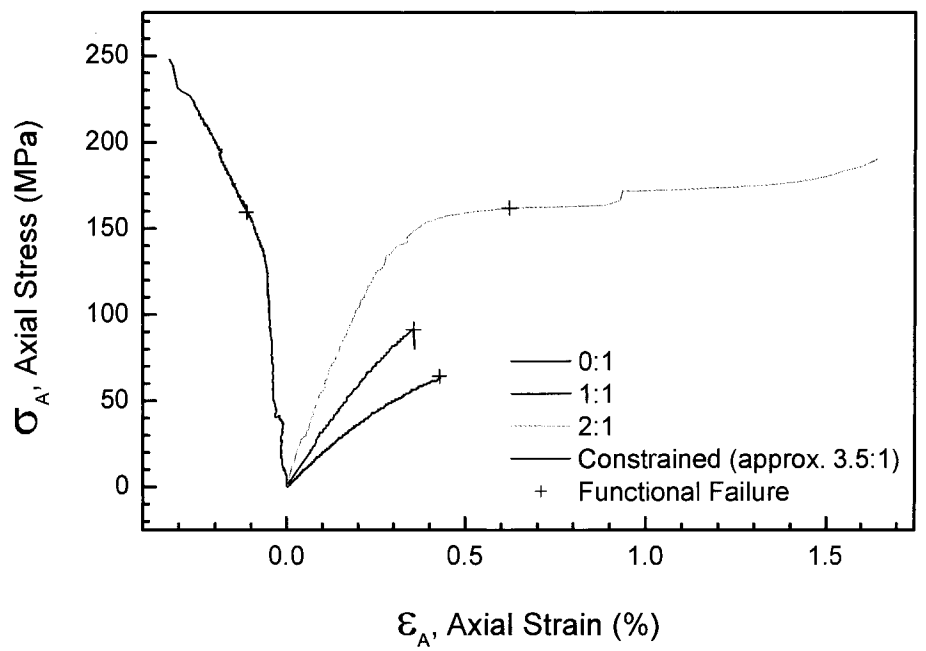

Figure 4.7: Axial stress-strain response and functional failure of composite tube at tested hoop stress/axial stress ratios of 0:1, 1:1, 2:1 and with constrained axial deformation.

A very unusual stress/strain response is displayed for the 2:1 stress ratio shown in Figure 4.6. After weepage failure, the loading continues until the volume of the intensifier is exhausted. The point of weepage coincides with a change in the stiffness allowing for large axial deformations and the apparent stiffness in the hoop direction changes to a negative value so that increasing pressure/axial load leads to negative hoop strain. As the stress ratio is increased (i.e. greater hoop stress) the behaviour becomes "more linear" and the failures more abrupt and catastrophic.

Figure 4.8 and Figure 4.9 provide the results for the hoop dominated load tests. The four stress ratios in this range all show a characteristic gentle change in stiffness at approximately 0.5% strain. In fact the hoop stiffness is observed to remain constant even as the jet leakage initiates marking the point of specimen failure. This "knee" is also observed in the axial response but at varying axial strains. It is noted that under hoop stress loading only, the maximum hoop strain achieved was 3.1% while the magnitude of the compressive axial strain was greater than 4.0%.

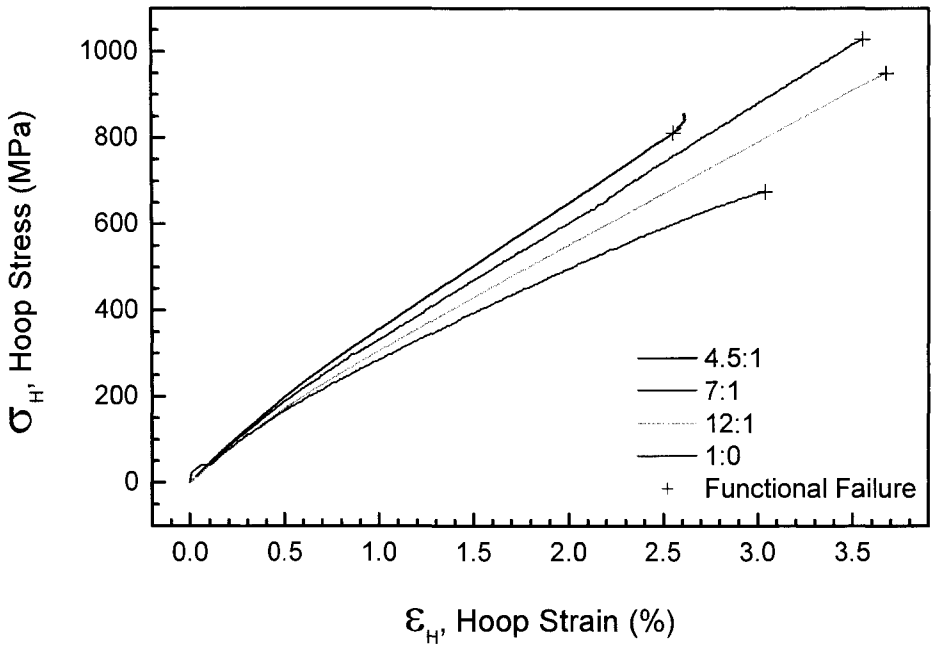

Figure 4.8: Hoop stress-strain response and functional failure of composite tube at tested hoop stress/axial stress ratios of 4.5:1, 7:1, 12:1 and 1:0.

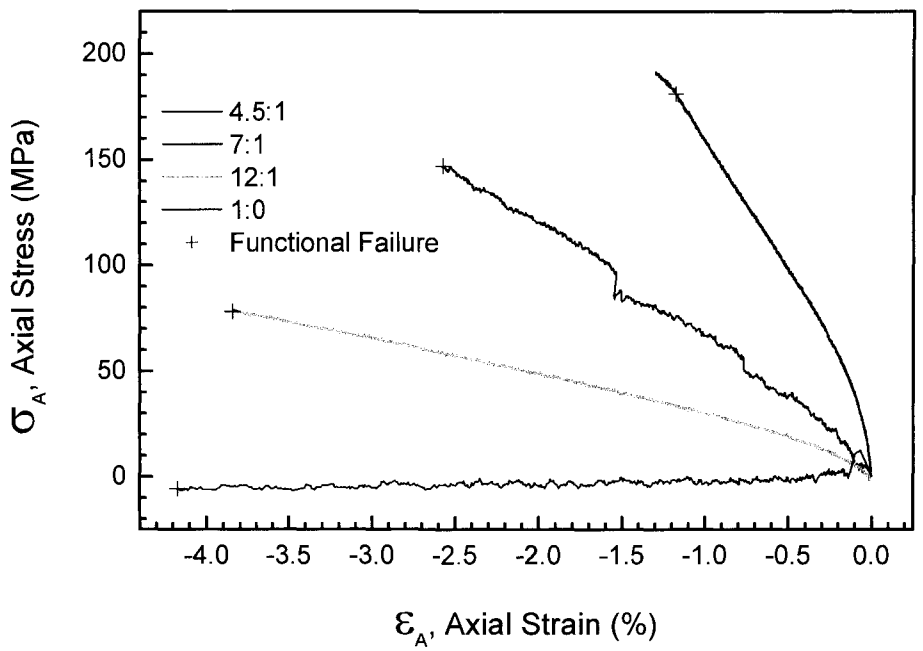

Figure 4.9: Axial stress-strain response and functional failure of composite tube at tested hoop stress/axial stress ratios of 4.5:1, 7:1, 12:1 and 1:0.

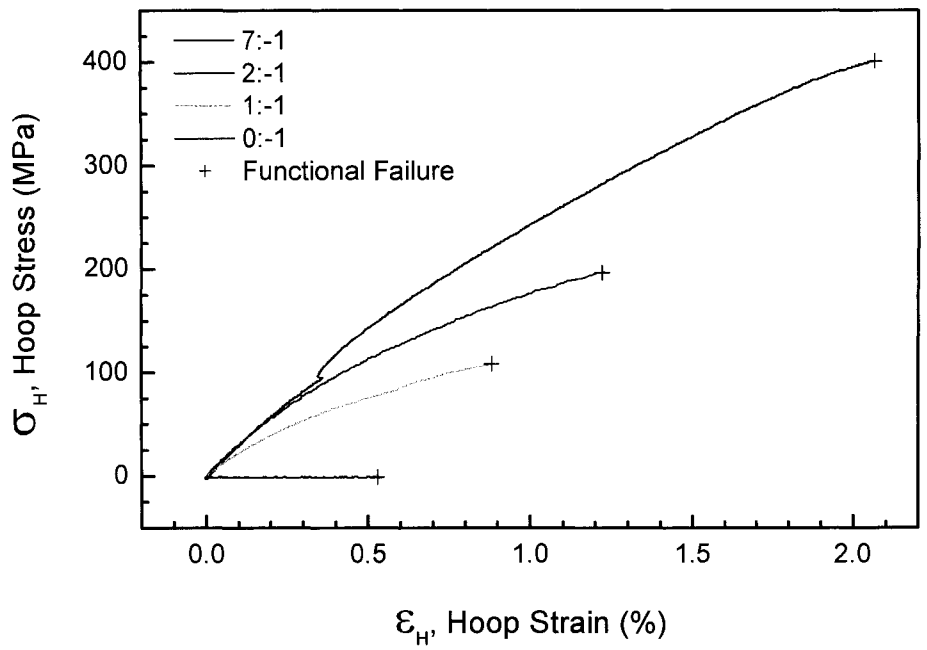

Figure 4.10: Hoop stress-strain response and functional failure of composite tube at tested hoop stress/axial stress ratios of 7:-1, 2:-1, 1:-1 and 0:-1.

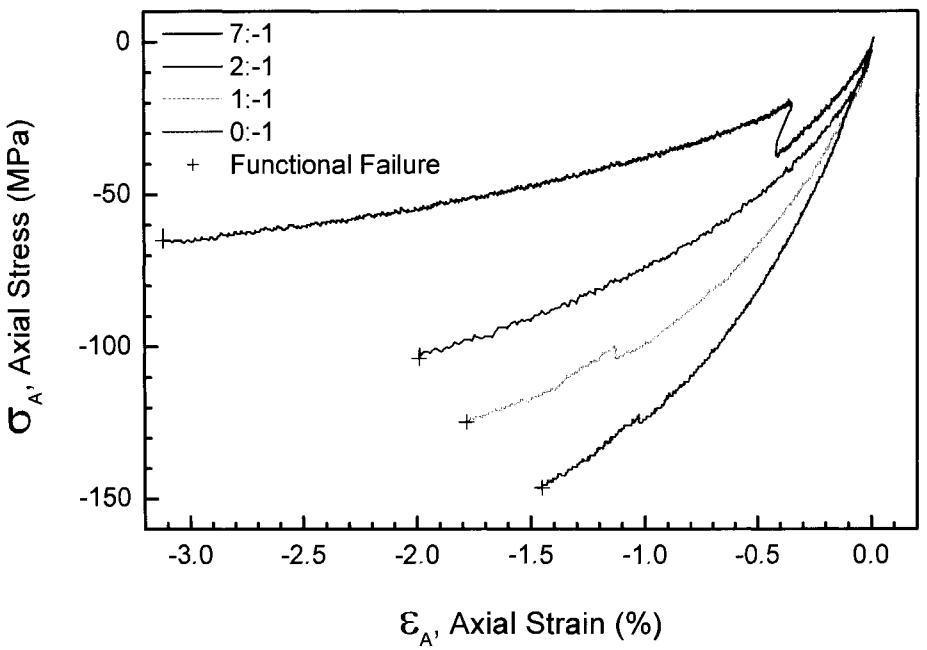

Figure 4.11: Axial stress-strain response and functional failure of composite tube at tested hoop stress/axial stress ratios of 7:-1, 2:-1, 1:-1 and 0:-1.

Figure 4.10 and Figure 4.11 show the hoop and axial stress-strain responses for load cases with compressive axial stress. It is observed that neither the hoop nor axial responses demonstrate any range of linear behaviour. As the stress and strain magnitudes increase the stiffness drops. The slop of the hoop response decreases as the ratio of axial load is increased but the slope of the axial response increases.

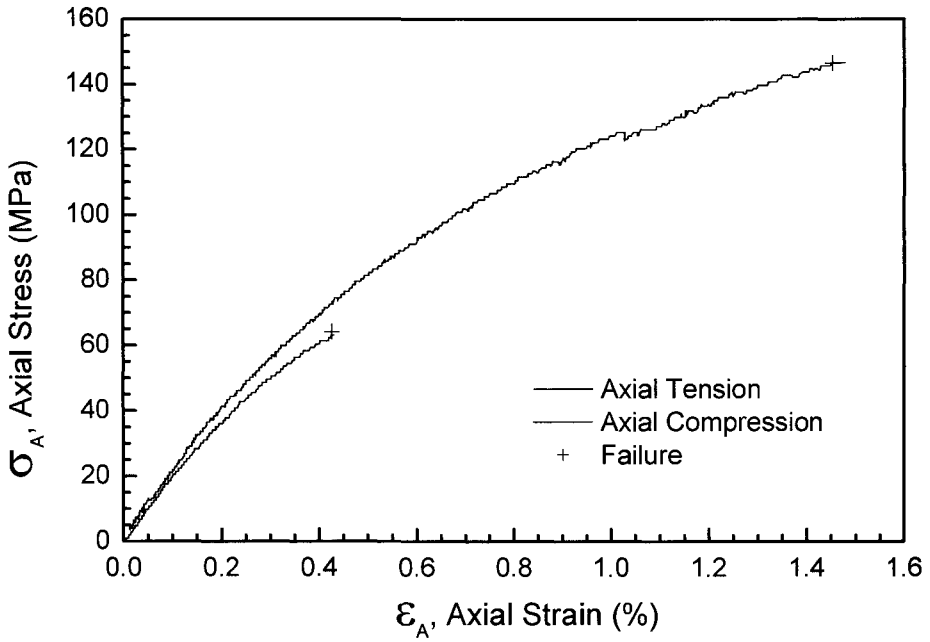

Figure 4.12: Axial tension and compression stress/strain response.

Figure 4.12 provides a comparison of the axial response of the tube under tension and compression. Both curves show nonlinear behaviour; the initial elastic region extending no farther than 20 MPa stress or 0.1% strain. The initial responses in tension and compression are similar. However, while tensile failure occurred at 64 MPa and 0.43% strain the compressive failure occurred at 146 MPa stress and 1.45% strain. The appearance of the fractures under these two load conditions differed significantly as described Section 4.1.

4.4 FAILURE ENVELOPES

A failure envelope may be produced by the locus of points defined by the failure stress in three dimensional space in the axes σ_1, σ_2 and τ_{12}. In all the load conditions studied, the

loads are applied along the principal axis in the hoop and axial directions with respect to the tube. No shear loading was imposed on the tubes thus we can plot the failure points in terms of σ_H and σ_A on the plane where $\tau_{HA} = 0$.

This study considers the first failure or functional failure envelope. Functional failure indicates that the tube no longer fulfills its design function to contain a pressurized fluid whether the failure is by weepage, leakage, burst or a structural collapse. While weepage and leakage indicate the functional failure of the tube, they do not reflect the strength capacity of the structure. Tests by others, using a bladder or liner to contain the pressurisation fluid even after the initiation of leakage have demonstrated that filament wound glass fibre/epoxy tubes can withstand much high internal pressures when a liner is used (Soden et al, 1989; Mertiny and Ellyin, 2002).

All the failure envelopes demonstrate the anisotropic nature of the composite tube. With the glass reinforcement aligned at an angle of 60° to the axis of the pipe, the failure envelope demonstrates a much greater hoop failure stress than the failure stress in the axial direction. This is evident in the Figure 4.13 and Figure 4.14 which show the stress and strain failure envelopes respectively. It is shown in Figure 4.13 that the failure envelope, in the first and fourth quadrants, is of a parallelogram shape with an approximately constant axial failure stress for stress ratios from 2:1 to 7:1. This is different from the first-failure results of Soden et al. (1993) from biaxial tests on ±45° and ±55° filament wound E-glass/epoxy tubes. They found an approximately linear trend, of positive slope, from pure axial loading to the stress ratio producing the maximum hoop stress. The reduced axial stress, shown here, may be the result of stress concentrations due to the grip system. In Chapter 2 it was shown that internal pressure loading results in high axial stresses near the ends of the gauge length due to bending.

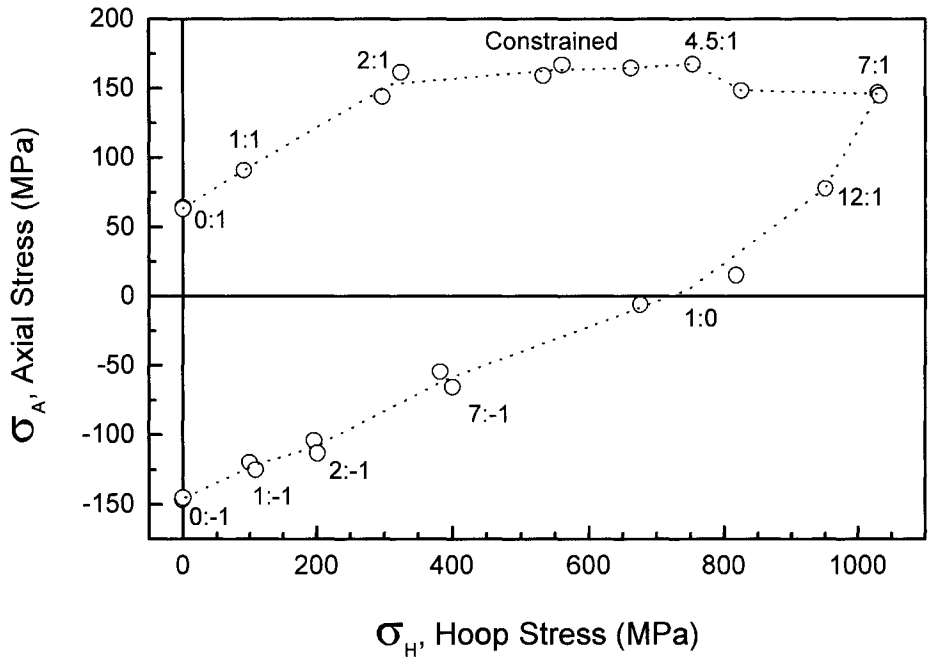

Figure 4.13: Experimental stress failure points and effective failure envelope.

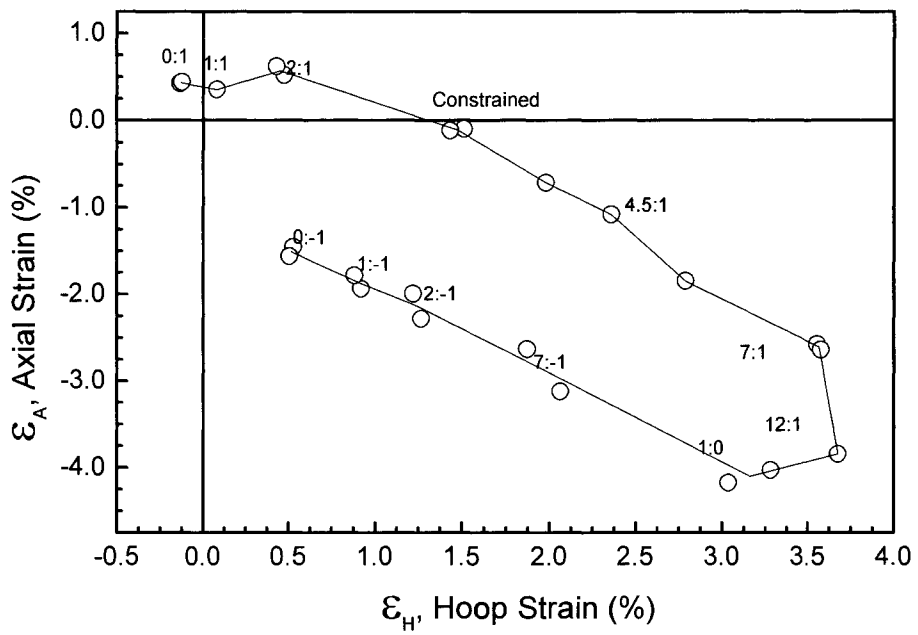

Figure 4.14: Experimental strain failure points and effective strain failure envelope.

However, it must be noted that the failures were in the central portion of the specimen at the stress ratios of 5.5:1 and 7:1. Therefore, it is unclear if this reduction in axial strength is the result of stress concentrations, constituent material properties or manufacturing process.

It is common to transform the strain envelope into the ply coordinate system since failure analysis is usually done ply by ply. When this is done the stresses and strains are no longer principle values and a shear component must be considered. The results are shown as three-dimensional graphs for stress in Figure 4.15 and strain in Figure 4.16. Since this representation is difficult to use for assessing the data, the following discussion will be based on the stress and strain representations on the appropriate stress and strain planes.

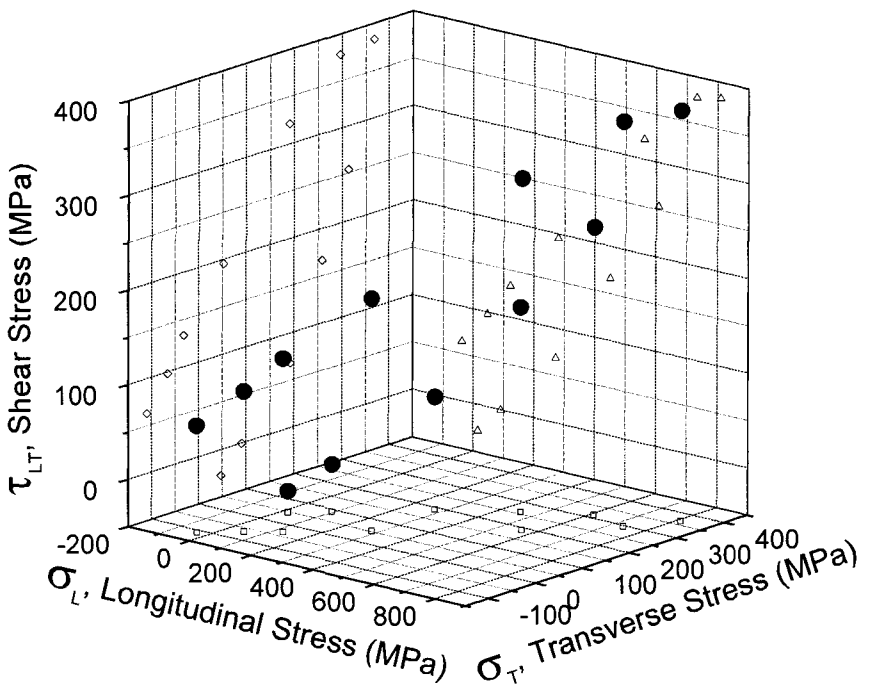

Figure 4.15: Stress failure envelope transformed to the σ_L-σ_T-τ_{LT} stress space with projections onto stress planes.

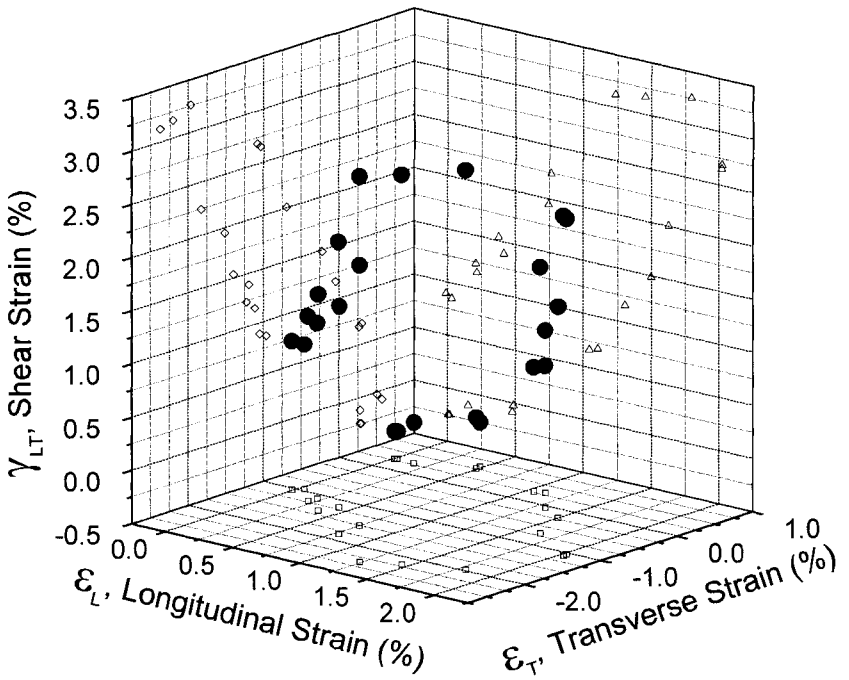

Figure 4.16: Strain failure envelope transformed to the ε_L-ε_T-γ_{LT} stress space with projections onto strain planes.

While it is reasonable and common to assume that the strain is constant through the laminate this is clearly not true for the stress. Therefore, the simple stress transformation of Figure 4.17 provides only an average stress value in one properly aligned ply and one complementary ply in the $\pm\theta°$ laminate. A more accurate representation is achieved by using the classical laminate theory to reduce the biaxial failure stress state to that in an individual ply, also provided in Figure 4.17. The classical laminate theory result shows a much more directional response with a maximum longitudinal failure stress of approximately 1125 MPa and a maximum transverse failure stress of 100 MPa. It must be remembered the classical laminate theory is based upon a linear analysis without consideration for material nonlinearity, damage or possible realignment of the reinforcement.

The transformed strain failure envelope is shown in Figure 4.18 and maximum strain bounds can be estimated. The horizontal portion, for stress ratios between 0:1 and constrained end condition, suggests a maximum transverse strain of 0.3% while the right hand bound indicates a maximum tensile fibre strain of 2.025%. Transverse compressive

and engineering shear strain values of 2.25% and 3.2%, respectively, are suggested but difficult to verify from the results. No compressive failure results for the reinforcement could be produced using this lay-up in the testing apparatus.

The ply failure strains calculated using the classical laminate theory and the laminate failure stresses is also shown. It is clear that the strain magnitudes, particularly for axial compression, are under estimated due to the assumption of linear response.

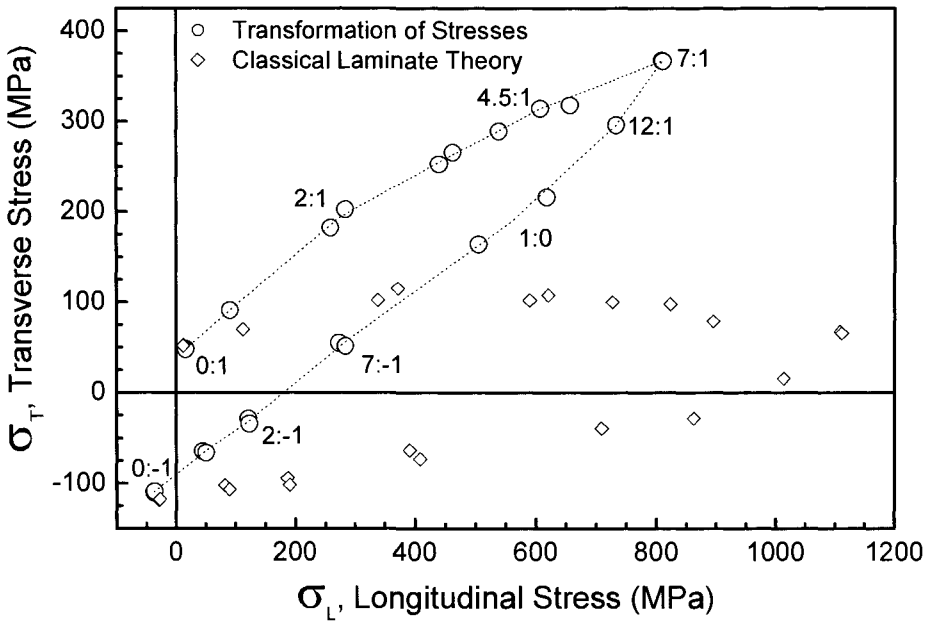

Figure 4.17: Stress failure points when stresses are transformed to material axes.

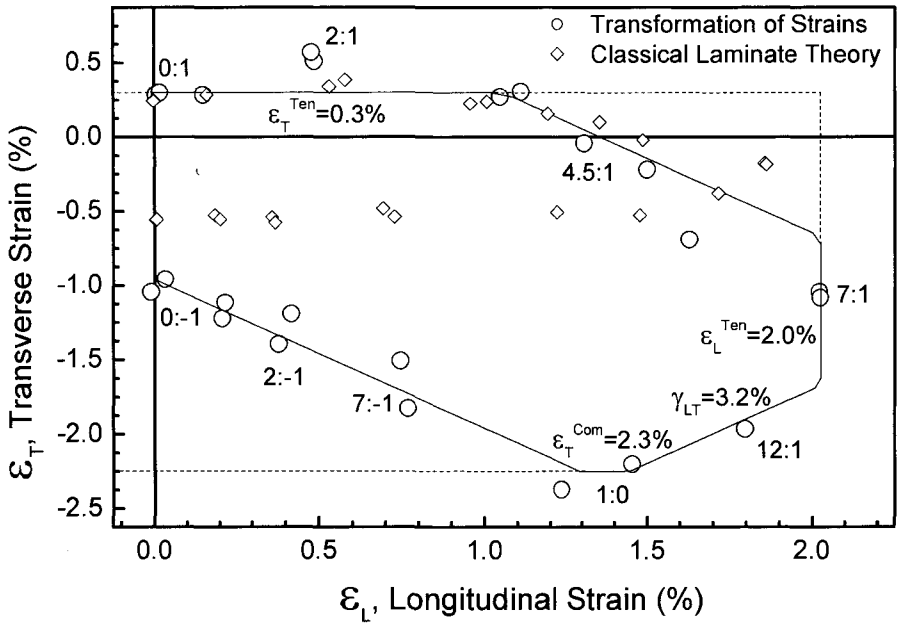

Figure 4.18: Strain failure points when strains are rotated to material axes.

While the maximum strain criterion provide reasonable bound on the test data, there are two areas where it does not predict the data trend. These are the range of stress ratios between 2:1 and 7:1 and all tests with axial compression.

The tests of stress ratios between 2:1 and 7:1 have been singled out in the discussion of the stress failure envelope. The reduction in axial stress is now shown to coincide with a reduction in transverse strain. It was noted that the failures at stress ratios of 4.5:1, 4:1 and 5.5:1 were localised jetting of fluid and this suggests that these stress states are particularly susceptible to local defects such as voids, damaged fibres, poor fibre distribution or even cross-overs in the woven structure.

In the zone of axial compressive stress, the axial failure stress magnitude increases while the axial strain magnitude decreases as the internal pressure is reduced. The reduction in strain magnitude is expected since the strain due to Poisson's ratio contraction will decrease as the hoop stress is reduced. In fact, it is observed in Figure 4.8 and Figure 4.9 that the magnitude of the axial strain is greater than that of the hoop strain under pure internal pressure loading. Use of the failure stresses in the classical laminate theory

predicts a constant transverse lamina strain of approximately -0.5% for all tests with axial compression, as shown in Figure 4.18. Of course the classical laminate theory assumes a linear material response and it is clear from Figure 4.10 and Figure 4.11 that this is not accurate.

It is also observed that the transverse failure strains at the 2:1 stress ratio are considerably high than those neighbouring values. This is due to the difficulty of determining the initial point of leakage, particularly for this stress ratio which failed by low volume weepage.

Figure 4.19 shows the failure shear strain as a function of the longitudinal strain in the lamina while Figure 4.20 shows the relation ship between the transverse and shear failure strains. The values of shear strain are larger under load conditions producing compressive axial strains (ie. Stress ratios 12:1 to 0:-1). A maximum shear strain of approximately 3.25% is achieved at the 12:1 and 1:0 stress ratios and this is supported by the maximum stress failure criterion plotted in Figure 4.18. Once again the classical laminate theory under estimates the magnitude of the strains under compressive axial loads.

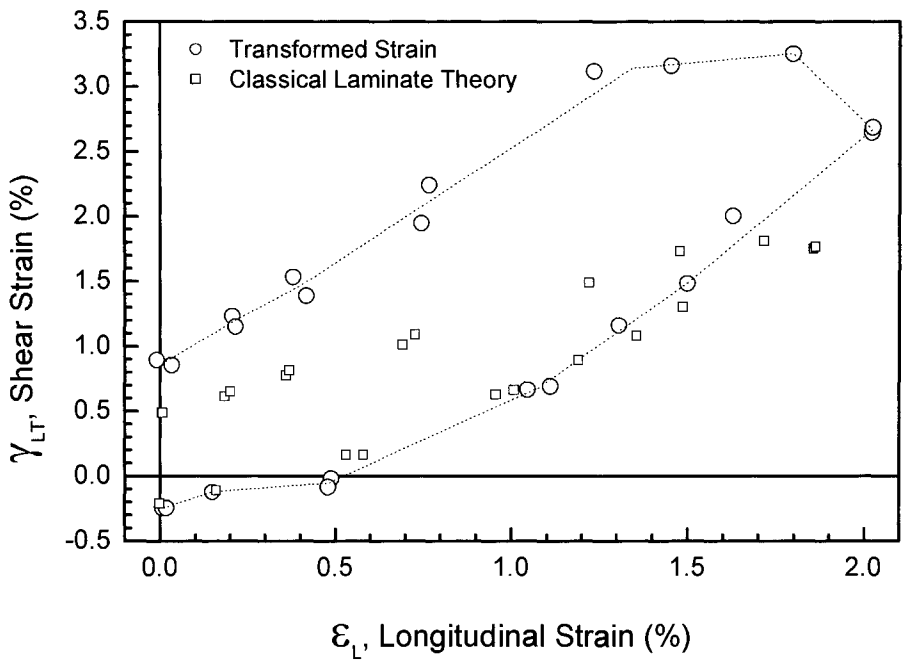

Figure 4.19: Shear strain failure envelope.

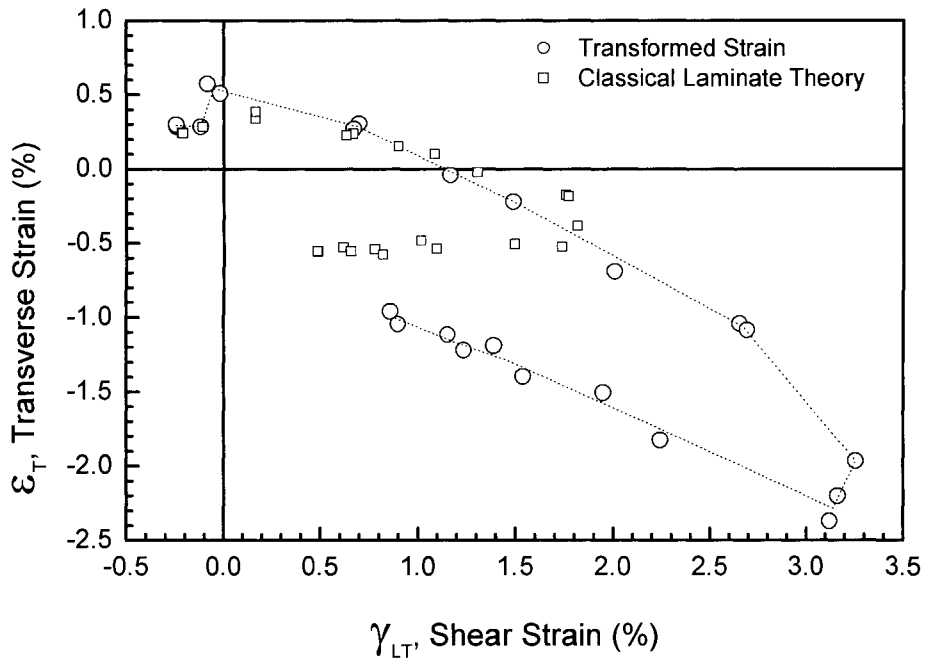

Figure 4.20.: Transverse failure strain as a function of shear strain

It is of interest that in all of the strain failure envelopes, Figure 4.18, Figure 4.19 and Figure 4.20, that the two sections not well fit by the maximum strain criteria have similar slopes and the shear strain are in the same range. It is unclear if this is an indication of similar damage mechanisms since the stress states producing axial strain had first failure due to fluid loss. Under axial compression, however, leakage is delayed or avoided by eliminating matrix cracking or compressive loads keeping the cracks closed. Puck has described shear failure of the matrix by the formation of cracks at a 45° inclination to the fibre reinforcement (see Puck and Schnieder, 1969 and Hart-Smith, 1998). Such cracks will stop when reinforcement is encountered. Under axial tension, such cracking may lead to the initiation of delamination and leakage but since the deformations are much higher under axial compression, the shear displacement may result in kinking of the complementary reinforcement.

4.5 SUMMARY OF RESULTS

Multiaxial tests with tensile and compressive axial loads and internal pressure were conducted to develop stress and strain failure envelopes for the $[\pm 60°_3]_T$ filament wound

E-glass epoxy tubes. Results show that the material response in the axial direction is very nonlinear. The hoop response is also nonlinear but not to such a large extent. The strength under axial compression is greater than twice that of tension (ie. 140 MPa compared to 60 MPa) although the initial modulus is the same.

Failure envelopes, developed from the failure stresses and strains, clearly demonstrate the directional (anisotropic) response of the laminate. The maximum strength in the hoop direction was approximately 1050 MPa at a stress ratio of 7:1. The maximum magnitude of axial stress was about 150 MPa at stress ratios in the range between 2:1 and 7:1 and under pure axial compression, 0:-1. Failure envelopes were also plotted for the transformed stresses and strains as well a ply values calculated using the classical laminate theory. The simple transformation of stress results in a stress value for two plies consecutive plies making up the $\pm\theta$ laminate. One ply is properly aligned while the other is at an angle of 2θ. Due to the directional dependence in stiffness, the stresses in these two laminae will be significantly different. The use of the classical laminate theory is more appropriate however it is based on a linear response which is shown to be inadequate.

Use of a maximum strain criterion is shown to provide reasonable bounds except in two ranges. In the stress ratio range between 2:1 and 7:1 the failures are local and occur at lower stresses and strains than expected. Others have shown a linear trend from pure axial loading to the maximum hoop functional failure stress. The maximum strain criterion is also inadequate for tests conducted with compressive axial stress. The axial strain failure magnitude is assumed constant for this range which results in overestimating the test values. However, use of the classical laminate theory severely underestimates the axial strain magnitude because it neglects the nonlinear behaviour.

The two segments discussed above show similarity in terms of shear strain range and slopes with respect to transverse and longitudinal strain. While the range having axial tension failed by leakage and that under compression failed by intersecting helical cracks, both may be the result of shear failure of the matrix. Shear failure by matrix cracking

may result in delamination and crack coalescence in tension and fibre kinking under compression.

CHAPTER 5 ADDITION OF A POLYETHYLENE TAPE INTERLEAF

The application of an interleaf to a laminate has been shown to reduce damage due to impact loads by reducing the delamination between plies, as discussed in Chapter 1. Furthermore, analytical studies have demonstrated that the interleaf may also influence the growth of transverse cracks. In this investigation, a polyethylene tape interleaf was applied to both thick cross-ply plates and thin walled $[\pm 60°_3]_T$ tubes and the effects under uniaxial and multiaxial loads were observed.

5.1 COUPON SPECIMENS

Coupon specimens were manufactured and tested to study the influence of a soft interleaf on a progressing transverse crack. Coupon specimens and plates have generally been used in the study of interleaves, because suitable materials are generally available in sheet form, and the manufacturing and testing process and equipment is less complicated and less expensive. Details of the experimental results and initial finite element analysis of the soft interleaf in thick cross-ply laminates may be found in Meijer and Ellyin (2004).

5.1.1 Coupon Specimen Production

The coupon specimens were produced by the hand lay-up of unidirectional E-glass fibre sheets pre-impregnated with epoxy resin. 152x203 mm sheets were individually cut from a 305 mm width roll of CYCOM 1003 (formerly 3M ScotchPly 1003) prepreg using a steel template and utility knife. The stock material is approximately 0.25 mm thick, with a reinforcement weight of 288 to 300 g/m^2 and a resin content of 33 to 39% (as per manufacturer provided test results). Release film was used to prevent the bare surface of the prepreg from sticking to the template. Sheets were cut in the 90° and 0° orientations as required. They were then stacked one by one using the curing mould as a guide, with care taken to ensure that no bubbles or creases occurred between sheets. 3M Preservation tape, 76.2 mm wide, 0.25 mm thick (0.2 mm thick polyethylene substrate, made black by carbon, with rubber adhesive) was applied to produce the interleaf. Control specimens, $[90°_{35}, 0°_5]_S$, and interleaf specimens, $[90°_{25}, I, 90°_{10}, 0°_5]_S$, were produced. A schematic of the specimen lay-up is shown in Figure 5.1. The specimens were made symmetric to

resist bending and the interior 0° plies were added to avoid catastrophic failure resulting in damage to the extensometers.

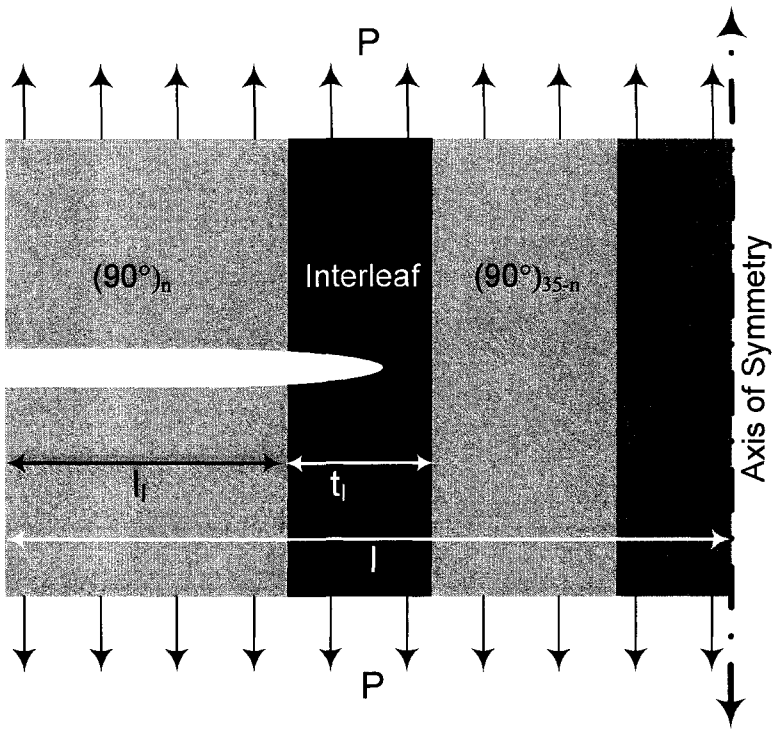

Figure 5.1: Schematic of coupon crack specimen lay-up where n = 25 plies.

Upon completion of the stacking, the laminate was wrapped in release film, placed in the mould and the mould bolted shut. The ends of the mould allow for the release of excess resin that may flow out during cure. The mould incorporates an air bladder pressurised to 172 kPa to consolidate the laminate. The laminate was placed in an oven at 149°C for 12 hours followed by slow cooling within the oven. The polyethylene has a melting temperature in the range of 120 to 140° C and was expected to undergo melt-solidification cycle during the cure. The resulting plate, 18.65 mm thick, was then cut into narrow coupon specimens, 3.70 mm wide, using a low speed diamond blade saw lubricated with light oil.

5.1.2 Coupon Testing

A notch was produced in each side of the symmetric specimen using a razor blade mounted in a jig in an Instron screw driven material testing system. The razor blade was

first brought into contact with the specimen, as indicated by reaction of the load indicator, and then continued to penetrate the specimen at 0.0254 mm per minute for 15 minutes. The selection of this speed and time interval was based on several notching trials where it was observed that, at higher speeds, the razor blade would behave as a wedge and rapidly drive a crack through the 90° plies. This method was found to be more successful than following the procedure specified in ASTM D5045-96.

All testing of the notched coupons was conducted on a 89 kN MTS load frame with a load cell sensitivity of 10 V/8.9 kN in load control at a frequency of 0.5 Hz, $R \approx 0$ ($R = P_{min}/P_{max}$), and ambient room temperature and humidity.

A simple grip system consisting of one static jaw and a second jaw which is simply tightened by bolting to the fixed jaw was used. This system was designed for the tested specimens such that the axis of the specimens aligned with the centre line of the grip. These grips were found to be easier to apply and had zero backlash compared to the complicated wedge grips supplied with the system. In order to prevent damage to the specimens by the grips, aluminum tabs were bonded to the specimen surfaces to be held. The tabs were bonded to the specimen using 3M Scotchweld DP-460 epoxy adhesive.

A 25.4 mm extensometer, mounted on the central 0° plies at the centre of the gauge length (over the notch), was used to measure specimen strain. Force, and strain hysteresis loop data was recorded by a personal computer for a specific load cycle interval and the stiffness was calculated and plotted in real time. In this investigation, the load levels were low and the hysteresis loops were linear and elastic. All data was saved directly to the hard disk to ensure it was safe in the event of a power disruption or other unfortunate event.

The fatigue tests were done at a minimum stress of zero. Since the control system for this apparatus is analogue, the span and set-point had to be adjusted to provide the required mean load and range. While this could be done to some degree prior to starting the test, small adjustments were required during the first few cycles to get better accuracy of the

loads. The loads were found to have little variation during the test, except when final failure occurred.

5.1.3 Results from Coupon Interleaf Specimens

The fatigue tests on the coupons produced load and strain data for a given load cycle interval. The specimen stiffness, over the gauge length of the extensometer and including the notch, was calculated. Thus the tests produced output in the form of specimen stiffness over the time of the test. The specimen stiffness may be correlated to the length of the crack, or more correctly to the width of the remaining ligament and therefore the stiffness is used as an indication of crack propagation.

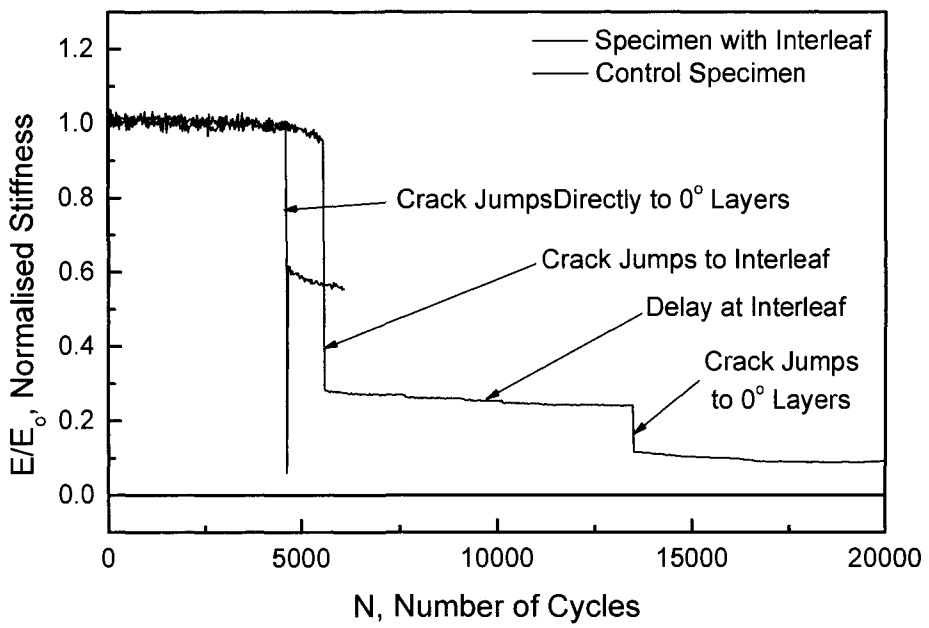

Figure 5.2: Example change in stiffness as crack progresses through the coupon specimen.

In these tests the transverse fracture of the 90° layers was found to be rapid and only a small fraction of the total specimen life (where the end of the specimen life has occurred when the crack tip meets the interior 0° plies). For the control specimens, the crack propagation occurred as a single rapid event but for the interleaved specimens crack growth was two events separated by a pause at the interleaf. This is clearly displayed in

Figure 5.2 that shows an example of the normalized stiffness as a function of number of load cycles. The two distinct drops in stiffness are observed; first when the crack rapidly propagates to the interleaf and the second when the crack grows from the interleaf to 0° layers.

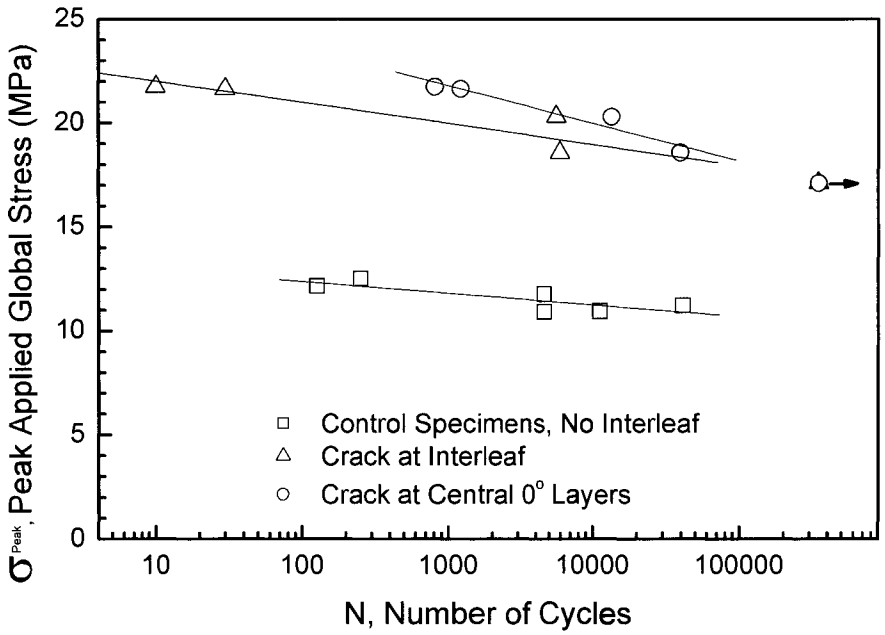

Figure 5.3: S-N curves for control specimens and laminates with an interleaf. Number of cycles for crack to propagate to the interleaf provided for specimens with interleaf and number of cycles to for crack to reach central 0° layer for all specimens.

This procedure was repeated at a number of load magnitudes for the control and interleaf specimens, to generate the curves of applied global stress vs. number of cycles to failure shown in Figure 5.3. Two lines represent the interleaved specimens indicating the first and second crack events. Of significance is the delay between the crack progressing to the interleaf and then continuing from the interleaf to the 0° layers. Also of note is the narrow range of stresses and the difference in stress required for the control and interleaf specimens.

It is clearly demonstrated that the crack growth is delayed when the crack tip hits the interleaf. Inspection using a dye penetrant showed that debonding occurred along the

polyethylene tape interleaf/glass fibre reinforced epoxy interface and at high cycles this debonding extended outside of the gauge length. This phenomenon occurs because of poor adhesive bonding between the low reactivity polyethylene and the epoxy matrix. In fact, polyethylene does not bond very well to most adhesives. It is also noted that the glass transition temperature of polyethylene is below 0° C therefore there is an amount of molecular mobility at room temperature. Thus the polyethylene interleaf may experience flow while loaded. Due to this poor load transfer, it is expected that the crack continues to advance only after damage and a new crack has initiated on the opposite side of the interleaf. This progression is supported by Figure 5.4 that shows that the crack after the interleaf occurs on a different plane than the manufactured notch and original crack. Thus the crack delay may be the result of the poor bonding effectively producing a new, uncracked surface. The effect of interface debonding is studied using finite element analysis in Chapter 7.

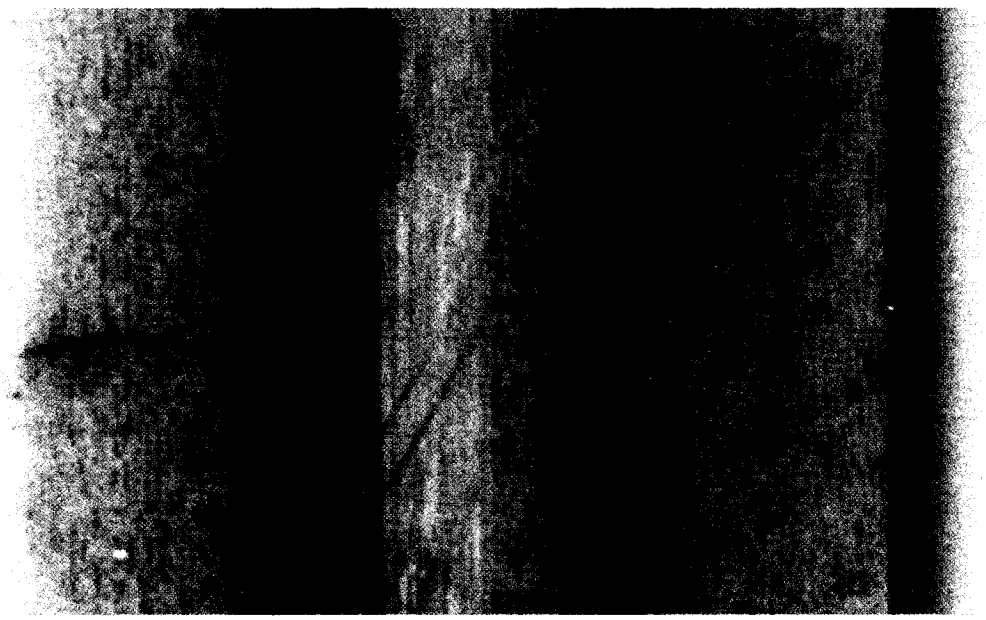

Figure 5.4: Photo of crack path in specimen with interleaf.

Controlled cracking under cyclic loading is shown to occur within a narrow band of applied global stress. Crack growth occurs within 10 cycles at a stress of 22 MPa but at 17.1 MPa the crack did not advance from the initial notch. This is also observed in the control specimens that failed at much lower stresses.

The stress required in the control specimens was approximately 59% of that for the interleaf specimens. This may be explained by how the interleaf serves to isolate the outer 90° plies from the residual stresses generated by the difference in the coefficients of thermal expansion of the 0° and 90° plies. This was demonstrated by completing a plane strain, elastic finite element analysis of the specimen subjected to a temperature decrease. The elastic mechanical properties of the orthotropic composite are provided in Table 3.3 and the coefficients of thermal expansion of the glass reinforced epoxy ply are in Table 3.8. The isotropic polyethylene was assigned an elastic modulus of 1,450 MPa, Poisson's ratio of 0.45 and coefficient of thermal expansion of 150x10-6/°C. It is acknowledged that the properties of both materials are highly temperature dependent with the epoxy having a glass transition temperature of approximately 110°C and high density polyethylene melts in the range of 120 to 140°C.

Figure 5.5 shows the residual stress, perpendicular to the notch, resulting from a temperature drop of 90°C from the epoxy glass transition temperature (110°C) to the test environment (20°C). The interleaf is shown produce a compressive normal stress in the outer composite layers due to its large thermal contraction upon cooling. This compressive stress tends to keep any cracks at the notch closed. When the interleaf is not present, the normal stresses drop to approximately zero at the outer 90° layers.

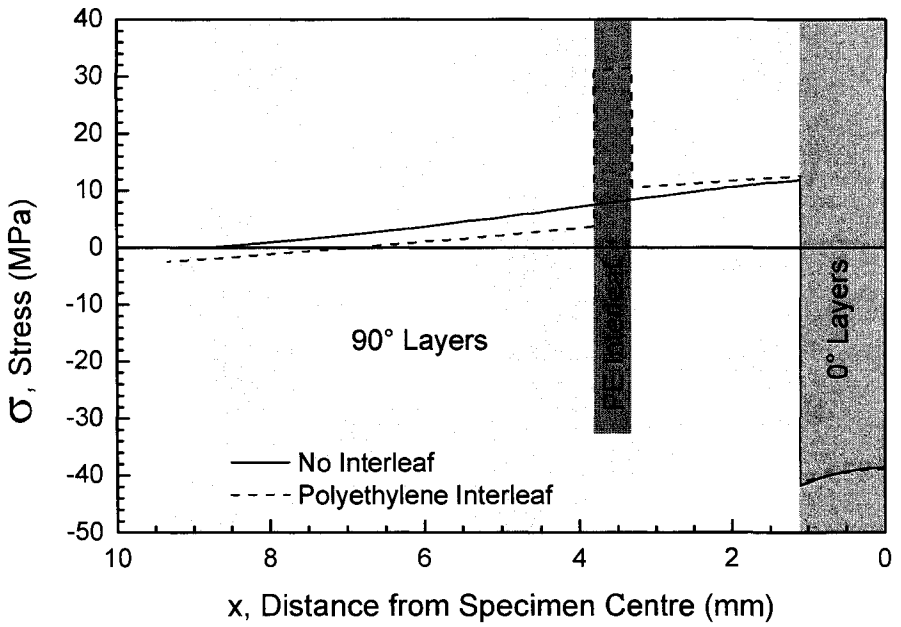

Figure 5.5: Residual thermal stress perpendicular to the notch in the cross-ply due to a 129°C temperature drop.

The rapid crack advance suggests that the initiation of the crack, from the notch, is of primary importance. This would lead one to believe that it is the influence of the interleaf on the strain energy release rate at the point of crack initiation that should be investigated. The notch produced was approximately 0.38 mm deep and we may use the results of the elastic finite element analysis provided by Meijer and Ellyin (2004). Figure 5.6 shows the results for short crack lengths.

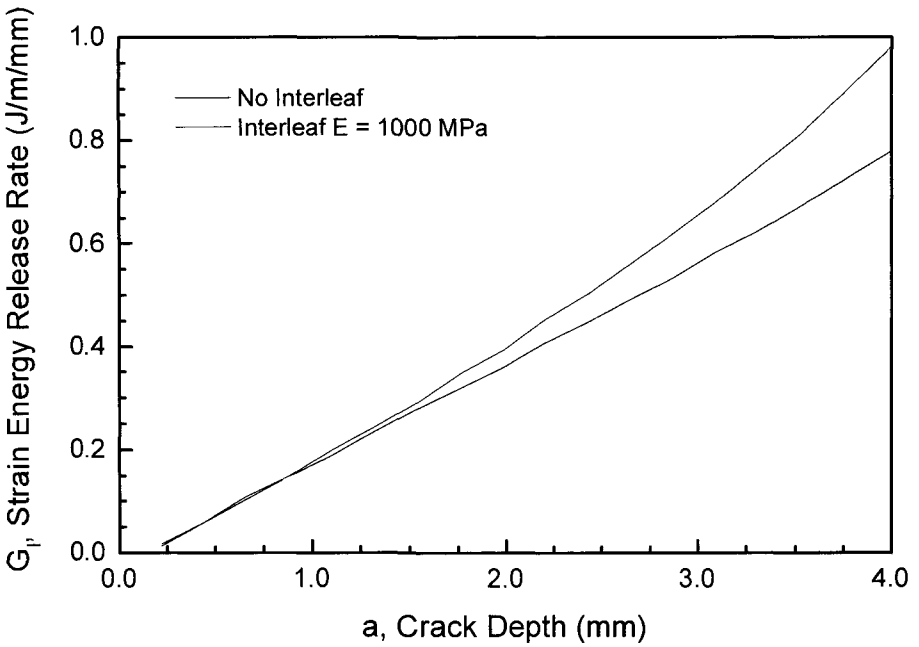

Figure 5.6: Strain energy release rate at short crack depths from the elastic finite element analysis of Meijer and Ellyin (2004).

Figure 5.6 shows that the strain energy release rates for the laminates with and without an interleaf converge for short crack depths therefore this does not appear to explain the difference in initiation stresses observed in Figure 5.3. The results shown in Figure 5.6 are very similar to that of Li et al. (1993) who performed a similar analysis of the effect of a soft inclusion. They demonstrate that near the edges of the crack body, away from the inclusion the strain energy release rate with the inclusion present is very similar to the case without a soft inclusion.

Chapter 7 provides the results of elastic and viscoelastic analyses on this thick cross-ply geometry and the influence of interleaf position, thickness and material properties. Also included is an investigation of the effect of debonding at the interleaf in front of the crack tip.

5.2 TUBULAR SPECIMENS

Tubular interleaf specimens were also produced. These specimens of $[\pm 60°, I, \pm 60°_2]_T$ were tested under internal pressure and axial load to approximate a biaxial stress state.

Under this application, the interleaf may not only act to arrest cracks but may also act as an impermeable barrier to the pressurisation fluid. Therefore, weepage may not occur and failure will more likely be the result of a burst type failure.

5.2.1 Manufacturing and Testing

The manufacturing process for the filament wound tubes was modified to allow for application of the polyethylene tape interleaf. A three step procedure was used. First a ±60° layer of 200% coverage was wound at a tow tension of 27 N and cured as per the typical procedure. The mandrel was not extracted. Second, the tape was wound around the existing layer at an angle of 76.5° to produce 200% coverage in a single pass using the 76.2 mm bandwidth. A special tape laying head was made and used in the filament winding machine to lay the tape. In the third step two ±60° layers of 200% coverage were wound around the existing layers and tape at a tension of 44.5 N per tow. The high tension was used to consolidate the tape layers. The assembly was then cured following the regular cure schedule.

The specimens were tested in a manner identical to that for the plain $[\pm 60°_3]_T$ tubes described in Chapter 2. The interleaved tubes were tested at hoop to axial stress ratios of 0:1, 1:1, 2:1, constrained ends, 7:1 and 1:0. Stresses were calculated based upon the cross-section area of composite structure, neglecting the interleaf. Therefore, the wall thickness used for area calculations was the same as that for the plain tubes, as calculated in Chapter 2.

5.2.2 Failure Descriptions for Interleaved Tubes

The interleaved specimens failed by various mechanisms depending on the applied stress ratio. While many of the effects described here are similar to those of the tubes without interleaves, the addition of the soft layer has produced some unique effects and changed the failure mode under some of the load conditions.

0:1 Stress Ratio: Axial Tension

The specimens tested in axial tension failed by a dominant helical crack similar to the plain tubes. The failure stresses and strains are approximately the same as well. The

exterior of the tube shows failure by a dominant helical crack with a coarse brush like failure of the complementary fibre bands. The outside layer had fine white striations visible throughout the gauge length. After large deformation, the interior of the tube showed delamination of coarse fibre bands from complementary layers and the interleaf, on a large portion of the surface.

1:1 Stress Ratio

Failure under the 1:1 stress ratio was very similar to that of pure axial loading. Failure was by a dominant helical crack along a band of reinforcement with a coarse brush-like failure of the complementary layers. The interior also demonstrated delamination of the bands from the complementary layers as well as the interleaf.

2:1 Stress Ratio: Pressure Vessel Load

The specimen tested under pressure vessel loading, 2:1 stress ratio, showed coarse cracking of the outside resin rich layer and the fine striations associated with matrix cracking in the reinforcement bands that corresponds with the observed failure by weepage. This damage is shown in Figure 5.7, with narrow regions of delamination between the coarse cracking.

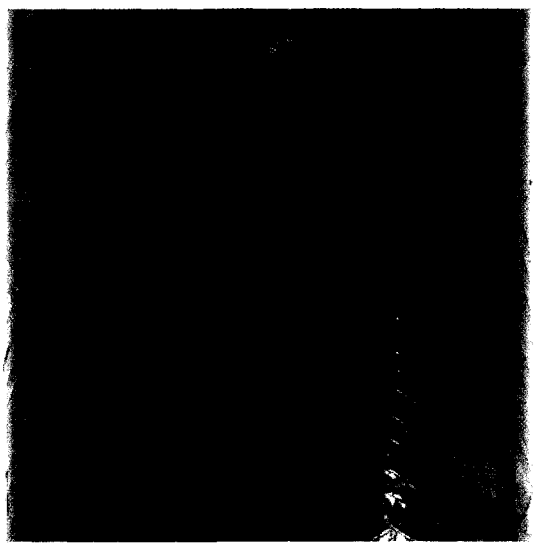

Figure 5.7: Exterior of interleaf specimen tested under the 2:1 stress ratio.

Figure 5.8 shows the surface on the interior of the 2:1 specimen that was cut along the axis after testing. Matrix failure and delamination along a helical path are observed but this interior crack path did not correspond with cracks on the exterior.

Figure 5.8: Interior of specimen tested under pressure vessel load.

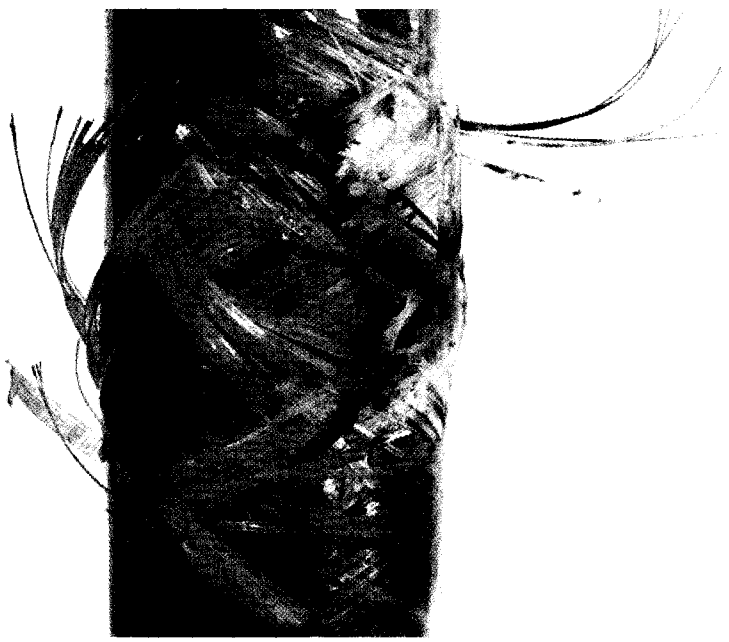

Figure 5.9: Burst failure under constrained axial deformation with internal pressure.

Constrained Ends: Simulated Long Pipe

With constrained ends and internal pressure, the specimens burst at a distance of approximately 30 to 50 mm from the aluminum tabs. A diamond shaped patch of the tube wall was thrust outward with coarse brush-like failure around three sides as demonstrated in Figure 5.9. The interleaf was also pushed outward by the internal pressure. Long strands of reinforcement were delaminated from the exterior surface of the tube, after fibre fracture. This was also observed on the interior, but only for a small number of fine fibre strands. Failure in the second specimen was of similar description but lead to separation of the tube into two parts. It was seen from this specimen that the interior and exterior structural layers had failed along different paths.

7:1 Stress Ratio

Failure under the 7:1 stress ratio was similar to that for the constrained end condition, described above, but generally the blown out section of tube wall was smaller in size. The damage is shown in Figure 5.10.

Figure 5.10: Burst failure resulting from 7:1 stress ratio.

The fibres and matrix have fractured producing a brush-like appearance. Under this stress ratio the brush appearance is quite fine. Coarse striations are also observed on the remainder of the specimen surface.

Figure 5.11: Fracture due to a pure hoop stress state.

1:0 Stress Ratio: Pure Pressurisation

Specimens tested under a pure hoop stress state failed by burst such that both specimens were fractured into two pieces. An example is provided in Figure 5.11. The specimen was slightly crushed after failure due to the compressive load applied to counter the pressure load on the specimen ends. The glass fibre and matrix have failed leaving long, fine strands of reinforcement. The interleaf has been forced out of the fibre structure but it was observed that the inner and outer composite structures failed along similar paths. Closer inspection showed that the inner layers had delaminated from the interleaf and the failure displayed a failure by intersecting helical cracks similar to the specimens without an interleaf.

5.2.3 Stress-Strain Response

Examples of stress-strain responses for each of the stress ratios tested are shown in Figure 5.12 to Figure 5.15. These may be compared to those of the tubes without interleaves in Figure 4.6 to Figure 4.9. The curves for internal pressure loading are very similar in shape and magnitude. When comparing Figure 5.12 and Figure 5.13 to

Figure 4.6 and Figure 4.7, one can see that the results for 0:1, axial loading, are also very similar but those of 1:1 and 2:1 (pressure vessel loading) are quite different from the plain composite specimens. In these cases the axial stiffness has dropped and for 1:1 the failure stresses have remained the same while at 2:1 the failure stresses have dropped.

Failure under the 2:1 stress ratio was by weepage, as it was for the plain specimens. Matrix cracking due to transverse loading occurs in all the composite layers providing a leakage path through the structural components. Under this loading the interleaf fails to act as an impermeable barrier. It is possible that the large axial deformations coupled with internal pressure, lead to slippage and tearing of the interleaf with possible extrusion of the soft interleaf into the open matrix cracks. It is also observed from Figure 5.12 and Figure 5.13 that the weepage was slow and the test progressed well beyond the initiation of leakage to an axial strain of 1.5% before the pressure intensifier volume was exhausted. Use of a continuous interleaf, as opposed to a tape, with sufficient toughness to accommodate the strain concentrations may improve performance under this load condition.

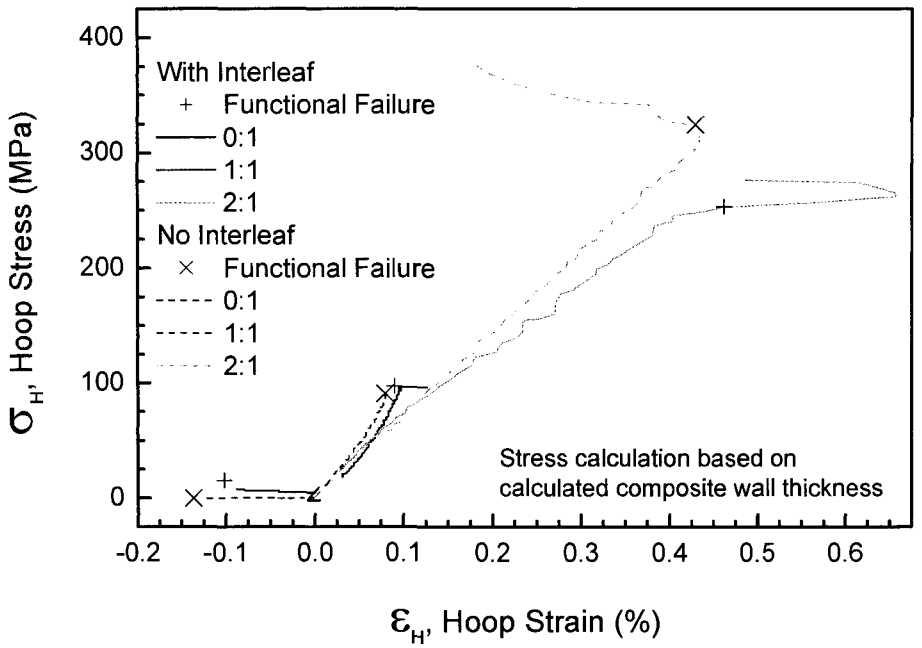

Figure 5.12: Hoop stress-strain responses of tubular specimens with interleaf at stress ratios of 0:1, 1:1 and 2:1.

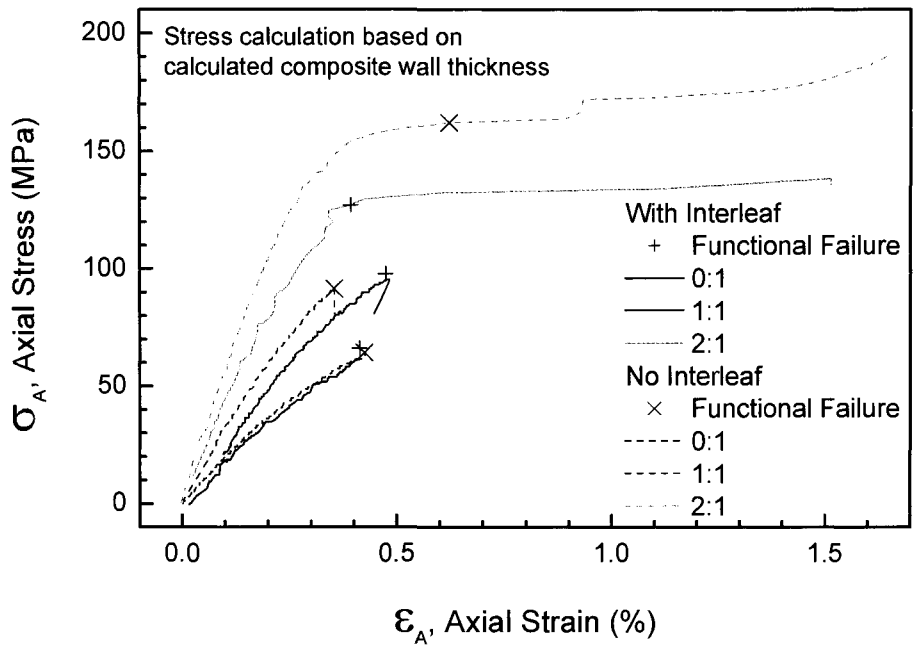

Figure 5.13: Axial stress-strain responses of tubular specimens with interleaf compared to tubes without an interleaf at stress ratios of 0:1, 1:1 and 2:1.

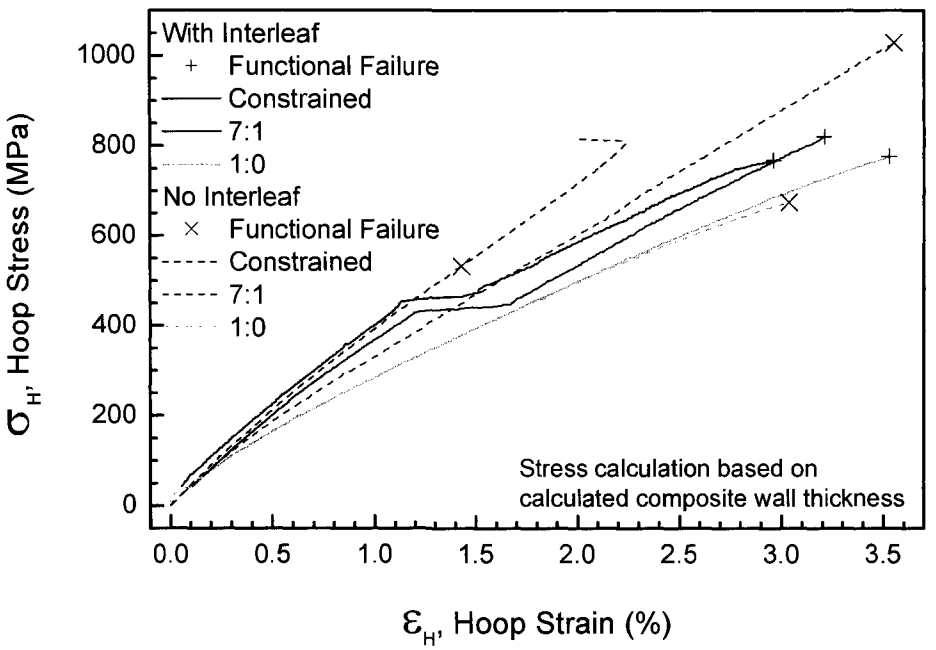

Figure 5.14: Hoop stress-strain responses of tubular specimens with interleaf compared to results of specimens without an interleaf at stress ratios of constrained axial deformation, 7:1 and 1:0.

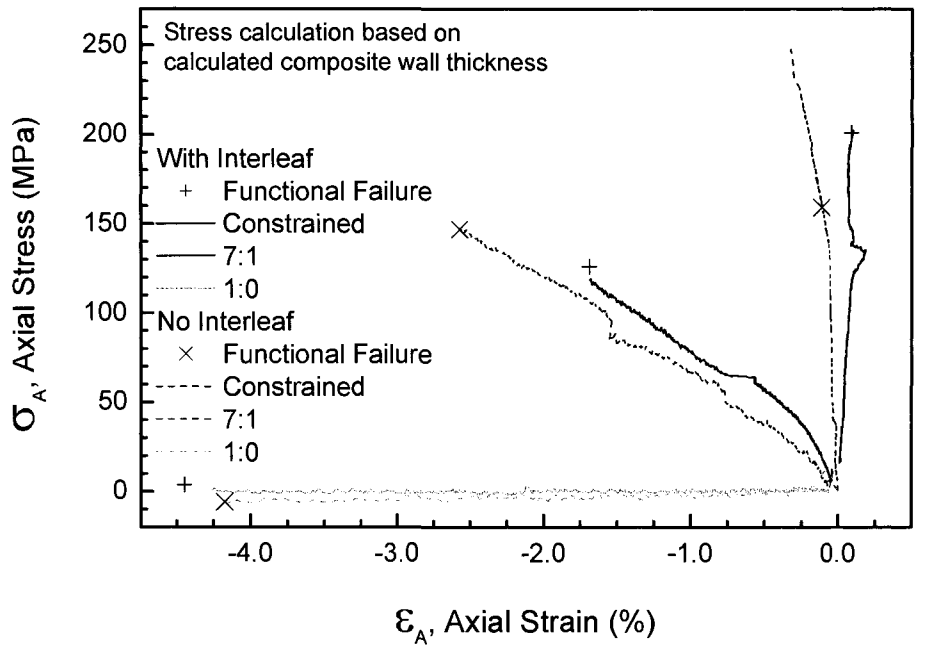

Figure 5.15: Axial stress-strain responses of tubular specimens with interleaf compared to results of tubes without an interleaf at stress ratios of constrained axial deformation, 7:1 and 1:0.

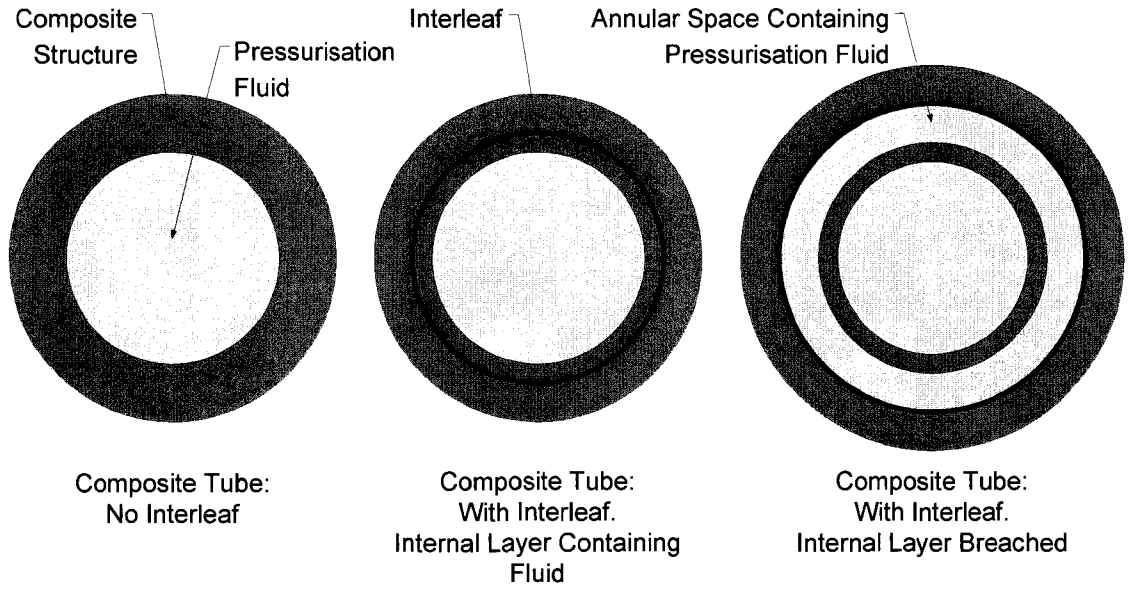

Figure 5.16: Schematic showing how, upon breach of the interior structural layer, an annular space of pressurisation fluid separates the interior and exterior structures reducing the effective wall thickness from three ±60° layers to two leading to lower failure stress.

Unique hoop stress-strain behaviour is shown in the curves for the constrained and 7:1 load conditions in Figure 5.14. For the 7:1 stress ratio the stress-strain curve increases monotonically with a gently changing slope due to accumulated damage. The hoop strain then increases rapidly, from 1.2% to 1.7%, at an approximately constant stress and then then continues monotonically increasing but at a lower slope. The specimens failed by bursting. This behaviour is a result of adding the interleaf which acts as an impermeable barrier.

The interleaf failed to act as a barrier under the 2:1 stress ratio because large axial deformations lead to slippage or tearing of the polyethylene tape. However, under the constrained and 7:1 load conditions the axial strains are approximately zero and slightly negative, respectively, so the interleaf is not damaged and remains effective in containing the fluid. Unfortunately, as noted previously in this chapter, the polyethylene tape has poor bonding characteristics and divides the composite structure into distinct inner and outer parts. Damage leading to weepage and local leakage will allow the pressurisation fluid to pass through the interior composite layer and due to poor bonding, the annular

space, between the inner composite layers and the interleaf, is filled with the fluid. Loading on the inner structure due to internal pressure is then relieved as is demonstrated in Figure 5.16. The fluid is then contained by the interleaf and the entire pressure load taken by the remaining two composite layers outside the interleaf. It is noted from Figure 5.15 that the hoop stiffness drops to about two thirds the initial value corresponding to the two outer layers of the total of three ±60° layers that are the structure of the tube. In the case of the 7:1 stress ratio, the pipe then fails at a lower stress because the effective wall thickness is reduced by one third. This cannot be said for the case of constrained ends because the failure changes from localised weepage in the specimens without an interleaf to burst resulting in greater failure stresses.

In the case of the 1:0 stress ratio, the axial strain is compressive and the inner composite layer does not leak prior to specimen failure. Therefore, the interleaf has no function under this load condition and may be removed. The similarity of the failure stresses and strains indicate that the interleaf is not detrimental and failure is structural, unrelated to leakage or matrix cracking. It is also unlikely that this failure is a result of buckling since the failure stress is very similar to that of the specimen without interleaf even though the wall thickness is now divided into two distinct structures.

5.2.4 Failure Envelopes

The differences noted in the stress-strain curves are also observed in the stress and strain first failure envelopes. Figure 5.17 compares the stress failure envelope of the specimens with and without interleaves. Similar strengths are observed at stress ratios of 0:1, 1:1 and 1:0. These are stress ratios that did not produce weepage or leakage and the interleaf provides no benefit or detriment. Under the constrained end condition the failure strengths are increased as the failure mode is changed from local weepage to burst. It should also be noted that under the constraint condition the resulting effective stress ratio is slightly increased when the interleaf is added. At a stress ratio of 7:1 the interleaf divides the composite into two weaker structures and the failure strength is reduced.

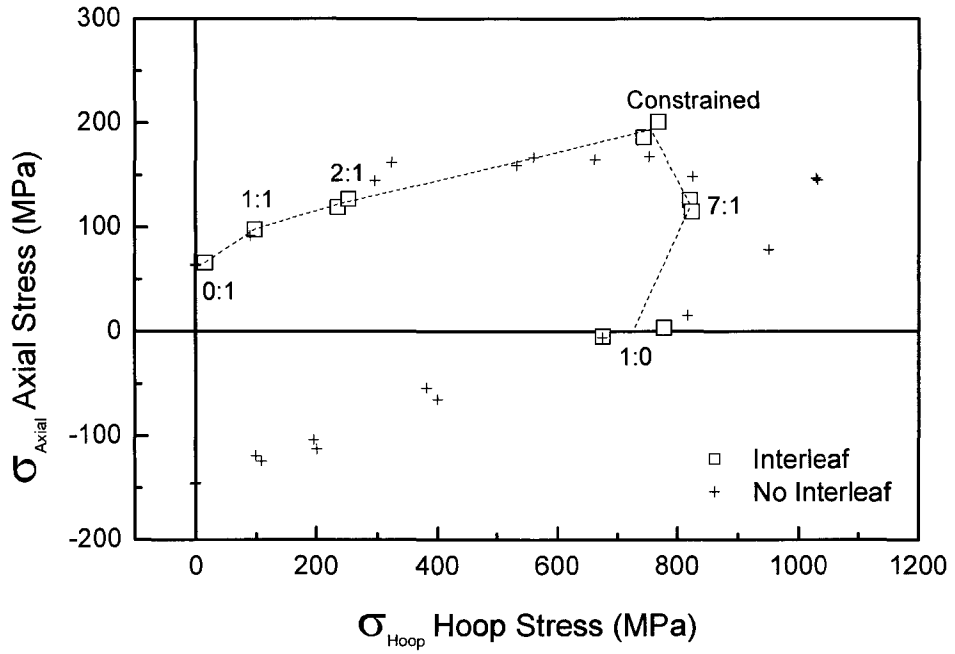

Figure 5.17: Stress first failure envelope of interleaf specimens. Stresses are in the specimen coordinate system.

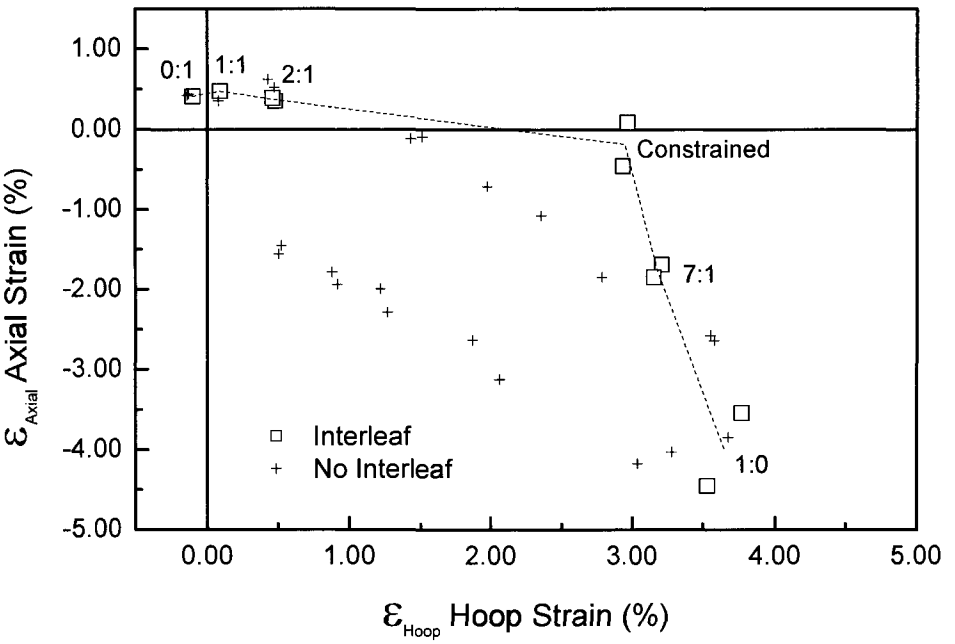

Figure 5.18: Strain first failure envelope for interleaf specimens. Strains are in the specimen coordinate system.

Figure 5.18 shows the failure strains in the specimen coordinate system. As expected, the strains with and without the interleaf are similar for the stress ratios of 0:1, and 1:1. However, the strains are outside the failure envelope of the control specimens for both the constrained, 7:1 and 1:0 conditions although at the 7:1 stress ratio the interleaf specimen failed at lower stress values. While the failure stresses under pure hoop stress are similar to those of the specimen without an interleaf, the hoop strain is increased by about 0.5%.

Once again we may transform the stresses and strains into the ply coordinate system. The three-dimensional representation of the stress and strain states are shown in Figure 5.19 and Figure 5.20 respectively.

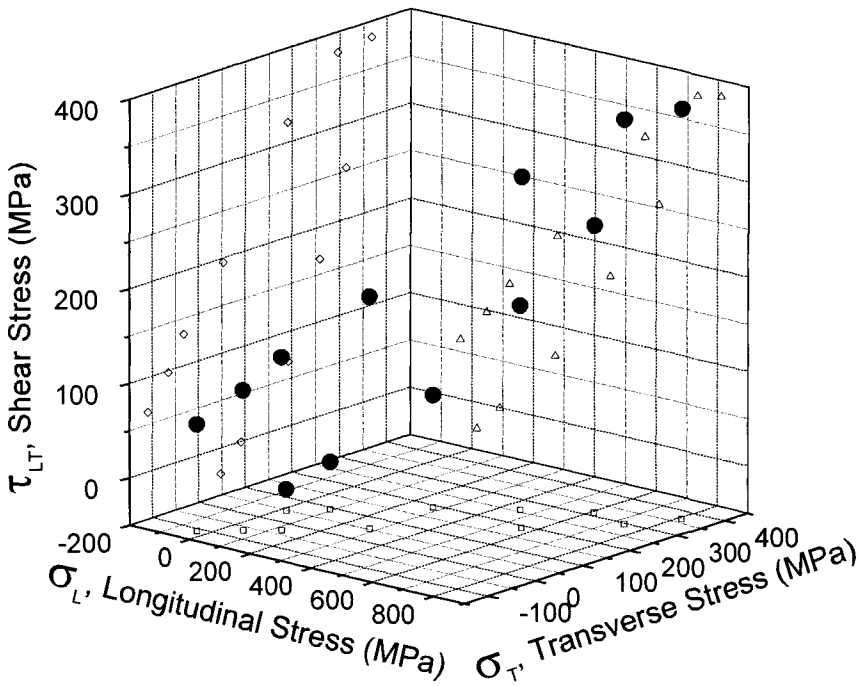

Figure 5.19: Stress first failure envelope for interleaf specimens. Stresses are in the specimen coordinate system σ_L-σ_T-τ_{LT}.

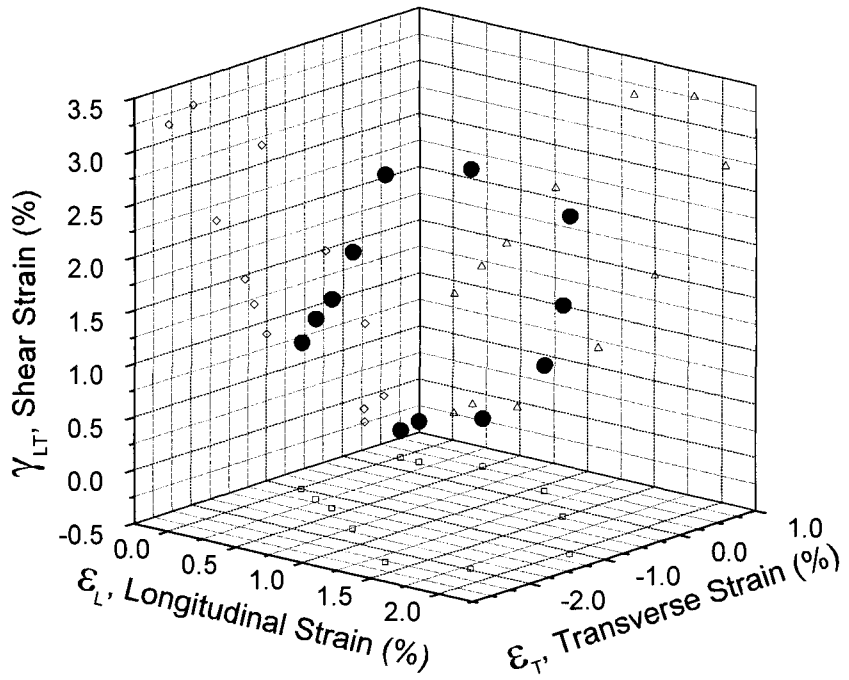

Figure 5.20: Strain first failure envelope for interleaf specimens. Strains are in the specimen coordinate system ε_L-ε_T-γ_{LT}.

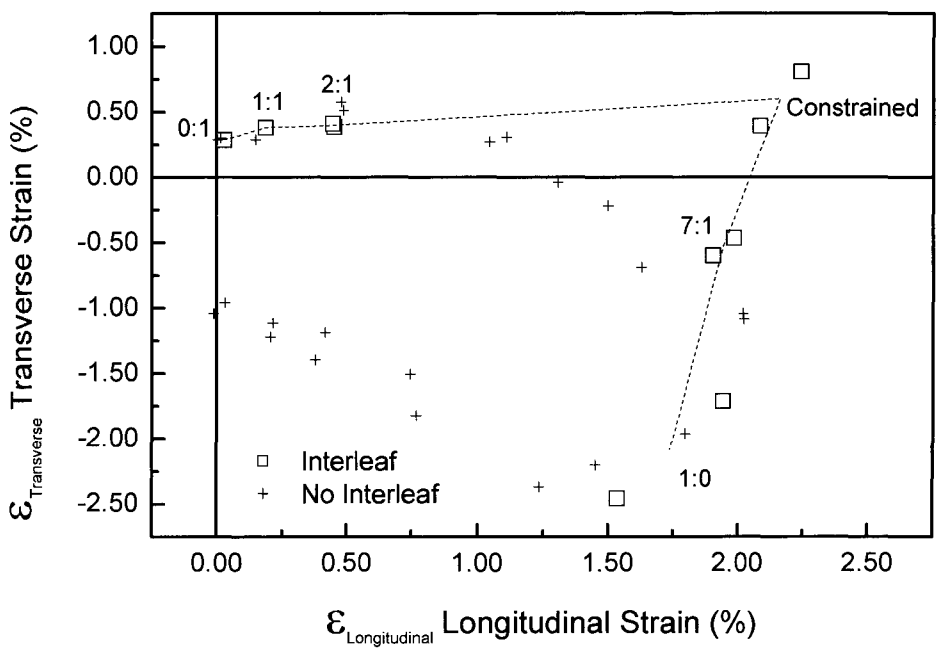

Figure 5.21: Strain first failure envelope. Strains are transformed to the ply coordinate system.

Since these are difficult to interpret, the failure strains are usually on the strain plain in Figure 5.21.

While Figure 5.21 shows there is little change in the behaviour under the 0:1, 1:1, 2:1 and 1:0 stress ratios, there is some difference in the transverse strain at the 7:1 ratio and large increases in both the transverse and longitudinal failure strains under constrained end loading.

For the latter case, it is observed, that the strains in both directions are approximately twice that than for the samples without an interleaf. This corresponds in a change in first failure mode from localised weepage at the ends of the specimen to burst near the gripping tabs. This behaviour reflects the lower compliance once the inner structural layer is breached but also that the tape interleaf has acted as an impermeable barrier. Since the axial deformation is constrained, the interleaf does not readily tear or slip and is therefore much more effective.

At the 7:1 stress ratio, the transverse strain had a decrease in magnitude while the longitudinal strain remained similar. It is shown that the remaining hoop stiffness has dropped but it is expected that the axial stiffness remained the same, or dropped only slightly, therefore for the lower stresses at failure (due to the thinner effective wall thickness containing the pressure) the axial strain magnitude will decrease.

5.3 SUMMARY OF THE EFFECTS OF ADDING THE INTERLEAF

The polyethylene tape interleaf was added to the composite structure with the expected benefits of delaying or arresting matrix crack growth and acting as an impermeable barrier.

It was shown in thick cross-ply specimens that the addition of the interleaf reduced load transfer of thermal residual stresses to the notch in the outer layers and this contributed to a higher crack growth initiation stress. The interleaf produced delays in the crack growth for periods of 100 to 100,000 cycles. However, it was observed that the crack path was not along the same plane in front and behind the interleaf. This indicates that a new crack

is initiated at the interleaf due to the poor bonding of the polyethylene to the epoxy matrix.

Addition of the interleaf to the filament wound tubes was done by a multi-step procedure of filament winding, tape wrapping and a final filament wound layer. This resulted in poor bonding of the interleaf to the composite structure, effectively dividing the composite tube wall into two separate structures, one layer thick on the inside and two layers thick on the outside. The interleaf was shown to have little or no effect at stress ratios of 0:1, 1:1 and 1:0. At the stress ratio of 2:1 the interleaf specimen failed by weepage as the axial tensile deformations resulted in slippage or tearing of the interleaf. In the case of the 7:1 stress ratio the inside structure failed first allowing an annular space between the inside structure and the interleaf to fill with pressurised fluid. With only two external layers of composite left to contain the internal pressure, the specimen burst at a lower stress state. Only under the constrained end condition did the failure stress state and hoop strains increase. The interleaf acted as an impermeable barrier and the failure mechanism changed from local weepage at the specimen ends to a burst.

It is recognised that the polyethylene tape interleaf is not the ideal material as it results in a discontinuous structure. While this is shown to be beneficial in the case of the transverse crack in the thick cross-ply the poor bonding and load transfer resulted in reductions in strength when subject to internal pressure combined with axial tension. In this case the internal structural layer was sacrificial and served only as a platform for the interleaf. Should a high ductility polymer with better bonding compatibility be used, the inner layer may continue to contribute to the tube strength even after having been damaged by transverse cracking.

CHAPTER 6 NONLINEAR TRANSVERSE ISOTROPIC VISCOELASTIC MODELLING

It is acknowledged that polymer matrices display viscous, time dependent behaviour which is observed as creep strain and stress relaxation. An isotropic viscoelastic constitutive model recently developed by Xia, Ellyin and Hu has been modified and calibrated to represent a transversely isotropic material such as a fibre reinforced polymer composite.

6.1 A TRANSVERSELY ISOTROPIC VISCOELASTIC MATERIAL MODEL

The current isotropic viscoelastic model by Xia and Ellyin, briefly described in Chapter 1, is based on the differential formulation of a linear spring in series with a number of Kelvin-Voigt type elements. The creep strain rate may be calculated by equation 1.3 where the total strain rate is the sum of the elastic and creep components. This rate dependent material model has been implemented in the user subroutines of ANSYS and ADINA finite element packages for the analyses of representative volume elements with thermal residual stresses, damage development and debonding (Zhang et al., 2005; Zhang et al., 2004). While this approach has been very successful, it has been restricted to micro damage and has required that the physical microstructure of the composite be adequately modelled.

In this study it is the intention to study a macro crack through a laminated structure, but it is not required to model the independent constituents. Therefore the aforementioned viscoelastic material model has been modified to represent homogenised transversely isotropic behaviour. In the transversely isotropic materials the response transverse to the longitudinal coordinate axis is independent of direction on the plane which has a normal vector identical to the longitudinal axis. In a fibre reinforced composite the longitudinal axis is defined by the fibre axis. Using a transversely isotropic response to represent fibre reinforced composites is a fair assumption when the fibres are randomly placed.

Modifying the current viscoelastic model to a transversely isotropic one is achieved by modifying the elastic and creep compliance matrices. The total strain rate may be

expressed as the sum of the elastic and creep strain rate components as shown in equation 6.1.

$$\{\dot{\varepsilon}_{total}\} = \{\dot{\varepsilon}_{elastic}\} + \{\dot{\varepsilon}_{creep}\} \tag{6.1}$$

where

$$\{\dot{\varepsilon}_{elastic}\} = [S]\{\dot{\sigma}\} \tag{6.2}$$

and [S] is the compliance matrix. For orthotropic materials

$$[S] = \begin{bmatrix} \frac{1}{E_1} & \frac{-\nu_{12}}{E_1} & \frac{-\nu_{13}}{E_1} & 0 & 0 & 0 \\ \frac{-\nu_{21}}{E_2} & \frac{1}{E_2} & \frac{-\nu_{23}}{E_2} & 0 & 0 & 0 \\ \frac{-\nu_{31}}{E_3} & \frac{-\nu_{32}}{E_3} & \frac{1}{E_3} & 0 & 0 & 0 \\ 0 & 0 & 0 & \frac{1}{G_{23}} & 0 & 0 \\ 0 & 0 & 0 & 0 & \frac{1}{G_{31}} & 0 \\ 0 & 0 & 0 & 0 & 0 & \frac{1}{G_{12}} \end{bmatrix} 0 \quad \text{where} \quad \frac{\nu_{12}}{E_1} = \frac{\nu_{21}}{E_2}, \; \frac{\nu_{13}}{E_1} = \frac{\nu_{31}}{E_3}, \; \frac{\nu_{23}}{E_2} = \frac{\nu_{32}}{E_3} \tag{6.3}$$

For a transversely isotropic material

$$\begin{aligned} &E_2 = E_3 \\ &G_{12} = G_{31} \\ &\frac{1}{G_{23}} = \frac{2(1+\nu_{23})}{E_2} \\ &\nu_{12} = \nu_{13} \rightarrow \nu_{21} = \nu_{31} \\ &\nu_{23} = \nu_{32} \end{aligned} \tag{6.4}$$

therefore

$$[S]=\begin{bmatrix} \frac{1}{E_1} & \frac{-\nu_{12}}{E_1} & \frac{-\nu_{12}}{E_1} & 0 & 0 & 0 \\ \frac{-\nu_{12}}{E_1} & \frac{1}{E_2} & \frac{-\nu_{23}}{E_2} & 0 & 0 & 0 \\ \frac{-\nu_{12}}{E_1} & \frac{-\nu_{23}}{E_2} & \frac{1}{E_2} & 0 & 0 & 0 \\ 0 & 0 & 0 & \frac{2(1+\nu_{23})}{E_2} & 0 & 0 \\ 0 & 0 & 0 & 0 & \frac{1}{G_{12}} & 0 \\ 0 & 0 & 0 & 0 & 0 & \frac{1}{G_{12}} \end{bmatrix} \qquad 6.5$$

The creep response is also assumed to be transversely isotropic therefore the creep strain rate is modified in a similar manner. The creep strain rate is defined by

$$\{\dot{\varepsilon}_{creep}\}=\sum_{i=1}^{n}\left[[S_i^*]\{\dot{\sigma}\}-\frac{1}{\tau_i}\{\varepsilon_{creep,i}\}\right] \qquad 6.6$$

where

$$[S_i^*]=\begin{bmatrix} \frac{1}{E_{1,i}\tau_i} & \frac{-\nu_{12}}{E_{1,i}\tau_i} & \frac{-\nu_{12}}{E_{1,i}\tau_i} & 0 & 0 & 0 \\ \frac{-\nu_{21}}{E_{2,i}\tau_i} & \frac{1}{E_{2,i}\tau_i} & \frac{-\nu_{23}}{E_{2,i}\tau_i} & 0 & 0 & 0 \\ \frac{-\nu_{21}}{E_{2,i}\tau_i} & \frac{-\nu_{23}}{E_{2,i}\tau_i} & \frac{1}{E_{2,i}\tau_i} & 0 & 0 & 0 \\ 0 & 0 & 0 & \frac{2(1+\nu_{23})}{E_{2,i}\tau_i} & 0 & 0 \\ 0 & 0 & 0 & 0 & \frac{1}{G_{12,i}\tau_i} & 0 \\ 0 & 0 & 0 & 0 & 0 & \frac{1}{G_{12,i}\tau_i} \end{bmatrix} \qquad 6.7$$

and

$$\begin{aligned} E_{1,i} &= E_1^1(\sigma_{eff}) \\ E_{2,i} &= E_2^1(\sigma_{eff}) \\ G_{12,i} &= G_{12}^1(\sigma_{eff}) \\ \tau_i &= \alpha^{i-1}\tau_1 \end{aligned} \qquad 6.8$$

This yields two extra unknowns, α and τ_1, and three functions of effective stress for E_1^1, E_2^1 and G_{12}^1.

This viscoelastic formulation assumes that the Poisson's ratios are be identical to the elastic values and independent of time. While there is mathematical argument that the Poisson's ratio should be time dependent under all but a limited number of load cases (Hilton, 2001; Hilton and Yi, 1998), there is little experimental verification of this. Most experimental results, such as Hu et al. (2003), demonstrate a fairly constant Poisson's ratio under a uniaxial load and it is very difficult to measure the relaxation strains to an accurate degree to confidently state a Poisson's ratio during relaxation.

The effective stress used in this model is the von Mises equivalent stress of the average matrix stress state where the matrix stress state is estimated using a method describe by Sun and Chen (1991). They idealised the composite ply as a simple unit cell, divided into four areas, to which the law of mixtures (constant strain, equation 3.10) and its inverse (constant stress, equation 3.11) can be applied to determine the average stresses within the reinforcement and the matrix. To simplify the problem, the reinforcement is represented as a square inclusion in a square unit cell as shown in Figure 6.1. The dimensions a and b are determined from the volume fraction of reinforcement given the unit cell has an overall dimension of one. In this case the area is equal to the volume fraction of reinforcment. Where longitudinal properties are considered, the unit cell is given a depth of one. The area AR is entirely reinforcement material and area AM is matrix. These two areas are then homogenised using the rule of mixtures as area A. The rule of mixtures is then extended to area A and area B, which is entirely matrix, to determine the mechanical properties of the homogenised unit cell.

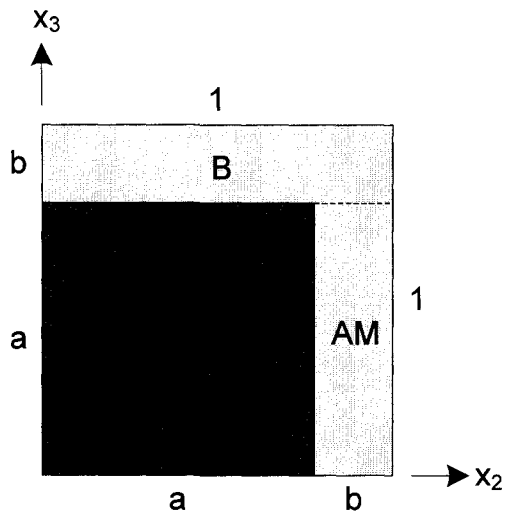

Figure 6.1: Simplified unit cell model of Sun and Chen (1991) used to determine average matrix stress state.

In the longitudinal direction, x_1, the rule of mixtures (equation 3.10), stating that the strain on the cross-section is constant, may be applied.

$$\varepsilon = \varepsilon_M = \varepsilon_R$$

$$\frac{\sigma}{E} = \frac{\sigma_M}{E_M} = \frac{\sigma_R}{E_R}$$

$$V_R = \frac{A_{AR}}{A} = \frac{a \cdot a}{1 \cdot 1} = a^2 \qquad 6.9$$

$$E_1 = E_M \cdot (1 - V_R) + E_R \cdot V_R$$

$$\frac{\sigma_M}{\sigma} = \frac{E_M}{E_M \cdot (1 - V_R) + E_R \cdot V_R}$$

It is found that the matrix stress, for a volume fraction of 72.69%, is approximately 6.4% of the magnitude of the applied stress, σ_{11}.

In the transverse direction, x_2, two steps must be done. First, constant stress is assumed through areas AR and AM to determine the stiffness in these areas (equation 6.10).

$$\begin{aligned} \sigma &= \sigma_{AM} = \sigma_{AR} \\ V_{AR} &= \frac{A_{AR}}{A_A} = \frac{a \cdot a}{a \cdot 1} = a \\ \frac{1}{E_A} &= \frac{1 - V_{AR}}{E_M} + \frac{V_{AR}}{E_R} \end{aligned} \qquad 6.10$$

Constant strain in the parallel areas A and B is then assumed to estimate the total stiffness and stress distribution in A and B, as in equation 6.11. The average stress of areas AM and B is then used as an estimate of the average transverse stress in the matrix.

$$\begin{aligned} \varepsilon &= \varepsilon_M = \varepsilon_R \\ \frac{\sigma}{E_2} &= \frac{\sigma_M}{E_M} = \frac{\sigma_R}{E_R} \\ V_A &= \frac{A_A}{A} = \frac{a \cdot 1}{1 \cdot 1} = a \\ E_2 &= E_M \cdot (1 - V_A) + E_A \cdot V_A \\ \frac{\sigma_B}{\sigma} &= \frac{E_M}{E_2} \\ \frac{\sigma_A}{\sigma} &= \frac{E_A}{E_2} \\ \left(\frac{\sigma_M}{\sigma}\right)_{Average} &= \frac{\frac{E_A}{E_2} \cdot A_{AM} + \frac{E_M}{E_2} \cdot A_B}{A_{AM} + A_B} = \frac{\frac{E_A}{E_2} \cdot a \cdot b + \frac{E_M}{E_2} \cdot b}{b \cdot (a+1)} \end{aligned} \qquad 6.11$$

The total transverse modulus may be found by substituting the value E_A, from equation 6.10, into equation 6.11. It is found that the average transverse stress in the matrix is 63% of the applied normal stress. The transverse and longitudinal shears are considered in an identical manner as the transverse stress and yield a similar result. The resulting ratios of average stress in the matrix to the stress in the RVE are provided in Table 6.1.

Table 6.1: Ratio of average matrix stress components to applied unit cell stress components for the calculation of effective stress

Stress Component	Ratio of Average Matrix Stress to Unit Cell Stress
Longitudinal, σ_{11}	0.0635
Transverse, $\sigma_{22} = \sigma_{33}$	0.6240
Longitudinal Shear, $\tau_{12} = \tau_{13}$	0.6215
Transverse Shear, τ_{23}	0.6215

These matrix stresses are applied to the calculation of von Mises equivalent stress to find the effective stress subsequently used in determining the creep moduli. This method of determining the stress state in the matrix is a simplified approximate method. However, it does account for high longitudinal stresses in the composite ply that yield little viscoelastic effect. It must also be noted that the stress state in the matrix is a function of time as the matrix creeps and load is transferred to the reinforcement.

6.2 CALIBRATION OF THE TRANSVERSELY ISOTROPIC VISCOELASTIC MODEL

The viscoelastic model must be calibrated to determine the functions and constants noted above. This is typically done by conducting experimental creep tests on the material at a number of load magnitudes and then using best fit curves to define the functions and constants. An example of this process for the isotropic model for the EPON 826/EPICURE 9551 epoxy system is provided by Hu (2001). Here the load tests will be conducted numerically using the established isotropic model to represent the viscoelastic polymer matrix.

Calibration of the transversely isotropic model for the composite system was done by finite element analysis of the hexagonal fibre packing representative volume element described in Chapter 3. However, the matrix is now modelled using the isotropic viscoelastic model by Xia and Ellyin with parameters for the epoxy matrix from Hu (2001) as given in Table 6.2. The glass fibre reinforcement was modelled by linear elastic behaviour.

Table 6.2: Material properties used in representative volume element finite element analysis of glass fibre reinforced epoxy.

Property	Value	
Glass Fibre		Elastic Properties
E_r, Modulus (MPa)	72,400	
G_r, Rigidity (MPa)	29,700	
ν_r, Poisson's Ratio	0.22	
Epoxy		
E_m, Modulus (MPa)	3,400	
G_m, Rigidity (MPa)	1,197	
ν_m, Poisson's Ratio	0.42	
R, Yield Stress Ratio	1.15	
E^1, Creep Modulus (MPa)	$=105{,}500e^{\frac{\sigma_{eqv}-22.764}{18.000}}$	Creep Properties#
G^1, Creep Rigidity (MPa)	$=37.1e^{\frac{\sigma_{eqv}-22.764}{18.000}}$	
α, Multiplier	10	
τ_1, Retardation Time (s)	6.116	

The Poison's ratio used in the creep formulation is identical to the elastic values

Uniaxial and shear loads were applied rapidly and held and the responses recorded. Figure 6.2 provides an example of the creep strain response at an applied equivalent stress of 50 MPa. While it may be proven that the linear elastic response is transversely isotropic (Edelglass, 1966) this is not true for the nonlinear viscoelastic analysis. There is a large difference in the creep strain response in the transverse directions demonstrated in Figure 6.2. This is due to the different dimensions of the hexagonal packing RVE in the 2 and 3 directions to model the reinforcement array. Thus the stress/strain distributions are different for each of the applied load directions, resulting in different RVE viscoelastic responses. The response in the x_2 direction agreed with the values predicted for the transverse shear stress and was used for the calibration.

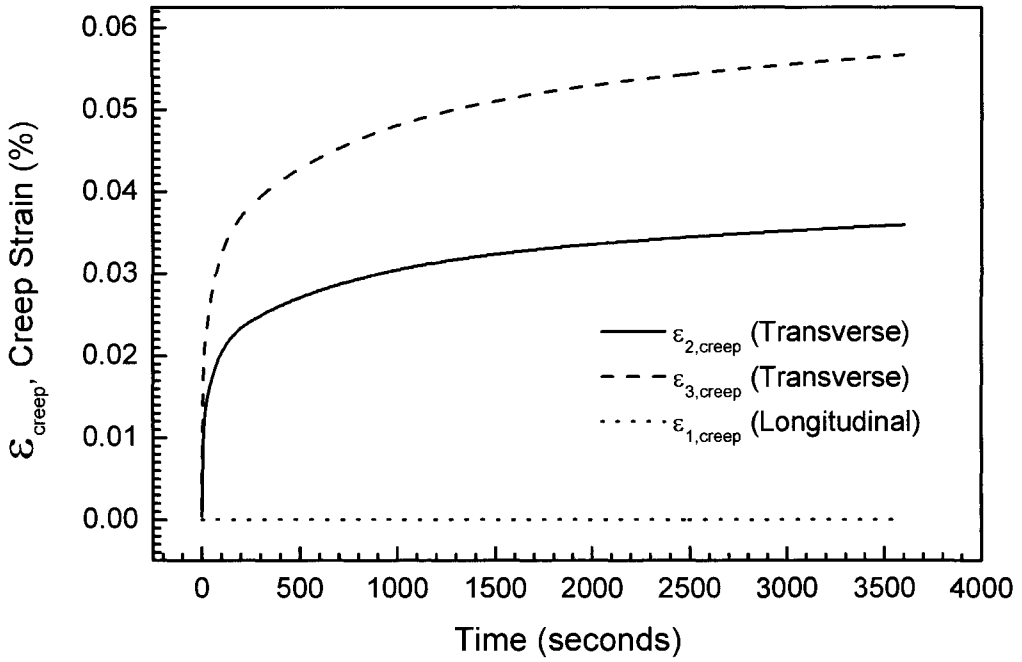

Figure 6.2: Example of the creep strain response under uniaxial loading in each of the three RVE directions. Load is rapidly increased to an equivalent stress of 50 MPa and held.

Integration of equation 6.6 yields

$$\{\varepsilon_{creep}\} = \sum_{i=1}^{n} [S^*]\{\sigma\}\left(1 - e^{\frac{-t}{\alpha^{i-1}\tau_1}}\right) \qquad 6.12$$

and this was fit to the creep responses using best fitting techniques. In all cases α was set to a value of ten leaving four material functions to determine, τ_1, E_1^1, E_2^1 and G_{12}^1.

The creep moduli, determined for various average effective stresses, are shown in Figure 6.3. Values for the creep modulus, E_1^1, are not displayed since they were found to be extremely large. This was expected since this corresponds to the fibre axis and the fibre was modelled as an elastic material with a much higher stiffness, and volume, than the matrix. Therefore, in the resulting modeling E_1^1 is set to a very high value effectively eliminating the component from the creep compliance matrix, [S*].

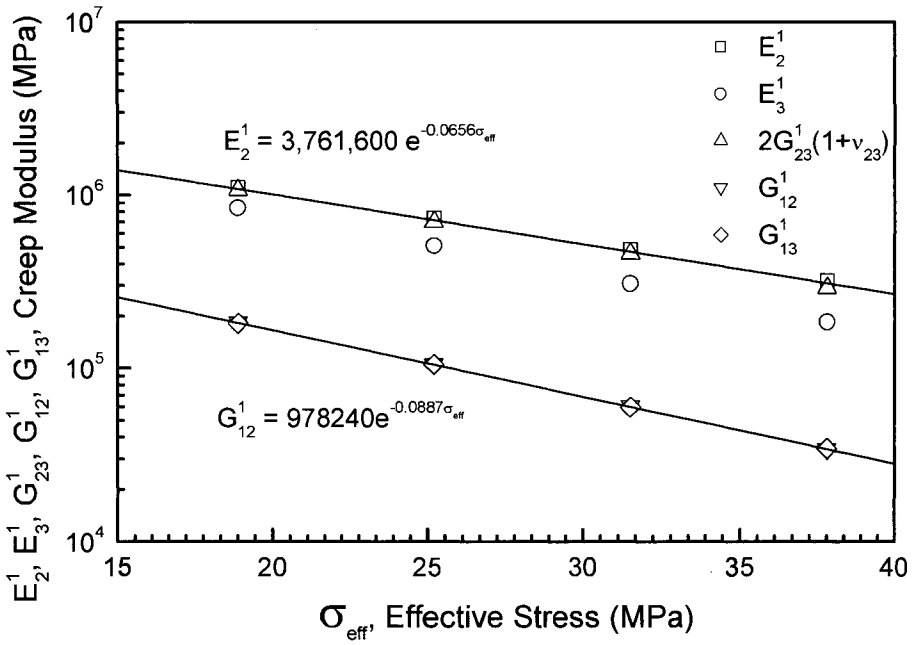

Figure 6.3: Creep moduli determined from calibration procedure.

It is seen in Figure 6.3 that the creep moduli are an exponential function of the average matrix equivalent stress and the functions are provided on the figure. It is also clear here, as in Figure 6.2, that the creep moduli, E_2^1 and E_3^1, are quite different due to the RVE geometry. The material model of the transversely isotropic composite was calibrated using the results of E_2^1 and G_{23}^1. The value of τ_1 was found to be nearly constant and an average value of $\tau_1 = 6.215$ s was applied in the analyses.

Table 6.3: Material Properties required for transversely isotropic viscoelastic material model of glass fibre reinforced EPON 826/EPICURE 9551 epoxy.

Property	Value	
E_1, Longitudinal Modulus, (MPa)	53,514	Elastic Properties
$E_2 = E_3$, Transverse Modulus, (MPa)	20,832	
$G_{12} = G_{13}$, Longitudinal Rigidity, (MPa)	6199	
G_{23}, Transverse Rigidity, (MPa)	7166	
$\nu_{12} = \nu_{13}$, Longitudinal Poisson's Ratio	0.260	
ν_{23}, Transverse Poisson's Ratio,	0.452	
E_1^1, Longitudinal Creep Modulus,	$\approx \infty$	Creep Properties#
$E_2^1 = E_3^1$, Transverse Creep Modulus, (MPa)	$= 3{,}761{,}595e^{-0.06599\sigma_{eqv}}$	
$G_{12}^1 = G_{13}^1$, Longitudinal Creep Rigidity, (MPa)	$= 978{,}241e^{-0.08866\sigma_{eqv}}$	
G_{23}, Transverse Creep Rigidity, (MPa)	$= 1{,}295{,}315e^{-0.06599\sigma_{eqv}}$	
α, Multiplier	10	
Retardation Time, τ_1, (s)	6.215	

The Poison's ratios used in the creep formulation are identical to the elastic values

The resulting calibrated constants for the compliance matrix in the transversely isotropic viscoelastic model are provided in Table 6.3.

6.3 TRANSVERSELY ISOTROPIC MATERIAL MODEL RESULTS

Finite element analysis of a simple single material using the model described and calibrated was completed for comparison to the calibration data. Due to the anisotropic creep response in the transverse direction, it is expected that there will be some variation

between the two sets of results. Figure 6.4 shows the equivalent strain response under unidirectional normal loads, σ_{11}, σ_{22} and σ_{33} and shear loads τ_{12}, τ_{13} and τ_{23}.

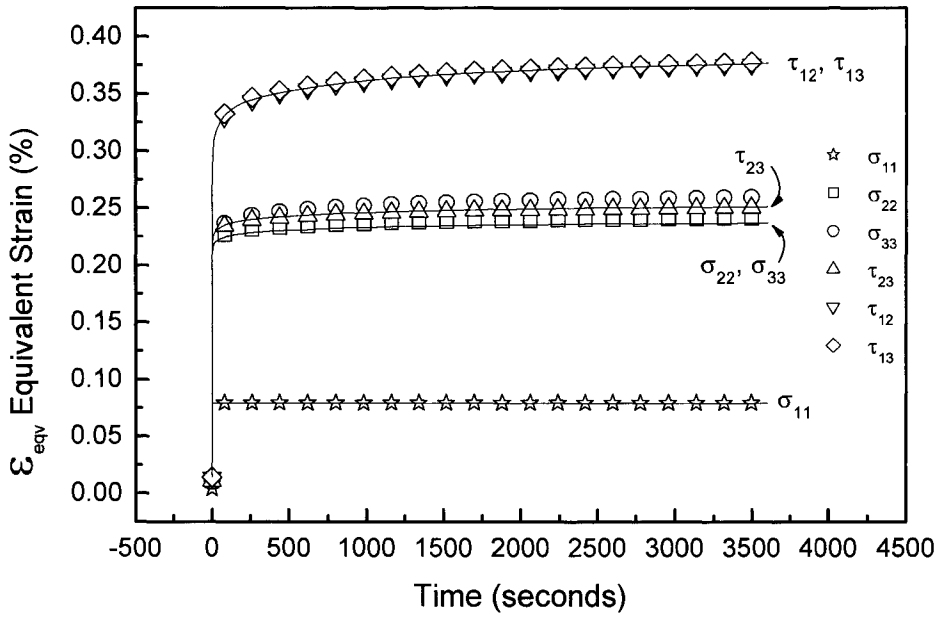

Figure 6.4: A comparison of calibration data and transversely isotropic model results. Calibration data is represented as symbols and model results by solid lines.

Figure 6.4 shows the creep results of the transversely isotropic material model are very similar to that of the calibration data obtained from the hexagonal packing arrangement representative volume element. The elastic response is not shown clearly at this time scale, but it is the creep strain behaviour that is difficult to predict with accuracy. Note that there is no creep observed under the σ_{11} load because the elastic glass fibres are assumed to dominate the behaviour in this direction. The difference in response under applied stresses σ_{22} and σ_{33} is observed as expected since the time dependent response of the hexagonal packing arrangement is not truly isotropic.

6.4 SUMMARY OF THE TRANSVERSELY ISOTROPIC MATERIAL MODEL

In this chapter, an isotropic viscoelastic material model was modified to represent transversely isotropic behaviour associated with fibre reinforced composites. This is a

useful assumption of mechanical response where the fibre reinforcement is randomly spaced in a unidirectional ply. The model was then calibrated using the results of a finite element analysis on a representative volume element of the composite. Hexagonal packing geometry was used because of its transversely isotropic elastic response but it was shown that the creep strain produced was not transversely isotropic. Therefore the model was calibrated using E_2^1 and G_{23}^1. Results from the model agree with the calibration data. In the following chapter this material model will be used to study the propagation of a crack through a thick, viscoelastic cross-ply laminate.

CHAPTER 7 VISCOELASTIC ANALYSIS OF TRANSVERSE CRACK PROPAGATION IN A THICK CROSS-PLY WITH AN INTERLEAF

A previous elastic analysis of the transverse crack in the thick cross-ply by the author (Meijer and Ellyin, 2004) demonstrated the influence of interleaf geometry and stiffness on the crack driving force. Here, it is acknowledged that the composite and polymer interleaf response are time dependent. In this chapter a finite element simulation of crack growth through thick cross-ply laminate with an interleaf, using viscoelastic material models, is done to demonstrate the influence of the interleaf on the progression of a crack in the 90° plies. The analysis makes use of the transversely isotropic viscoelastic material model developed and calibrated in the previous chapter. Thus one can study the effects of geometry, material properties, viscoelasticity and time.

7.1 THE FINITE ELEMENT MODEL

A model of the geometry was produced in the ANSYS pre-processor and appropriate boundary conditions were applied to represent a plane strain state. The following sections describe the geometry, model generation, boundary conditions and load schedule.

7.1.1 Geometry

Geometry was produced to represent the cross-ply laminate structure tested in Chapter 5. It is assumed that symmetric edge cracks exist in the laminate and that the crack tips travel along a line of symmetry as shown in Figure 7.1. Therefore only one quarter of the model need be analysed. The laminate plate lies in the X-Y plane with a macro crack growing in the –Z direction. The transversely isotropic material model requires the reinforcement angle to be input as θ° measured from the +X axis towards the +Y axis. Plane strain behaviour is assumed for this analysis so that the laminate is very deep into the page. The width of the model corresponds to the thickness of the laminate and the height of the model need only be sufficient to be away from the local crack tip effects.

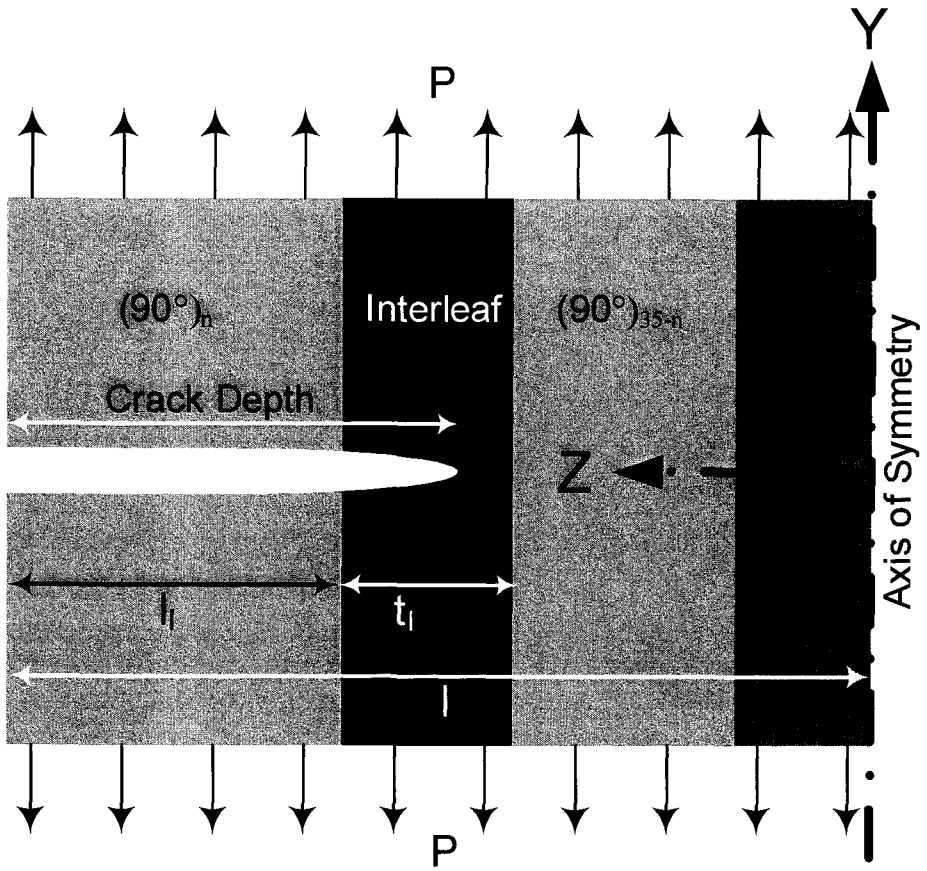

Figure 7.1: Schematic of coupon crack specimen lay-up.

Parameters studied are interleaf material, position and thickness. For all analyses of interleaf material the interleaf thickness, t_I, is 0.5 mm and it is placed between the 25th and 26th 90° ply so that l_I = 5.525 mm. Interleaf thicknesses of 0.25, 0.5 and 1.0 mm, placed l_I = 5.525 mm from the outside surface, are compared to study the effect of thickness. To study the influence of position, 0.5 mm thick interleafs are placed on the surface and 2.122 and 5.525 mm below the surface (i.e. l_I = 0, 2.122, 5.525 mm). All the analyses, and the variables tested, are listed in tables in Section 7.4.

7.1.2 Mesh Generation

The model geometry was meshed using node by node element definition and automatic parametric element generation in regular rectangular shaped areas. The fine element mesh is required to adequately represent the high stress gradient at the crack tip. In this analysis

the crack tip is propagating therefore the entire zone of propagation was meshed at an appropriate element density. It should be noted that there are programs which allow for modification of the mesh between crack propagation steps however this is generally for material models which do not require recording of the stress or strain history. In this viscoelastic material model, the material response is a function of the accumulated creep strain at each integration point therefore changing the mesh during the analysis would greatly increase the complexity.

To reduce the total number of degrees of freedom in the analysis, a very fine mesh is used only at the highest stress gradients near the crack tip and the element size is progressively increased with distance from the crack tip. To produce a regular mesh, the element size is doubled at each step using transition elements. The initial transition elements must be generated manually but are easily reproduced using mesh copying and reflection. These functions were used to significantly reduce the number of commands required to produce the refined mesh which is symmetric about the centre line of the interleaf layer. The remaining dimensional requirements were fulfilled by meshing simple rectangular areas.

Element material numbers and data sets were assigned at the time of mesh generation and values were then entered for material and element properties, prior to the solution phase. The resulting meshes for all the models used in this analysis are shown in Figure C.2 to Figure C.13 in Appendix C.

7.1.3 Boundary Conditions

The free surfaces, axes of symmetry, loads and the crack are defined by the appropriate boundary conditions as shown in Figure 7.2. As noted above, the plane strain condition is enforced by constraining the model in the X direction so that no deformation can occur and $\varepsilon_x = 0$. The left hand boundary is a free surface and not subject to constraint, while the right side is a plane of symmetry and therefore is constrained to zero displacement in the Z direction. The top edge of the model is loaded by a distributed force. It is assumed that away from the crack the strain through the laminate thickness is constant, and therefore this surface is allowed to move in the Y direction, but all nodes on the surface

must have the same Y displacement. The bottom surface is a plane of symmetry that contains the crack. Therefore, along the uncracked ligament the node deformation is constrained in the Y direction and along the crack the deformation is unconstrained.

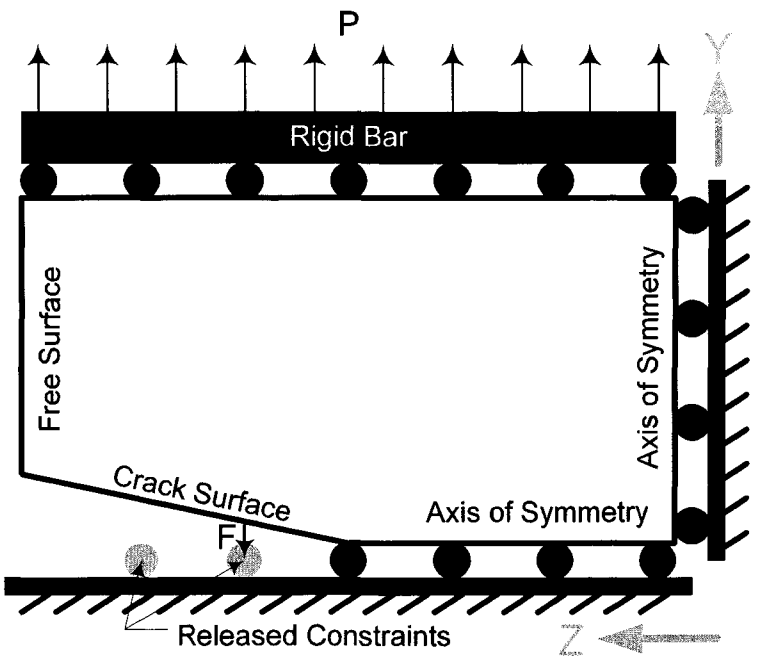

Figure 7.2: Boundary conditions applied to cracked laminate model.

These constraints, shown in Figure 7.2, are summarised as:

$$\begin{aligned} U_x^{x+} &= 0 \\ U_x^{x-} &= 0 \end{aligned} \quad \text{Plane strain condition}$$

$$\begin{aligned} U_y^{y+} &= C_y \\ U_y^{y-} &= 0 \end{aligned} \quad \text{Uncracked plane of symmetry} \qquad 7.1$$

$$U_z^{z-} = 0$$

where the + and – superscripts signify the boundaries with normal outward vectors in the positive and negative axis orientations, respectively.

7.2 CRACK MODEL SOLUTION

The method used in this investigation is for quasi-static crack growth through multiple elastic and viscoelastic material layers. The solution of the propagating crack finite element model in viscoelastic composite materials consists of four distinct steps: application of load, saturation of creep strain and stress relaxation, propagation of the crack tip and a delay between crack tip propagation steps.

7.2.1 Application of Load

A constant load is applied to the upper boundary as a single rapid ramp in $1x10^{-5}$ s such that the response is essentially independent of time and therefore elastic. The force is applied as a pressure distributed over the element faces while the involved nodes are in a coupled set such that all have the same displacement in the Y direction.

7.2.2 Saturation of Viscoelastic Strain and Stress Relaxation

Since the material behaviour is dependent on time and pre-existing creep strain it is important that all specimens have an identical history or that the history be erased. In experimental testing this is often done by relieving the material through an "annealing" process. In this numerical analysis the stress/strain state at the start of crack progression is made to be approximately independent of crack length by providing a saturation period. This is achieved by applying the constant load and waiting until the change in global deformation is small or zero. This was achieved numerically by stepping the time in constant one second increments until a displacement criterion was satisfied. The criterion used was similar to a solution convergence criterion. The saturation was complete when the creep deformation in the load direction over a one second increment was less than or equal to a specified percentage of the total accumulated creep deformation in the load direction. Analyses were also completed without this initial creep saturation period to demonstrate the effects of load history.

7.2.3 Propagation of the Crack Tip

Crack tip propagation was achieved by releasing the constraints on the crack tip nodes and moving the crack tip forward by one element. To aid in this process, the nodes along

the crack tip path were consecutively numbered beginning at one with the odd number nodes defining the x- edge and even nodes on the x+ edge. The nodes were released a pair at a time to move the crack front one element length.

Of special concern, when releasing the constraints, is a resulting rapid change in stiffness and difficulties achieving convergence of the solution. If the change in stiffness is too large due to release of a constraint or a large time step convergence may not occur or the displacements may become unrealistically large. To avoid a large change in stiffness the constraint was removed and immediately replaced with a nodal force equal to the previous reaction force. The nodal force was then reduced over ten time steps of 0.001 s so that the model stiffness changed gradually in terms of solution steps but rapidly in time to minimize relaxation and creep. At the end of the ten steps the nodal force was removed and the crack tip was considered to have propagated.

7.2.4 Crack Growth Delay

To study the effects of viscoelasticity on the crack growth a time period is required to develop viscoelastic strain and stress relaxation. Therefore, after the rapid crack propagation was complete a hold period was applied. Hold times of 0.05 to 50 s were applied to determine the influence of crack growth rate on the strain energy release rate.

The last two steps, crack tip propagation and the delay, are repeated numerous times to propagate the crack tip through the laminate including the 90° plies and the interleaf.

7.2.5 Geometric Crack Growth Increment and Time Substepping

Nonlinear finite element analysis of crack growth requires that the solution be found incrementally. In this case the crack must be propagated incrementally in space while the time is also progressed in steps.

Since the body is modelled by dividing it into "finite" divisions the propagation of the crack is restricted to minimum steps of length equal to the dimensions of the elements. Three meshes were generated having crack tip elements 0.0221, 0.0442 and 0.0884 mm in length to evaluate the influence of the mesh size on the strain energy release rate results. In an elastic analysis it was found that the fine mesh provided more accurate

representation of the strain energy release rate at the critical points when the crack tip enters and leaves the interleaf. The verification procedure and results are provided in Appendix C.

Mesh comparison under viscoelastic conditions is more difficult due to the combination of stress and time dependence. In the first comparison, viscoelastic analyses were conducted so that the crack propagation rate was the same for the three mesh density models by adjusting the delay time based on the element size. In the second comparison, the crack growth increment, Δa and time delay were kept the same. This required releasing the crack over multiple elements at each step. Oscillation of the solution was observed and was particularly evident in the analyses where more than one element length was released in a single propagation step. This issue tended to occur where the model stiffness was rapidly changing but was reduced by significantly decreasing the solution increment size. This dramatically increased the solution time.

The nonlinear problem must be solved incrementally using a solution technique such as Newton-Raphson. This technique was used with the ANSYS automatic time stepping procedure. The user is required to enter the time at the start of the solution step and the time at the end of the solution step along with an initial substep size, minimum substep size and maximum substep size for which the nonlinear solution procedure will be executed. The finite element software then automatically adjusts the substep size based on satisfying the convergence criteria.

The response of the viscoelastic model is a nonlinear function of the stress state. At high stresses the creep strain may grow rapidly leading to different solution requirements. This has been found to be a particular issue when starting the crack propagation and when the crack tip encounters a change in stiffness at the interleaf interfaces.

7.3 INTERLEAF MATERIALS

Three interleaf materials have been implemented in this investigation: EPON 826/EPICURE 9551 epoxy, ColdCure epoxy and High Density Polyethylene (HDPE). The first two are two part epoxy systems while the latter is a thermoplastic often

used in pipe applications. They are listed above in order of increasing ductility. The ColdCure has a greater ductility than the EPON 826/EPICURE 9551 system due to the room temperature cure and reduced cross-linking. The HDPE is a semi-crystalline thermoplastic with a low glass transition temperature. At room temperature, deformation can exceed 200%. These materials are reasonable alternatives for tough materials that may be applied as an interleaf in a laminate.

The EPON 826/EPICURE 9551 and ColdCure epoxies were used by Hu (2002) to formulate and verify the original isotropic viscoelastic model implemented here. Calibration of the model for the HDPE was done using experimental creep results from Zhang and Moore (1997a, 1997b). The calibration procedure was similar to that shown in Chapter 6 for the transversely isotropic model. The properties required to model these three materials are given in Table 7.1.

Table 7.1: Viscoelastic material model input values for isotropic interleaf materials.

Material Property	**EPON 826/ EPICURE 9551**	**ColdCure Epoxy**	**High Density Polyethylene**
E, Elastic Modulus, (MPa)	3400	2755	1450
ν, Poisson's Ratio	0.42	0.4	0.45
R, Yield Stress Ratio	1.15	1.08	1
E_1, Creep Modulus (MPa)	$=105500e^{\frac{\sigma_{eqv}-22.764}{18.000}}$	$=12245.6-432.6\cdot\sigma_{eqv}+4.49\cdot\sigma_{eqv}^2$ when $\sigma_{eqv}\geq 27.5$ MPa $=3744.7-75.7(\sigma_{eqv}-27.5)$ when $\sigma_{eqv}<27.5$ MPa	$=2291.8e^{-0.0804\cdot\sigma_{eqv}}$
τ_1, Retardation Time (s)	6.116	657.895	65.000
α, Multiplier	10	10	10

Examples of the calculated creep response for the three interleaf materials at four applied uniaxial stresses are shown in Figure 7.3 for comparison. The low elastic stiffness and

creep modulus of the high density polyethylene is particularly evident. A comparison to the retardation time may also be made. The ColdCure retardation time of greater than 650 s results in a much slower development of creep strain and longer times are required to reach saturation. However, the creep modulus is quite low compared to the EPON 826/EPICURE 9551 system and so the magnitude of the creep strain is greater.

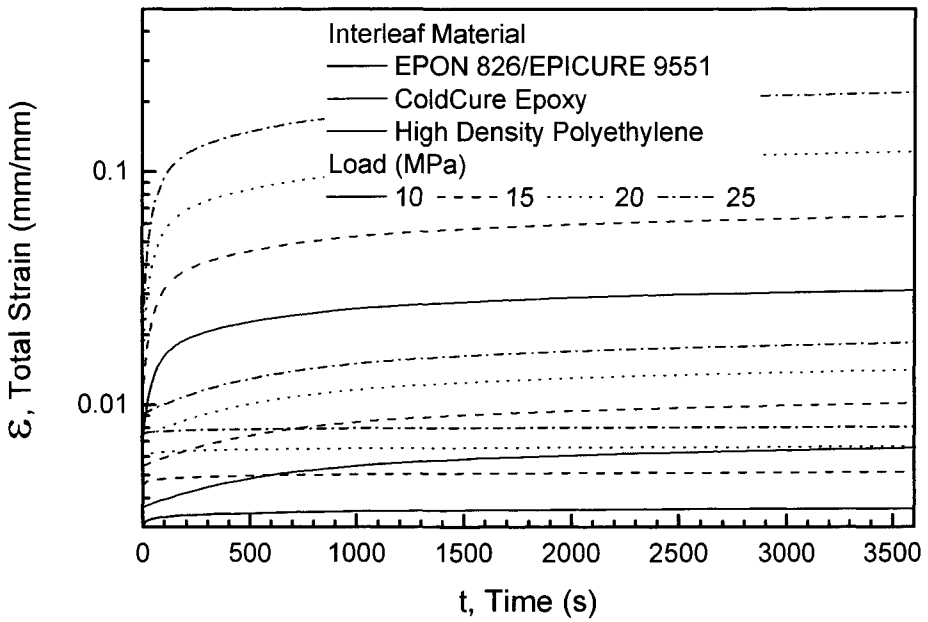

Figure 7.3: A comparison of the mechanical response of the three interleaf materials calculated using values in Table 7.1.

It must be noted that the EPON 826/EPICURE 9551 resin system is identical to that used as the matrix in the composite layers. Therefore using this material as an interleaf is identical to modelling a resin-rich layer.

7.4 FINITE ELEMENT ANALYSIS RESULTS

This investigation was completed to determine the effect of the interleaf and interleaf parameters on the crack driving force as the crack progresses through the laminate. The selection of an appropriate interleaf material and geometry is of primary concern where the interleaf is to slow or arrest crack propagation through the laminate.

In the following sections the influence of interleaf material, interleaf location and interleaf thickness on the energy release rate are discussed. Results are presented for elastic and viscoelastic analyses of the laminate. It is noted that there are special requirements of the viscoelastic analysis that will have an impact on the numerical results. The effects of initial saturation, crack growth rate and stress magnitude are discussed.

The elastic and viscoelastic analyses performed are listed in Table 7.2 and Table 7.3, respectively.

Table 7.2: Elastic crack growth analytical cases.

Interleaf Material #	**Interleaf Location, l_1 (mm)**	**Interleaf Thickness (mm)**	**Applied Load (MPa)**
340	5.525	0.5	25
3400	5.525	0.5	25
34,000	5.525	0.5	25
826	5.525	0.5	25
826	0	0.5	25
826	2.122	0.5	25
826	None	0	25
826	5.525	0.25	25
826	5.525	0.5	25
826	5.525	1.0	25
*826	5.525	0.5	25

\# 340 = Isotropic material, E = 340 MPa
3400 = Isotropic material, E = 3400 MPa
34,000 = Isotropic material, E = 34,000 MPa
* Debonding at interleaf interface in front of crack tip.

Table 7.3: Viscoelastic crack growth analytical cases.

Interleaf Material #	Interleaf Location (mm)	Interleaf Thickness (mm)	Applied Load (MPa)	Saturation (% ε_{creep}/s)	Hold Time (s)
826	5.525	0.5	25	1.0	0.05
826	5.525	0.5	25	1.0	0.1
826	5.525	0.5	25	1.0	0.5
826	5.525	0.5	25	1.0	1.0
826	5.525	0.5	25	1.0	5.0
826	5.525	0.5	25	1.0	10.0
826	5.525	0.5	25	1.0	50.0
826	5.525	0.5	25	None	5.0
826	5.525	0.5	25	0.1	5.0
826	5.525	0.5	25	None	0.05
826	5.525	0.5	25	0.1	0.05
826	5.525	0.5	15	1.0	5.0
826	5.525	0.5	25	1.0	5.0
CC	5.525	0.5	25	1.0	0.05
CC	5.525	0.5	25	1.0	0.5
CC	5.525	0.5	25	1.0	5.0
CC	5.525	0.5	25	1.0	50.0
CC	5.525	0.5	25	None	5.0
CC	5.525	0.5	25	0.1	5.0
PE	5.525	0.5	25	1.0	0.05
PE	5.525	0.5	25	1.0	0.5
PE	5.525	0.5	25	1.0	5.0
PE	5.525	0.5	25	1.0	50.0
PE	5.525	0.5	25	None	5.0
PE	5.525	0.5	25	0.1	5.0
826	0	0.5	25	1.0	5.0
826	2.122	0.5	25	1.0	5.0
826	None	0	25	1.0	5.0
826	5.525	0.25	25	1.0	5.0
826	5.525	0.5	25	1.0	5.0
826	5.525	1.0	25	1.0	5.0
*826	5.525	0.5	25	1.0	5.0

\# 826 = EPON 826/EPICURE 9551
CC = ColdCure Epoxy System
PE = High Density Polyethylene
* Debonding at interleaf interface in front of crack tip.

7.4.1 Strain Energy Release Rate

The numerical results are presented as the Mode I strain energy release rate, G_I, as a function of the crack depth, a. The methods of calculating the crack driving force using the J-integral and strain energy release rate were discussed in Chapter 1. These methods

are primarily used in models of a single material or where the crack propagates through a single material. It was verified that for a crack propagating through as single material the two methods do yield identical results. However, for a laminate of transversely isotropic layers of different orientations and the additional soft interleaf, the J-integral proved to be insensitive to the material interfaces and produced incorrect results. The development of the J-integral is based upon homogeneous linear material response in which superposition may be used. This is not the case with multiple nonlinear materials employed in this analysis.

The mode I strain energy release rate is expressed in units of J/m/mm that correspond to units of work per unit of model thickness per unit of crack advance. The strain energy release rate, per unit thickness, is calculated based on the difference between the deformation before and after the crack tip node release using eqn. 1.11 which is repeated here.

$$G = \frac{P}{2}\frac{\partial \Delta}{\partial a} \qquad 7.2$$

The force P is applied directly to a single node but through the coupled node set indicated by the beam in Figure 7.2 acts on the entire top surface. The applied pressure is equal to P divided by the area of the top surface. Since all nodes on the loaded surface have the same vertical displacement, the deflection of only one node need be recorded. Therefore only one value of nodal force and nodal displacement, and the crack increment need to be recorded for each load step to calculate the strain energy release rate.

While the J-integral was found to be inappropriate, the potential energy method of calculating the strain energy released rate is successful. The calculation of G by the potential energy method relies on values of force and displacement at the boundaries and what lies within is homogenised into a single body with a global stiffness. However G is sensitive to the crack tip position because the local stress/strain distribution is dependent on the local material properties near the crack tip.

The strain energy release rate does not include the deformation due to creep which may have accumulated during the delay period between crack increment steps. It is understood that if this time is considered creep deformations may occur leading to lower strain energy release rates.

7.4.2 Elastic Interleaf Stiffness

The results of an elastic analysis of three different interleaf stiffnesses are shown in Figure 7.4. The 3400 MPa stiffness value corresponds to the modulus of the EPON 826/EPICURE 9551 epoxy system.

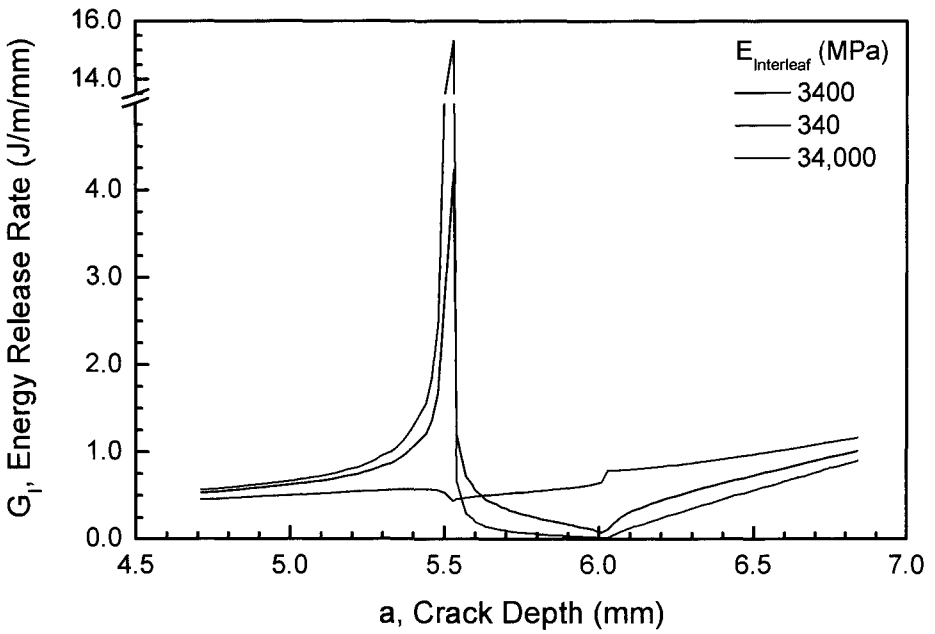

Figure 7.4: Variation of elastic energy release rate results for a 0.5 mm thick interleaf of three stiffnesses.

It is observed that the basic trend for the soft interleaf is a rapid increase in the energy release rate as the crack tip approaches the soft interleaf ($E_{Interleaf}$ = 340, 3400 MPa) followed by a rapid decrease to a minima as the crack passes through the interleaf. The energy release rate then steadily increases as it progresses away from the interleaf. This trend is reversed when the stiffness of the interleaf is greater than the surrounding laminate (E_2 = 20,832 MPa) as is the case for $E_{Interleaf}$ = 34,000 MPa.

It is shown that for both interleaves of lesser and greater stiffness than the surrounding laminate there is a maxima and minima in the energy release rate as a result of the crack interacting with the interleaf. The magnitude of these values is affected by interleaf stiffness. The low stiffness interleaf, E = 340 MPa, produced the highest maximum value, approximately 15.4 J/m/mm, and the lowest minimum, less than 0.010 J/m/mm. Thus, the crack is expected to propagate rapidly to the interleaf but then be arrested in the very soft interleaf. It must be noted that an interleaf modulus of 340 MPa is lower than that of polyethylene and would provide little load transfer. The effect of this low stiffness may be similar to the condition of poor bonding described in Chapter 5.

For the interleaf stiffness of 3400 MPa the maximum achieved is 4.23 J/m/mm and the minimum value is 0.078 J/m/mm. When the interleaf modulus is raised to 34,000 MPa the maximum drops to 1.16 J/m/mm and the minimum increases to 0.433 J/m/mm. However, as the stiffness of the interleaf becomes larger than E_2 of the surrounding 90° layers, the energy release rate trend reverses. The energy release rate now drops as the crack tip approaches the interleaf and increases in value as it passes through the interleaf. The rapid increase in energy release rate corresponds to the reduction in the ligament thickness of the high modulus interleaf and thus a rapid reduction in the model stiffness. The drop in G_I as the crack tip passes through the soft interleaf occurs because the crack is propagating but the change in model stiffness is small.

7.4.3 EPON 826/EPICURE 9551 Epoxy Viscoelastic Interleaf

This section provides the results for an interleaf material identical to the matrix of the composite layers. This is similar to studying the effect of a resin rich layer on the crack progression. Since the material response is now nonlinear and dependent on time, as well as the stress/strain state, the effect of crack growth rate and initial crack conditions, and the applied load must be investigated.

7.4.3.1 Crack Growth Rate

The results of varying the delay time between crack propagation steps are shown in Figure 7.5.

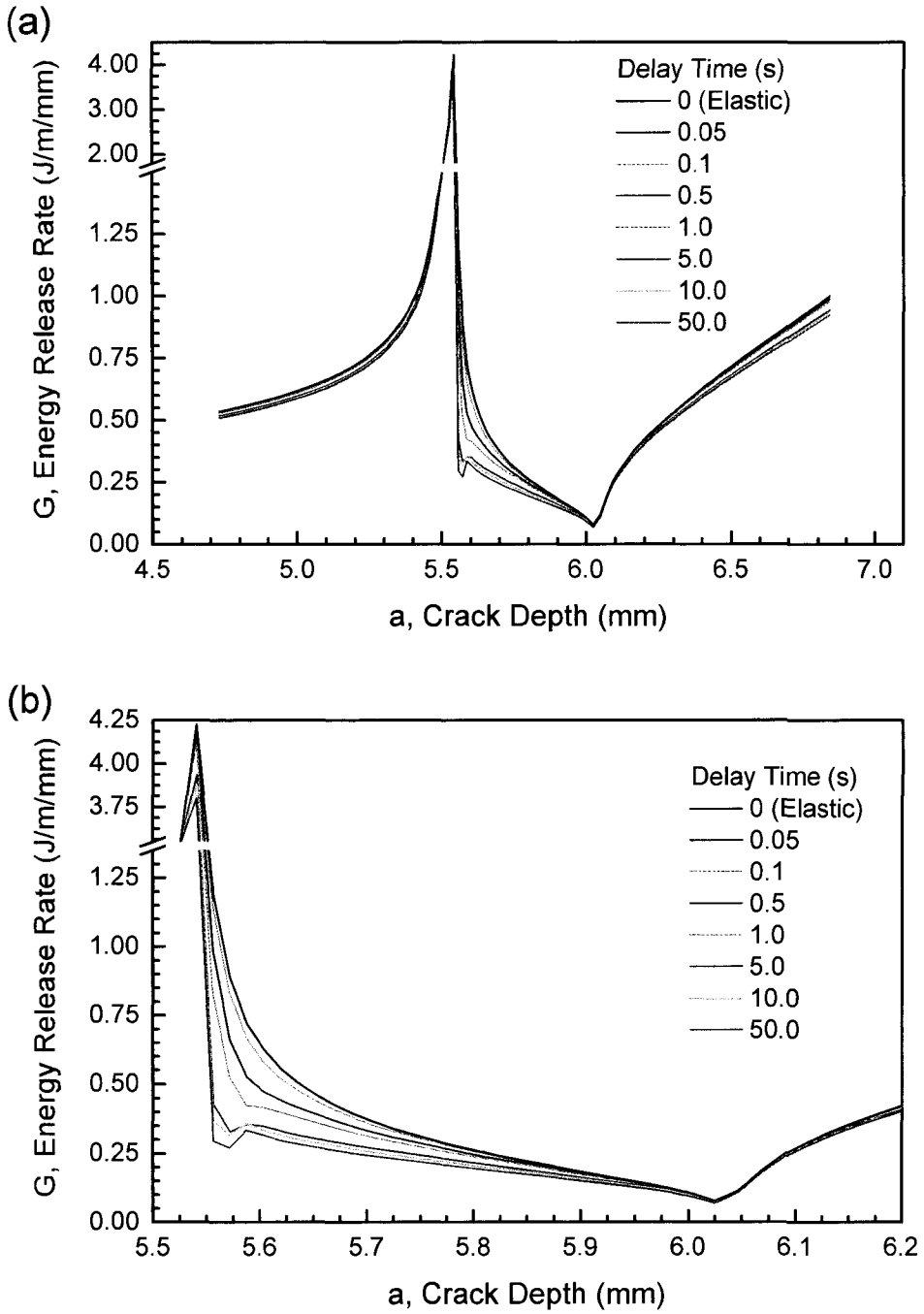

Figure 7.5: Viscoelastic energy release rate results for a 0.5 mm thick EPON 826/EPICURE 9551 interleaf with various delay times to produce different crack propagation rates. (a) Full results. (b) Enlarged to differentiate decrease of energy release rate for delay times.

This analysis was done on the standard 0.5 mm thick interleaf of the EPON 826/EPICURE 9551 resin system. Also shown is the elastic result and it should be noted that the vertical axis has been broken so that the results within the interleaf may be differentiated but the elastic peak, of significantly high magnitude, is also shown.

As the delay time is decreased, the solution approaches that of the elastic analysis. As the time is increased, the amount of creep strain and stress relaxation around the crack tip, after a crack propagation step, increases and the strain energy release rate is lower. However, the creep strain/stress relaxation saturates quite quickly in this material system and the results for crack growth delays of five seconds and greater are very similar. It must be observed that both the maximum and minimum points of the energy release rate curves decrease as the delay is increased. Therefore a slowly propagating crack is more likely to be arrested than a rapid crack advance. While the difference between the curves is quite large between the maxima and minima as the crack tip exits the interleaf, the difference at the minimum value is very small. The range in minima values is from 0.078 J/m/mm from the elastic solution to 0.067 J/m/mm when a 50 second delay is imposed between crack steps.

7.4.3.2 Initial Saturation Time

Another factor that arises from the viscoelastic analysis is the effect of load history on the material. Creep strains increase and stresses relax as time progresses at a fixed load and when time becomes large, they converge to a fixed value. Therefore it is important to understand how such a time history affects subsequent crack propagation and this is done by applying the global load followed by a period in which the creep strains and stress relaxation may saturate for a specified time as described in Section 7.2.2. The results for three saturation times at two crack delay times are provided in Figure 7.6.

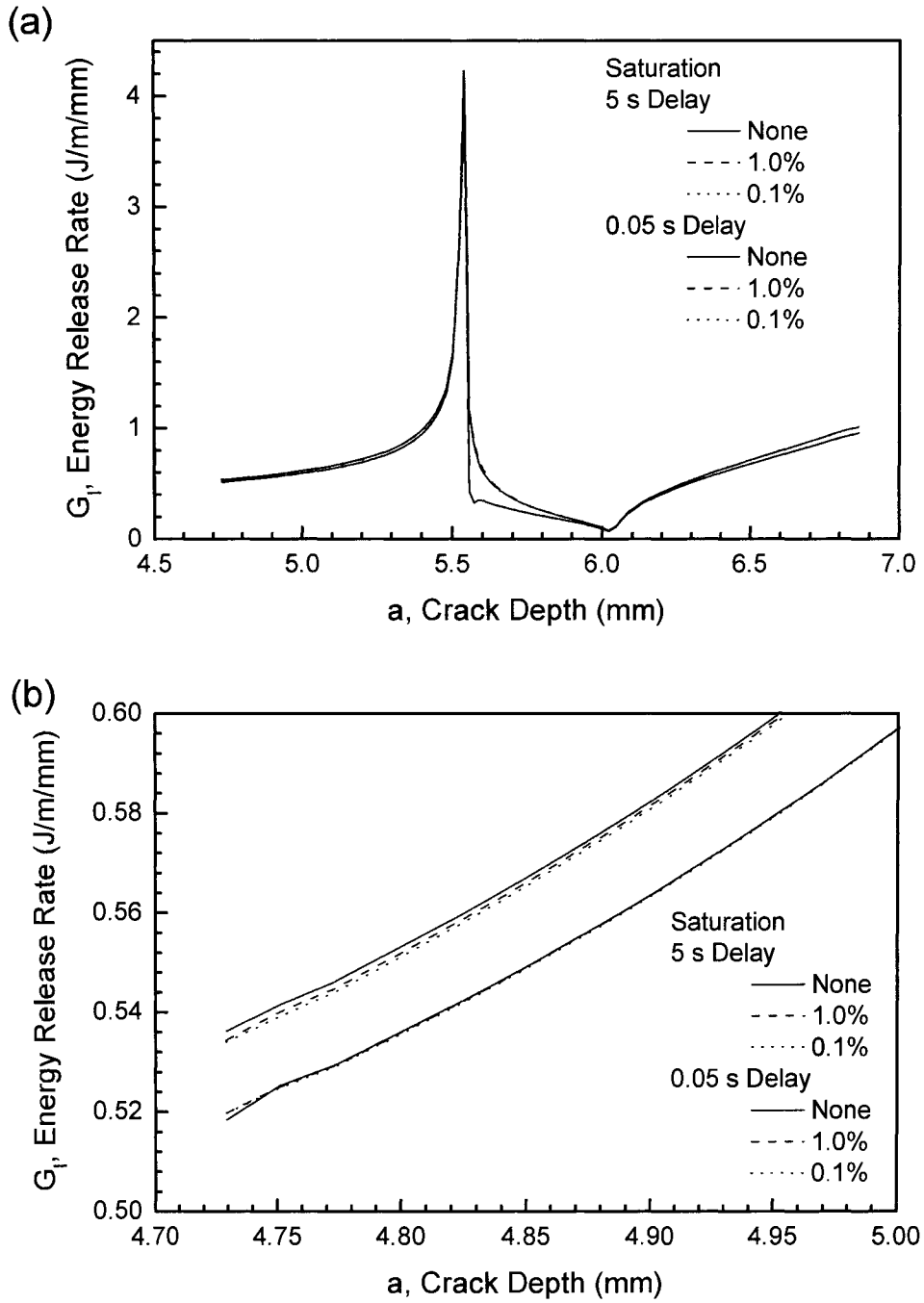

Figure 7.6: Effect of initial saturation on viscoelastic energy release rate results for EPON 826/EPICURE 9551 interleaf with crack propagation delays of 0.05 and 5 seconds. (a) Full solution set. (b) Enlargement of initial solution steps.

The three creep saturation requirements: no saturation, 1.0% and 0.1% correspond to times of 1, 26 and 172 s. At 26 s the creep displacement in the global y direction in one

second is less than 1.0% of the accumulated creep displacement. This value drops to below 0.1% after 172 s.

It is observed that for a slow crack growth rate, with a delay of five seconds, there is no observable difference after the first few crack steps. The delay time allows for the viscoelastic materials to nearly saturate within that period and the previous history is quickly erased. When the delay is decreased to 0.05 s the difference in saturation is evident by how slowly the three curves converge to a common response, based on the number of crack growth steps. Time, creep and relaxation accumulate comparatively slowly at such a quick crack propagation rate,. However, the effects of the variable saturation time are eliminated after a crack travel of approximately 0.6 mm and are well dissipated by the time the crack tip intercepts the interleaf. There is only minimal difference on the impact of the interleaf on the energy release rate. Therefore it is concluded that the amount of saturation prior to starting the crack is of relatively low importance since its effect is very local in time and crack length for this interleaf material. For other materials with significantly larger time constants, τ_1, the length of saturation time may be more important.

7.4.3.3 Stress Level

The nonlinear viscoelastic material model for both the composite layers and the interleaf are dependent on the stress state. In the transversely isotropic model the creep moduli are a function of an effective matrix stress which is calculated from the stress applied to the homogenised material element (see Chapter 6). Therefore, the creep strain and stress relaxation in the lamina will be dependent on the applied global stresses and the strain energy release rate may become a function of the stress state. This is also true for the interleaf materials modelled by the isotropic viscoelastic model in which the creep moduli are dependent on the von Mises equivalent stress.

Figure 7.7 shows the strain energy release rate for crack growth under global loads of 15, 25 and 35 MPa. As the stress is increased, the values of both the maxima and minima are increased. The strain energy release rate at the start of crack propagation is different for

the three loads due to different states of stress and strain near the crack tip due to the development of creep strain and stress relaxation. It is observed that the curve for a 15 MPa stress is much different than those for 25 and 35 MPa.

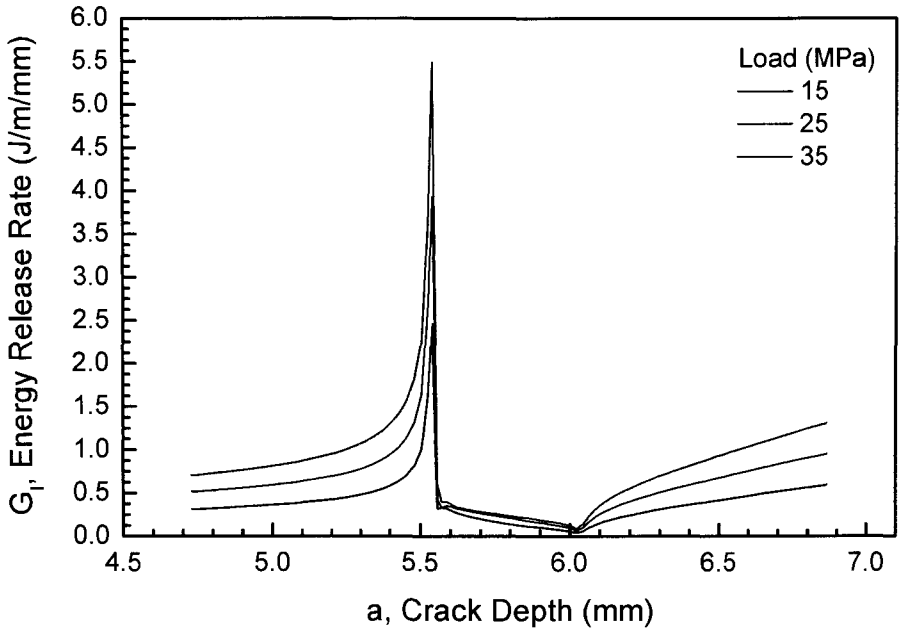

Figure 7.7: The influence of applied load on the strain energy release rate.

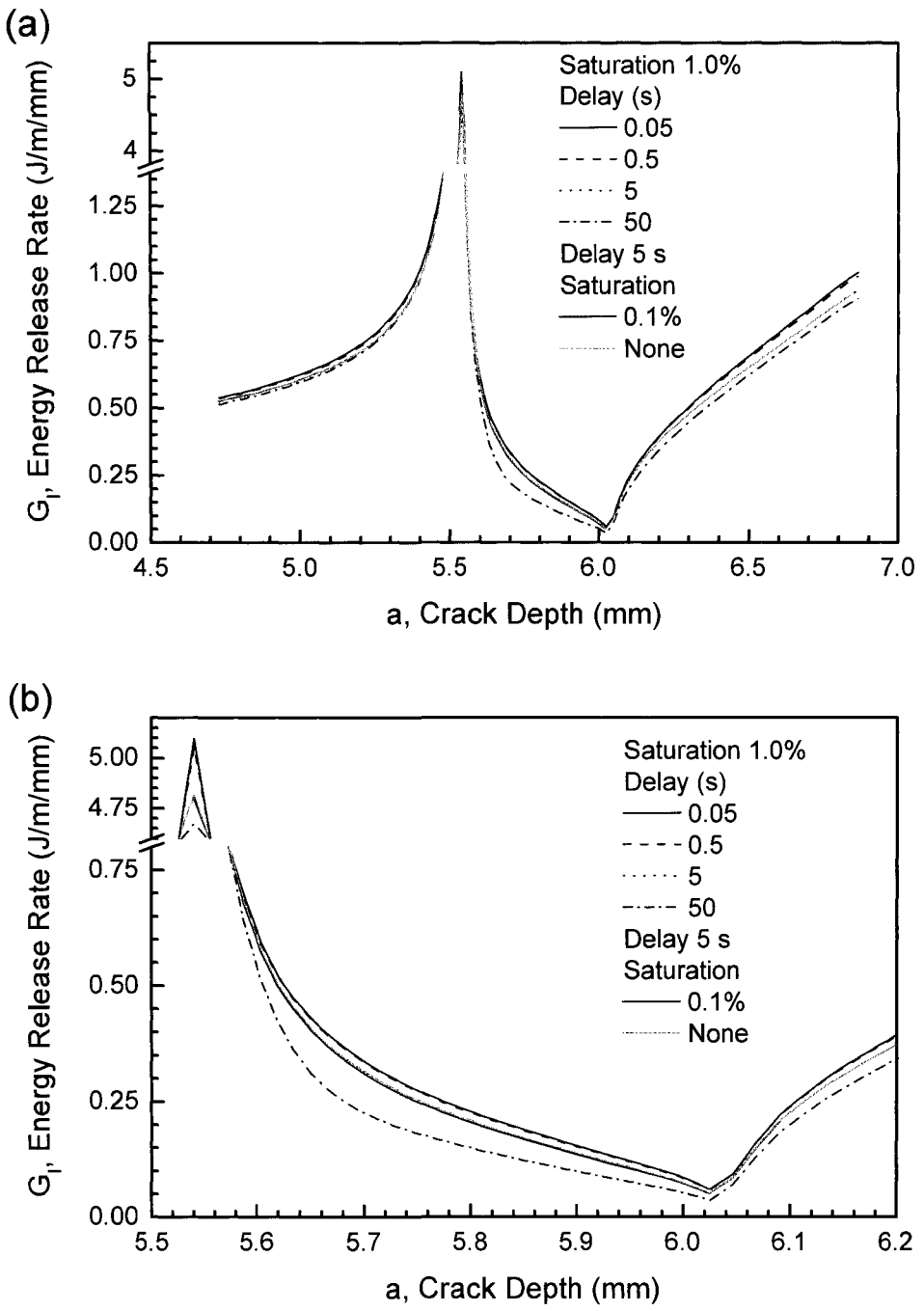

Figure 7.8: The variation of the minimum energy release rate for different crack increment delays, corresponding to three different crack growth rates in a laminate with a ColdCure epoxy interleaf. (a) Entire set of results. (b) Close-up of interleaf region.

7.4.4 ColdCure Epoxy Viscoelastic Interleaf

The strain energy release rate results for a cross-ply laminate with a ColdCure interleaf are provided in Figure 7.8. The results were generated using a laminate model with a 0.5 mm thick interleaf located 25 plies below the surface and an applied load of 25 MPa. Curves are provided to show the effect of increasing the delay between crack tip propagation steps and the influence of initial creep strain/stress relaxation saturation time.

Similar trends to that of the EPON 826/EPICURE 9551 epoxy interleaf are displayed. A maximum is encountered as the crack tip enters the interleaf and a minimum is found as it leaves the interleaf. The maximum achieved for a delay time of 0.05 seconds is approximately 5.10 J/m/mm and this converges rapidly down to approximately 4.68 J/m/mm as the delay time is extended to 50 seconds. Similarly, the minimum decreases from 0.059 J/m/mm to 0.036 J/m/mm.

The change in the initial saturation time from 1 second to 155 seconds has little impact on the strain energy release rate curve other than at the start of crack propagation. There is no appreciable change in the minimum value while the maximum changes by less than 0.01 J/m/mm when the saturation time is increased from 1 to 155 seconds.

7.4.5 High Density Polyethylene Viscoelastic Interleaf

Figure 7.9 shows similar results for the thick laminate with a high density polyethylene interleaf. Curves are provided for crack propagation delay times of 0.05, 0.5, 5 and 50 s and initial saturation times of 1, 52 and 166 s.

A maximum is achieved as the crack enters the interleaf. The maximum value drops from 8.26 to 8.14 J/m/mm as the delay time is increased from 0.05 to 50 s. The minimum value found as the crack tip exits the interleaf drops from 0.041 to 0.013 J/m/mm as the delay time is increase from 0.05 to 50 seconds. There was little dependence of the values on the initial saturation time. The minimum showed change in value of less than 0.001 J/m/mm, while the maximum changed by less than 0.017 J/m/mm.

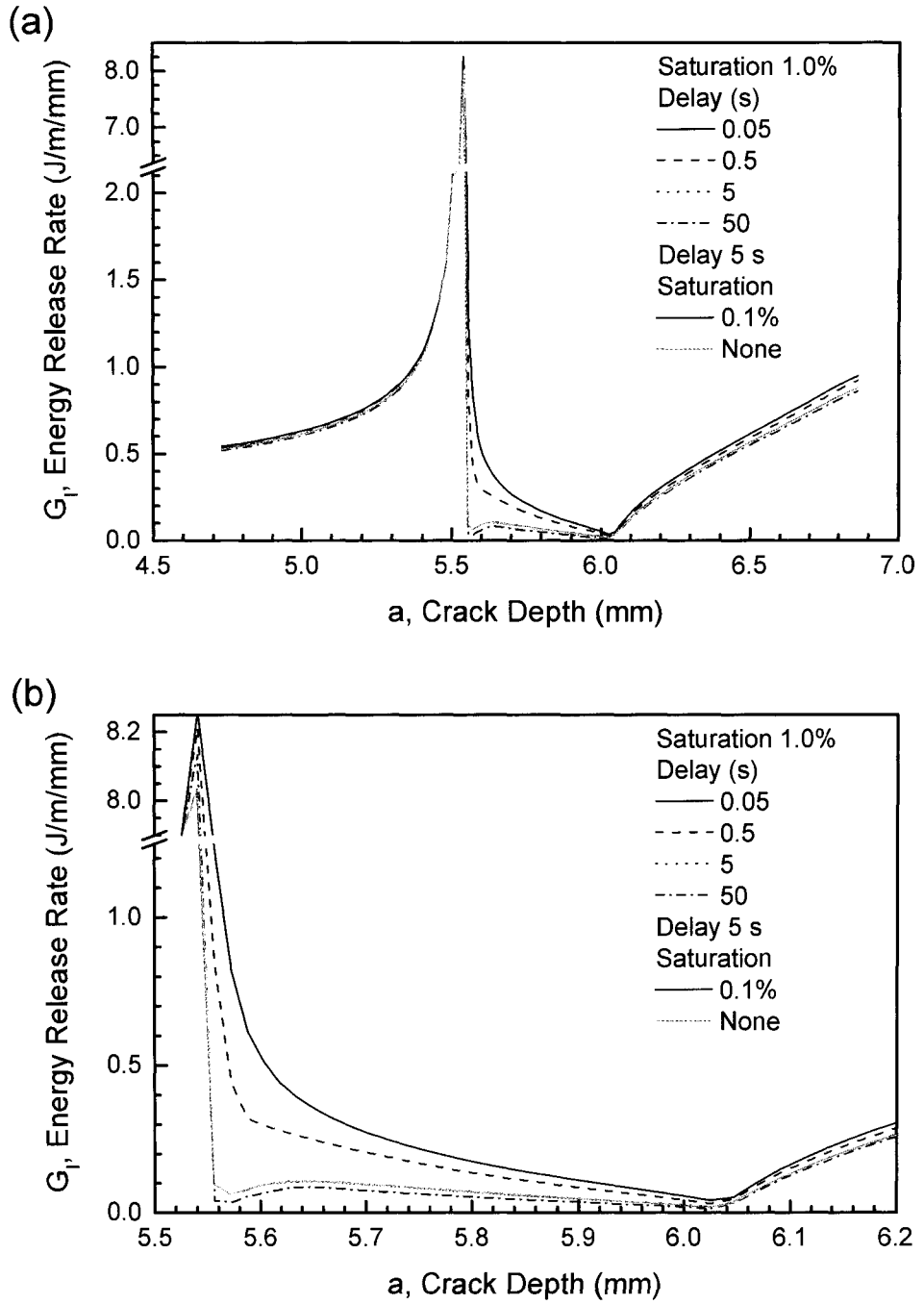

Figure 7.9: The variation of the minimum energy release rate for different crack increment delays, corresponding to three different crack growth rates in a laminate with a polyethylene tape interleaf. (a) Complete set of results. (b) Interleaf region enlarged to show detail.

As the length of delay between crack propagation steps was increased to 50 seconds the strain energy release rate dropped more rapidly as the crack tip progressed through the interleaf. This is a result of the great amount of creep strain and stress relaxation that can develop in the high density polyethylene.

7.4.6 Comparison of Viscoelastic Material Results

The three interleaf materials, EPON 826/EPICURE 9551, ColdCure and high density polyethylene, may clearly be compared through the strain energy release rate behaviour as a function of crack depth as well as the magnitudes of the maxima and minima that occur as the crack tip enters and leaves the interleaf, respectively.

There is a clear correlation between the interleaf stiffness and the recorded maxima and minima. As with the elastic analysis, the maxima increase and the minima decrease as the stiffness drops. Therefore the high density polyethylene produces the lowest minimum value and therefore the greatest likelihood of delaying or arresting the crack. The values of the minima, for the three materials, and their dependence on the delay time between crack growth steps is shown in Figure 7.10

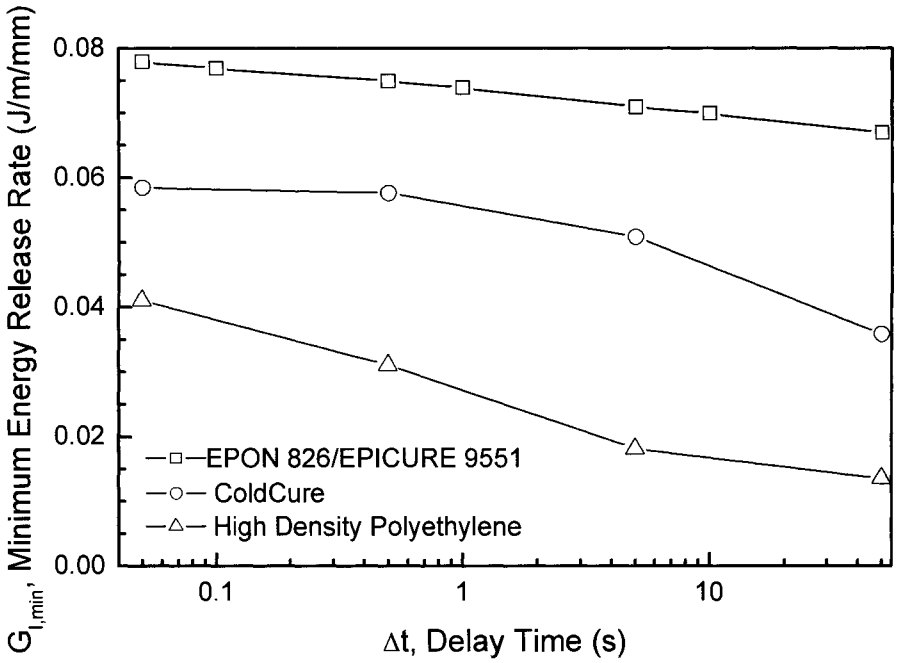

Figure 7.10: The variation of the minimum energy release rate for different crack increment delays, corresponding to different crack growth rates.

Figure 7.10 also indicates that the delay time has a similar influence on the minima values for all three interleaf materials. However, while there is difference in the minima, maxima and the behaviour within the interleaf, Figure 7.11 shows that away from the interleaf the behaviour is very similar. In this figure the interleaf is 0.5 mm thick and the crack is propagated under a 25 MPa load after a saturation period, such that the creep strain in one second was equal to 1% of the total creep strain, with a 5 s delay between crack steps. When the crack tip is not near the interleaf, the crack tip stress/strain field is predominantly determined by the properties of the 90° ply layers. It is in the crack tip zone that high stresses are developed leading to large creep strains and stress relaxation. When the crack tip has passed through the high density polyethylene interleaf the results are slightly lower than the other materials due to the much lower elastic modulus and greater creep strains. This large difference in the mechanical response of the interleaf produces only a small effect on the response of the laminate made up of 90° and 0° layers with much greater stiffnesses and creep moduli.

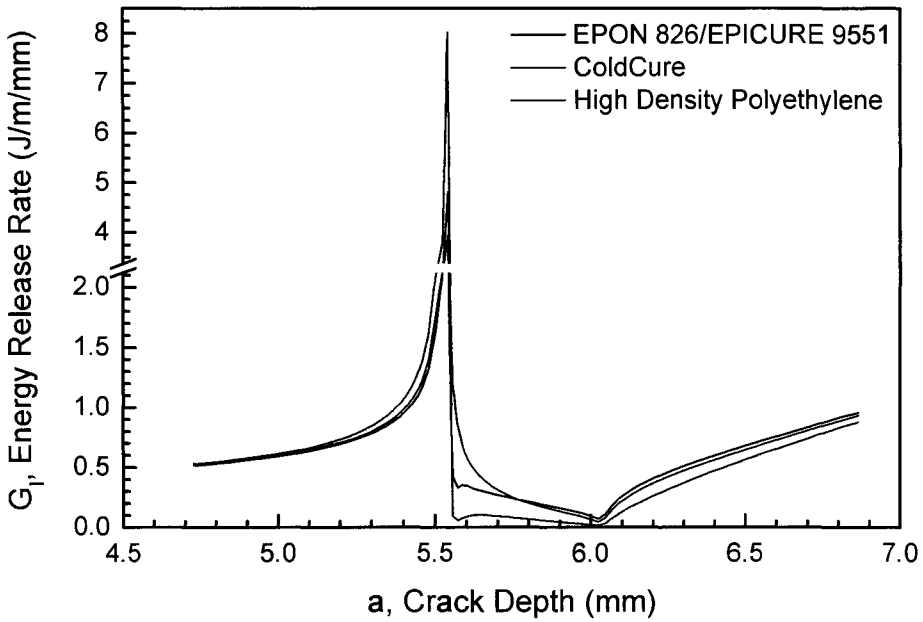

Figure 7.11: The strain energy release rate as a function of crack depth for the three interleaf materials.

Although the three interleaf materials have varying viscoelastic responses, Table 7.4 shows that changing the length of the initial saturation period has very little effect on the minimum value. The minimum value is important when considering crack arrest.

Table 7.4: The variation of the minimum energy release rate for four material models at three initial creep saturation states.

Interleaf Model	**$G_{I,min}$, Minimum Energy Release Rate (J/m/mm)**		
	No Saturation	0.1% Saturation	0.01% Saturation
EPON 826/EPICURE 9551 5 s Delay	0.0711	0.0710	0.0710
EPON 826/EPICURE 9551 0.05 s Delay	0.0776	0.0777	0.0772
ColdCure 5 s Delay	0.0511	0.0508	0.0494
High Density Polyethylene 5 s Delay	0.0182	0.0181	0.0179

Therefore, all three materials, having a lower stiffness than the 90° plies, show the rapid rise in strain energy release rate as the crack tip approaches the interleaf and the ligament

of composite layer decreases. A maximum strain energy release rate is reached as the crack progresses into the interleaf and the ligament is broken. Due to the low stiffness of the interleaf, there is little change in the global deformation as the crack progresses through the interleaf. Therefore the strain energy release rate rapidly drops and reaches a minimum value as the crack tip exits the interleaf. The strain energy release rate then begins to climb as the crack tip progresses through the remaining layer of 90° plies.

7.4.7 Interleaf Location

There have been several experimental studies on the importance of interleaf position within a laminate relative to laminate geometry and ply orientation. This is particularly true for studies concerning the use of interleaves to reduce or eliminate delamination.

In this investigation the laminate is thick and the emphasis is on arresting a transverse crack in the layer of 90° plies. It is logical to assume that, like cracks in bodies of a single, isotropic material, it is beneficial to stop a crack while it is small and the driving force, K, is relatively low.

This is verified in Figure 7.12 that shows the results of elastic analyses on models with the soft interleaf at various positions in the laminate. If the interleaf is applied as an external surface veil, there is little increase in the energy release rate as the crack propagates through the interleaf. The crack driving force increases more significantly as the crack propagates through the layers with 90° reinforcement. In the forward position (l_1 = 2.122 mm), it is seen that the maximum energy release rate achieved is much higher than that of the interior position used in the physical specimen. This suggests that the thin layer of 90° plies will fracture quickly. However the minimum energy release rate is lower than that of the interior position interleaf thus the crack is more likely to be arrested within the interleaf. The strain energy release rate for a model without an interleaf is shown for comparison with the response of the model of the specimen tested in Chapter 5.

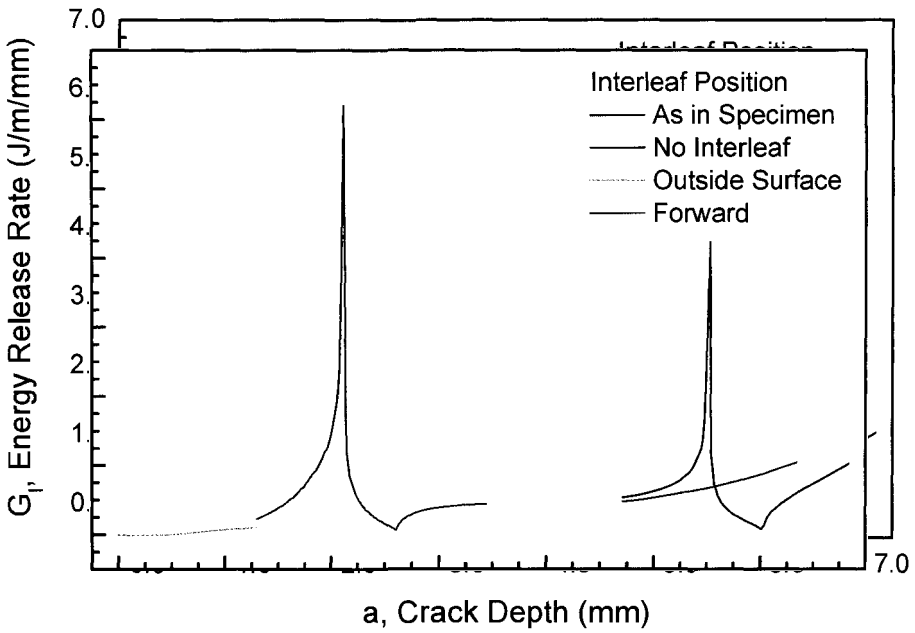

Figure 7.12: Elastic energy release rate results for a 0.5 mm thick EPON 826/EPICURE 9551 interleaf at outer surface of laminate, 2.122 mm from outer surface, 5.525 mm from outer surface (experimental coupon position) and through region experimental coupon position but when no interleaf is present.

Figure 7.13 shows similar results for viscoelastic analyses of models with a 0.5 mm thick EPON 826/EPICURE 9551 interleaf at various positions. The crack propagation was commenced after a 28 s saturation period, with a delay of 5 s between steps and under a load of 25 MPa. The results are similar to the elastic data however the maxima achieved when the interleaf is in the forward position is significantly reduced to a magnitude less than that when the interleaf is farther in the structure. The viscoelastic results continue to show reduced strain energy release rates due to the generation of creep strain and stress relaxation about the crack tip.

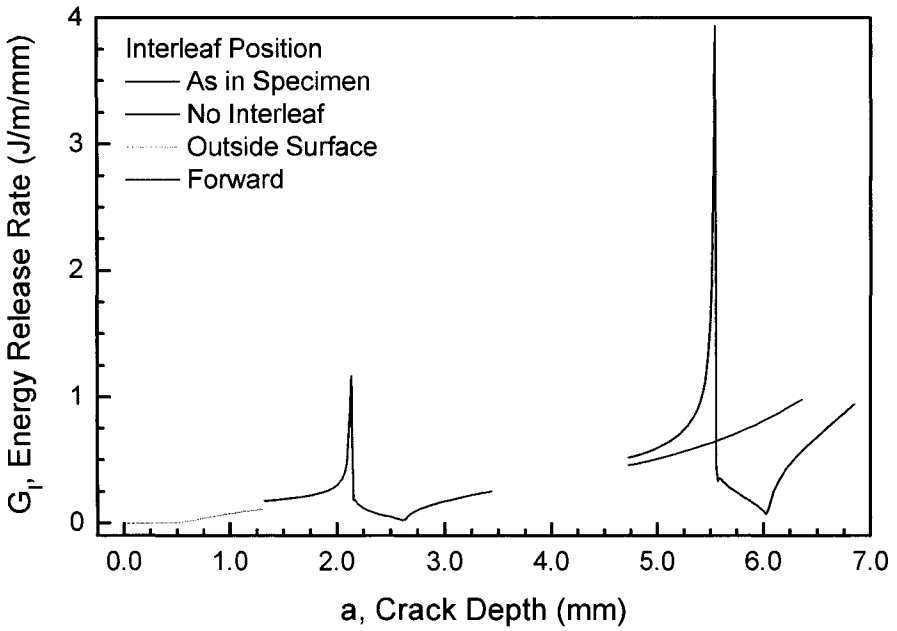

Figure 7.13: Energy release rate results from viscoelastic finite element analyses for a 0.5 mm thick EPON 826/EPICURE 9551 interleaf at outer surface of laminate, 2.122 mm from the outer surface, 5.525 mm from the outer surface (experimental coupon position) and through the region of the experimental coupon position but with no interleaf is present.

The results of the elastic and viscoelastic analyses confirm that positioning the interleaf on or near the surface of the specimen results in a lower minimum strain energy release rate at which the crack may be arrested. This would correspond to the interior surface of a tube containing interior pressure where cracks would initiate under greater levels of hoop stress and where the interleaf will be more successful as an impermeable barrier.

Note that it is not only the interleaf that is affecting the energy release rate but also the thickness of the 90° layer outside the interleaf. The change in compliance with thickness will have a significant impact on the behaviour of the energy release rate as the crack is propagated.

7.4.8 Interleaf Thickness

The second geometric parameter studied is the thickness of the applied interleaf. This is of importance since additional thickness leads to greater material cost and increased

weight and the associated costs. Models were analysed with interleaf thicknesses of 0.25, 0.5 and 1.0 mm, 25 plies below the surface as in the case of the tested coupon specimens. Elastic and viscoelastic results are provided in Figure 7.14 and Figure 7.15 respectively. In Figure 7.14 the elastic analysis was completed on an interleaf with a stiffness of 3400 MPa. The viscoelastic results shown in Figure 7.15 are for the EPON 826/EPICURE 9551 epoxy interleaf after a 26 s saturation period with a 5 s delay between crack steps under a 25 MPa load.

It is shown in the elastic analysis that there is only a slight dependence of the energy release rate minimum value on the interleaf thickness. The value drops from 0.095 J/m/mm for an interleaf 0.25 mm thick to 0.057 J/m/mm when it is increased to 1.0 mm thick.

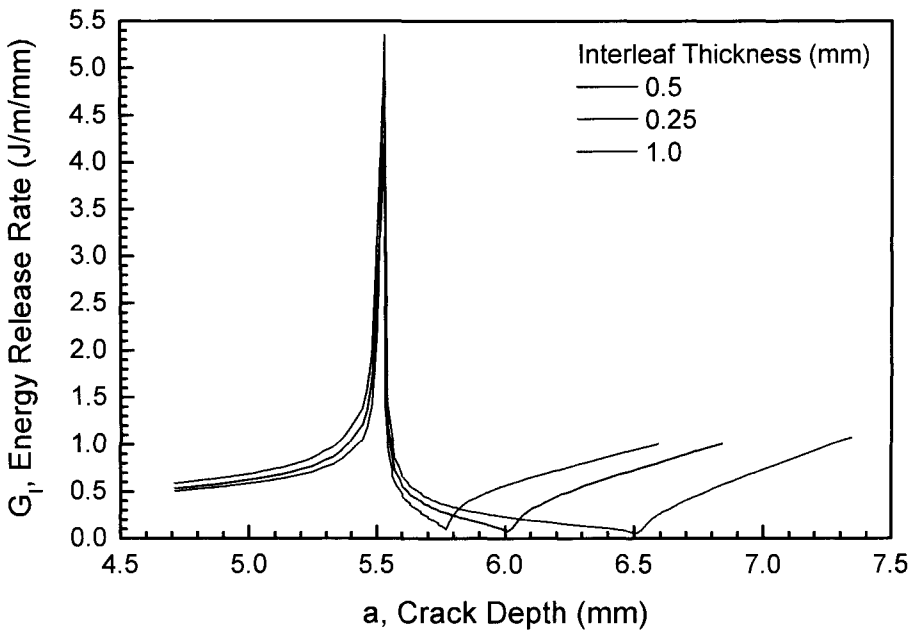

Figure 7.14: Elastic energy release rate results for EPON 826/EPICURE 9551 interleaves of 0.25, 0.5 and 1.0 mm thickness.

The viscoelastic analyses yield similar results but with the time dependent effect further reducing the magnitude of the recorded values. As the thickness is increased from 0.25 to 1.0 mm the strain energy release rate decreases from 0.080 to 0.053 J/m/mm. This drop is

relatively small and it must be considered if the cost of additional material is worth the minor gain in strain energy release rate reduction.

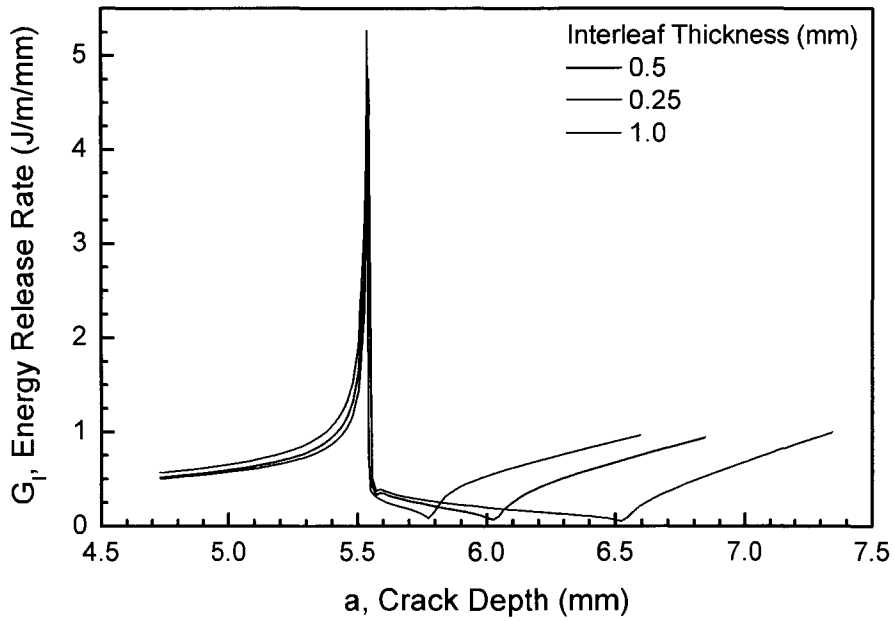

Figure 7.15: Viscoelastic energy release rate results for EPON 826/EPICURE 9551 interleaves of 0.25, 0.5 and 1.0 mm thickness.

7.4.9 Debonding at the Interleaf

It was discussed in Chapter 5 and observed in Figure 5.4 that the interface between the composite layers and the PE tape was weak and readily debonded. It was concluded that this debonding assisted in producing a delay in crack growth by producing a fresh surface in which a new crack must be initiated. Elastic and viscoelastic finite element analyses were conducted to investigate such debonding on the crack strain energy release rate. All aspects of the model and analysis are identical to that conducted for the solidly bonded PE interleaf discussed early in this chapter with the exception of the debonded zone. This zone, reaching 0.31 mm up the interface between the interleaf and the outer 90° composite layer is modeled by using separate overlapping nodes for the elements on each side of the interface. Thus the element faces may pull apart or shear along one another without friction.

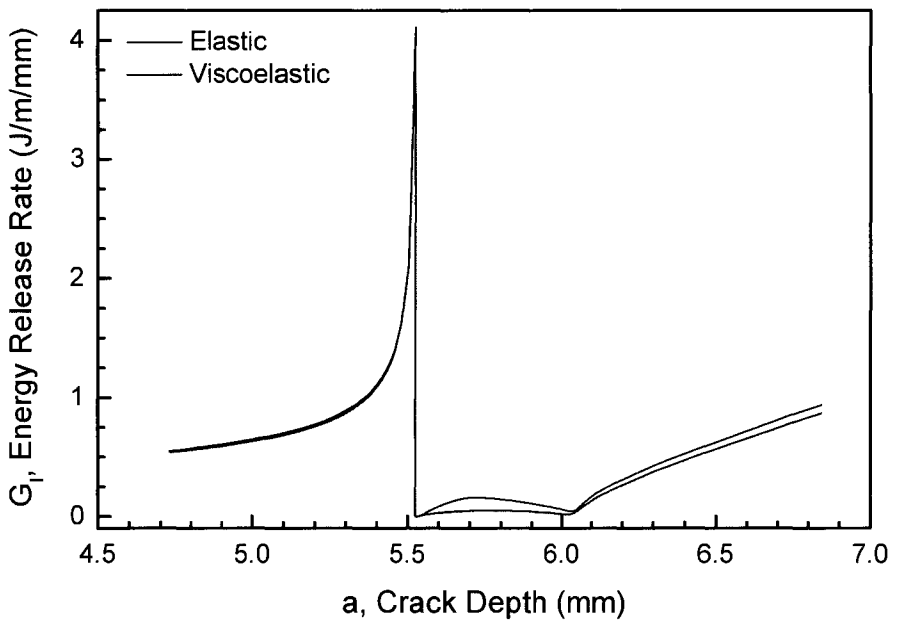

Figure 7.16: Elastic and viscoelastic strain energy release rates when debonding occurs at the composite/interleaf interface.

Figure 7.16 shows the effect of the interface debonding on the strain energy release rate as the crack is progressed towards and past the interface. As with previous analyses, the energy release rate increases as the crack approaches the interface due to the increasing compliance in the outer 90° composite layer. However, when the crack tip hits the defective interface the energy release rate immediately drops to zero. With no crack driving force crack propagation will stop. When the crack is continued along the same path, into the interleaf, the energy release rate slowly rises and then drops as the crack tip approaches the intact interface of the interleaf with the inner 90° composite layer. Here the energy release rate drops to 0.050 J/m/mm in the elastic analysis and 0.019 J/m/mm in the viscoelastic analysis. Therefore, the second, and intact, interface provides a resistance to further crack growth. It is observed that in this model the elastic and viscoelastic results are very similar except when the crack tip is in the interleaf.

7.5 SUMMARY OF FINITE ELEMENT ANALYSIS

Analyses using the nonlinear transversely isotropic model to simulate composite plies and a nonlinear isotropic viscoelastic model to represent the interleaf were completed to investigate the influence of interleaf mechanical properties and interleaf position and thickness. Elastic analyses were also done for comparison.

Three viscoelastic interleaf materials were compared; EPON 826/EPICURE 9551 epoxy system, ColdCure epoxy and high density polyethylene. The first of these is identical to the polymer matrix used in the composite laminate and therefore represents a resin rich layer. The three materials as listed, have decreasing moduli and the polyethylene shows a very large amount of creep strain under uniaxial load conditions. The numerical results clearly demonstrate that, when the interleaf is less stiff than the surrounding 90° plies, the strain energy release rate reaches a maximum as the crack tip enters the interleaf and a minimum value as the crack tip exits the interleaf. Furthermore, as the interleaf stiffness drops, the maximum increases and the minimum value decreases. This would correspond to a crack rapidly progressing to the interleaf but then being arrested or delayed by the soft interleaf. The energy release rate may be correlated to the change in the model stiffness as the crack progresses through the laminate. As the crack progresses through the relatively stiff 90° material the stiffness drops rapidly with every crack increment and the strain energy release rate increases. When the crack is progressing through the soft interleaf, the change in model stiffness is small and the strain energy release rate drops. It is shown that when the interleaf has a greater stiffness than the surrounding 90° plies the trend is reversed. The strain energy release rate decreases as it approaches the interleaf and increases while passing through the interleaf. It was also observed that the behaviour of the strain energy release rate when the crack is not near the interleaf is independent of the interleaf material and defined by the characteristics of the composite.

The viscoelastic response is shown to have an influence on the exact magnitude of the strain energy release rate. When doing the crack analysis using the nonlinear time dependent material one must consider the load history, load rate and load magnitude.

It is shown that the effect of a saturation period on subsequent loading is dependent on the rate of crack growth. For slow crack growth any influence of the prior history on the strain energy release rate dissipated after only a few steps. This occurs because creep strain and stress relaxation in the highly stress material near the crack tip tending form a common stress distribution over a defined period of time. The strain energy release rates recorded for the crack tip in the interleaf were not affected by variations in saturation time.

The rate of crack growth, as produced by a delay time between crack increments, was shown to have an impact on the energy release rate. As the delay time is decreased the strain energy release rate response approaches that of the elastic analysis, independent of time. When the time is increased, the results quickly converged to a single curve with little difference between delay times of 5 and 50 seconds. This indicates that the creep strains quickly saturate in the model and there is little change with increased time. This effect varies according to the viscoelastic properties of the model materials with the retardation time having a particular impact.

The viscoelastic models used have a creep modulus that is a function of the current stress state. Therefore it was expected that the strain energy release rate would depend upon the load under which the crack was propagated. As the load is increased the creep strains form rapidly and saturation is reached more rapidly. While the energy release rate curves under loads of 25 and 35 MPa are quite similar, the values have dropped when the load is decreased to 15 MPa.

It was found that as the interleaf thickness is increased, the minimum value as the crack tip exits the interleaf decreases. This is beneficial to the possibility of arresting the crack. However the advantage of increasing the thickness by four times is small and one must consider if this is worth the possible added cost of materials

A more likely means of improving the performance of the interleaf is to select the ideal location. Given this thick laminate with a large layer of 90° plies, changing the position within the laminate is simple and independent of ply orientation. It is clearly shown in

elastic and viscoelastic analyses that it is most advantageous to put the interleaf as close as possible to the crack origin. In fact, if the interleaf is placed on the outer surface of the laminate the energy release rate remains very near zero as the crack tip, with crack depth equal to zero, is forced through the interleaf. Once the crack has greater length, and the crack driving force is large, the magnitude of the strain energy release rate also becomes large.

It was further demonstrated that if the interleaf has debonded from the outer layer of composite, the crack strain energy release rate will drop to zero as the crack tip approaches and intersects the debond region. It is proposed that this is the effect observed during testing of the thick cross-ply specimens with the polyethylene tape interleaf in Chapter 5.

Therefore it is shown that an interleaf may successfully be implemented to influence the strain energy release rate and delay or arrest the crack. The most beneficial material is one that has low modulus to result in little change in structural stiffness as the crack grows. This, of course, means that the interleaf will provide little load transfer effectively separating structural elements should the load be poorly distributed between the structural layers. Such an interleaf should be placed as close to the crack origin and while adding additional interleaf thickness does show minor improvement it does lead to requirement of additional material. The viscoelastic behaviour of the interleaf and laminate is shown to have only a small impact on the overall performance and as the crack propagation speed is increased the crack driving force is increased suggesting that the crack growth rate will rise further.

CHAPTER 8 CONCLUSIONS

This investigation was conducted to determine the influence of an interleaf on the first failure of composite pipe. It was proposed that the additional interleaf would a) act as an impermeable barrier to a pressurised fluid and b) delay or possibly arrest matrix cracks. These mechanisms have been studied experimentally and numerically.

8.1 CHARACTERISATION AND THEORETICAL PROPERTIES OF $[\pm 60°_3]_T$ LAMINATE

Tubular composite specimens of $[\pm 60°_3]_T$ were fabricated, with and without a polyethylene tape interleaf, by the filament winding method in a controlled laboratory setting. The tension was carefully controlled to provide consistent consolidation and resulting material properties. The tubes were subsequently tested under biaxial stress conditions by applying an internal pressure and tensile/compressive axial load in a modified material testing system.

A burn-out test of the laminate found that it was 72.69% fibre reinforcement and 1.68% voids by volume fraction. This value of reinforcement volume fraction is high for composite components. While the high percentage of fibre will lead to great strength in direction parallel to the fibre axis, the resistance to transverse cracking may be reduced by the high stress/strain concentrations between the tightly packed fibres. The low volume fraction of voids is consistent with a component filament wound under tight quality control.

The mechanical properties of the specimen were determined for the laminate using empirical and numerical techniques. The mechanical properties of a ply were calculated using the Halpin-Tsai equations, and its modifications, and a finite element representative volume element technique. The results of these two methods were found to be very similar. It was noted that the elastic response of a hexagonal fibre packing array are transversely isotropic where as the square packing periodic array is not. The ply properties were then used in the classical laminate theory to predict the two-dimensional properties of the laminate. The extension to three-dimensions, presented by Kollar and Springer, was used to predict the through-thickness mechanical properties of the

laminate. Values calculated by the classical laminate theory were in close agreement with the experimentally determined values for moduli. The Poisson's ratio is more difficult to measure due to the sensitivity to error in strain measurements in the small linear zone of loading. A representative volume element of the [±60°] laminate was then constructed from simple cubic unit cells and analysed by the finite element method. It was found that the results of this approach were not as reliable as those of the classical laminate theory when compared to the experimental data. This is concluded to be a result of the anisotropy of the simple cubic unit cell derived from an assumed square fibre packing array.

It was observed that the fabricated filament wound tubes had a resin rich outer layer. This is the result of resin leaching due to consolidation by fibre tension during winding and curing. Inclusion of this resin layer in the classical laminate calculation resulted in even closer agreement with the measured moduli but had little impact on the Poisson's ratio.

Residual stresses and strains, due to the difference in the coefficients of thermal expansion of the glass fibre and epoxy matrix, may be a large proportion of the failure stress/strain. The coefficients of thermal expansion of the plies and laminate were calculated using empirical techniques. The thermal strain mismatch between the plies and laminate are found to produce ply stresses of $\sigma_1 = -14.5$ MPa, $\sigma_2 = 14.5$ MPa and $\tau_{12} = 8.4$ MPa.

8.2 $[\pm 60°_3]_T$ TUBULAR MULTIAXIAL STRESS-STRAIN RESPONSE AND FIRST FAILURE ENVELOPE

The tubular composite specimens were tested under various ratios of internal pressure to axial tension/compression. It was found that the first failure modes could be divided into five broad categories: axial collapse, weepage, local leakage, burst and crush.

The axial collapse occurs under axial dominated tensile loads and is a catastrophic failure of the matrix leading to a dominant helical crack with fibre fracture. Weepage is described as the slow loss of the pressurisation fluid first showing as the formation of droplets uniformly distributed on the exterior of the specimen. This was the observed first

failure mode under a stress ratio of 2:1. Local leakage was noted for stress ratios between 2:1 and 7:1 and it is characterised by weepage near the ends of the gauge length and jets of fluid resulting rapid loss of pressure retaining capacity. This failure mode is associated with local damage due to stress concentration and manufacturing defects, made more severe by high internal pressure opening the matrix cracks.

Under the 7:1 stress ratio the specimen burst at a high hoop stress consistent with a fibre failure. Under this load condition the axial strains in the specimen are compressive so any matrix cracks are kept closed. A similar failure is observed under pure hoop stress loading but the axial strains are more compressive and global fracture may be related to a shear failure of the matrix as this part of the failure envelope may be bounded by an in-plane maximum shear criterion.

All tests with applied axial compressive stress showed an indication of crush damage with characteristic intersecting helical cracks. Failure under axial compression appears to be the result of compression of the matrix leading to the formation of kink bands and fibre failure. Fibre buckling may occur under the axial compression dominated stress ratios although the applied compressive stress in the initial fibre orientation was generally very low under all of the tested stress ratios

Failure envelopes in the stress and strain planes clearly show the anisotropic response of the laminate. The reinforcement is predominantly wound in the hoop direction and the tubes are much stronger under hoop stress load conditions. Transformation of the strains to the ply coordinate system shows that the failure strains are enclosed by a maximum strain criterion. This criterion, however, overestimates the maximum strength when local leakage and axial compressive failures occur.

Transformation of the stresses to the ply coordinate system yields an average stress distributed over the $\pm\theta$ layers. The classical laminate theory, based on a linear elastic material response, may be used to differentiate the stress in the principal ply directions however this is shown to be particularly inaccurate under compressive axial loads where

a large amount of nonlinearity is observed due to a much large failure strain than under tensile axial stress.

8.3 ADDITION OF A POLYETHYLENE TAPE INTERLEAF

The influence of a polyethylene tape interleaf on transverse cracking and fluid containment was experimentally tested on coupon and tube specimens. The coupons were specifically designed to study the effect of the interleaf on the progression of a transverse crack. The tubular specimens provide an indication of the interleaf effect on damage under multiaxial stress states but also if the interleaf will contain the pressurisation fluid once the damage has penetrated the interior composite layers.

The coupon specimens were loaded under fatigue loading at a constant stress amplitude with a minimum stress of approximately zero. Progression of the crack was monitored by measuring the stiffness via the slope of the hysteresis loops. It was consistently found that the crack rapidly propagated to the interleaf, stopped for a number of cycles, and then rapidly jumped from the interleaf to the interior layers of the specimen. The crack propagation delay was found to be a greater number of cycles at lower stress amplitudes.

Upon examination of the failed specimens it was noted that often the plane of the second crack propagation event did not coincide with that of the initial crack. It is concluded that the initial crack event terminates at the weakly bonded interleaf and that a new crack is then initiated in the fresh composite surface on the opposite side of the interleaf. This was later verified by a viscoelastic analysis of the crack approaching the debonded interleaf that showed the strain energy release rate will drop to zero at the debond.

To determine the influence of an interleaf on the tube failure strength and mechanism, a polyethylene tape interleaf was added between the first and second ±60° composite layers. Structural collapse and weepage were found to occur at similar strengths as the specimens without an interleaf. The similarity of structural failure stresses may be expected as the interleaf adds little to the axial strength. Weepage occurred due to slippage or tearing of the interleaf under relatively large axial deformations.

For the fixed end condition loading, which resulted in failure by local leakage in the tube without an interleaf, the failure mode became a burst because the interleaf did successfully perform as a barrier. This was the only case where the interleaf contributed to a greater strength than the tube without an interleaf.

At the 7:1 stress ratio it was clearly demonstrated that failure of the internal structural layer occurred first allowing for the pressurised fluid to fill an annular space inside the interleaf. This separation of the structural elements led to a drop in the stiffness as the internal structural layers became ineffective producing a corresponding reduction in failure strength. While the stiffness dropped by about one third, the ratio of internal structure, the hoop strength was reduced by only one fifth. Under pure hoop stress, the failure strength was very similar to that of the tube without an interleaf. This load condition produces compressive axial strains in the tube which tend to prevent transverse cracking and close cracks that do occur. Therefore, it may be expected that the interleaf will not have a large impact on the strength under pure hoop stress loads.

It was concluded that the interleaf may be most successful at stress ratios where failure is by weepage or localised leakage. However, the tested interleaf was subject to slippage or tearing under moderate axial deformations leading to failure by weepage at the 2:1 stress ratio. At higher hoop stress ratios the interleaf debonded from the inner structural layers leading to only the outer composite layers retaining the pressure load. This resulted in a reduction of strength. Improvement of interleaf bonding and toughness to axial tensile strain will improve performance.

8.4 VISCOELASTIC ANALYSIS OF TRANSVERSE CRACK PROPAGATION IN A THICK CROSS-PLY WITH AN INTERLEAF

To investigate the effect of an interleaf on the progression of a transverse crack through a laminate, a new transversely isotropic nonlinear viscoelastic material model was formulated to represent the composite plies in a finite element analysis. The model is simplified by assuming an isotropic viscoelastic response in directions perpendicular to the reinforcement axis and that no creep deformation occurs along the axis of the reinforcement. Therefore two constants and two equations for creep modulus, as

functions of effective matrix stress, were required. The material model was calibrated using a representative volume element for a hexagonal periodic array implementing a previously formulated isotropic nonlinear viscoelastic response for the matrix material. During calibration it was noted that the creep response was not precisely transversely isotropic. The Poisson's ratios used in the viscoelastic derivation are identical to the elastic values but may be eliminated from the creep response by implementing individual creep moduli functions for each component of the compliance matrix.

The geometry modelled was identical to the tested coupon specimens with plane-strain assumed through the coupon thickness. Boundary conditions were applied to enforce symmetry and load conditions but were removed, node by node, to simulate crack propagation. A fine mesh was used along the crack tip path to adequately represent the large stress/strain gradients within the vicinity of the crack tip.

Three interleaf materials were used; EPON 826/EPICURE 9551 epoxy, ColdCure epoxy and high density polyethylene. All are suitable candidates for use as an interleaf material. EPON 826/EPICURE 9551 was also used as the matrix material in the composite component therefore using this material for an interleaf is similar to modelling a resin-rich layer. Analyses were conducted to investigate the influence of material properties, viscoelastic properties, and interleaf geometry.

From the analyses it was found that when the interleaf has a lower modulus than the surrounding material the energy release rate rapidly rises as the crack tip approaches the interleaf and then rapidly drops to a minimum as it exits the interleaf. The energy release rate then consistently rises as the crack tip moves away from the interleaf. When the interleaf has greater modulus than the laminate the reverse trend is observed.

From the three interleaf materials analysed, EPON 826/EPICURE 9551 epoxy, ColdCure epoxy and high density polyethylene, it was found that the polyethylene, with a low modulus and low creep modulus, produced the lowest strain energy release rates and is most likely to arrest the crack. Unfortunately polyethylene has a low reactivity leading to poor bonding characteristics that results in minimal load transfer to the outside structural

layers. This was observed in the experimental tests of Chapter 5. However, it is shown numerically that as the crack tip intersects the debonded region the strain energy of release rate drops to near zero. The difference between the three viscoelastic interleaves is demonstrated when the crack tip is near and in the interleaf. When it is away from the interleaf, the behaviour is dominated by the surrounding composite layers and the energy release rates are similar.

The difference in the modulus of the three interleaf materials accounts for the range of minima and maxima. Decreasing interleaf modulus from EPON826/EPICURE 9551 to polyethylene leads to increasing maxima and decreasing minima. The variation in viscoelastic properties is most evident in the shape of the strain energy release rate curve where the crack tip is inside the interleaf. A lower creep modulus contributes to a more rapid drop of the energy release rate from the maximum value encountered as the crack tip enters the interleaf. Use of the nonlinear viscoelastic model introduces new parameters that must be considered; load history, stress level and crack growth rate.

The effect of history was analysed by applying various times between the application of the external load and initial crack propagation to allow the creep strains and stress relaxation to saturate. It was observed that the time of saturation did influence the strain energy release rate over the first number of crack propagation steps but in this analysis the effect had dissipated by the time the crack tip encountered the interleaf. The effect was found to dissipate in fewer crack steps when the propagation was slower providing time for creep straining/stress relaxation during crack growth and is dependent on the retardation time constant of the material.

The strain energy release rate is also affected by the load magnitude. Lower applied stress led to lower strain energy release rates but it was observed for the EPON 826/EPICURE 9551 epoxy system that the energy release rate values quickly converged as the load is increased due to the exponential relationship of the creep modulus to the stress state.

The crack growth rate was found to strongly influence the energy release rate. As the time between crack tip propagation steps was increased, the energy release rate curves

converged to a single curve of low magnitude. As the crack growth rate was increased, the solution approached that of an elastic analysis. It is interesting to note that while the rate has a large effect on the maximum achieved as the crack tip enters the interleaf, the change in the magnitude of the minimum is much smaller. The influence of the delay time implemented to control crack growth rate is dependent on the retardation time constant of the material. Materials with larger time constants require a greater amount of time to reach stress relaxation and creep strain saturation. However it is the magnitude of the creep moduli that will determine the scale of the final effect.

The polyethylene interleaf is found to be most promising interleaf material in terms of arresting (or delaying) transverse crack propagation. The low modulus and large creep strains lend to a very low strain energy release rate as the crack tip traverses the interleaf. This, of course, does not account for the poor bonding characteristics of the polyethylene observed in experimental analyses. However, a similar numerical analysis has shown that when the crack tip intercepts a debonded region, the strain energy release rate will drop to near zero.

Furthermore, it is shown that increasing the interleaf thickness by four times has only a minor influence on the minimum strain energy release rate observed. It may be questionable whether the expense of added material is worth the slight benefit. Location of the interleaf is shown to have a much larger impact. It is clear that it is beneficial to intercept the crack when it is small and has low "driving force". If the cracks are known to initiate from one surface, then the interleaf should be placed near the surface. This suggests that multiple intermittently spaced interleaves may be useful if transverse cracking is occurring within the structure.

8.5 TOPICS FOR FURTHER STUDY

While research is performed to find understanding, it is well known that research inevitably uncovers new questions. Certainly the topics of this investigation have provided insight to better techniques and future challenges. These will be addressed as divided into the natural sections; production and testing of filament wound tubes with and

without an interleaf, the interleaf as a crack arrest device in a laminate and the viscoelastic analysis of a laminate with an interleaf.

8.5.1 Filament Wound Tubes With and Without an Interleaf

The variables of filament winding are known to have a significant impact on the final composite part quality and mechanical properties. Many properties have been studied with respect to structural failure strength but few consider the impact of these variables on weepage. For example, increased fibre volume fractions are known to increase structural strength. It is expected that increased fibre volume fractions will lead to decreased weepage strength due to higher stress/strain concentrations in the matrix. It would be an advantage to quantify these relationships although it is difficult to manufacture components of varying volume fractions.

With regard to application of an interleaf in wet filament winding, it has been revealed that this is a difficult task. The multiple-cure process employed is not ideal as it contributes to the segregated structure observed. Other materials used in winding trials showed that: a) use of a thin film, whether thermoplastic or thermoset, is impractical due to the development of resin pockets under the film; and b)Wet resin interleaves will be displaced and mix with the matrix when over wrapped with tensioned fibres.

A considerable amount of time may be consumed considering which interleaf candidates may be applied to filament winding.

The testing of filament wound tubes under combined loading has become quite common. However, there is no standardised method and tests are done on various geometries at different load rates. An interesting example exposed in the results presented here is the failure under compression. Other researchers have modified the geometry of specimens to ensure a particular compressive failure. It would be of significance to understand the compressive failure observed in this study.

In addition, tests done here were conducted at a constant rate of pressurisation. Acknowledging that the matrix has a rate dependent (i.e. viscoelastic) response it would

have been better to performed the tests under a constant axial load rate since the axial response is dominated by the matrix in the $[\pm 60°_3]_T$ laminate.

8.5.2 The Interleaf as a Crack Arrest Device

The initial testing of the thick cross-ply specimens with an interleaf was to monitor the crack progression through the specimen. The geometry itself is not used in practice because laminae are known to be subject to a thickness effect. It is generally observed that strength decreases as the thickness of a lamina increases. It may be of greater use to study the influence of the interleaf on transverse cracking in a more realistic laminate geometry. The performance could then be related to the stiffness drop as a function of stress or strain and characteristic damage states compared to specimens without an interleaf. This could be performed under monotonic and cyclic loading.

Matrix cracking is a greater concern in glass reinforce composites due to the compliance of glass fibre. Perhaps a hybrid composite with only low volume fractions of more stiff reinforcement could be applied to prevent transverse cracking in the internal layers. This may be more efficient than introducing a tough or ductile interleaf.

8.5.3 Viscoelastic Analysis of a Laminate with an Interleaf

The transversely isotropic viscoelastic model produced provides a good representation of the composite material in general. However, it fails to address the fact that as the matrix experiences creep strain and stress relaxation the reinforcement carries more and more load. This changes the effective stress in the matrix yielding a different viscoelastic response. The calibration procedure employed does account for this to some extent but only if the calibration is done at stresses close to those produced by the finite element model.

The calculation of effective stress used in the transversely isotropic viscoelastic model is based on a simplification of the actual composite. It may be useful to investigate other ways of calculating effective stress or other stress based parameters that may be used.

The analyses of the crack propagation through the laminate with an interleaf concentrated on the influence of the interleaf as the crack tip encountered it. Therefore the reduced

mesh was limited to the vicinity of the interleaf. It may be productive to investigate more closely at the influence of the interleaf as the crack travels through the other regions of the laminate.

8.6 SUMMARY

This investigation of $[\pm 60°_3]_T$ glass fibre reinforced epoxy tubes and the influence of an interleaf on transverse cracking and fluid containment has demonstrated that the interleaf is beneficial in both roles but materials must be carefully selected. The first failure envelope of the $[\pm 60°_3]_T$ laminate tubes may be bounded by a maximum strain criteria but over estimates the measured strengths where the tubes failed by local leakage or under combined compressive axial stress. The addition of the polyethylene tape interleaf is shown to influence the failure stresses and strains however the poor bonding characteristics are shown to cause division of the structural elements, ultimately leading lower strength. This interleaf was also found to be unreliable under large tensile axial deformations.

While the weak bonding characteristics were a liability in the pressure retaining tubes, it was found to assist in the delay of a transverse crack through a thick cross-ply. Cracks were observed to initiate on a new plane following intersection with the poorly bonded interleaf. This was verified by numerical analysis.

Nonlinear viscoelastic finite element analyses were completed to investigate the influence of interleaf parameters on crack propagation through the thick cross-ply. It was observed that, when the interleaf is less stiff than the composite, a maximum strain energy release rate was achieved as the crack tip approached and entered the interleaf but this rapidly dropped to a minimum as the crack tip exited the interleaf. The minimum value is influenced by geometric parameters such location within the cross-ply and interleaf thickness.

Interleaf material parameters also had a significant impact on the strain energy release rate. Most notably, the maximum value increased and the minimum value decreased as the interleaf modulus is decreased. Time dependent viscoelastic response further

decreased the strain energy release rate by allowing stress relaxation and creep deformation around the crack tip. Slower crack growth, as regulated by a delay between propagation steps, resulted in lower strain energy release rates. However, the effect was dependent on the delay times and the retardation time constant of the material. For the material investigated the effects of history were found to dissipate rapidly upon initiation of crack growth. However, it was found that applied stress magnitude had a significant impact on the strain energy release rates.

REFERENCES

Aksoy, A. and Carlsson, L.A. (1991) Crack tip yield zone estimates in mode II interlaminar fracture of interleaved composites. *Engineering Fracture Mechanics*, **39**(3):525-534

Bailey, J.E. and Parvizi, A. (1981) On fibre debonding effects and the mechanism of transverse-ply failure in cross-ply laminates of glass fibre/thermoset composites. *Journal of Materials Science*, **16**:649-659

Berthelot, J-M. (2003) Transverse cracking and delamination in cross-ply glass-fiber and carbon-fiber reinforced plastic laminates: Static and fatigue loading. *Applied Mechanics Reviews*, **56**(1):111-147

Carroll, M., Ellyin, F., Kujawski, D. and Chiu, A.S. (1995) The rate-dependent behaviour of ±55° filament-wound glass-fibre/epoxy tubes under biaxial loading. *Composites Science and Technology*, **55**:391-403

Chan, W.S. (1986) Delamination arrester – An adhesive inner layer in laminated composites. Composite Materials: Fatugue and Fracture, ASTM STP 907, Hahn, H.T. (ed.), ASTM Philadelphia, pp. 176-196

Chan, W.S., Rogers, C. and Aker, S. (1986) Improvement of edge delamination strength of composite laminates using adhesive layers. Composite Materials: Testing and Design (Seventh Conference), ASTM STP 893, Whitney, J.M. (ed.) ASTM, Philadelphia, pp. 266-285

Chateauminois, A., Chabert, B., Soulier, J.P. and Vincent, L. (1993) Hygrothermal ageing effects on the static fatigue of glass/epoxy composites. *Composites*, **24**(7):547-555

Chen, S.F. and Jang, B.Z. (1991) Fracture behaviour of interleaved fiber-resin composites. *Composites Science and Technology*, **41**:77-97

Chen, H-J. and Tsai, S.W. (1996) Three-dimensional effective moduli of symmetric laminates, *Journal of Composite Materials*, **30**:906-917

Chen, Y., Xia, Z. and Ellyin, E. (2001) Evolution of residual stresses induced during curing processing using a viscoelastic micromechanical model. *Journal of Composite Materials*, **35**(6):522-542

Clyne, T.W. (1990) A compressibility-based derivation of simple expressions for the transverse Poisson's ratio and shear modulus of an aligned long fibre composite. *Journal of Materials Science Letters*, **9**:336-339

Cohen, D., Mantell, S.C. and Zhao, L. (2001) The Effect of fiber volume fraction on filament wound composite pressure vessel strength. *Composites: Part B*, **32**:413-429

Cohen, D. (1997) Influence of filament winding parameters on composite vessel quality and strength. *Composites Part A*, **28A**:1035-1047

Cook, T.S. and Erdogan, F. (1972) Stresses in bonded materials with a crack perpendicular to the interface. *International Journal of Engineering Science*, **10**:677-697

Dvorak, G.J. and Suvorov, A.P. (2000) The effect of fiber pre-stress on residula stresses and the onset of damage in symmetric laminates. *Composites Science and Technology*, **60**:1129-1139

Edelglass, S.M. (1966) Engineering Materials Science – Structure and Mechanical Behavior of Solids, The Ronald Press Company, New York

Ehrenstein, G.W. and Spaude, R. (1984) A study of the corrosion resistance of glass fibre reinforced polymers. *Composite Structures*, **2**:191-200

Ellyin, F. (2004) Durability of glass-fibre reinforced polymer composites in aqueous and high temperature environments. *Polymers and Polymer Composites*, **12**(4):277-288

Ellyin, F. (1997) Fatigue Damage, Crack Growth and Life Prediction, Chapman & Hall, New York

Ellyin, F. and Maser, R. (2004) Environmental effects on the mechanical properties of glass-fiber epoxy composite tubular specimens. *Composites Science and Technology*, **64**:1863-1874

Ellyin, F. and Rohrbacher, C. (2003) The influence of aqueous environment, temperature and cyclic loading on glass-fibre/epoxy composite laminates. *Journal of Reinforced Plastics and Composites*, **22**(7):615-636

Ellyin, F., Xia, Z. and Chen, Y. (2002) Viscoelastic micromechanical modeling of free edge and time effects in glass fiber/epoxy cross-ply laminates. *Composites: Part A*, **33**:399-409

Ellyin, F. and Martens, M. (2001) Biaxial fatigue behaviour of multidirectional filament-wound glass-fiber/epoxy pipe. *Composites Science and Technology*, **61**:491-502

Ellyin, F. and Rohrbacher, C. (2000) Effect of aqueous environment and temperature on glass-fibre epoxy resin composites. *Journal of Reinforced Plastics and Composites*, **19**(17):1405-1427

Ellyin, F., Wolodko, J., Dorling, D., Glover, A. and Jack, T. (2000) Fibre reinforced composites in pipeline applications: Design issues and current research. *Proceedings of IPC 2000: The 3rd International Pipeline Conference*, Calgary, Canada, IPC00-0083

Ellyin, F., Carroll, M., Kujawski, D. and Chui, A.S. (1997) The behaviour of multidirectional filament wound fibreglass/epoxy tubulars under biaxial loading. *Composites Part A*, **28A**:781-790

Enie, R.B. and Rizzo, R.R. (1970) Three-dimensional laminate moduli. *Journal of Composite Materials*, **4**:150-154

Foral, R.F. (1988) Local damage effects on performance of filament wound composite tubes. *American Society of of Mechanical Engineers, Applied Mechanics Division (AMD)*, **92**:135-142

Foral, R.F. and Gilbreath, D.R. (1989) Delamination failure modes in filament-wound composite tubes. *Composite Material: Fatigue and Fracture, Second Volume, ASTM STP 1012*, Lagace, P.A. (ed.), ASTM, Philadelphia, pp. 313-325

Frost, S.R. and Cervenka, A. (1994) Glass fibre-reinforced epoxy matrix filament-wound pipes for use in the oil industry. *Composites Manufacturing*, **5**(2):73-81

Gecit, M.R. and Erdogan, F. (1978) The effect of adhesive layers on the fracture of laminated structures. *Transactions of the ASME*, **100**(January):2-9

Gibson, A.G., Hicks, C., Wright, P.N.H. and Fahrer, A. (2000) Development of glass fibre reinforced polyethylene pipes for pressure applications. *Plastics, Rubber and Composites*, **29**(10):509-519

Gillespie, J.W. and Hansen, U. (1997) Transverse cracking of composite laminates with interleaves: a variational approach. *Journal of Reinforced Plastics and Composites*, **16**(12):1066-1091

Goree, J.G. and Venezia, W.A. (1977a) Bonded elastic half-planes with an interface crack and a perpendicular intersecting crack that extends into the adjacent material – I. *International Journal of Engineering Science*, **15**:1-17

Goree, J.G. and Venezia, W.A. (1977b) Bonded elastic half-planes with an interface crack and a perpendicular intersecting crack that extends into the adjacent material – II. *International Journal of Engineering Science*, **15**:19-27

Grove, S. (1999) Optimum Fiber Orientation in Filament Wound Structures, *Journal of Materials Science Letters*, **18**:1203

Halpin, J.C. and Kardos, J.L. (1976) The Halpin-Tsai Equations: A Review. *Polymer Engineering and Science,* **16**(5):344-352

Han, X., Ellyin, F. and Xia, X. (2001) A crack near the interface of bonded elastic-viscoelastic planes. *International Journal of Solids and Structures*, **38**:3453-3468

Hart-Smith, L.J. (1998a) Predictions of the original and truncated maximum-strain failure models for certain fibrous composite laminates. *Composites Science and Technology*, **58**:1151-1178(*)

Hart-Smith, L.J. (1998b) Predictions of a generalized maximum-shear-stress failure criterion for certain fibrous composite laminates. *Composites Science and Technology*, **58**:1179-1208(*)

Hart-Smith, L.J. (1994) Predicting the strength of fibrous composites by an orthotropic generalization of the maximum-shear-stress (Tresca) criterion. *Proceedings of the Institute of Mechanical Engineers: Part G, Journal of Aerospace Engineering*, **208**:9-18

Hart-Smith, L.J. (1990) A strain-based maximum-shear-stress failure criterion for fibrous composites, *AIAA/ASME/ASCE/AHS Structures, Structural Dynamics and Materials Conference*, AIAA-90-0958-CP pp.714-722

Henninger, F. and Friedrich, K. (2002a) Thermoplastic filament winding with online-impregnation. Part A: Process technology and operating efficiency. *Composites: Part A*, **33**:1479-1486

Henninger, F., Hoffmann, J. and Friedrich, K. (2002b) Thermoplastic filament winding with online-impregnation. Part B. Experimental study of processing parameters. *Composites: Part A*, **33**:1677-1688

Hewitt, R.L. and De Malherbe, M.C. (1970) An Approximation for the Longitudinal Shear Modulus of Continuous Fibre Composites, *Journal of Composite Materials*, **4**:280-282

Highsmith, A.L. and Reifsnider, K.L. (1982) Stiffness-reduction mechanisms in composite laminates. *Damage in Composite Materials, ASTM STP 775* Reifsnider, K.L. (ed.), 103-117

Hill, R. (1964) Theory of Mechanical Properties of Fibre-Strengthened Materials: I. Elastic Behaviour. *Journal of Mechanics and Physics of Solids*, **12**:199-212

Hilton, H.H. (2003) Comments regarding "Viscoelastic properties of an epoxy resin during cure" by D.J. O'Brien, P.T. Mather and S.R. White. *Journal of Composite Materials*, **37**(1): 2003

Hilton, H.H. (2001) Implications and constraints of time-independent Poisson ratios in linear isotropic and anisotropic viscoelasticity. *Journal of Elasticity*, **63**:221-251

Hilton, H.H. and Yi, S. (1998) The significance of (an)isotropic viscoelastic Poisson ratio stress and time dependencies. *International Journal of Solids and Structures*, **35**(23):3081-3095

Hinton, M.J., Kaddour, A.S. and Soden, P.D. (2002) A comparison of the predictive capabilities of current failure theories for composite laminates, judged against experimental evidence, *Composite Science and Technology*, **62**:1725-1797(*)

Hoover, J.W., Kujawski, D. and Ellyin, F., (1997) Transverse cracking of symmetric and unsymmetric glass-fibre/epoxy-resin laminates. *Composites Science and Technology*, **57**:1513-1526

Hu, Y. (2002) Multiaxial behaviour and viscoelastic modelling of epoxy polymers. Ph.D. Dissertation, University of Alberta, Edmonton, Alberta

Hu, Y., Xia, Z. and Ellyin, F. (2003) Deformation behaviour of an epoxy resin subject to multiaxial loadings. Part I: experimental investigations. *Polymer Engineering and Science*, **43**(3):721-733

Ilcewicz, L.B., Dost, E.F., McCool, J.W. and Grande, D.H. (1991) Matrix Cracking in composite laminates with resin-rich interlaminar layers. *Composite Materials: Fatigue and Fracture (Third Volume), ASTM STP 1110*, O'Brien, T.K. (ed.) 30-55

Jiang, W., Tjong, S.C., Chu, P.K., Li, R.K.Y., Kim, J.K. and Mai, Y.W. (2001) Interlaminar fracture properties of carbon fibre/epoxy matrix composites interleaved with polyethylene terephthalate (PET) films. *Polymers and Polymer Composites*, **9**(2):141-145

Jones, F.R., Rack, J.W. and Wheatley, A.R. (1983) Stress corrosion cracking and its implications for the long-term durability of E-glass fibre composites. *Composites*, **14**(3):262-269

Jones, M.L.C. and Hull, D. (1979) Microscopy of failure mechanisms in filament-wound pipe. *Journal of Materials Science*, **14**:165-174

Jorgensen, O. and Horsewell, A. (1997) On the indentation failure of carbon-epoxy cross-ply laminates, and its suppression by elasto-plastic interleaves. *Acta Materialia*, **45**(8):3431-3444

Kaddour, A.S., Hinton, M.J. and Soden, P.D. (2004) Predictive capabilities of nineteen failure theories and design methodologies for polymer composite laminates. Part B: comparison with experiments. Failure Criteria in Fibre Reinforced Polymer Composites: The World-Wide Failure Exercise, Hinton, M.J., Kaddour, A.S. and Soden, P.D. (eds.) Elsevier, New York, pp. 1073-

Kaddour, A.S., Hinton, M.J. and Soden, P.D. (2003) Behaviour of ±45° glass/epoxy filament wound composite tubes under quasi-static equal biaxial tension-compression loading: experimental results. *Composites: Part B*, **34**:689-704

Kaddour, A.S., Soden, P.D. and Hinton, M.J. (1998) Failure of ±55 degree filament wound glass/epoxy composite tubes under biaxial compression. *Journal of Composite Materials*, **32**:1618-1645

Kanninen, M.F. and Popelar, C.H. (1985) Advanced Fracture Mechanics, Oxford University Press, New York

Kaw, A.K. and Goree, J.G. (1990a) Effects of interleaves on fracture of laminated composites: part I analysis. *Transactions of the ASME*, **57**(March):168-174

Kaw, A.K. and Goree, J.G. (1990b) Effects of interleaves on fracture of laminated composites: part II solution and results. *Transactions of the ASME*, **57**(March):175-181

Kieger, R.B. (1985) Advances in toughness of structural composites based on interleaf technology. Progress in Advanced Materials and Processes: Durability, Reliability and Quality Control, Bartelds, G. and Schliekelmann, R.J. (eds.) 189-199

Knight, M.G., Wrobel, L.C. and Henshall, J.L. (2003) Fracture response of fibre-reinforced materials with macro/microcrack damage using the boundary element technique. *International Journal of Fracture*, **121**:163-182

Kollar, L.P. and Springer, G.S. (2003) Mechanics of Composite Structures, Cambridge University Press, New York, USA pp. 398-410

Kruijer, M.P., Warnet, L.L. and Akkerman, R. (2005) Analysis of the mechanical properties of a reinforced thermoplastic pipe (RTP). *Composites: Part A*, **36**:291-300

Kujawski, D. and Ellyin, F. (1995) Rate/frequency-dependent behaviour of fibreglass/epoxy laminates in tensile and cyclic loading. *Composites*, **26**:719-723

Lagace, P.A. and Bhat, N.V. (1992) Efficient use of film adhesive interlayers to suppress delamination. Composite Materials: Testing and Design (Tenth Volume), ASTM STP 1120, Grimes, G.C. (ed.) ASTM, Philadelphia, USA pp. 384-396

Lai, J. and Bakker, A. (1996) 3-D Schapery representation for non-linear viscoelasticity and finite element implementation. *Computational Mechanics*, **18**:182-191

Lang, E. and Chou, T.-W. (1998) The effect of strain gage size on measurement errors in textile composite materials. *Composites Science and Technology*, **58**:539-548

Lee-Sullivan, P. (1995) The effects of thermoplastic film-interleaving on stiffness loss due to matrix cracking and subsequent delamination in composite laminates. *Proceedings of ICCM-10*, **4**:3-10

Li, L., Lee-Sullivan, P. and Liew, K.M. (1996) The influence of thermoplastic film interleaving on the interlaminar shear strength and mode I fracture of laminated composites. Journal of Engineering Materials and Technology, 118(July):302-309

Li, R., Wu, S., Ivanonova, E., Chudnovsky, A., Sehanobish, K. and Bosnyak, C.P. (1993) Finite element modle and experimental analysis of crack-inclusion interaction. *Journal of Applied Polymer Science*, **50**:1233-1238

Lo, H., Crate, H. and Schwartz, E.B. (1951) Buckling of thin-walled cylinder under axial compression and internal pressure. NACA Report 1027

Lossie, M. and van Brussel, H. (1994) Design principles in filament winding. *Composites Manufacturing*, **5**(1):5-13

Lossie, M., Peters, J., and van Brussel, H. (1989) Influence of winding strategy on the characteristics of filament wound structures. *Revue Machanique*, **33**:107-117

Lou, Y.C. and Schapery, R.A. (1971) Viscoelastic characterization of a nonlinear fiber-reinforced plastic. *Journal of Composite Materials*, **5**:208-234

Lundberg, C., Stringfellow, W.D., Walsh, T. and Reynolds, H. (2001) Application of spoolable composite tubing to oil and gas industry flowlines. SAMPE 2001 Conference Proceedings, 2001: A Materials and Processes Odyssey, Long Beach, USA 2622-2633

Marsh, G. (2005) Airframers exploit composites in battle for supremacy. *Reinforced Plastics*, 49(3):26-32

Martens, M.and Ellyin, F. (2000) Biaxial monotonic behaviour of a multidirectional glass fiber epoxy pipe. *Composites: Part A*, **31**:1001-1014

Masters, J.E. (1989) Improved impact and delamination resistance through interleaving. *Key Engineering Materials*, **37**:317-348

McCartney, L.N., Schoeppner, G.A. and Becker, W. (2000) Comparison of models for transverse ply cracks in composite laminates. *Composites Science and Technology*, **60**:2347-2359

Meijer, G. and Ellyin, F. (2004) Effect of a soft interleaf on transverse cracks in thick glass fibre-epoxy cross-ply laminates. *Journal of Composite Materials*, **38**(24):2199-2211

Melo, J-D.D. and Radford, D.W. (2004) Time and temperature dependence of the viscoelastic properties of PEEK/IM7. *Journal of Composite Materials*, **38**(20):1815-1830

Mertiny, P. and Ellyin, F. (2002) Influence of the filament winding tension on physical and mechanical properties of reinforced composites. *Composites: Part A*, **33**:1615-1622

Nay, J.C., Pitt, W.G. and Armstrong-Carroll, E. (1995) Improving adhesion in interleaf composites using plasma processing. *Journal of Applied Polymer Science*, **56**:461-469

Ogihara, S., Takeda, N., Kobayashi, S. and Kobayashi, A. (1999) Effects of stacking sequence on microscopic fatigue damage development in quasi-isotropic CFRP laminates with interlaminar-toughened layers. *Composites Science and Technology*, **59**:1387-1398

Ogihara, S., Takeda, N., Kobayashi, S. and Kobayashi, A. (2002) Damage mechanics characterization of transverse cracking behaviour in quasi-isotropic CFRP laminates with interlaminar-toughened layers. *International Journal of Fatigue*, **24**:93-98

Owens Corning (1999) 158B Type 30 Roving, Pub. No. 1-PL-17111-D, Owens Corning, Toledo, USA

Ozdil, F. and Carlsson, L.A. (1992) Mode I interlaminar fracture of interleaved graphite/epoxy. *Journal of Composite Materials*, **26**(3):432-459

Perreux, D. and Joseph, E. (1997) The effect of frequency on the fatigue performance of filament-wound pipes under biaxial loading: Experimental results and damage model. *Composites Science and Technology*, **57**:353-364

Perreux, D. and Suri, C. (1997) A study of the coupling between the phenomena of water absorption and damage in glass/epoxy composite pipes. *Composites Science and Technology*, **57**:1403-1413

Perreux, D., Maire, J.-F., Siqueira, C., Varchon, D. and Oytana, C. (1994) Multiaxial testing of composite materials. *Materiaux et Techniques*, **82**(6-7):37-40

Peters, S.T., Humphrey, W.D. and Foral, R.F. (1999) Filament Winding Composite Structure Fabrication, 2nd Ed. SAMPE, Covina CA

Puck, A. and Schürmann, H. (1998) Failure analysis of FRP laminates by means of physically based phenomenological models. *Composites Science and Technology*, **58**:1045-1067(*)

Puck, A. and Schneider, W. (1969) On failure mechanisms and failure criteria of filament-wound glass-fibre/resin composites. *Plastics and Polymers*, **37**(February):33-44

Resolution Performance Products (2001) Starting formulation: Resin system for filament winding and RTM – EPON resin 826 with EPI-CURE curing agent 9551. No. 8023 SC:2441-01, Resolution Performance Products, Houston, USA

Rodriguez, E.L. (1989) Microdelamination due to resin shrinkage in filament-wound fibreglass composites. *Journal of Materials Science Letters*, **8**:116-118

Rousseau, J., Perreux, D. and Verdière, N. (1999) The influence of winding patterns on the damage behaviour of filament-wound pipes. *Composites Science and Technology*, **59**:1439-1449

Rybicki, E.F. and Kanninen, M.F. (1977) A finite element calculation of stress intensity factors by a modified crack closure integral. *Engineering Fracture Mechanics*, **9**:931-938

Schapery, R.A. (1969) On the characterization of nonlinear viscoelastic materials. *Polymer Engineering and Science*, **9**(4):295-310

Schapery, R.A. (1968) Thermal expansion coefficients of composite materials based on energy principles. *Journal of Composite Materials*, **2**(3):380-404

Sheinman, I. and Soffer, M. (1989) Effect of delamination on the nonlinear behaviour of composite laminated beams. *American Society of Mechanical Engineers, Pressure Vessels and Piping Division (PVP)*, **174**:91-96

Salpekar, S.A., O'Brien, K.T. and Shivakumar, K.N. (1996) Analysis of local delaminations caused by angle ply matrix cracks. *Journal of Composite Materials*, **40**(4):418-440

Shivakumar, K.N., Tan, P.W. and Newman, J.C., Jr. (1988) A virtual crack-closure technique for calculating stress intensity factors for cracked three dimensional bodies. *International Journal of Fracture*, **36**:R43-R50

Soden, P.D., Kaddour, A.S. and Hinton, M.J. (2004) Recommendations for designers and researchers resulting from the World-Wide Failure Exercise. *Composites Science and Technology*, **64**:589-604

Soden, P.D., Hinton, M.J. and Kaddour, A.S. (2002) Biaxial test results for strength and deformation of a range of E-glass and carbon fibre reinforced composite laminates: failure exercise benchmark data. *Composites Science and Technology*, **62**:1489-1514(*)

Soden, P.D., Hinton, M.J. and Kaddour, A.S. (1998) A comparison of the predictive capabilities of current failure theories for composite laminates, *Composites Science and Technology*, **58**:1225-1254(*)

Soden, P.D., Kaddour, A.S. and Hinton, M.J (2004) Recommendations for designers and researchers resulting from the World-Wide Failure Wxercise, *Composites Science and Technology*, 64:589-604(*)

Soden, P.D., Kitching, R., Tse, P.C., Tsavalas, Y. and Hinton, M.J. (1993) Influence of winding angle on the strength and deformation of filament-wound composite tubes subjected to uniaxial and biaxial loads. *Composites Science and Technology*, **46**:363-378

Soden, P.D., Kitching, R.and Tse, P.C. (1989) Experimental failure stresses for ±55° filament wound glass fibre reinforced plastic tubes under biaxial loads. *Composites*, **20**(2):125-135

Soden, P.D., Leadbetter, D., Griggs, P.R. and Eckold, G.C. (1978) The strength of a filament wound composite under biaxial loading. *Composites*, October 247-250

Stevanovic, D., Jar, P.-Y.B. Jar, Lowe, A. and Kalyanasundaram, S. (1999) The influence of rubber particle concentration on fracture toughness of interlayer-toughened vinyl-ester/glass fibre composite. *12th International Conference on Composite Materials*, Massard, T. and Vautrin, A. (eds.)

Sun, C.T. and Chen, J.L. (1991) A micromechanical model for plastic behaviour of fibrous composites. *Composites Science and Technology*, **40**:115-129

Sun, C.T. and Liao, W.C. (1990) Analysis of thick section composite laminates using effective moduli. *Journal of Composite Materials*, **24**:977-993

Sun, C.T. and Li, S. (1988) Three-dimensional effective elastic constants for thick laminates. *Journal of Composite Materials*, **22**:629-639

Sun, C.T. and Vaidya, R.S. (1996) Prediction of composite properties from a representative volume element. *Composites Science and Technology*, **56**:171-179

Swanson, S.R. (1998) Overview of biaxial test results for carbon fiber composites. Composite Materials: Fatigue and Fracture, Seventh Volume, ASTM STP 1330, Bucinell, R.B. (ed.), 19-33

Tafreshi, A. (2004) Efficient modelling of delamination buckling in composite cylindrical shells under axial compression. *Composite Structures*, **64**:511-520

Tanimoto, T. (2002) Interleaving methodology for property tailoring of CFRP laminates. *Composite Interfaces*, **9**(1):25-39

Tanimoto, T. (1999) Enhanced fatigue resistance in carbon/epoxy laminates by use of interleaf layers. *12th International Conference on Composite Materials*, Massard, T. and Vautrin, A. (eds.)

Tsai, S. (1992) Theory of Composites Design, Think Composites, Dayton

Tucker, C.L. and Liang, E. (1999) Stiffness predictions for unidirectional short-fiber composites: Review and evaluation. *Composites Science and Technology*, **59**:655-671

Vejen, N. and Pyrz, R. (2002) Transverse crack growth in glass/epoxy composites with exactly positioned long fibres. Part II: numerical. *Composites: Part B*, **33**:279-290

Wang, A.S.D. (1998) Free-edge delamination in layered composites – a historical review of the past 30 years. American Society of Mechanical Engineers, Materials Division (MD), **84**:223-226

Wang, A.S.D. (1989) An overview of the delamination problem in structural composites. *Key Engineering Materials*, **37**:1-20

Wang, J.T.-S. (1988) Analysis of composite structures with delaminations. *American Society of Mechanical Engineers, Pressure Vessels and Piping Division (PVP)*, **146**:49-54

Wolodko, J. (2000) Biaxial Fatigue and Leakage Characteristics of Fiber Reinforced Composite Tubes, Ph.D. Thesis, University of Alberta, Edmonton, Alberta

Wolodko, J., Mertiny, P., Meijer, G. Martens, M. and Ellyin, F. (2001) Development of a facility for filament winding GFRP tubulars. Proceedings of the SAMPE 46th International Symposium. Long Beach, USA, pp.1271-1282

Xia, Z. Hu, Y. and Ellyin, F. (2003) Deformation behaviour of an epoxy resin subject to multiaxial loadings. Part II: constitutive modeling and predictions. *Polymer Engineering and Science*, **43**(3):734-748

Xia, Z. and Ellyin, F. (1998) Time-dependent behaviour and viscoelastic constitutive modelling of an epoxy polymer. *Polymers and Polymer Composites*, **6**(2):75-82

Xia, Z., Zhang, Y. and Ellyin, F. (2003) A unified periodical boundary conditions for representative volume elements of composites and applications. *International Journal of Solids and Structures*, **40**:1907-1921

Zhang, C. and Moore, I.D. (1997a) Nonlinear mechanical Response of high density polyethylene. Part I: Experimental investigation and model evaluation. *Polymer Engineering and Science*, **37**(2):404-413

Zhang, C. and Moore, I.D. (1997b) Nonlinear mechanical Response of high density polyethylene. Part II: Uniaxial constitutive modelling. *Polymer Engineering and Science*, **37**(2):414-420

Zhang, Y., Xia, Z. and Ellyin, F. (2005) Nonlinear viscoelastic micromechanical analysis of fibre-reinforced polymer laminates with damage evolution. *International Journal of Solids and Structures*, **42**:591-604

Zhang, Y., Xia, Z. and Ellyin, F. (2004) Evolution and influence of residual stresses/strains of fiber reinforced laminates. *Composites Science and Technology*, **64**:1613-1621

Zienkiewicz, O.C., Watson, M. and King, I.P. (1968) A numerical method of visco-elastic stress analysis. *International Journal of Mechanical Science*, **10**:807-827

(*)These papers may also be found in the special publication Failure Criteria in Fibre Reinforced Polymer Composites: The World-Wide Failure Exercise, Hinton, M.J., Kaddour, A.S. and Soden, P.D. (eds.) Elsevier, New York, 2004

APPENDIX A THE ACME FILAMENT WINDING FACILITY

The Advanced Composite Materials Engineering (ACME) research group was funded from numerous sources to develop a filament winding laboratory for the production of composite pipe prototypes. The desire was to assemble a facility that would represent actual industrial manufacturing practises but with reliable control of a number of process variables. While all the equipment is described, there is an emphasis on those items which the author played a significant role in the procurement and/or design and construction.

The equipment purchased or manufactured are:

- McClean Anderson WMS Series 4 axis Filament Winding Machine
- Wisconsin Oven
- Drum Type Resin Bath
- Creel Tensioning Stand and associated fibre handling equipment
- Series of mandrels

A.1 THE FILAMENT WINDING MACHINE

A state-of-the-art McClean Anderson WMS Series commercial filament winding machine was purchased to provide the backbone of the facility. This filament winding machine has a mandrel capacity of lengths up to 3.6 m and 600 mm in diameter. The machine has four axis of freedom: rotation of the mandrel, carriage travel, carriage translation and rotation of the payout eye. The machine is shown in Figure A.1 and the rates of travel for these motions are provided in Table Table A.1.

This particular machine is equipped with one spindle for winding a single component at a time. The WMS model has the carriage supported by an overhead beam and was chosen to reduce cleanup requirements and improve component handling in the confined space allowed for the facility. For large parts, a cart is rolled within the footprint of the winding machine below the chucked part. The part is then lowered onto the car and wheeled into the curing oven.

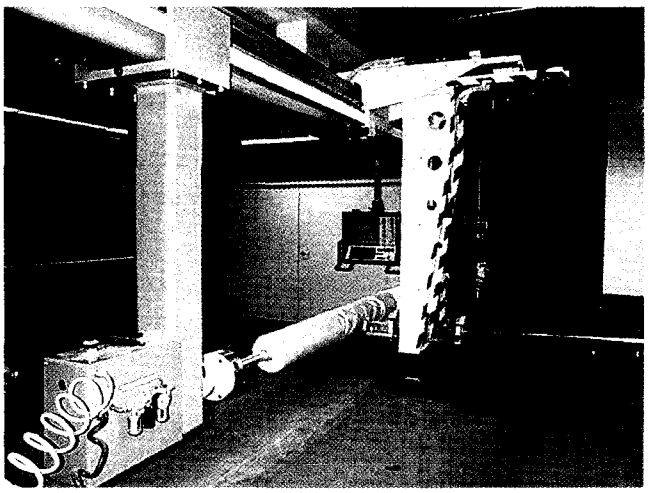

Figure A.1: McLean Anderson WMS series filament winding system demonstrated with dry glass fibre and a temporary mandrel.

Table A.1: Capacities of the McClean Anderson WMS Series Filament Winding Machine

Degree of Freedom	Capacity
Mandrel (with part)	
Length	3.6 m
Diameter	25 mm to 660 mm
Weight	907 kg
Spindle	
Speed	0 to 150 RPM
Horizontal Carriage Travel	
Stroke	3.96 m
Travel Speed	0 to 1 m/s
Cross-feed Carriage Travel	
Stroke	381 mm
Travel Speed	0 to 0.64 m/s
Delivery Eye Rotation Travel	
Stroke	±90°
Travel Speed	0 to 360 °/s

A.1.1 Computer Control

The filament winding machine is computer controlled and is operated through a monitor/keyboard interface. All winding patterns are computer generated and translated into machine code by the supplied software. Complicated, closed end patterns may be defined but only helical and circumferential winding has been exercised in this project.

A.1.2 Pattern Generation

The path generation software "Composite Designer" was provided with the filament winding machine to produce machine code based on the user input. Specific pattern generation routines are provided for:

Helical Wind: Helical winding is used on simple tubular structures with a $\pm\theta$ layup. Input parameters include the wrap angle, θ, the bandwidth of fibre layed in one pass, the mandrel diameter, the turn around contact angle and the turn around range.

Circumferential Wind: Circumferential wind produces a pattern which covers the mandrel in one circuit. Given the bandwidth and mandrel diameter, the angle that produces full coverage in a single pass is calculated and the routine generated. For a true circumferential wrap the bandwith must approach zero so realistically circumferential winding can only be approximated by angles approaching 90°.

Axial winding: Axial winding is notably more complicated since there is no support of the wet fibres by convex surfaces. Therefore it requires the use of pin rings on the mandrel to catch the fibres at the mandrel ends and prevent slipping of the fibre bands.

Bottle Wind: produces a pattern for a closed end vessel. The vessel must have at least one opening where the mandrel is attached to the spindle. Mandrels are often made from a dissolvable material system or are left in the final product as a liner.

The machine code files generated by "Composite Designer" are loaded into the filament winding machine operation program "Omniwind". This program allows for the selection of the appropriate winding routine files, specification of motion offset values, controls the

machine speed (including a hold function) and provides feed back during the winding procedure.

A.2 FIBRE TENSIONING AND HANDLING EQUIPMENT

Upon development of the filament winding facility, it was decided that control of tow tension was desirable and was to be implemented. Providing adequate tow tension during winding reduces fibre waviness and enhances fibre bed consolidation considerably. Both may result from insufficient tension and the crossovers produced in a standard helical $\pm\theta$ pattern. Reducing fibre waviness and increasing consolidation increases the fibre volume fraction, decreases the void volume fraction and reduces the possibility of fibre buckling due to eccentric fibre compression loads. Decreasing voids and fibre buckling directly produces a higher quality composite system with improved mechanical properties. Increasing the fibre volume fraction may have the desirable effect of increased mechanical stiffness and strength but may also reduce transverse cracking toughness due to greater stress/strain concentrations in the matrix. Pretensioning the reinforcement will counteract the compressive thermal residual stresses generated in the fibres during cooling from an elevated cure temperature. Large differences in the coefficients of thermal expansions of the reinforcement and the matrix often result in deformations such as warping and possibly even damage. Tensioning the fibre, however, does result in greater slipping as the reinforcement band is wound on the mandrel and does produce more damage during fibre handling, particularly where the dry fibre slides over fixed surfaces of small radius.

In many general, manufacturing facilities rely on the friction of running the fibre tows through eyelets to produce a tension. This means of tensioning provides only approximate control and results in more damage to the fibre bundle.

To satisfy the requirements of the filament winding facility, the fibre tensioning system shown in Figure A.2 was designed and built in-house. The tensioning stand was designed in a standard multiple row, vertical arrangement that minimises space requirements. Ten standard E-glass, inside pull creels mounted on three inch cardboard centres are bolted on

shafts protruding from the front of the stand. Pulling from the outside of the creel eliminates the twist associated with pulling from the centre of the creel. Each tensioner shaft is driven by a 1 HP AC motor via a cogged belt at a reduction ratio of 1:2.5. This reduction allows for a tow tension of 89 N on creels between 152 and 356 mm in diameter. Each motor has a built-in cooling fan, since they operate near stall conditions, and a position encoder for integration with the motor controller.

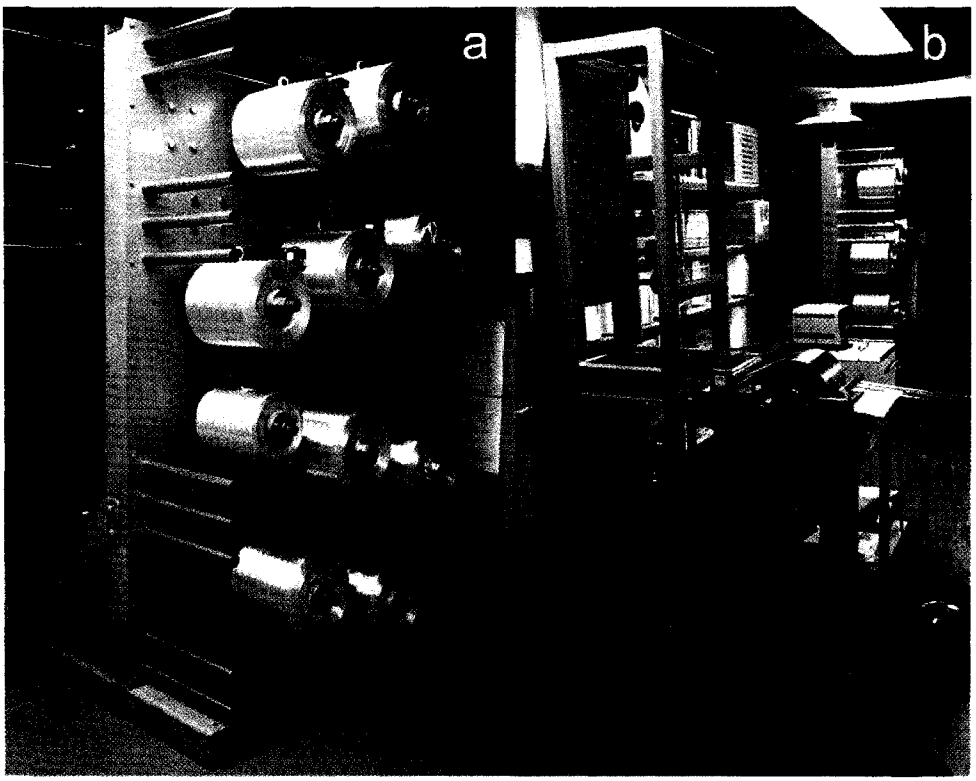

Figure A.2: Tow tensioning equipment; a) creel stand with tensioning motors, b) tow redirection stand, resin bath and resin bath heater.

A.2.1 Fibre Path and Tension Stand Structure

Fibre redirection is done using 50.8 mm diameter chrome surface round bars and 76.2 mm diameter pulleys. The chrome bars were placed to have the fibres leave the tension stand at a known height. Pulleys could not be used at this location, close to the creel, because the manner in which the tow is wound around the creel results in a large amount of horizontal travel during unwinding. The sliding contact at this location is acceptable since the contact angle remains small.

Due to space limitations in the filament winding facility, and a desire to maximise the distance between the resin bath and the mandrel to reduce side loads on the filament winding machine carriage, the tension stand is actually placed perpendicular to the axis of the winding machine. Thus the fibres must be turned 90° towards the winding machine in a turn around stand, also shown in Figure A.2. An additional 90° turn is required to bring the tows to the level of the resin bath entrance. Upon leaving the creel and passing over the chrome bar the tow travels horizontally for approximately three metres where they pass 90° around a pulley and follow a vertical path to the height of the resin bath. These pulleys are mounted on cantilever arms that may be replaced with load cells at some time in the future. By orienting the load cells at 45°, and knowing the change in tow direction is exactly 90°, the tension can be measured and used as direct feedback into the controllers to control motor torque.

At the level of the resin bath, all tows are redirected by pulleys to run horizontally to the resin bath and the winding machine. These pulleys are mounted in a cartridge that is easily removed from the turn around stand and provides for fine vertical alignment. These pulleys, close to the resin bath, were made removable in case wet tows are accidentally pulled back through the pulley system and the pulleys need to be cleaned.

A.2.2 Tension Motor Control

Each tension motor is driven by a RISC processor based regenerative drive controller manufactured by Control Techniques. The controller is equipped with both volatile and non-volatile memory and can store parameters and programs uploaded from a personal computer via the serial port. The parameters may be viewed and set from an onboard control panel or from a personal computer connection, while the system is running. The combination of a user specified program and directly accessible parameters allows for rigid control of the motor, and hence creel speed, torque, position, etc.

The controllers are programmed using a basic programming language with variables, functions and standard conditional and loop structures. The program implemented for tensioning the tows utilises three standard segments.

1) The "Initial" segment is run when the controller is started or reset. In the "Initial" segment parameters are defined and basic calculations for calibrating the creel radius feedback and motor torque to tow tension conversion are done.

2) The "Background" segment is run in a continuous loop while the controller is operating and no other segment is running. This routine does the calculation of creel radius and motor torque required to produce the desired tow tension.

3) The "Clock" segment interrupts the "Background" segment at prescribed increments according to the system clock. This routine checks that the creel radius has not dropped below a prescribed value and that the creel is not freely rotating, indicating a broken tow.

A flowchart of the tension controller logic is shown in Figure A.3.

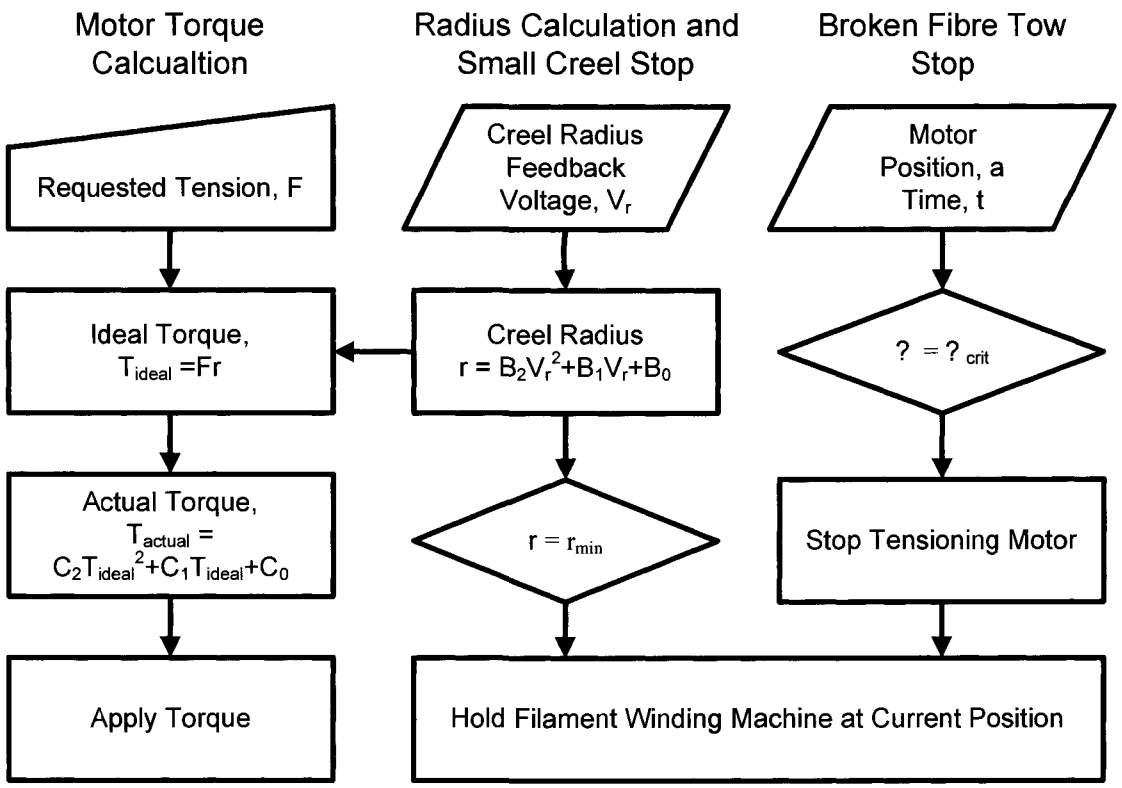

Figure A.3: Flowchart of controller functions for applying torque and holding filament winding machine for an empty creel or broken glass fibre tow.

The calculation of the required motor torque, processed in the "Background" routine, is done based on the filament winding operator's requested tow tension, the measured creel

radius and a predetermined calibration curve. The coefficients for quadratic calibration curves for tension calculations (C_2, C_1 and C_0) and radius calculations (B_2, B_1 and B_0) are stored in the non-volatile memory of the controller. First the ideal motor torque needed, T_{ideal}, is calculated based on the requested tow tension, F, and the measured creel radius, $r = B_2V_r^2 + B_1V_r + B_0$. The ideal torque is then multiplied by a quadratic calibration curve to give the actual torque needed, $T_{actual} = C_2T_{ideal}^2 + C_1T_{ideal} + C_0$, which compensates for bearing and sliding friction and gives the desired tow tension at the mandrel based on calibration measurements.

Meanwhile, in the "Clock" routine an error condition check is done to ensure that a creel is not spinning freely, indicating that a tow has broken. This is achieved by calculating the fibre velocity based on the change in creel rotation since the last "Clock" routine was executed, the time between calls to the clock routine and the creel radius. If the velocity of fibre take-up is greater than an operator specified limit and the system is set to detect this error condition, the controller stops the defective creel while the others remain active and the filament winding machine is sent a signal to HOLD. The operator can then correct the problem creel, reactivate the tension on the stopped controller, and resume the filament winding routine. This procedure is also followed if the creel radius falls below an operator specified value.

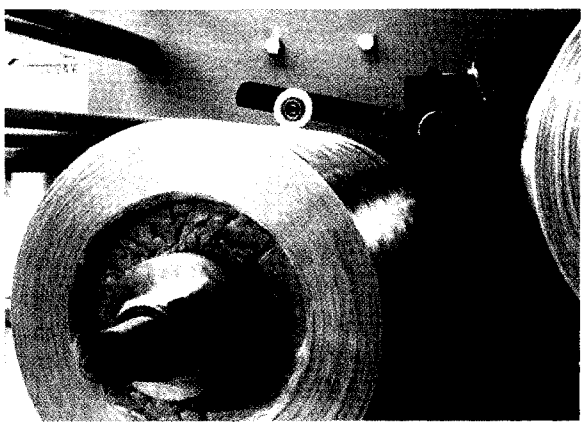

Figure A.4: Creel follower to measure creel radius.

The creel radius is measured using a roller follower attached to an arm as shown in Figure A.4. A linear rotational potentiometer provides a voltage signal that varies with

angular position to the motor controller and this signal is manipulated using the input calibration parameters to provide the creel radius.

A suite of software call "Systemwise" provided with the controllers allows the user to build and use a personal computer operator interface for the controllers. Connection of the computer to the controllers is via an integral RS-232 serial port. Numerous controls such as sliders, dials, text boxes, number pads, images and buttons are available to build a multi-page computer control panel. Two operator interfaces have been developed: one for normal filament winding operation and another for calibration.

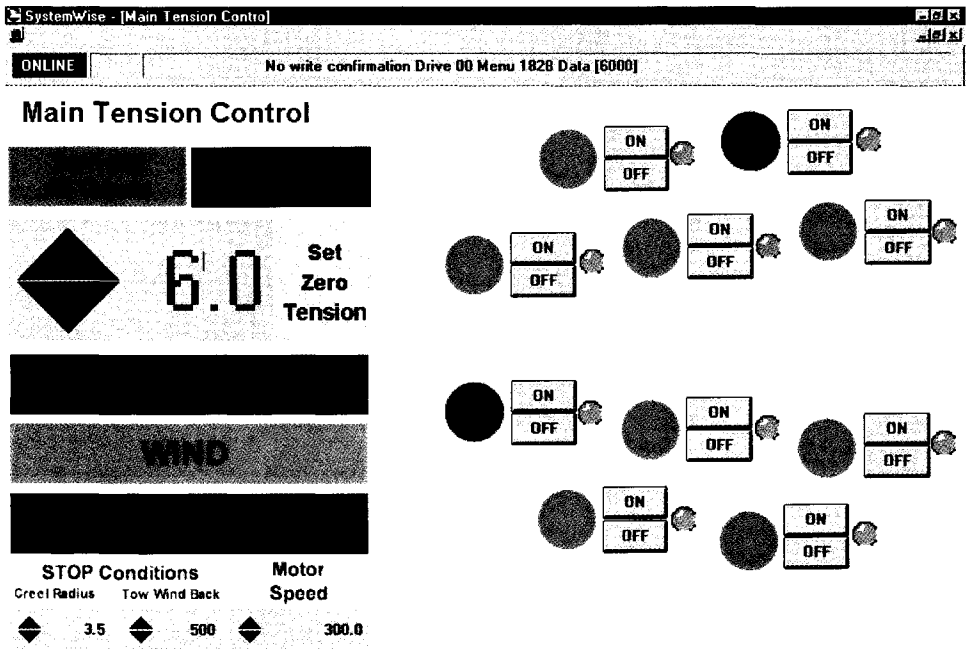

Figure A.5: Tension control panel used during filament winding.

The basic filament winding panel, shown in Figure A.5, allows the operator to control the tension of all tows, set the tension of all tows to zero, turn all creels off and on, turn individual creels off and on, set the operation mode to either Remove Slack, Wind or Provide Slack and set the limits for small creel radius stop condition, r_{crit}, and tow rewind rate stop condition, v_{crit}. Values can be changed at any time during operation. Each creel has two indicators. The first indicator shows whether creel tension is off (red) or on

(green). The second indicator shows the mode of operation: Remove Slack (yellow), Wind (green) and Provide Slack (grey).

The "Remove Slack" condition disables the error detect allowing the creels to take-up the glass fibre to remove slack from the fibre path. The motor speed is reduced to eliminate a snap-back when this mode is enabled. The snap-back was found to be severe enough to break the glass fibre tows.

The "Wind" condition is for the filament winding process. The motor speed is increased to prevent any slack due to changes in velocity of the mandrel rotation and the error conditions, broken tow and small creel, are detected. On detection of an error, only the effected creel motor is disabled and the winding machine stops at the current position. The remaining tows remain under tension while the operator corrects the problem. When fixed, the operator then restarts the disabled tension motor and then continues the winding process.

The "Provide Slack" setting is used when the component is complete and the operator wishes to cut the glass fibres. This mode pays out a set length of fibre very slowly providing a length that will not pull back through the combs on the carriage due to the wet fibre weight.

A.2.3 Tension Calibration

Calibration of the tension system consist of two parts: 1) calibration of the creel radius measurement and 2) calibration of the motor torque. As described above, the requested torque is calculated from the operator's desired tension and the measured creel radius and is then modified using the calibration curve to account for various effects such as friction to define the real motor torque to produce the desired tow tension.

Calibration for each creel is done with the aid of the "Systemwise" panel shown in Figure A.6. This panel allows the operator to set the motor torque, read the radius output value and then enter the calibration constants. Each calibration curve requires three constants and each constant requires three input values, an integer portion the exponent

value and the sign (e.g. positive or negative). The input of integer and Boolean data is required by the available controller non-volatile memory.

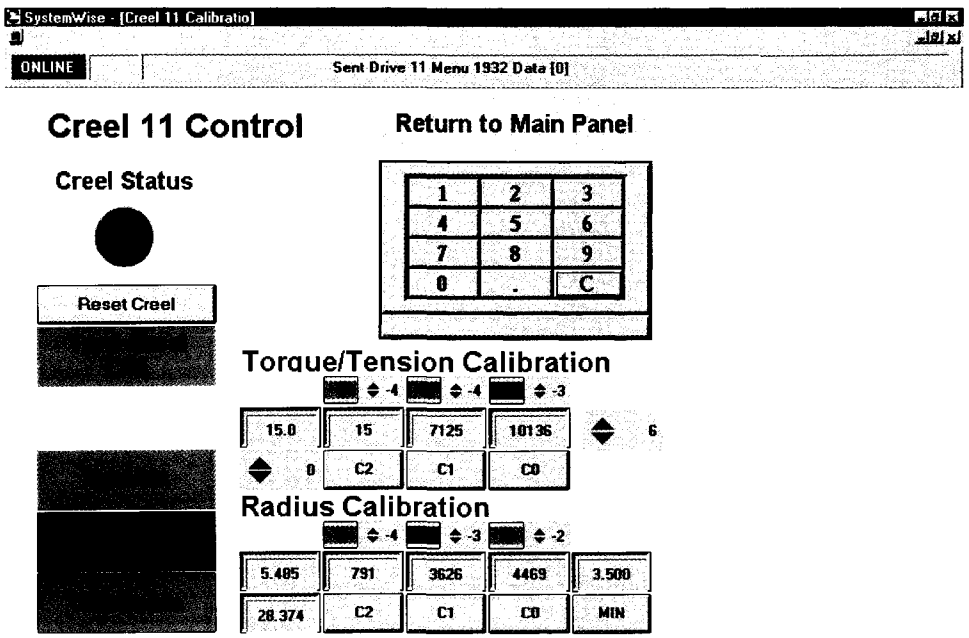

Figure A.6: Creel tension calibration control panel with number pad for data entry.

To calibrate the radius measurements, three wooden rolls of known radius are consecutively placed on the creel shaft and the radius output for each recorded. The data is then fit to a quadratic curve as described above and the constants B_0, B_1 and B_2 are stored in the controller.

The torque is then calibrated using a mandrel of known radius with an integral torsion load cell. The mandrel rotates as it is driven by the filament winding machine and therefore the load cell signal is transmitted via radio frequency to a receiver connected to an oscilloscope. The load cell is easily calibrated by wrapping a cord around the mandrel and then suspending a known weight from the end of the cord. The calibration is then done directly in tension from the weight of the mass, but the exact mandrel radius need not be known. The torque is then calibrated by measuring the tension in a tow strung from a creel mounted on the tensioner stand, along the typical winding path, and wrapped

around the calibration mandrel at a number of prescribed motor torque settings. The calibration curves have been calculated using the statistical method of least squares to determine the three constants, C_0, C_1 and C_2 for the torsion and B_0, B_1 and B_2 for the radius.

This tension system has proven to be reliable and easy to operate. Upon calibration it was found that the tension signal from the load cell contains a high frequency response about the constant value requested. It is anticipated that this is due to the excitation frequency of the motors or possibly the natural frequency of the system. Since the frequency is high the effect will not be observed in the wet fibres on the mandrel due to local sliding and force redistribution.

A.3 RESIN BATH

A McClean Anderson drum-type heated resin bath has been employed in this project. Although it is understood that the drum type resin bath is not commonly used in production, it was found to satisfactorily wet and impregnate the fibre bundles with resin. In addition, it has only a few parts for cleaning and is simple to assemble and rig the tows. The resin bath functions by directing the tow over a large diameter drum that turns through the resin bath. The contact of the moving tows with the drum causes it to turn thereby keeping the surface of the drum wet. The thickness of the resin layer on the drum is controlled using a "doctor blade" that scrapes excessive resin off the surface. At the contact on the drum, the fibres of the tensioned tow spread aiding in the impregnation of the tow. The original bath was modified by changing the inlet guide bar to a roller to reduce fibre damage by abrasion. It has been observed that dry, tensioned fibres may be seriously damaged via sliding contact where as the wet fibres are lubricated and no fuzzing occurs. The resin bath was heated to 30°C for the EPON 826/EPICURE 9551 resin system to reduce viscosity and promote wetting and impregnation. Heating the resin to 30°C reduces the pot life only marginally. To reduce resin bath clean-up, inserts to line the resin bath were produced and used. To ensure heat transfer from the water jacket to the resin, the space between the insert and the stainless steel resin bath was filled with water.

A.4 CURING OVEN

To facilitate curing large filament wound parts, a large convection oven was purchased. The Wisconsin oven has an internal envelope of 1.22 m x 1.22 m x 4.27 m and an operating temperature range of 120 to 205°C. The variation of temperature within the oven is declared to be a maximum of ±2.8°C. The oven was provided with a door on one end and a hole on the other to allow a drive shaft to pass into the oven and rotate curing parts. Rotation prevents dripping of the hot, low viscosity resin and ovalization of the completed parts.

The component and mandrel are placed on a cart fitted with rollers, to allow free part rotation, and the cart and component are rolled into the oven. The oven controller is programmable, allowing for eight programs of up to 16 ramp/hold steps. Each step is defined by a set point temperature and either a temperature ramp rate or a hold time. The cure schedule used for the parts produced for this investigation was suggested by the EPON 826/EPICURE 9551 epoxy resin supplier and is shown in Figure 2.2.

A.5 THE MANDREL SYSTEM AND EXTRACTION

The mandrels used for the production of the composite tubes in this investigation were made from readily available 50.8 mm diameter chrome surface bar stock used in manufacturing hydraulic cylinders. This material provides the required tolerance and surface finish without any extra machining. The mandrel ends were machined to fit generic flanged ends produced for a range of mandrel diameters used in the filament winding facility. The flanges provide a surface to be chucked in the winding machine, without damaging the mandrel surface, as well as allow for joining multiple mandrels together so that they may be rotated by a single drive system in the curing oven. Three mandrels, each 760 mm long, were used during each winding session. Using multiple mandrels allowed for the production of different winding sequences in a single session but more importantly were easy to handle and allowed for the use of existing equipment for extraction.

Extraction was done using a Tinius Olsen material testing system with a stroke of approximately 380 mm by pulling the steel mandrel through a brass eye. This effectively pushes the composite tube off the mandrel. Brass is used because it does not mar the chrome surface of the mandrel. Extraction loads were found to vary widely based on the tow tension applied during winding, the winding angle and the application of a release mechanism. To reduce extraction loads, Freekote 770-NC release agent (a Loctite product) was applied to all mandrels prior to winding.

A.6 SAFETY

Laboratory safety was a high priority during the development of the filament winding facility. The ventilation requirements were determined according to Alberta Occupational Health and Safety. Since the epoxy vapours are heavier than air, the ventilation system is designed to add fresh air over the mandrel and exhaust the fumes from the floor below the mandrel. An exhaust port is also located at the resin bath which has a large surface area of open resin. The facility also includes a fume hood for mixing resins and cleaning parts and a storage cabinet for flammable materials. For personal safety an eyewash/shower station has been installed and fire extinguishers are mounted near the door.

A.7 TENSION SYSTEM MECHANICAL COMPONENT DRAWINGS

This section provides the component drawings for the tension system including the creel stand and redirection tower. All dimensions provided are in inches as used by the machine shop.

Drawings are provided for:

- Creel Stand: Front and Top View — Figure A.7
- Creel Stand: Side View — Figure A.8
- Redirection Tower: Front, Top and Side Views — Figure A.9
- Glass Fibre Path — Figure A.10

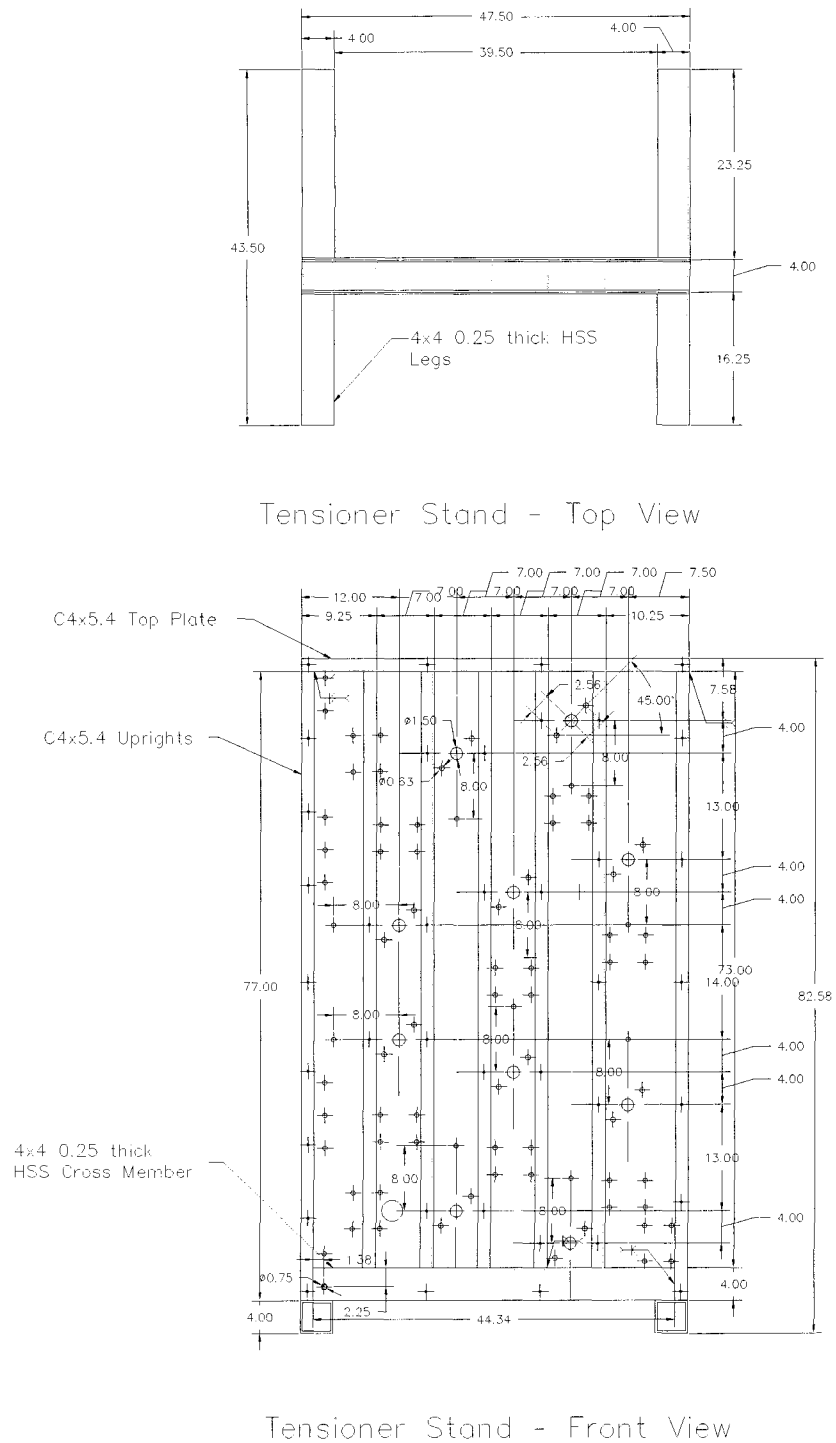

Figure A.7: Dimensioned Drawing of tension system creel stand.

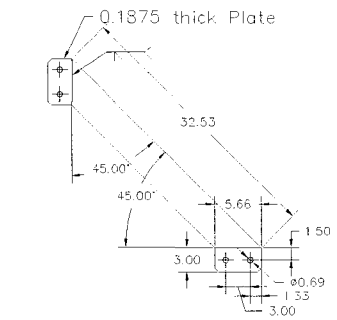

Figure A.8: Side view of creel stand.

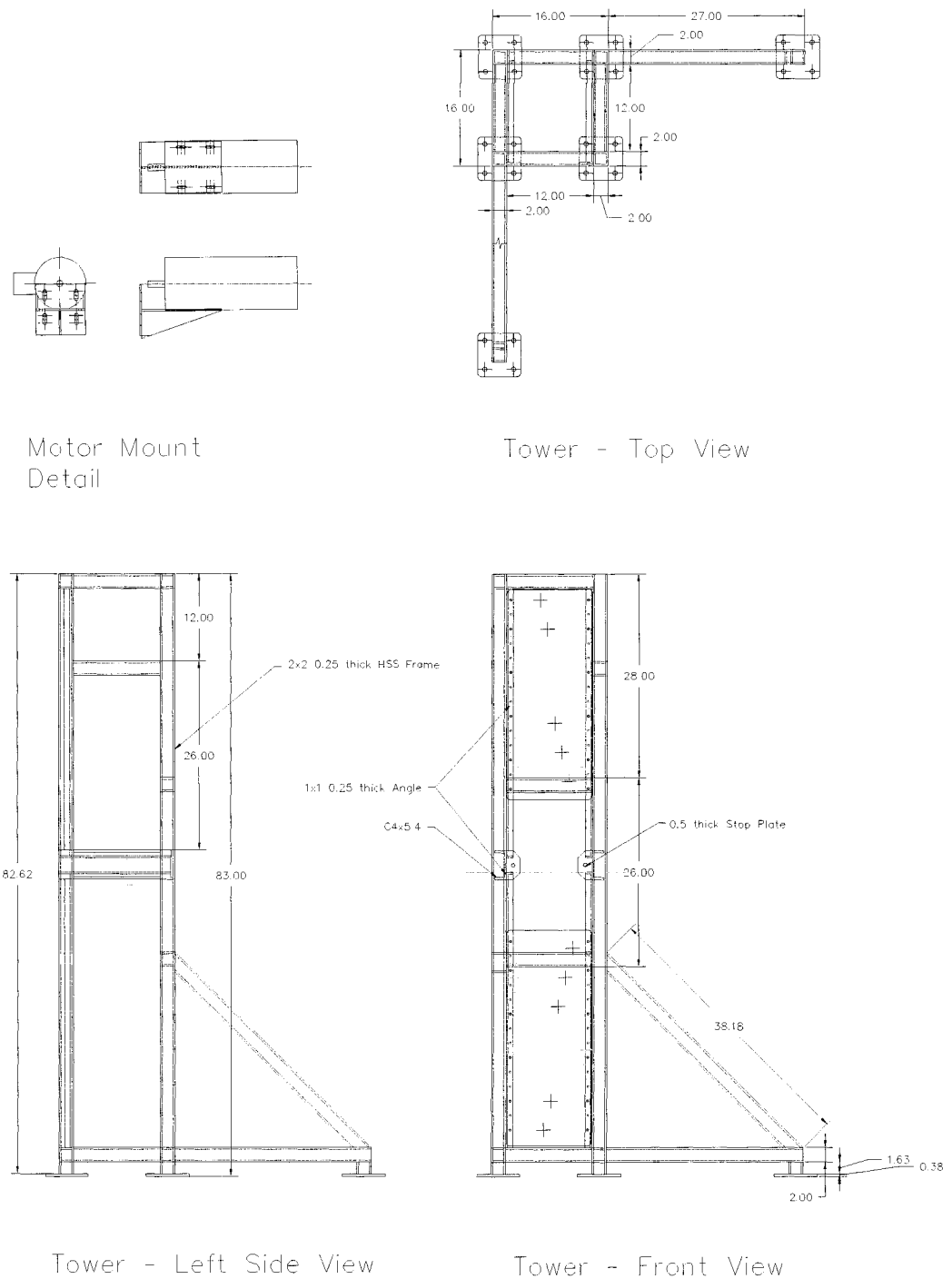

Figure A.9: Dimensioned drawing of fibre redirection tower.

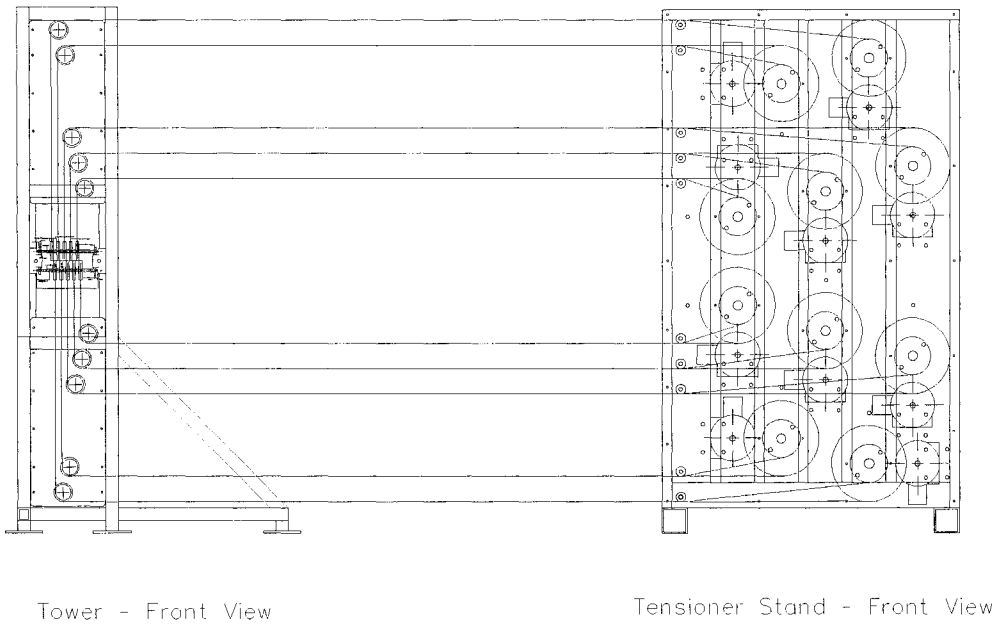

Figure A.10: Fibre path from creel stand and through redirection tower.

APPENDIX B COMPOSITE TUBE GRIP DESIGN

Multiaxial testing of the composite tubes was done by applying axial load and internal pressure. This was done on an existing material testing system with an added pressure intensifier. Specimens were mounted in the testing apparatus using a grip system designed by the author and constructed within the department of mechanical engineering. Component drawings are provided in Section B.4 for convenience.

B.1 GRIP SYSTEM

New grips, that attach the composite specimen to the material testing system, were designed and built. Reliable grips are fundamental to successful testing since they transmit the axial loads to the specimen in a uniform manner as well as seal the ends of the tubular specimen to contain the internal pressure. The goal of the new design was to accommodate the larger specimens, reduce the difficulty of filling the specimen with oil and make all parts interchangeable. The new grips are based on designs used for a number of years within the Advanced Composite Materials Engineering research laboratory. The new grips were designed and built to withstand test pressures of 103.4 MPa and axial load in excess of 44.5 kN. The capacity does depend on quality of surface treatment of the bonded substrates and interlaminar shear strength of specimen.

A grip is clearly shown in Figure 2.5 of Chapter 2. Each consists of a crown, a collar, a spoked endplate with a plug and the collet. All parts were machined from 4340 high strength steel.

A system utilising an external wedge collar/collet (parts D and E in Figure 2.5) and an internal plug (part C) was developed. An internal wedge collet system was not required because of the relatively low axial forces expected for the range of specimens to be tested. The plug, attached to the spoked end plate (part B), is fitted with dual o-rings to provide a seal for oil containment. The collar and collet are tapered at 5° to form a wedge which clamps around the specimen to transfer the axial loads. The collet was made very flexible by many longitudinal slits and can be compressed to fit tightly around the specimen end tab. Prior to assembly the collet is well greased to allow the surface to slip

to provide both a high clamping force as well as easy disassembly. A tight grip is ensured by clamping the collar and endplate together with a force of 89.0 kN in a screw driven material testing machine and then bolting the structures together. The collar is then bolted to the crown (part A) which is bolted directly to the crosshead of the testing machine. This maintains alignment, keeping critical bending stresses in the specimen to a minimum. Pulling on the collar, as opposed to the endplate, also produces a greater wedge action as the applied load is increased, reducing the possibility of the specimen slipping in the collet. Internal pressurisation is achieved via a port bored through an unused spoke on the endplate and through the plug. This arrangement places the ports in easily accessible locations for attaching the pressure line and filling of the specimen after it is mounted in the apparatus. A port on each grip allows for the specimen to be filled from the bottom while air can escape from the top port minimizing the amount of trapped air that may be compressed and the stored energy during testing. The spoked endplate has been manufactured so that it can accommodate plugs of various diameters for different sized composite tubes. Testing of tubes of significantly different diameter and wall thickness may require new end tabs as well a collet with a different internal diameter.

This type of specimen preparation was thoroughly tested previously on 38.1 mm diameter specimens and found to be satisfactory, even for the testing of axial reinforced specimens (Wolodko, 2000). In this study the reinforcement is dominantly circumferential and axial loads were not large. Therefore, some of the more elaborate features, such as tapering the inside surface of the annular region of the end tabs to produce an adhesive wedge, have not been implemented.

B.2 COMPONENT DRAWINGS

This section provides the component drawings for the specimen grip system and the jig used to align the tabs when bonding to the specimen ends. All dimensions provided are in inches as used by the machine shop. Tolerances are provided where required for fit and as specified by the o-ring manufacturer.

Drawings are provided for:

- Aluminum end tab — Figure B.1
- Tab bonding jig — Figure B.2
- Crown — Figure B.3
- Endplate — Figure B.4
- Plug — Figure B.5
- Collar — Figure B.6
- Collet — Figure B.7
- Grip system cross-section view — Figure B.8

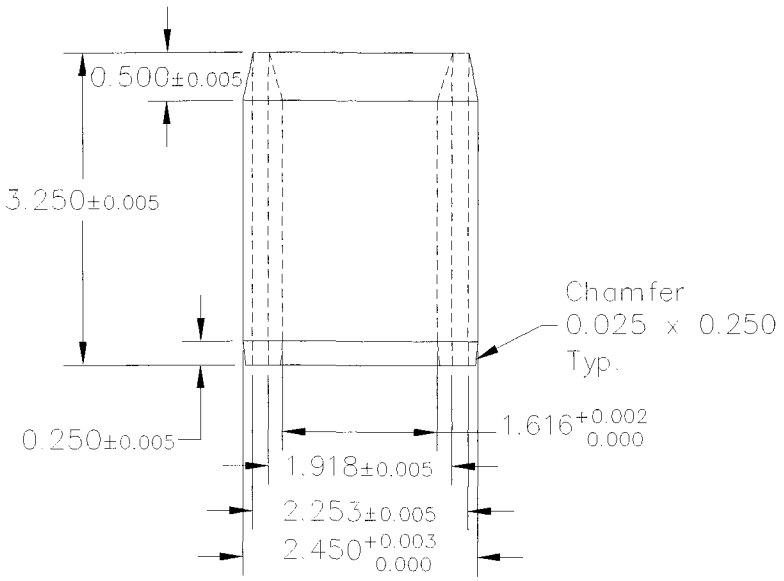

Figure B.1: Drawing of aluminum tabs that are bonded to specimen ends.

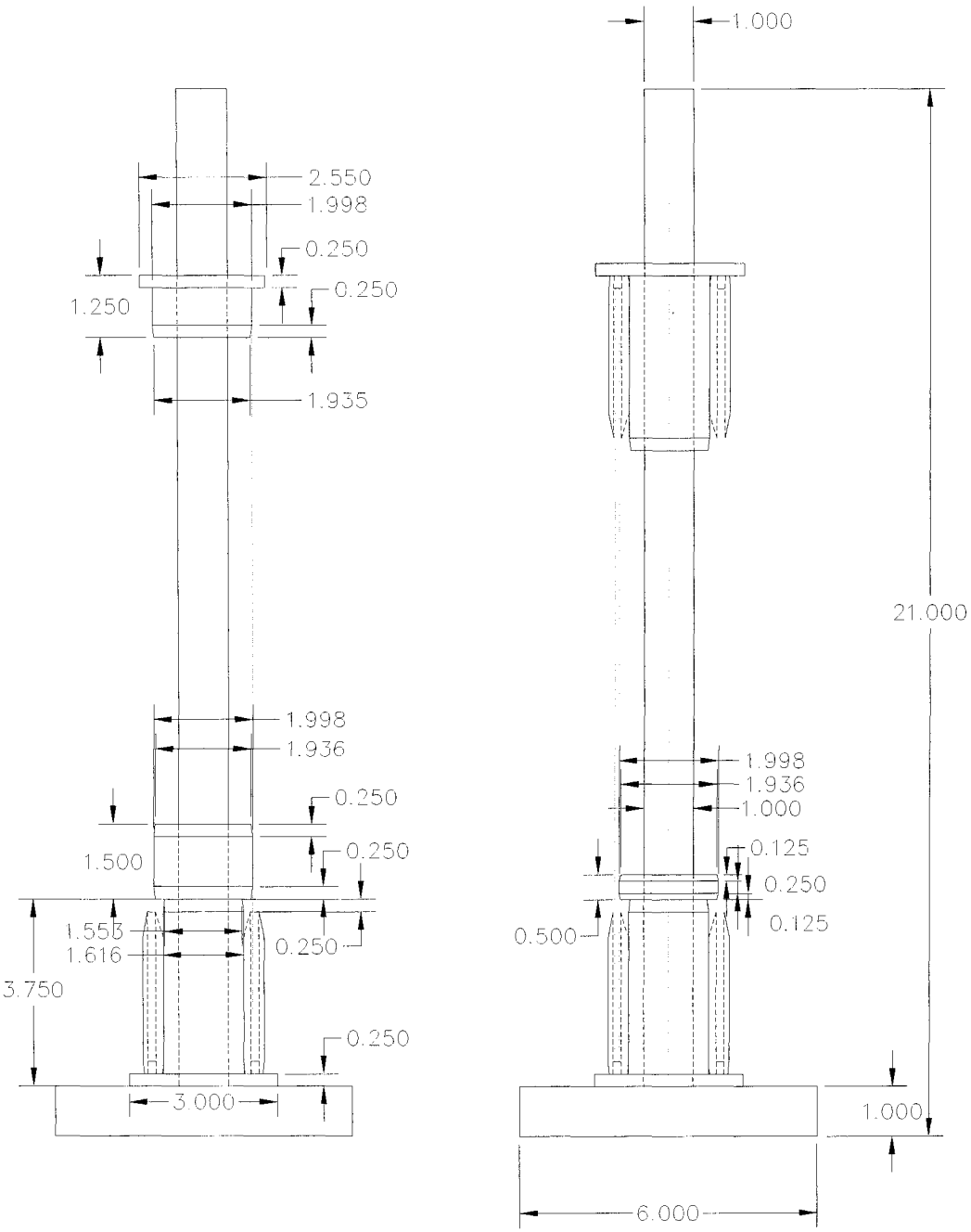

Figure B.2: Drawing of jig used to align aluminum tabs during bonding to the specimen ends.

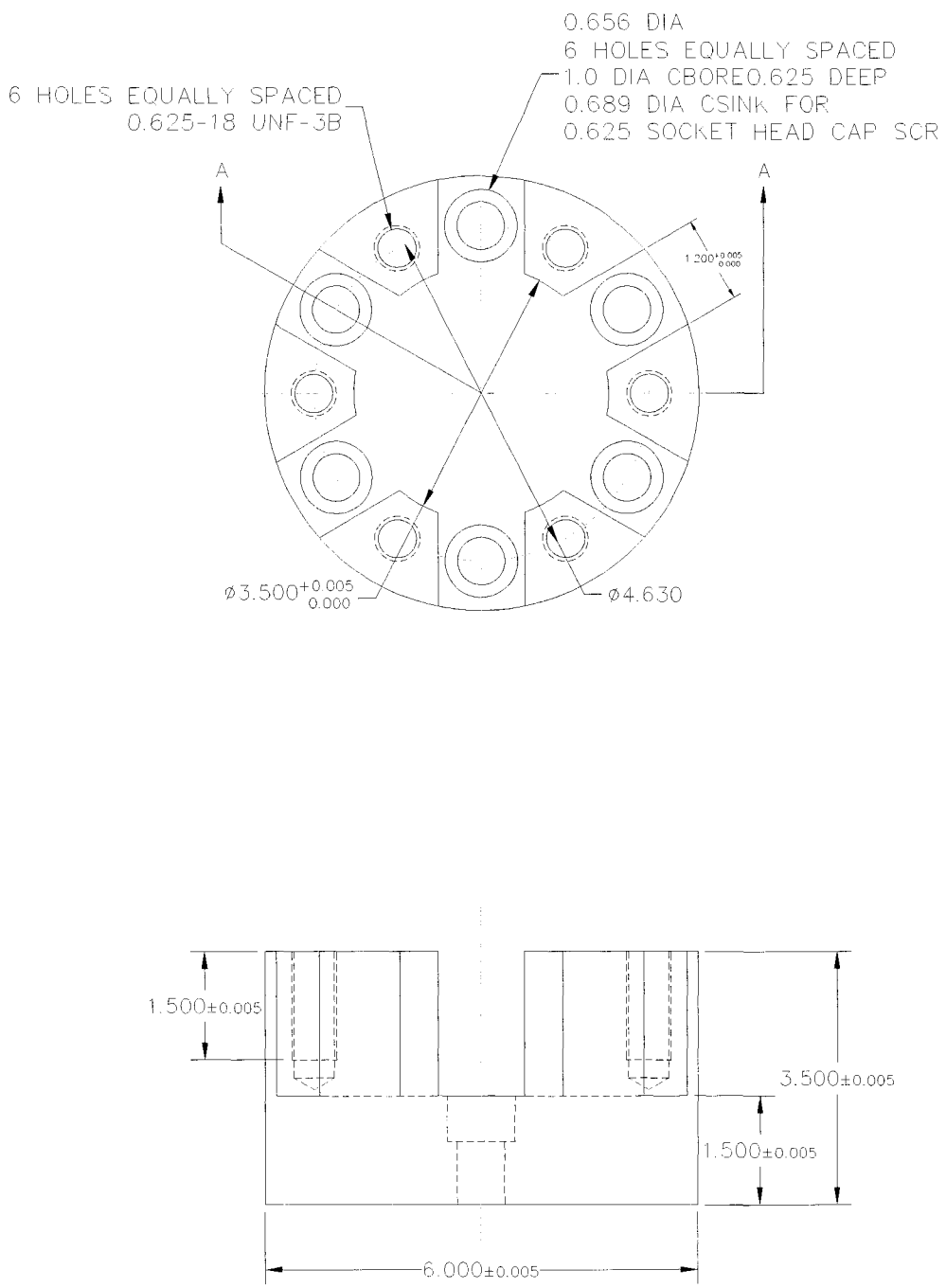

Figure B.3: The crown that adapts the specimen grip to the testing system.

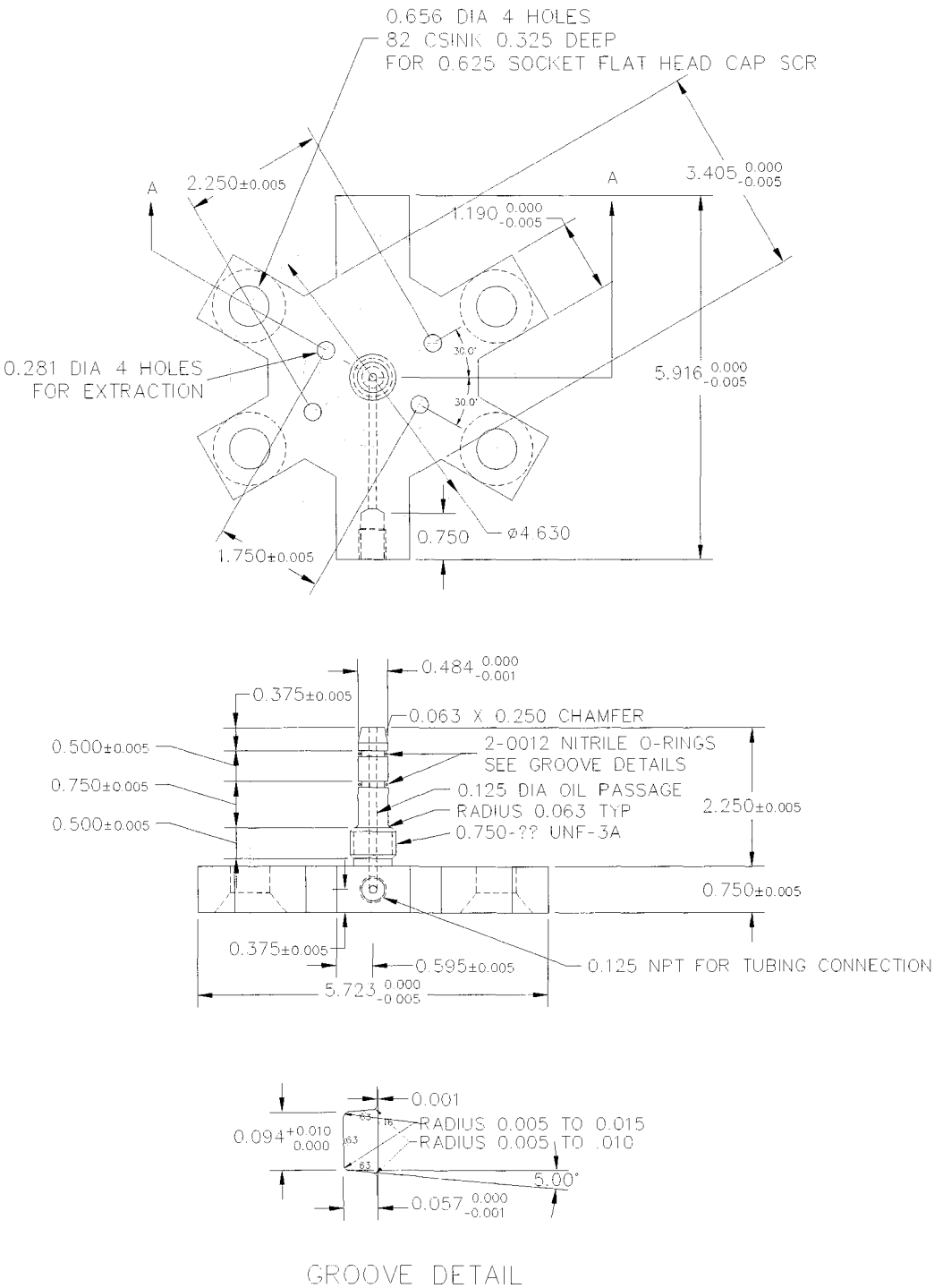

Figure B.4: Spoked endplate that receives the plug and bolts to the collar.

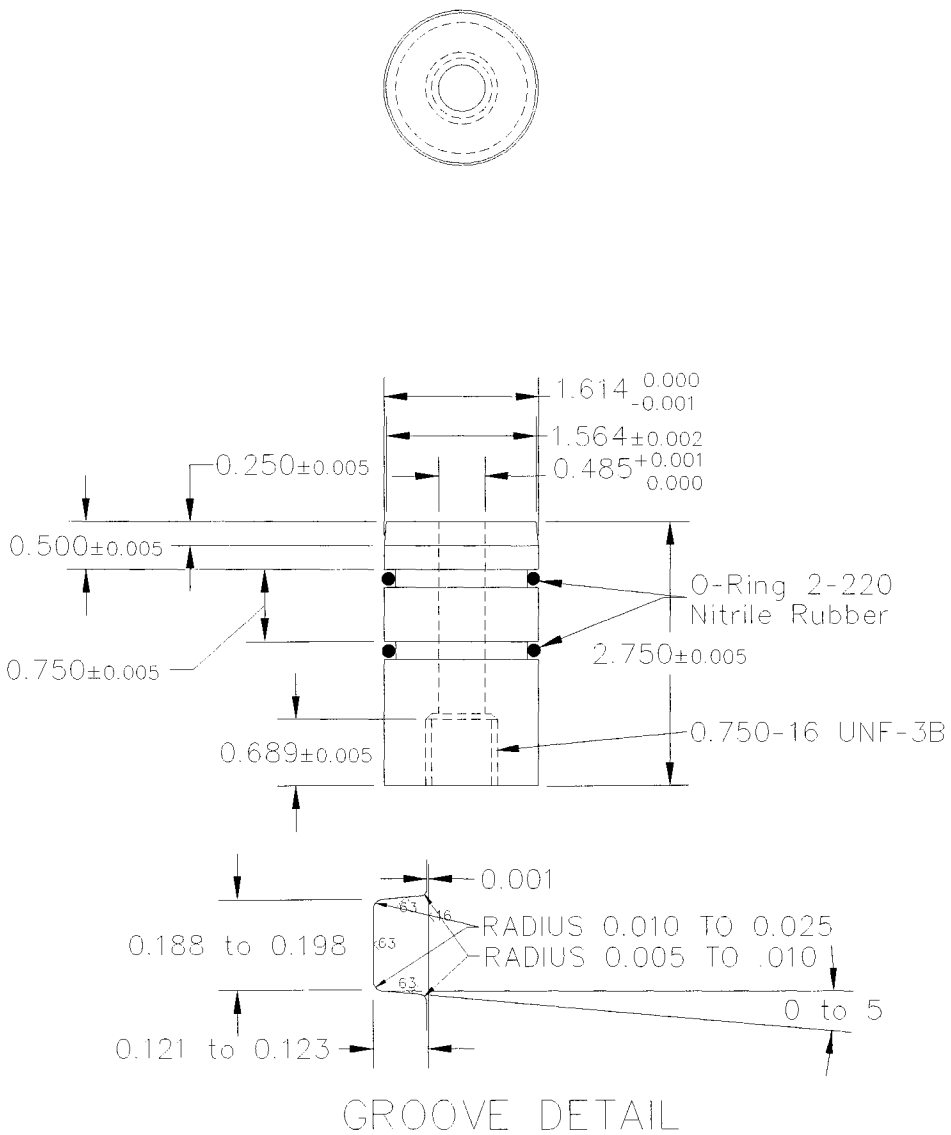

Figure B.5: Plug that fits into the aluminum tab at the specimen ends.

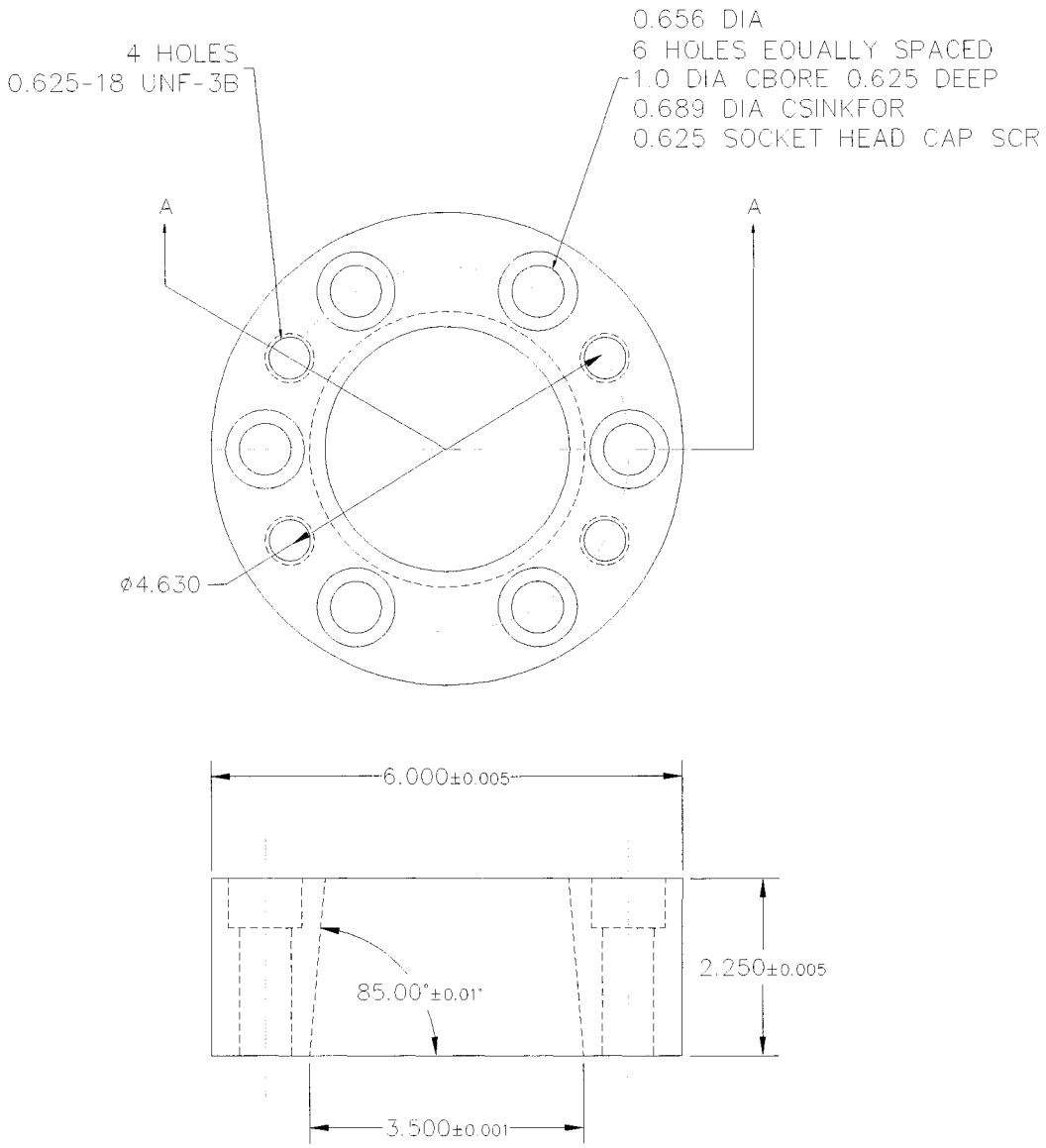

Figure B.6: Collar component of the tube grip system.

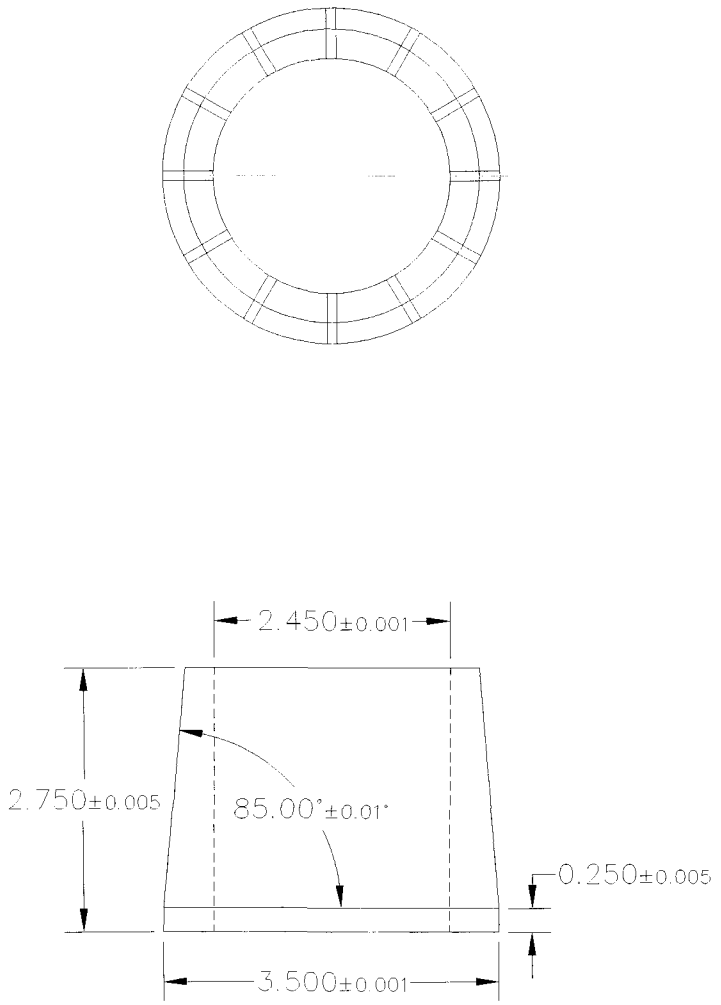

Figure B.7: Collet used to clamp around aluminum tab on specimen.

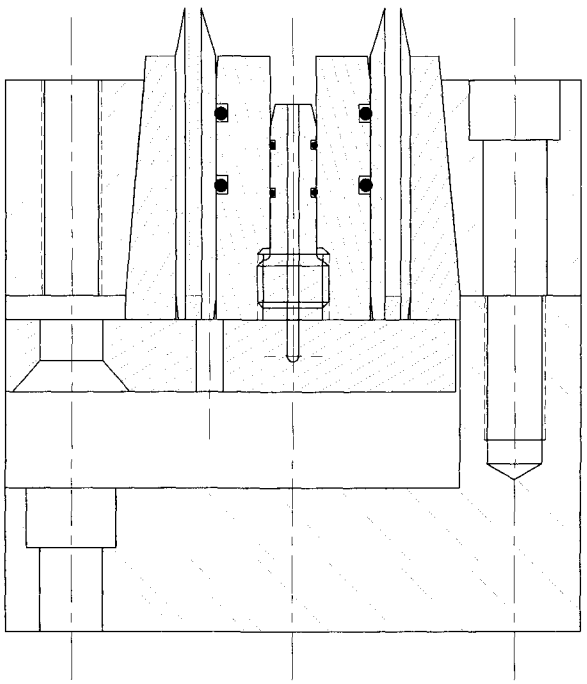

Figure B.8: Section view of the assembled grip system.

APPENDIX C FINITE ELEMENT MODELLING

The finite element method is used to solve the analysis of a crack propagating through a thick laminate. Special consideration has been given to model the polymer interleaf and glass fibre reinforced epoxy as isotropic viscoelastic and transversely isotropic viscoelastic materials, respectively. In addition, the model geometry and discretisation is described with details on the application of constraints and loads.

C.1 IMPLEMENTATION OF THE MATERIAL MODEL

The isotropic and transversely isotropic material models are implemented through the user-programmable-features of ANSYS. This allows the software user to produce a subroutine in FORTRAN code that models the material response based on material properties, current stress and strain state, temperature, time and numerous possible parameters.

Given the stress and strain at the beginning of the time increment and the strain increment, the subroutine must return the stress-strain relationship (instantaneous stiffness matrix) over the time increment. The software then uses the Newton-Raphson technique to solve the nonlinear problem for the stress and strain at the end of the time increment.

In this implementation, the user-programmed subroutine must consider both the isotropic and transversely isotropic derivations of the viscoelastic model. While the isotropic response is a sub set of the transversely isotropic domain, in this implementation they are solved by separate routines. This was done primarily to eliminate the coordinate translations, required to align the transversely isotropic material in the laminate, from the isotropic calculations which are independent of orientation.

A flow chart for the viscoelastic model is shown in Figure C.1.

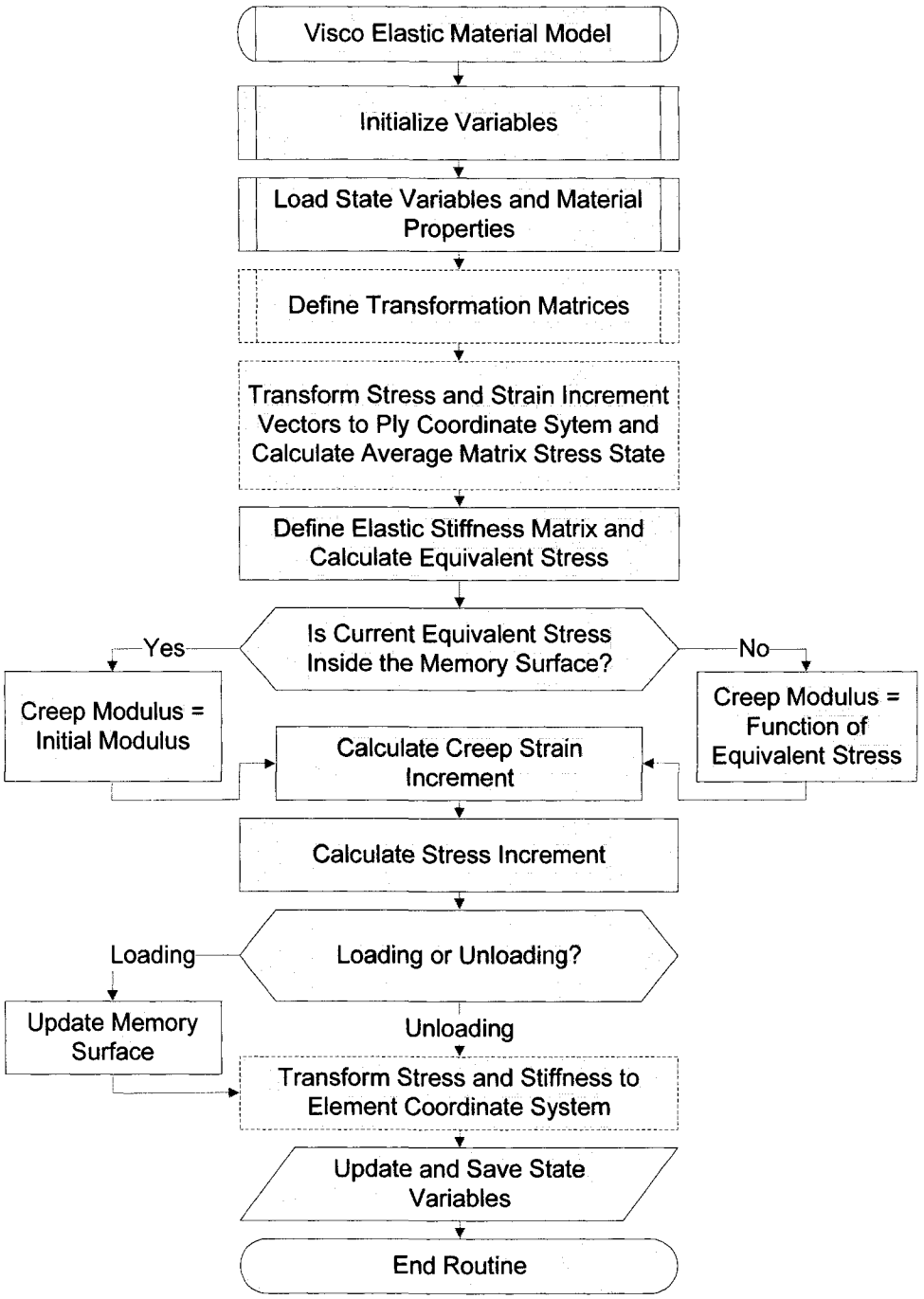

Figure C.1: Flow chart of subroutine execution for viscoelastic material model.

In Figure C.1 the solid out line boxes indicate actions related to both the isotropic and transversely isotropic viscoelastic material models and the actions surrounded by dashed lines are for the transversely isotropic model. These pertain mostly to transforming the

stress and strain vectors and stiffness tensors to the material coordinate system. The other significant difference is the use of equivalent stress of the matrix material only in the transversely isotropic model for the fibre reinforced polymer.

This subroutine in compiled in a visual FORTRAN and then linked to the ANSYS executable using the provided utilities.

C.2 NUMERICAL SOLUTION CONVERGENCE

It is well known that the division of the geometric model into finite elements has a great impact on the quality of results produced. Often a finite element mesh must be refined at stress concentrations to accurately model the stress/strain gradients. This becomes particularly true in nonlinear analyses. Also important in nonlinear analyses is the size of the solution increment. Using a convergence solution, such as Newton Raphson, can increase accuracy but it must be recognised that the incremental process still accumulates error. This is particularly important in this analysis of time dependent materials. At high stresses the viscoelastic material will undergo large creep strain rates which may lead to unrealistic deformations if the time increment is too long. In the case of this crack tip analysis, the creep strain rates are large at the crack tip but rapidly drop as the stress is relaxed. If the crack tip element is too large the stress singularity is distributed over too large of an area resulting in greater model deformation. If the time increment of solution is too long the high strain rate acts for too long yielding large displacements before the stress is relaxed and the strain rate drops.

To determine the effect of the finite element mesh three models of varying element size were compared. It is found that while there is little difference in the elastic results, there is significant variation in the viscoelastic response, as expected. The sizes of the models are provided in Table C.1 and they are shown in Figure C.2, Figure C.3 and Figure C.4.

Table C.1: Mesh sizes for convergence analysis.

Model	Number of Nodes	Number of Elements
Fine Mesh	9450	4560
Standard Mesh	5322	2556
Coarse Mesh	3432	1650

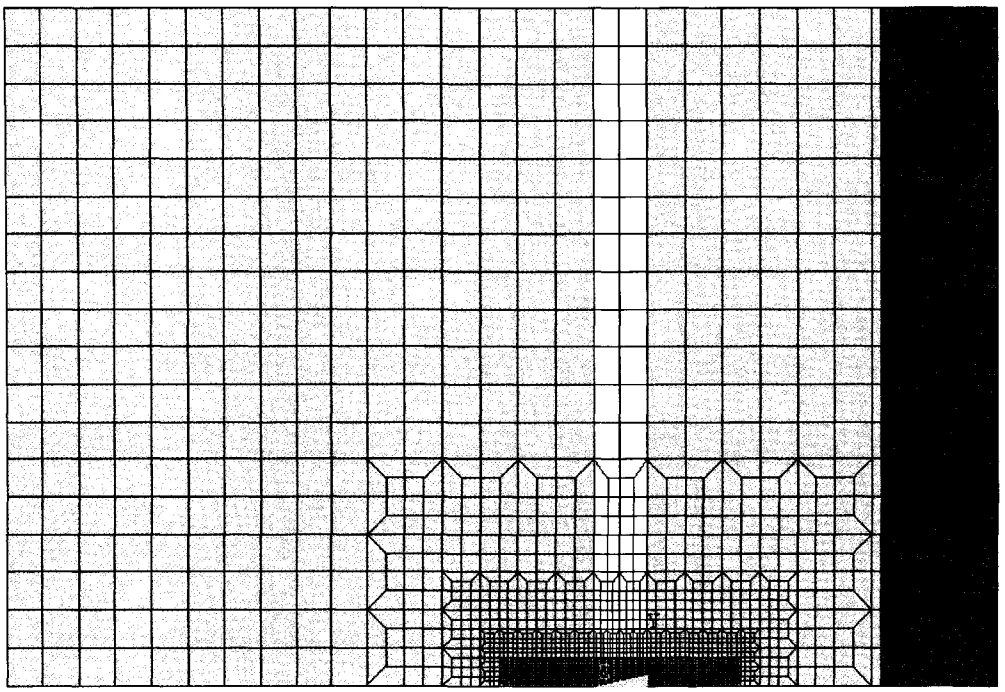

Figure C.2: Medium density finite element mesh.

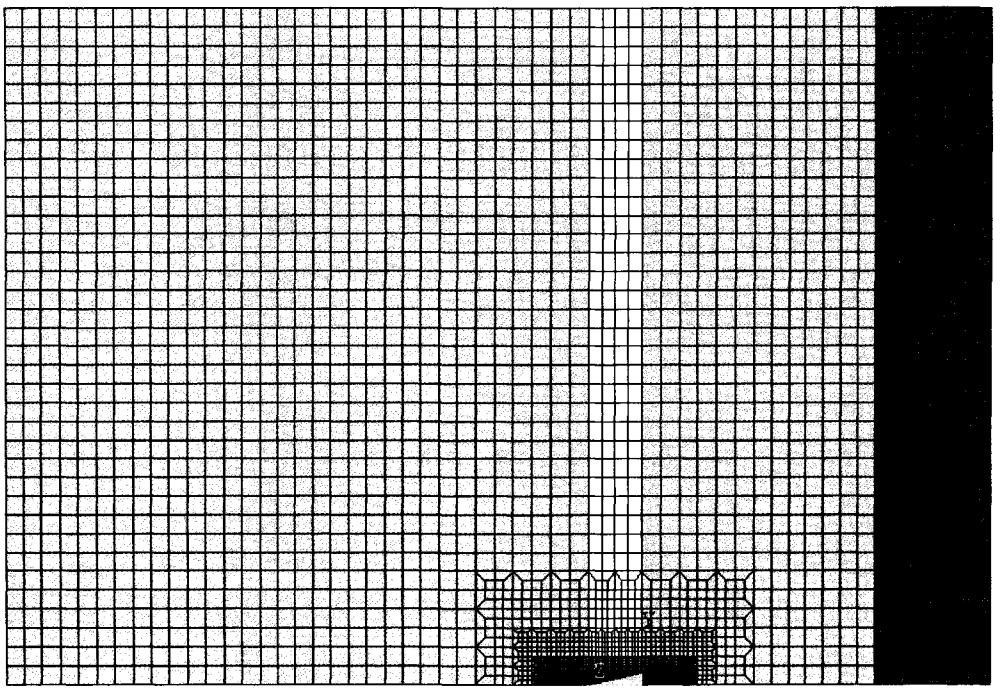

Figure C.3: Fine finite element mesh.

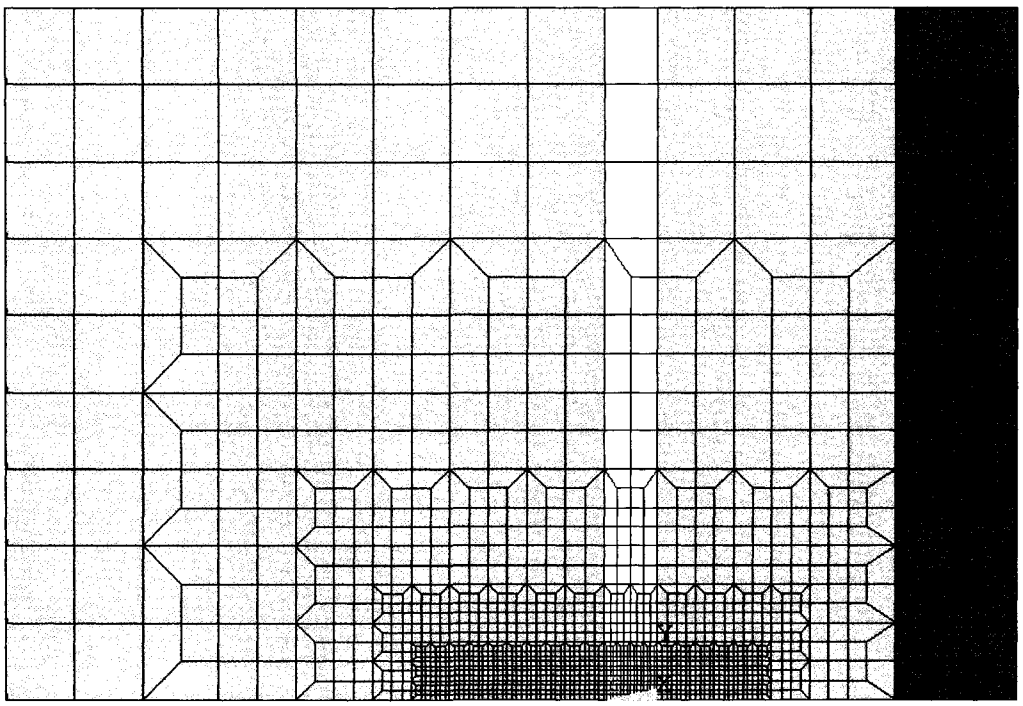

Figure C.4: Coarse finite element mesh.

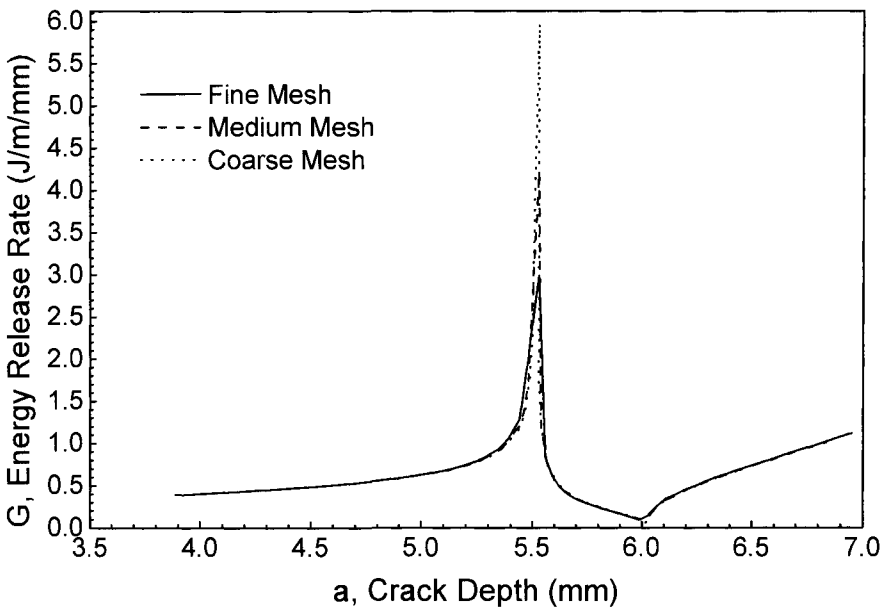

Figure C.5: Comparison of elastic results from the three mesh density models.

All of the models were generated starting with the common section of graded element sizes and applying a scaling factor. The elements in the fine mesh are one half the size of the corresponding elements in the medium density mesh and the elements in the coarse mesh are twice the size. While the elastic, or time independent material, solution accuracy will be influenced by mesh density, the viscoelastic solution is also affected by the new crack increment size and the hold period applied after each crack growth step. In order to keep the crack growth rate the same, when the crack increment is doubled the hold time should also be doubled. However, the viscoelastic effect, either creep strain or stress relaxation, is dependent on the current stress/strain state.

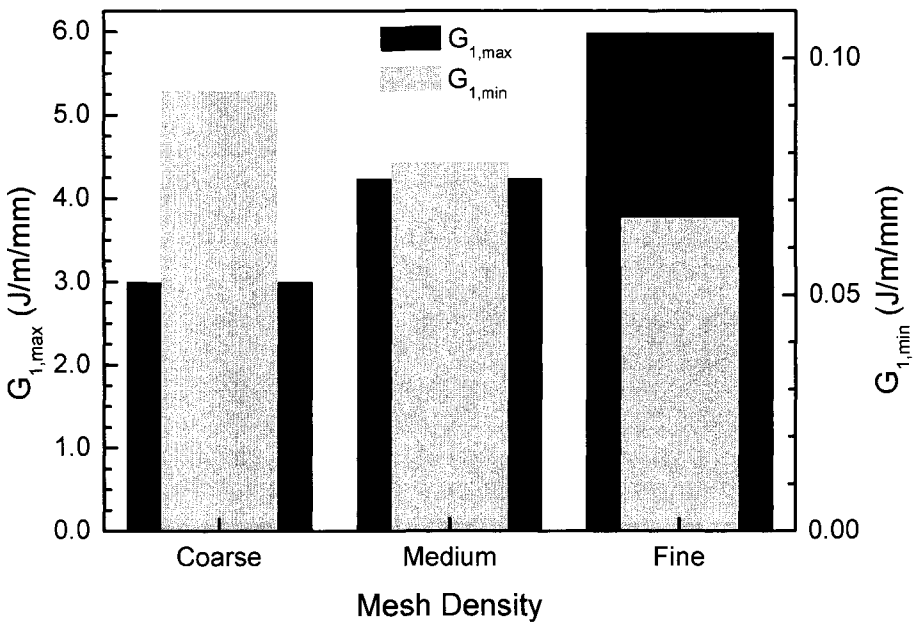

Figure C.6: Comparison of elastic results from the three mesh density models.

Figure C.5 shows the results of the strain energy release rate, G, as the crack progressed through the model when the materials are elastic. When the crack tip is away from the interleaf/laminate interfaces, G is independent of mesh density. However when the crack tip is at an interface, there is a change in model stiffness and the trend of G changes, there is a clear dependence on the finite element mesh. This is most obvious as the crack tip progresses from the 90° layers into the interleaf. There is a large change in stiffness and a

large spike in the energy release rate. The finer the mesh, the more accurately the gradient is represented therefore the maximum G increases with increasing mesh density. A minima is found as the crack exits the interleaf. Once again this effect is more accurately modelled by the fine mesh although the difference produced by the three meshes is not large like for the previously described maxima. The effect of mesh density on these important points are summarised in Figure C.6.

Comparison of the influence of mesh in a viscoelastic model is more difficult since the effect of time delay and crack step size become critical. Figure C.7 shows the effect of mesh size when the time delay between crack growth steps is adjusted so that the analyses have identical crack propagation rates.

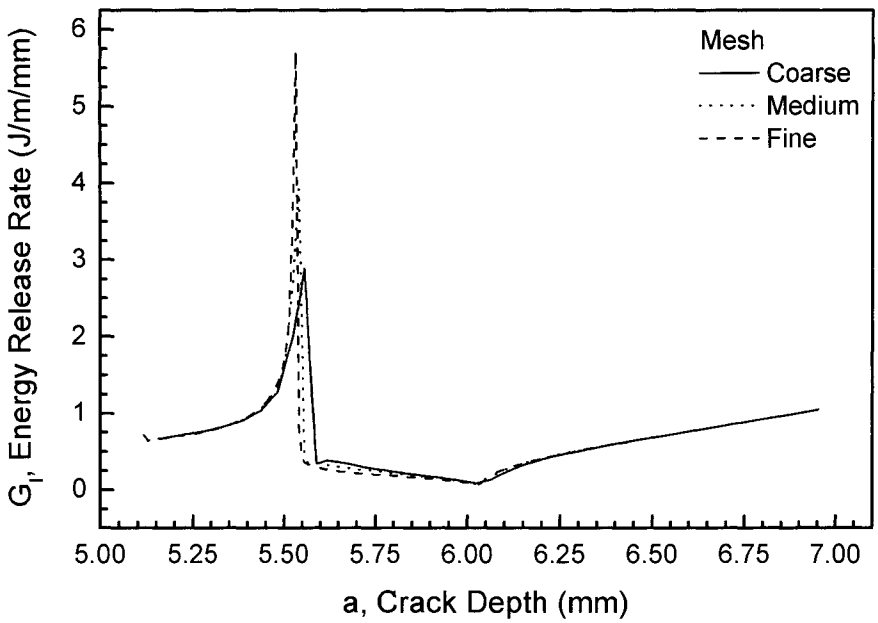

Figure C.7: Comparison of viscoelastic results from the three mesh density models where crack growth delay is adjusted to produce identical crack growth rates.

It is observed that decreasing the mesh size significantly decreases the calculated strain energy release rates. If this is in fact true, then the results of analyses with identical crack step sizes and time delays should produce similar results. This is plotted in Figure C.8.

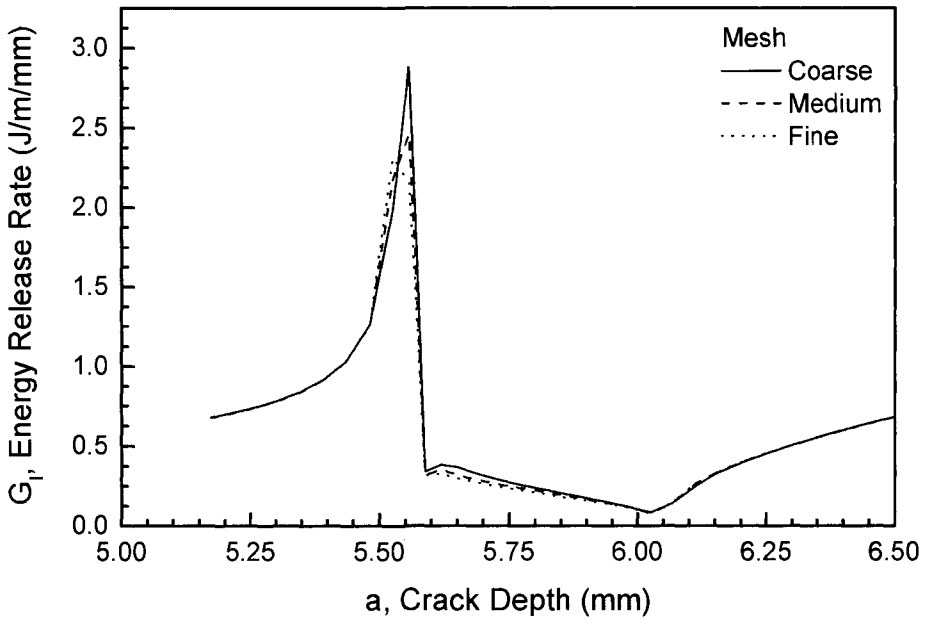

Figure C.8: Comparison of viscoelastic results from the three mesh density models where crack growth step size and delay time are identical in each analysis.

Of course the results for the coarse mesh are identical since no variables have changed. In the case of the medium and fine meshes the behaviour in the interleaf and beyond are very similar to the previous results but tend to be slightly higher than the previous results. Also note that there is little difference in the minima in Figure C.8 where there is greater variation in Figure C.7. Therefore it is confirmed that the results are converging to the correct values but it is also noted that the minima is more sensitive to ideal modeling of the time than to the mesh density.

C.3 FINITE ELEMENT MESHES

The numerical investigation includes a study of the geometric parameters, interleaf thickness and position within the laminate. Each situation requires a different finite element mesh. Once again, all the models were generated starting with the zone of varying element size to provide the resolution required in the crack growth zone. Models were varied by moving this zone and controlling the width of the zone. The models for

various interleaf positions and thickness are provided in Figure C.9 to Figure C.13. The thick interleaf is 1 mm thick and the thin interleaf is 0.25 mm thick.

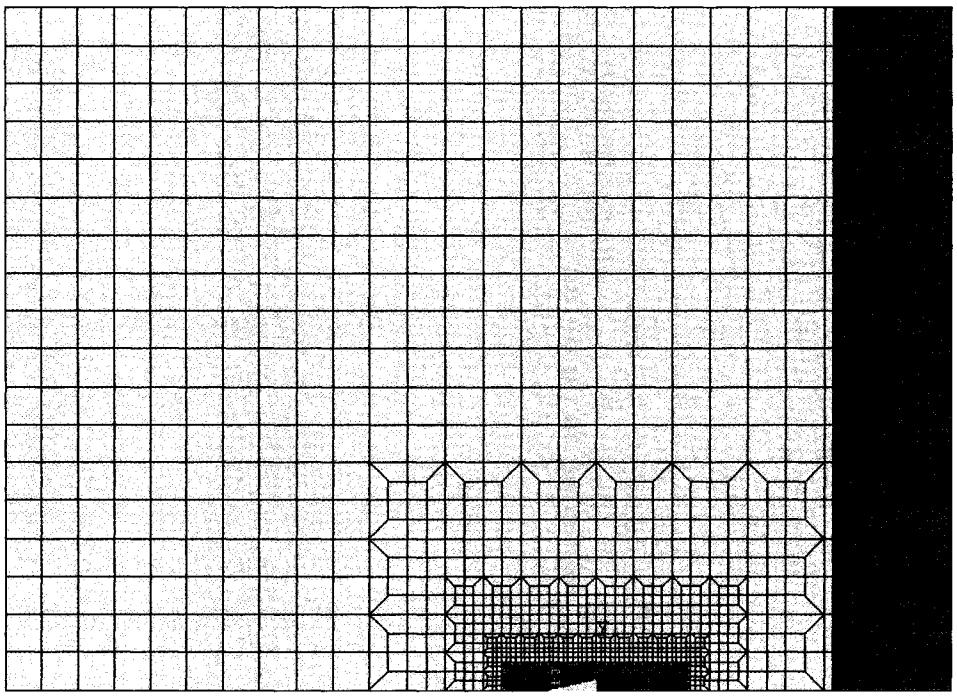

Figure C.9: Finite element mesh for laminate without interleaf.

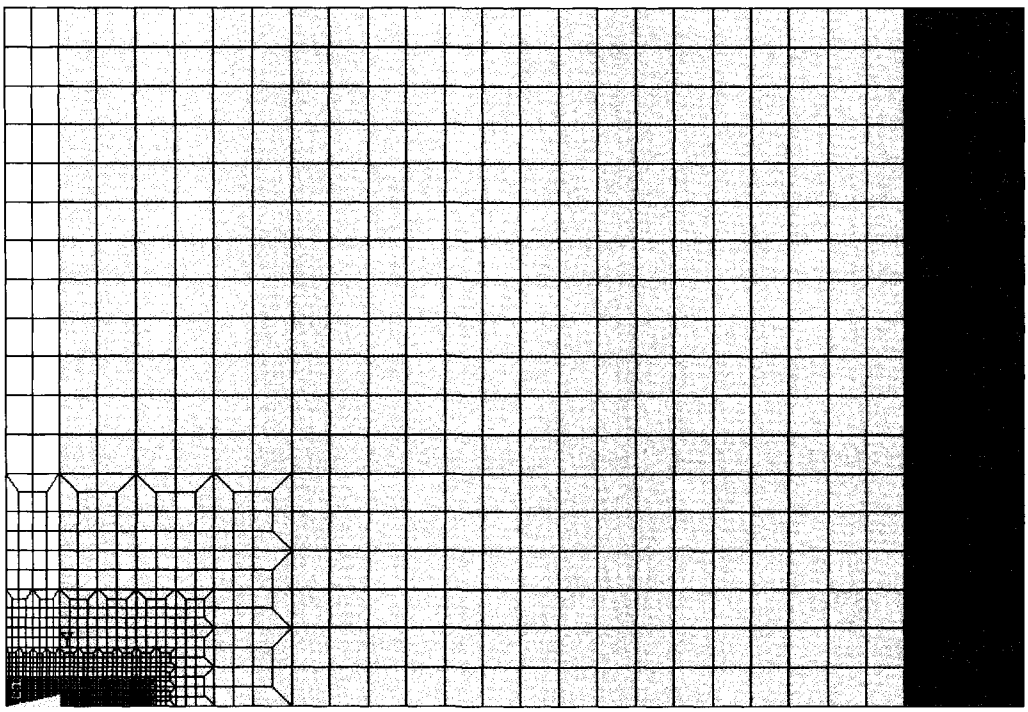

Figure C.10: Interleaf placed on outside surface of laminate.

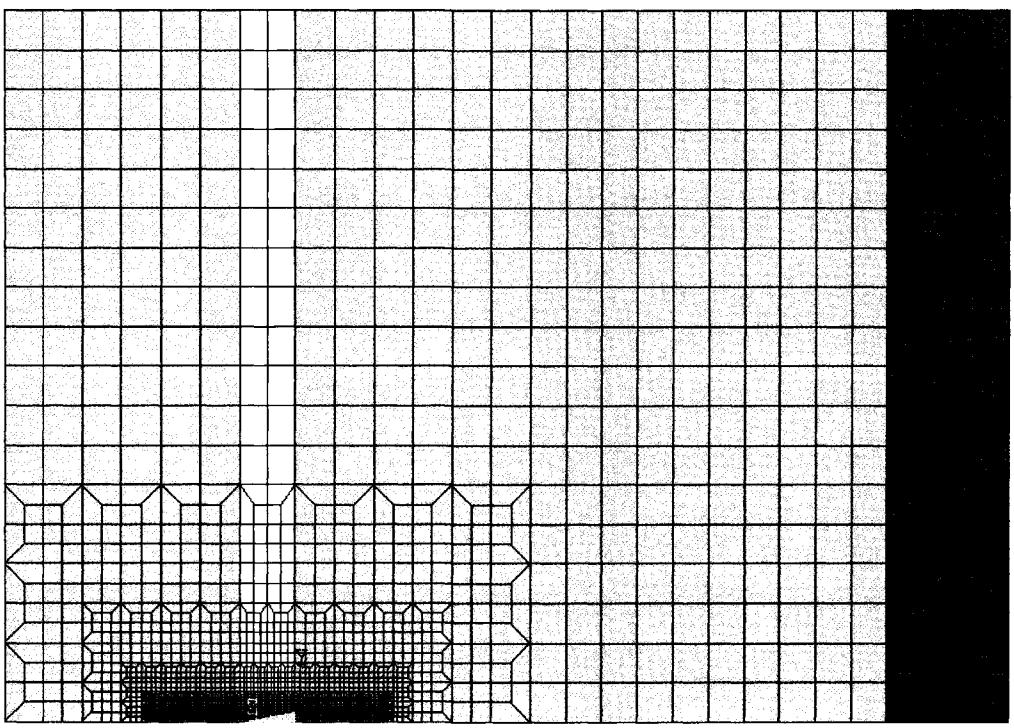

Figure C.11: Interleaf placed in a forward position.

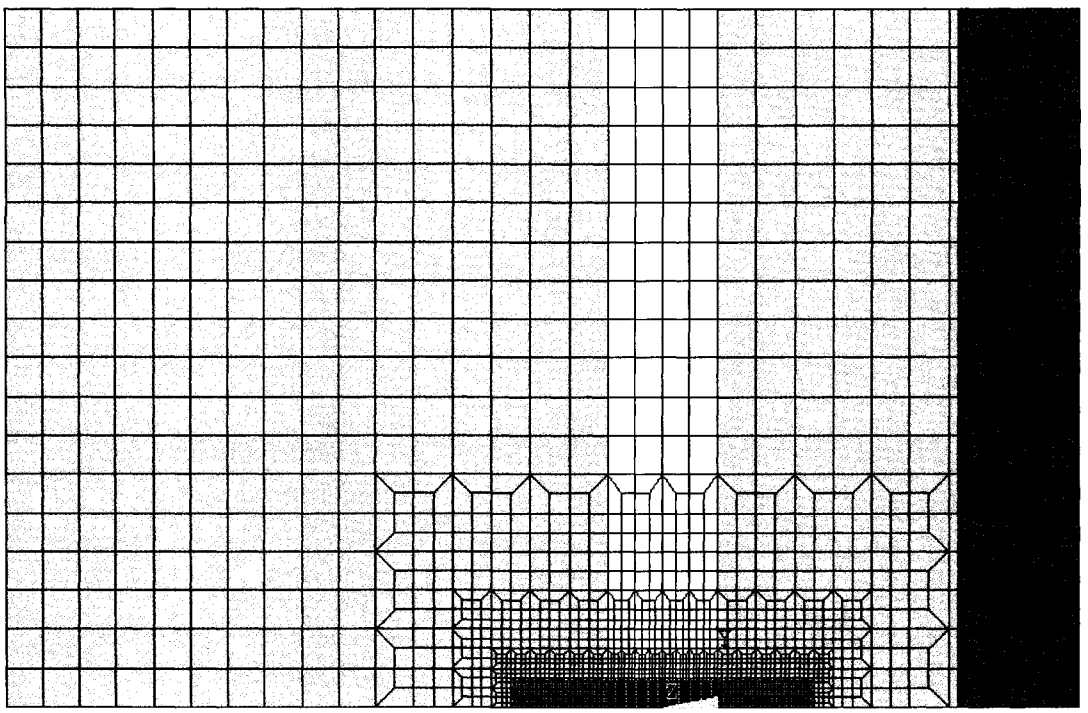

Figure C.12: Thick Interleaf model.

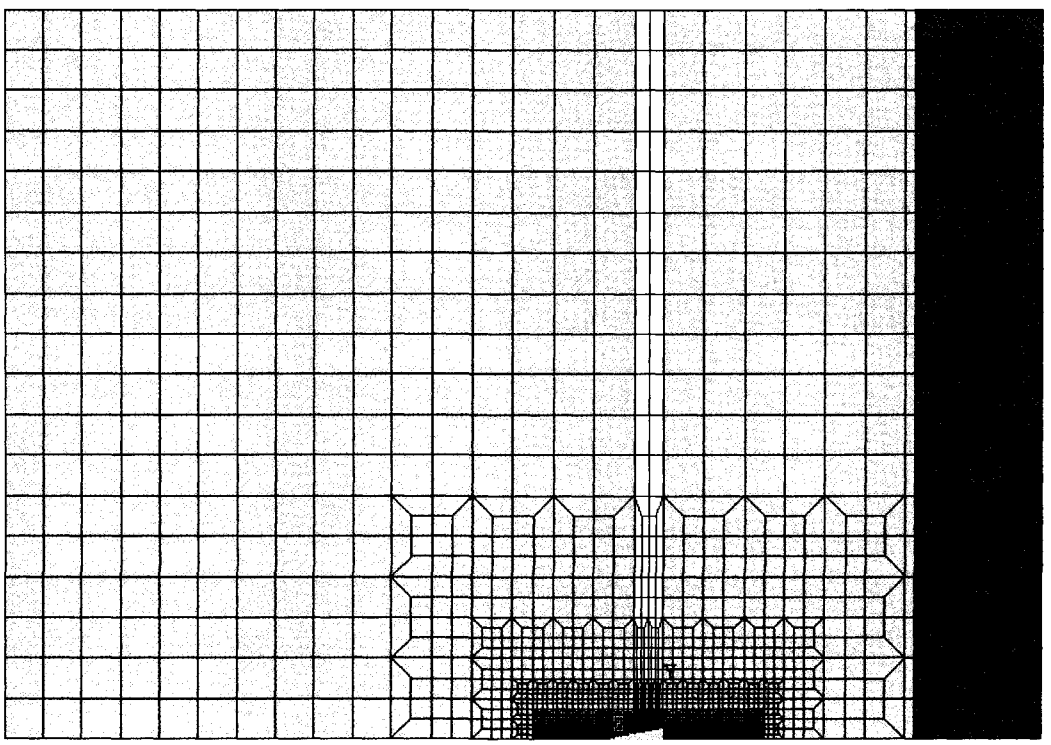

Figure C.13: Thin Interleaf model.